REFERENCE ONLY

2809288699

UNIVERSITY OF LONDON THESIS

Degree phd Year 2007 Name of Author SINEAD LOUISE FARRELL

COPYRIGHT

This is a thesis accepted for a Higher Degree of the University of London. It is an unpublished typescript and the copyright is held by the author. All persons consulting the thesis must read and abide by the Copyright Declaration below.

COPYRIGHT DECLARATION

I recognise that the copyright of the above-described thesis rests with the author and that no quotation from it or information derived from it may be published without the prior written consent of the author.

LOAN

Theses may not be lent to individuals, but the University Library may lend a copy to approved libraries within the United Kingdom, for consultation solely on the premises of those libraries. Application should be made to: The Theses Section, University of London Library, Senate House, Malet Street, London WC1E 7HU.

REPRODUCTION

University of London theses may not be reproduced without explicit written permission from the University of London Library. Enquiries should be addressed to the Theses Section of the Library. Regulations concerning reproduction vary according to the date of acceptance of the thesis and are listed below as guidelines.

A. Before 1962. Permission granted only upon the prior written consent of the author. (The University Library will provide addresses where possible).

B. 1962 - 1974. In many cases the author has agreed to permit copying upon completion of a Copyright Declaration.

C. 1975 - 1988. Most theses may be copied upon completion of a Copyright Declaration.

D. 1989 onwards. Most theses may be copied.

This thesis comes within category D.

☐ This copy has been deposited in the Library of UCL

☐ This copy has been deposited in the University of London Library, Senate House, Malet Street, London WC1E 7HU.

Bound By
Blissett Bookbinders
020 8992 3965

Satellite Laser Altimetry over Sea Ice

Sinéad Louise Farrell

A thesis submitted to the University of London for the degree of Doctor of Philosophy

Centre for Polar Observation and Modelling
Department of Space and Climate Physics
University College London

October 2006

UMI Number: U592799

All rights reserved

INFORMATION TO ALL USERS
The quality of this reproduction is dependent upon the quality of the copy submitted.

In the unlikely event that the author did not send a complete manuscript
and there are missing pages, these will be noted. Also, if material had to be removed,
a note will indicate the deletion.

UMI U592799
Published by ProQuest LLC 2013. Copyright in the Dissertation held by the Author.
Microform Edition © ProQuest LLC.
All rights reserved. This work is protected against
unauthorized copying under Title 17, United States Code.

ProQuest LLC
789 East Eisenhower Parkway
P.O. Box 1346
Ann Arbor, MI 48106-1346

I, Sinéad Louise Farrell, confirm that the work presented in this thesis is my own. Where information has been derived from other sources, I confirm that this has been indicated in the thesis.

Signed .....

Abstract

The Arctic region plays an important role in the global climate system through various feedbacks, involving surface albedo, oceanic deep-water formation, and sea surface salinity, which can amplify climate variability and change. We investigate the exploitation of data collected by the first Earth-orbiting laser altimeter carried onboard ICESat over the sea-ice covered regions of the Arctic Ocean. We extract parameters associated with the study of the polar climate system including the time-varying component of sea surface topography and sea ice freeboard.

We assess an existing method for the retrieval of Arctic sea surface height from ICESat data. We present an alternative method for sea surface height retrieval, based on surface reflectivity and analysis of parameters associated with the shape of the received echo. This method aims to discriminate echoes originating over leads or thin ice. We provide the first maps of Arctic sea surface height as derived from ICESat. We examine the accuracy of our results through comparisons with independent sea surface height estimates derived from ENVISAT radar altimetry.

We demonstrate the use of sea surface height data for oceanographic and geodetic applications in the Arctic Ocean. We derive an ICESat mean sea surface which, when combined with the recently developed Arctic hybrid geoid model, can be used to analyse mean dynamic ocean topography. In addition we investigate the use of ICESat sea surface height measurements to map marine gravity anomalies up to the limit of coverage at 86°N.

By combining ICESat surface elevation measurements with sea surface height estimates, we derive sea ice freeboard throughout the Arctic up to 86°N. We compare our results to coincident estimates of sea ice freeboard from ENVISAT. Finally, we explore the feasibility of combining satellite laser and radar altimetric measurements of sea ice freeboard to measure the depth of snow loading on sea ice.

Acknowledgements

I would first like to thank my supervisor Dr. Seymour Laxon for giving me the opportunity to conduct this research project. I am grateful for his guidance and for providing a critical review of this thesis. Thanks also to all the staff and students at CPOM and the Department of Earth Sciences, UCL. I would particularly like to acknowledge Andy Ridout for his timely assistance and useful discussions.

It is with great pleasure that I thank Dr. Dave McAdoo at NOAA for his unwavering encouragement, and furthermore for his collaboration on various aspects of my research.

I wish to thank Drs. Jay Zwally, Donghui Yi and Anita Brenner for hosting me at NASA Goddard and for their stimulating discussions during my stay. I thank the members of the ICESat Science team, particularly Dr. Helen Fricker, for useful discussions on the details of the ICESat data and their helpful comments.

I would like to thank my family (near and far) for the pep talks and the prayers – you are all a source of continued motivation and inspiration. I would especially like to thank my parents Jean and Michael, and sister Niamh, without whose love and support this would not have been possible. I am indebted to the Farrells of Hanwell for accommodating me in the last stages of my PhD. I thank Andy for his endless encouragement, help and love – thanks for always being there for me. I am grateful to all my friends who made my studies at UCL so enjoyable – laughter really is the best medicine. Although copious amounts of red wine (thanks mostly to Dr. Milica Todorovic) also helped!

This work was funded under National Environment Research Council studentship NER/S/A/2002/10425. I acknowledge NASA's ICESat Science Project and the NSIDC for distribution of the ICESat data.

To my family and Andy

Table of Contents

Title page 1
Abstract 3
Acknowledgements 4
Table of Contents 6
List of Figures 11
List of Tables 15

1. The Role of Sea Ice in the Climate System

1.1 Introduction 16
1.2 The Global Climate System 17
1.2.1 Components of the Global Climate System 17
1.2.2 Global Climate Change 18
1.2.3 Projections for the Global Climate System 20
1.3. The Arctic Climate System 23
1.3.1 Circulation and Structure of the Arctic Ocean 25
1.3.2 Arctic Climate Change 26
1.3.3 Projections for the Future Arctic Climate System 28
1.4 Sea Ice and the Climate System 29
1.4.1 Characteristics of Sea Ice 29
1.4.2 Influence of Sea Ice on the Climate System 30
1.4.2.1 Ocean-ice-atmosphere Interactions 31
1.4.2.2 Radiation Balance of the Earth's Surface 32
1.4.2.3 Global Thermohaline Circulation 32
1.5 Observing and Modelling Arctic Sea Ice 33
1.5.1 Sea Ice Extent - Observations and Trends 33
1.5.2 Current Knowledge of Sea Ice Thickness 35
1.5.3 Model Projections of Arctic Sea Ice 39
1.5.4 Current Status of Spaceborne Altimeter Estimates of Sea Ice Thickness 42
1.6 Summary 46

2. Satellite Laser Altimetry

2.1 Introduction 48

2.2 Overview of Satellite Altimetry 48

2.3 ICESat Mission Overview 51

2.4 Principles of Satellite Laser Altimetry 54

2.5 Range Corrections 56

2.5.1 Radial Orbit Error - Precision Orbit Determination 56

2.5.2 Pointing Determination – Precision Attitude Determination 57

2.5.3 Tropospheric Delay 59

2.5.4 Forward Scattering due to Clouds 60

2.6 GLAS Error Budget 61

2.7 Geophysical Effects on the Sea Surface Topography 64

2.7.1 The Geoid 65

2.7.2 Dynamic Ocean Topography 66

2.7.3 Tidal Corrections 67

2.7.4 Atmospheric Pressure Loading 68

2.8 Summary 71

3. Exploitation of ICESat Data over Sea Ice

3.1 Introduction 72

3.2 Data Description 72

3.2.1 ICESat Data 72

3.2.2 Other Data Sets 73

3.2.2.1 Satellite Radar Altimetry 74

3.2.2.2 Satellite Imagery 75

3.2.2.3 Sea Ice Drift Data 76

3.2.2.4 Sea Ice Concentration Data 76

3.3 Characteristics of ICESat Data 76

3.3.1 Parameters used in Geophysical Analysis of ICESat Data over sea ice 76

3.3.1.1 Transmitted and Received Pulse Waveforms 77

3.3.1.2 Procedure to Calculate Elevation and Geolocate Footprint 79

3.3.1.3 Footprint Time Tag 81

3.3.1.4 Received Energy 82

3.3.1.5 Received Pulse Gain 83

3.3.1.6 Reflectivity 83
3.3.1.7 Geoid Height 84
3.3.1.8 Dry Tropospheric Range Correction 85
3.3.1.9 Saturation Range Correction 85
3.3.2 Status of Selected ICESat Parameters 87
3.4 Applications of ICESat altimetry in the Arctic – review of recent results and current status 90
3.4.1 Deriving sea ice freeboard distributions from ICESat data 90
3.4.2 Analysis of ICESat data and RADARSAR imagery 92
3.4.3 ICESat data in combination with a geoid model for sea ice freeboard retrieval 92
3.4.4 Retrieval of ICESat elevations using the ArcGP geoid 94
3.4.5 Sea surface height retrieval over the open ocean 95
3.4.6 Reflectivity as an indicator of newly formed ice and leads 95
3.5 Aims of this Study 96
3.6 Summary 98

4. Retrieval of Altimetric Sea Surface Height Measurements in Ice Covered Seas

4.1 Introduction 99
4.2 Auxiliary Data 99
4.2.1 The Arctic Geoid 100
4.2.1.1 ArcGP 100
4.2.1.2 Hybrid Geoid 100
4.2.2 The Arctic Mean Sea Surface 101
4.2.2.1 ERS-2 Mean Sea Surface 101
4.3 Data Filtering and Pre-processing 104
4.3.1 Sea Ice Concentration Filter 104
4.3.2 Elevation Filter 105
4.3.3 Waveform Filter 105
4.3.4 High Gain Filter 105
4.3.5 Reflectivity Filter 107
4.3.6 Low Gain Saturation Correction 107
4.4 Methodology for the Retrieval of Sea Surface Height Measurements 107

4.4.1 Method 1: GSFC Algorithm 108
4.4.2 Method 2: UCL Algorithm 109
4.4.2.1 Parameters to Describe the Shape of a GLAS Pulse 109
4.4.2.2 Development of UCL Algorithm 112
4.4.3 Identification of Large Leads 115
4.5 Along track analysis 118
4.5.1. Results 118
4.5.1.1 Analysis of MODIS image 118
4.5.1.2 Analysis of AATSR image 123
4.5.2 Discussion 125
4.6 Summary 126

5. Assessment of Altimetric Sea Surface Height Measurements in Ice Covered Seas

5.1 Introduction 128
5.2 Sea Level Anomalies 129
5.3 Single Satellite Crossover Analysis 130
5.3.1 Key Results 134
5.4 Comparison of Sea Level Anomalies from ICESat and ENVISAT 135
5.4.1 Monthly SLA 135
5.4.1.1 Key Results 135
5.4.2 Short-term Variations in SLA in the Arctic Ocean 139
5.4.2.1 Key Results 140
5.4.3 Comparison of 3-day SLA Estimates from ICESat and ENVISAT 141
5.4.3.1 Key Results 144
5.4.4 Discussion 151
5.5 Comparison of Arctic Freeboard using the GSFC and UCL algorithms 154
5.5.1 Key Results 164
5.6 Conclusions 166

6. Applications of ICESat Altimetry for Arctic Oceanography and Marine Geophysics

6.1 Introduction 169

6.2 Ocean Circulation Studies and Model Comparison 170
6.2.1 Extension of the Mean Sea Surface beyond 81.5°N 170
6.2.2 Altimetric Measurements of the Time-invariant Dynamic Ocean Topography 172
6.3 Measurement of the Marine Gravity Field of the Arctic Ocean from ICESat 175
6.4 Conclusions 178

7. Cryospheric Applications of ICESat Altimetry in the Arctic Ocean

7.1 Introduction 180
7.2 Arctic Snow Freeboard from ICESat 180
7.2.1 Laser Altimetric and Radar Altimetric SSH Measurements for the Derivation of Snow Freeboard 181
7.3 Arctic Freeboard Estimates from Laser and Radar Altimetry 190
7.4 Snow Loading on Sea Ice 193
7.5 Conclusions 196

8. Conclusions

8.1 Introduction 198
8.2 Assessment of Achievements 198
8.2.1 Primary Aims 198
8.2.2 Summary of Key Findings 202
8.3 Directions for Future Work 206
8.3.1 Inclusion of supplementary ICESat data 206
8.3.2 Development of an optimised algorithm for sea surface height retrieval 206
8.3.3 Investigation of the sea level anomaly signal 207
8.3.4 Investigation of the differences between radar and laser altimetric estimates of sea surface height 207
8.3.5 Snow depth retrieval 207
8.3.6 Extending the analysis to Antarctic sea ice 208

Appendix A: List of Acronyms 209

Appendix B: Deriving Thresholds for Lead Discrimination 210

Bibliography 216

List of Figures

1. The Role of Sea Ice in the Climate System

1.1 The components of the global climate system 17

1.2 Northern Hemisphere temperature reconstruction and instrumental data from AD 1000 to 1999 19

1.3 Annual time-series of global temperature anomalies from 1861 to 2000 19

1.4 Changes in atmospheric composition 21

1.5 Projected global mean temperature change for the six SRES scenarios using a simple climate model tuned to seven AOGCMs 22

1.6 Political map of the Arctic Region 23

1.7 Bathymetric and topographic features of the Arctic 24

1.8 Surface currents of the Arctic Ocean 25

1.9 Arctic Ocean circulation and water mass structure in cross-section 26

1.10 Annual anomalies of land-surface air temperature in the Arctic 27

1.11 Aerial photography of Arctic sea ice in the Bering and Beaufort Seas 30

1.12 The global ocean thermohaline conveyor belt 33

1.13 Seasonal variability of sea ice extent 34

1.14 Historical record of sea-ice extent in April in the Nordic Seas 34

1.15 Sea ice extent and concentration anomalies for September 2002 – 2004 35

1.16 Regional and seasonal distribution of sea ice thickness 36

1.17 Changes in mean sea ice draft in the Arctic Ocean 38

1.18 The 14-model mean and intermodel spread of annual sea ice thickness for the Arctic region 41

1.19 The 14-model mean and intermodel spread of annual sea ice thickness differences between CO^2 doubling and the corresponding control runs 41

1.20 Schematic diagram of a sea ice floe in hydrostatic equilibrium 42

1.21 Mean winter sea ice thickness in the Arctic Ocean 44

1.22 The latitudinal coverage of satellite radar and laser altimeter 44

2. Satellite Laser Altimetry

2.1 Comparison of laser and radar altimetry 50

2.2 Spatial coverage of ICESat ground tracks over the Arctic 53

2.3 Satellite laser altimetry concept 55

2.4 Concept of the laser altimetry range error 58
2.5 Examples of forward scattering in GLAS waveforms 62
2.6 Satellite altimetric measurement of sea surface height 65
2.7 Amplitude of the main ocean tide constituents 69

3. Exploitation of ICESat Data over Sea Ice

3.1 Typical radar altimeter return waveforms over Arctic sea ice 74
3.2 An along-track elevation profile over Arctic sea ice derived from radar altimetry data 75
3.3 Schematic illustrating the concept of range to surface measurement for a transmitted and received laser pulse 77
3.4 Schematic illustrating the waveform fitting procedure used for calculating the range and elevation distribution from a typical set of transmitted and received GLAS pulses 80
3.5 Flow diagram describing the calculation of range corrections showing the order in which the parameters are computed 82
3.6 Flow diagram outlining the order in which range measurements are corrected, footprint geolocation calculated, and surface elevation estimated 82
3.7 Effects of saturation on GLAS received pulses acquired over the salar de Uyuni 87
3.8 Estimating sea level from ICESat altimetry data 91
3.9 The first Arctic sea ice freeboard estimates derived from ICESat altimetry 91
3.10 A comparison of near-coincident RADARSAT and ICESat data 93
3.11 Comparison of ICESat sea ice freeboards with freeboard estimates derived from airborne laser altimetry 94
3.12 ICESat elevations after the removal of a state-of-the-art geoid model 94

4. Retrieval of Altimetric Sea Surface Height Measurements in Ice Covered Seas

4.1 The Arctic hybrid geoid 101
4.2 The ERS-2 Arctic mean sea surface 102
4.3 Standard deviation of sea surface heights used to construct the ArcGICE MSS 103
4.4 Illustration of the along-track transition between clear and cloudy conditions over Arctic sea ice 106
4.5 Comparison of satellite imagery with a near-coincident ICESat overpass 113

4.6 Profiles of elevation, standard deviation of elevation, and reflectivity across a large lead acquired 117
4.7 Comparison of the UCL and GSFC algorithms with a near coincident MODIS image 120
4.8 ICESat elevation profile and selected ICESat waveforms across the centre of a MODIS image 121
4.9 Arctic sea ice drift map 123
4.10 AATSR image with two coincident ICESat overpasses 124

5. Assessment of Altimetric Sea Surface Height Measurements in Ice Covered Seas

5.1 Spatial coverage of ICESat and ENVISAT ground tracks over Arctic sea ice for a 3-day period 130
5.2 Single satellite crossovers over 3-day periods 132
5.3 Single satellite crossover statistics for the L1 through to the L3b campaigns 133
5.4 ICESat minus ENVISAT SLA differences for five ICESat laser campaigns 137
5.5 Distributions of ICESat minus ENVISAT SLA height differences for five ICESat laser campaigns 138
5.6 Mean 3-day ENVISAT SLA for the period 04 Oct – 15 Nov 2003 140
5.7 Dual satellite crossover height differences for 3-day periods 142
5.8 Distributions of dual satellite crossover height differences for 3-day periods 143
5.9 L2a campaign 3-day SLA dual-satellite crossover statistics 145
5.10 L3a campaign 3-day SLA dual-satellite crossover statistics 146
5.11 L1 campaign 3-day SLA dual-satellite crossover statistics 147
5.12 L2b campaign 3-day SLA dual-satellite crossover statistics 148
5.13 L3b campaign 3-day SLA dual-satellite crossover statistics 149
5.14 3-day mean ocean tide correction averaged over the ice-covered regions of the Arctic Ocean 152
5.15 Comparison of ENVISAT SLA and the MOG2D-G inverse barometer correction 153
5.16 Arctic snow freeboard, h_{sf_UCL}, during autumn 2003 156
5.17 Arctic snow freeboard, h_{sf_GSFC}, during autumn 2003 157
5.18 Arctic snow freeboard, h_{sf_UCL}, during spring 2004 158
5.19 Arctic snow freeboard, h_{sf_GSFC}, during spring 2004 159
5.20 Arctic snow freeboard, h_{sf_UCL}, during autumn 2004 160

5.21 Arctic snow freeboard, h_{sf_GSFC}, during autumn 2004 161
5.22 Arctic snow freeboard, h_{sf_UCL}, during spring 2005 162
5.23 Arctic snow freeboard, h_{sf_GSFC}, during spring 2005 163

6. Applications of ICESat Altimetry for Arctic Oceanography and Marine Geophysics

6.1 Arctic Ocean mean sea surface height estimated from ERS-2 and ICESat 171
6.2 Estimates of the mean dynamic topography (MDT) of the Arctic Ocean 173
6.3 Gravity field of the Arctic Ocean derived from ERS-1 and ICESat 177

7. Cryospheric Applications of ICESat Altimetry in the Arctic Ocean

7.1 Arctic snow freeboard, h_{sf_UCL}, from 21 Feb to 07 Mar 2003 184
7.2 Arctic snow freeboard, h_{sf_RA}, from 21 Feb to 07 Mar 2003 185
7.3 Arctic snow freeboard, h_{sf_RA}, from 04 Oct to 11 Nov 2003 186
7.4 Arctic snow freeboard, h_{sf_RA}, from 04 Oct to 11 Nov 2003 187
7.5 Arctic snow freeboard, h_{sf_RA}, from 09 to 26 Oct 2004 188
7.6 Arctic snow freeboard, h_{sf_RA}, from 09 to 26 Oct 2004 189
7.7 Comparison of satellite laser and radar altimetric estimates of Arctic sea ice freeboard during spring 2003 191
7.8 Comparison of satellite laser and radar altimetric estimates of Arctic sea ice freeboard during autumn 2003 192
7.9 Comparison of satellite laser and radar altimetric estimates of Arctic sea ice freeboard during autumn 2004 193
7.10 Arctic snow loading on sea ice during autumn 2003 195

List of Tables

2. Satellite Laser Altimetry

2.1 ICESat mission specifications 53
2.2 Single-shot error budget for ICESat elevation measurements 63
2.3 Magnitude of the components of the ICESat tide correction 68

3. Exploitation of ICESat Data over Sea Ice

3.1 Description of ICESat data releases 73
3.2 Description of ICESat parameters used in analysis presented in this thesis 78
3.3 Criteria for identifying low gain and high gain pulse saturation 87
3.4 Description of current status of relevant ICESat parameters 88

4. Retrieval of Altimetric Sea Surface Height Measurements in Ice Covered Seas

4.1 Description of filters applied to ICESat data prior to processing 104
4.2 Description of parameters associated with transmitted and received waveforms 110
4.3 Criteria for discriminating open water within the ice pack 113
4.4 Criteria for discriminating large leads within the ice pack 115
4.5 Comparison of the number of leads identified by the GSFC and UCL algorithms 123

5. Assessment of Altimetric Sea Surface Height Measurements in Ice Covered Seas

5.1 The mean and the standard deviation of ICESat minus ENVISAT sea level anomaly differences 135
5.2 Dates of observation periods I and II during four ICESat laser campaigns 155
5.3 Mean snow freeboard derived for the eight observation periods 164

7. Cryospheric Applications of ICESat Altimetry in the Arctic Ocean

7.1 Dates of the observation periods associated with consistent estimates of SSH from both ICESat and ENVISAT 183
7.2 Dates for comparison of ICESat snow freeboards with ENVISAT ice freeboards 191
7.3 Comparison of mean snow freeboard from satellite laser altimetry with mean ice freeboard from satellite radar altimetry 192

1 The Role of Sea Ice in the Climate System

1.1 Introduction

The main aim of the work described in this thesis is the exploitation of data collected by the first Earth-orbiting satellite laser altimeter over the sea-ice covered regions of the Arctic Ocean. We analyse altimetric data from NASA's Ice, Cloud and land Elevation Satellite (ICESat) with the aim of extracting specific parameters associated with the study of the polar climate system. These parameters include the time-varying component of sea surface topography and sea ice freeboard. The applications of this work include:

i. VALIDATION OF SATELLITE ALTIMETRY DATA: cross-calibration of satellite laser altimetry data over sea ice with a complementary observational dataset derived independently from satellite radar altimetry.
ii. ARCTIC OCEANOGRAPHY: analysis of mean and time-variant dynamic ocean topography on seasonal and inter-annual time scales.
iii. OCEAN MODEL VALIDATION: comparison of observational data with a numerical model of mean dynamic topography.
iv. POLAR GEODESY: exploitation of satellite altimetry to map gravity anomalies of the Arctic Ocean.
v. POLAR CLIMATOLOGY: measurement of sea ice freeboard, analysis of the distribution of first-year and multiyear sea ice, and studies of snow loading on sea ice.

We begin, in Chapter 1, by first discussing the global climate system, climate change, and projections for future climate change. The Earth's polar regions play an important role in the global climate system; various feedback systems involving surface albedo, oceanic deep-water formation, and sea surface salinity can amplify climate variability and change. We investigate the role of the Arctic in the global climate system, paying particular attention to the influence of sea ice on the system. We outline the characteristics of sea ice and the techniques available for observing the ice pack. Finally, we examine current knowledge of, and future projections for, the state of Arctic sea ice.

1.2 The Global Climate System

1.2.1 Components of the Global Climate System

The Earth's climate system consists of the following components: (i) atmosphere, (ii) hydrosphere, (iii) cryosphere, (iv) biosphere, and (v) geosphere. These components interact through complex physical, chemical and biological processes on wide spatial and temporal scales, and are influenced by external forcing mechanisms, of which the Sun is the most significant [*Baede et al.*, 2001]. Figure 1.1 illustrates the climate system and some of the natural and anthropogenic external forcing factors.

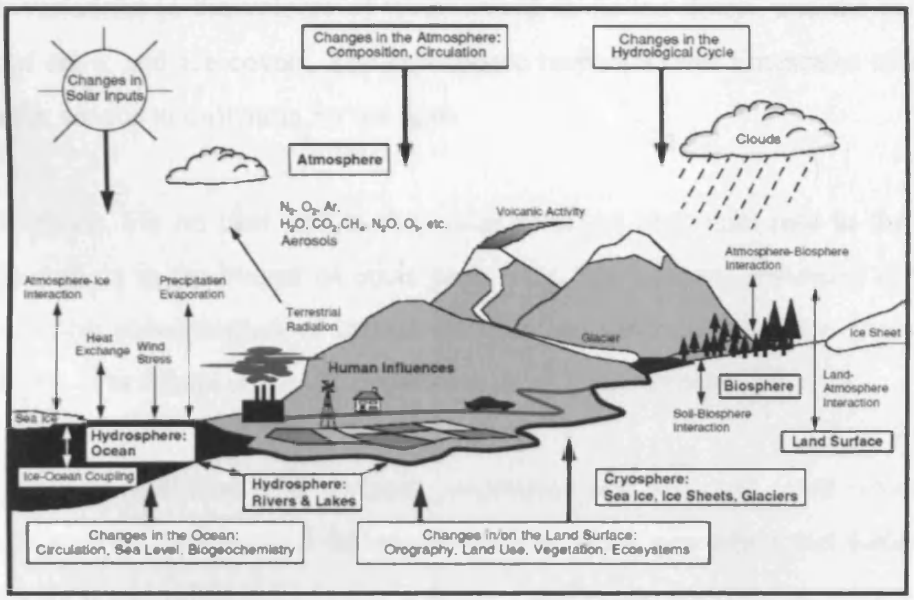

Figure 1.1 Schematic diagram illustrating the components of the global climate system (bold boxes). Internal processes and interactions are denoted by thin arrows, while bold arrows indicate parts of the system that may change. From *Baede et al.* [2001].

We now describe the five components of the climate system in more detail.

The atmosphere: processes include atmospheric circulation, radiative transfer, formation of clouds, evaporation, precipitation, and atmospheric chemical reactions. The atmosphere responds rapidly to its forcings on a timescale of the order of days to weeks [*Peixoto and Oort*, 1992].

The hydrosphere: processes include the transport of water around the globe, storage and transport of heat, storage of dissolved carbon dioxide, oceanic circulation driven by wind and density contrasts based on thermal and salinity gradients (the "thermohaline circulation"), and the exchange of mass and momentum with the atmosphere. The ocean responds over a range of timescales, from weeks to months in the upper mixed layer, to millennia in the deep ocean [*Peixoto and Oort*, 1992].

The cryosphere: includes the ice sheets of Greenland and Antarctica, continental glaciers and snowfields, sea ice, and permafrost. The cryosphere influences the climate system through its high albedo (reflecting incident solar radiation), its role in the circulation of oceanic deep water, its role as a potential source of sea level rise through variations in the volume of water stored in its ice sheets, and the insulating effects of snow and ice cover. The cryosphere responds over timescales of days or months for sea ice to millennia for ice ages.

The biosphere: life on land and in the ocean plays an important role in the carbon cycle as well as in the budget of other gases (e.g. nitrogen and methane) and hence influences the concentration of carbon dioxide and other greenhouses gases in the atmosphere. The biosphere reacts on timescales of hours to centuries.

The geosphere: includes land surfaces, vegetation and seasonal snow cover. The topography of the land surface influences airflow while vegetation and soils control the absorption and reflection of solar energy. Land processes react on a timescale of days to centuries.

1.2.2 Global Climate Change

Natural climate variability occurs on all time-scales and over a range of spatial scales. The climate is controlled by both external forcing factors (solar variability, volcanic eruptions, etc.) and internal forcing factors (atmospheric composition, cloud cover, etc.) [*Barry and Chorley*, 2003]. Superimposed on the natural variability are human-induced changes (anthropogenic effects) and feedback effects. Figure 1.2 shows temperature variations over the last millennium in the Northern Hemisphere derived

from annual averages of measurements from multi-proxy datasets (e.g. tree rings, ice cores, etc.). The Intergovernmental Panel on Climate Change (IPCC) reports that the warming of the 20th century is likely (defined as having a 66-90% chance) to be the largest of the last 1000 years and that the 1990s were in fact the warmest decade in this period [*Folland et al.*, 2001] .

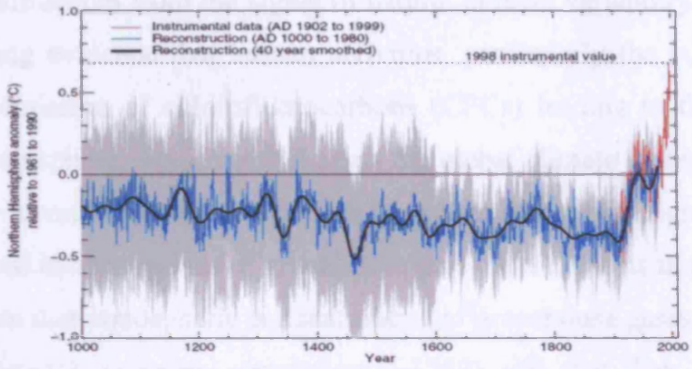

Figure 1.2 Northern Hemisphere temperature reconstruction (blue – tree rings, corals, ice cores, and historical records) and instrumental data (red) from AD 1000 to 1999. The forty-year smoothed version of the series (black), and two standard error limits (gray shaded) are also shown. From *Folland et al.* [2001], adapted from *Mann et al.*, 1999.

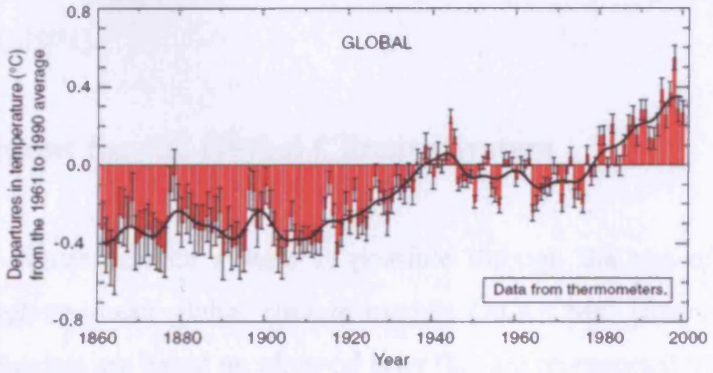

Figure 1.3 Annual time-series of global temperature anomalies from 1861 to 2000, relative to 1961 to 1990, combining land-surface air temperature and sea surface temperature (SST). Unsmoothed averages (red bars), twice their standard errors (black bars), and a smoothed curve (black curve), which was created using a 21-point binomial filter giving near-decadal averages, are shown. From *Albritton et al.*, [2001].

Since instrumental records began in 1861, global average surface temperature has increased by 0.6 ±0.2 °C (Figure 1.3) and 1998 was the warmest year in this period [*Folland et al.*, 2001]. There has been a corresponding rise in global mean sea level of between 1.0 – 2.0 mm yr^{-1} during the 20th century [*Church et al.*, 2001].

Due to the complex nature of the climate system, it is difficult to extract anthropogenic influences from the signal of natural climate variability. Nevertheless, there is gathering evidence that human activities, particularly the burning of fossil fuels, and the emission of chlorofluorocarbons (CFCs) leading to the depletion of ozone in the stratosphere, significantly impact the global climate system [*Baede et al.*, 2001]. The main result of these activities is an enhancement of the greenhouse effect through increased concentrations of greenhouse gases and aerosols in the atmosphere. Figure 1.4 shows that atmospheric concentrations of greenhouse gases were relatively constant prior to the industrial revolution (~1750) and that they have increased significantly since then. A change in the energy available to the atmosphere, due to changes in forcing factors, is termed radiative forcing of the global climate system. The radiative forcing of these greenhouse gases is also illustrated in Figure 1.4. The IPCC have investigated the anthropogenic influence on climate change through the use of attribution studies[1] and report that "most of the observed warming over the last 50 years is likely to have been due to the increase in greenhouse gas concentrations" [*Mitchell et al.*, 2001].

1.2.3 Projections for the Global Climate System

Predicting the future climate system is possible through the use of sophisticated coupled atmosphere-ocean global climate models (AOGCMs) [*Barry and Chorley*, 2003]. These models are based on physical laws that are represented by mathematical equations which are solved over three-dimensional global grids. Current AOGCMs typically have a horizontal resolution of 250 km and a vertical resolution of 1 km for the atmospheric component, with a horizontal resolution of 125 to 250 km and a vertical resolution of 200 to 400 m for the oceanic component. Equations are usually solved over a 30-minute time step [*Baede et al.*, 2001].

[1] Attribution studies investigate whether the magnitude of a simulated response to a particular forcing factor is consistent with the observational data [*Mitchell et al.*, 2001].

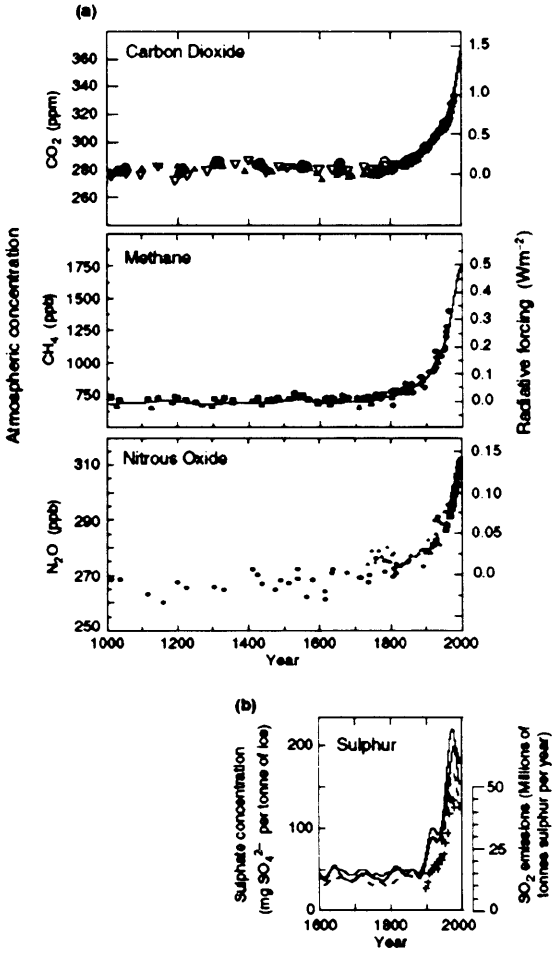

Figure 1.4 Changes in atmospheric composition. (a) Atmospheric concentrations of CO_2, CH_4 and N_2O over the past 1,000 years. Ice core and firn data for several sites in Antarctica and Greenland (shown by different symbols) are supplemented with the data from direct atmospheric samples over the past few decades (shown by the line for CO_2 and incorporated in the curve representing the global average of CH_4). The estimated radiative forcing from these gases is indicated on the right-hand scale. (b) Sulphate concentration in several Greenland ice cores with the episodic effects of volcanic eruptions removed (lines) and total SO_2 emissions from sources in the US and Europe (crosses) indicated on the right-hand scale. From *Albritton et al.* [2001].

Climate change (e.g. changes in temperature, precipitation, sea level rise) can be projected using various scenarios of forcing factors (e.g. concentration of greenhouse gases and atmospheric aerosols) in the model simulations. Future emissions of these forcing factors can be estimated by making assumptions about future demographic, socioeconomic, and technological changes.

The IPCC developed a set of six primary emissions scenarios, from the Special Report on Emission Scenarios ("SRES scenarios"), for use in projecting future climate change. Under all the IPCC emissions scenarios, globally averaged surface temperature, sea level, and atmospheric concentrations of CO_2 are projected to increase throughout this century. Figure 1.5 illustrates that surface temperature is projected to increase in the range 1.4 to 5.8 °C by the year 2100. The magnitude of such changes remain uncertain however due to the limitations of the current AOGCMs regarding uncertainties in radiative forcing, ocean processes and their atmospheric coupling, feedback processes, and the relation between regional-scale and large-scale phenomena, and how these processes are represented in AOGCMs [*Barry and Chorley*, 2003]. In order to better understand climate change and reduce uncertainties in projected climate change, additional observations, modelling and process studies are required [*Moore et al.*, 2001].

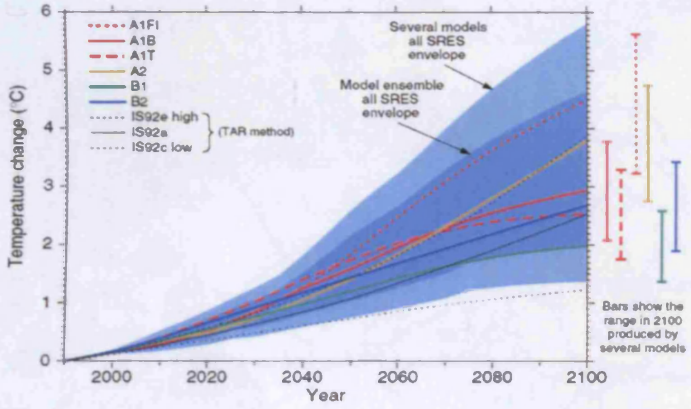

Figure 1.5 Projected global mean temperature change for the six SRES scenarios using a simple climate model tuned to seven AOGCMs. For comparison, results for the IS92a, IS92c, and IS92e scenarios[2] are also shown. The dark blue shading represents the envelope of the full set of thirty-five SRES scenarios using the average of the model results while the light blue shading is the envelope based on two particular model projections (GFDL_R15 and DOE PCM). The bars show, for each of the six illustrative SRES scenarios, the range of simple model results in 2100 for the seven AOGCM model tunings. From *Cubash et al.* [2001].

[2] The IS92 scenarios are a set of emissions scenarios used by the IPCC prior to their 2001 report and are presented in *IPCC* [1994].

1.3. The Arctic Climate System

The Arctic consists of the ice-covered Arctic Ocean, about 14 million km^2 in size [*Comiso and Parkinson*, 2004], bordered by the landmasses of North America and Eurasia. Figure 1.6 is a map of the Arctic region. The cryospheric component of the Arctic, consisting of ice sheets, glaciers, sea ice, snow cover and permafrost, is the most prominent feature of the Arctic region [*ACIA*, 2004]. In terms of the global climate system, the Arctic is an important component since (i) it acts as an energy sink for both the ocean and atmosphere [*Peixoto and Oort*, 1992] and (ii) it provides an early indicator of global climate change through feedback systems associated with factors such as the high albedo of snow and ice [*Comiso and Parkinson*, 2004].

Figure 1.6 Political map of the Arctic Region (*Perry-Castaneda Map Collection*[3])

[3] Perry-Castañeda Library Map Collection, Polar Regions and Ocean Maps, University of Texas Library, available at: http://www.lib.utexas.edu/maps/polar.html.

As a result of the permanent ice cover, knowledge of the bathymetric features of the Arctic Ocean is limited [*Laxon and McAdoo*, 1994]. Previously classified bathymetric information pertaining to the Arctic Ocean, gathered during submarine cruises throughout the region, has recently become available [*Cochran et al.*, 2006]. There has since been an international effort, under the International Bathymetric Chart of the Arctic Ocean (IBCAO) project, to construct state-of-the-art bathymetric maps of the Arctic Ocean. Figure 1.7 illustrates the major topographic and bathymetric features of the Arctic region.

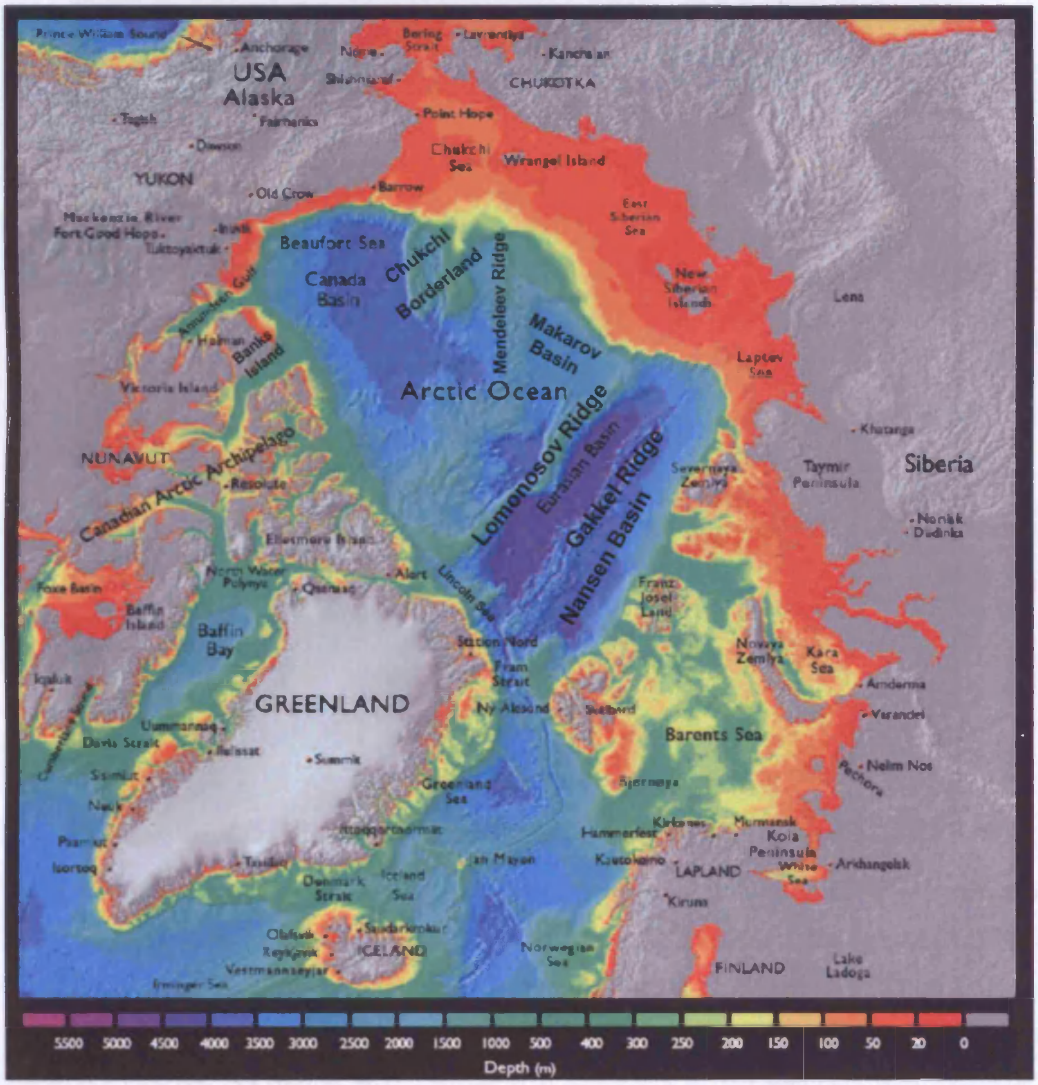

Figure 1.7 Bathymetric and topographic features of the Arctic (*International Bathymetric Chart of the Arctic Ocean*[4]).

[4] The International Bathymetric Chart of the Arctic Ocean is available at: http://www.ngdc.noaa.gov/mgg/bathymetry/arctic/arctic.html.

1.3.1 Circulation and Structure of the Arctic Ocean

Mean surface circulation in the Arctic Ocean, which has been deduced from the motion of sea ice drift, buoys, and research stations frozen into the pack ice [*Woodgate et al.*, 2001], is depicted in Figure 1.8. Circulation in the central Arctic is mainly wind-driven in the form of an anti-cyclonic gyre, known as the Beaufort Gyre, and translational motion along the Transpolar Drift current [*Wadhams*, 2000].

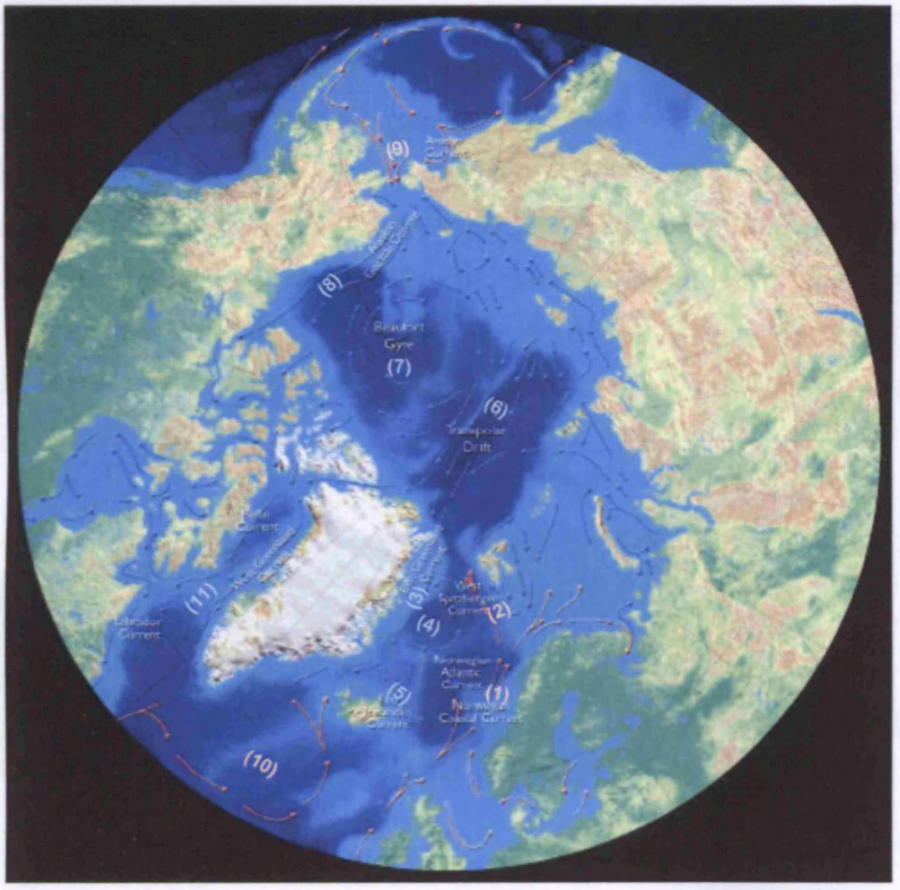

Figure 1.8 Surface currents of the Arctic Ocean. The most prominent circulation features are annotated in the diagram as follows: (1) Norwegian Atlantic Current, (2) West Spitsbergen Current, (3) East Greenland Current, (4) Greenland Gyre, (5) East Icelandic Current, (6) Transpolar Drift, (7) Beaufort Gyre, (8) Alaskan Coastal Current, (9) Bering Strait inflow, (10) Irminger Current, and (11) West Greenland Current. Adapted from *ACIA* [2004].

An inflow of relatively warm, Atlantic water, estimated by *Rudels* [1995] to be 5-8 Sv (1 Sv = 10^6 m^3 s^{-1}), enters the Arctic Ocean via the Barents Sea and Fram Strait, while

warm Pacific waters enter the Arctic through the Bering Strait, having a much lower mean transport estimated to be 0.8 Sv [*Coachman and Aagaard*, 1988]. Through cooling of the Atlantic inflow, freshwater flux from river runoff, and the formation and melting of sea ice, the Arctic Ocean is stratified into a cool, low-density (low salinity) surface layer, a relatively warmer intermediate layer, and a denser deep circulation [*Rudels*, 1995]. Cold water exits the Arctic Ocean primarily through the Fram Strait and the Canadian Arctic Archipelago [*Wadhams*, 2000]. The Arctic waters leaving through the Fram Strait are transported southward via the East Greenland Current partly as surface outflow into the Labrador Sea, and partly at depth, through overflows of cold, dense water through the Denmark Strait, and over the Iceland-Scotland Ridge, into the Atlantic. Figure 1.9 is a schematic illustrating the key components of Arctic Ocean circulation. The dense, deep-water outflow contributes to the North Atlantic deep water, while the low-salinity upper water influences the formation of Labrador Sea deep water [*Rudels*, 1995]. The circulation of the Arctic Ocean is therefore a key component of the global thermohaline circulation, and any changes could have consequences for the global climate system [*ACIA*, 2004].

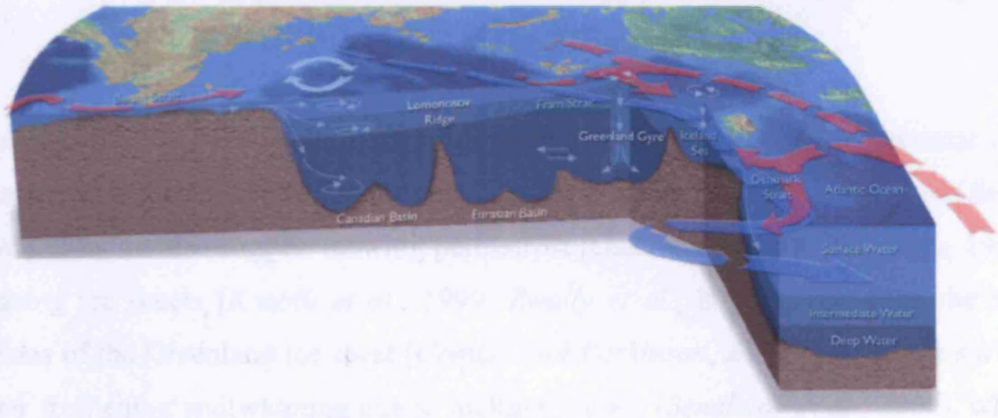

Figure 1.9 Schematic diagram illustrating Arctic Ocean circulation and water mass structure in cross-section. From *ACIA* [2004].

1.3.2 Arctic Climate Change

There is now widespread observational evidence that environmental change is occurring within the Arctic climate system [*ACIA*, 2004; *Comiso and Parkinson*, 2004; *Overpeck et al.*, 2005]. Annual anomalies of land-surface air temperature in the

Arctic (above 60°N), relative to the 1961–1990 average, are shown in Figure 1.10. Average annual temperatures have risen by 2 - 3 °C since the middle of the 20th century [*ACIA*, 2004]. Surface temperatures derived from satellite thermal infrared data provide complete polar coverage. Measurements collected between 1981 and 2003 over the Arctic (above 60°N) show a warming trend of 0.5 °C per decade, with more significant warming over land than over the sea ice [*Comiso and Parkinson*, 2004].

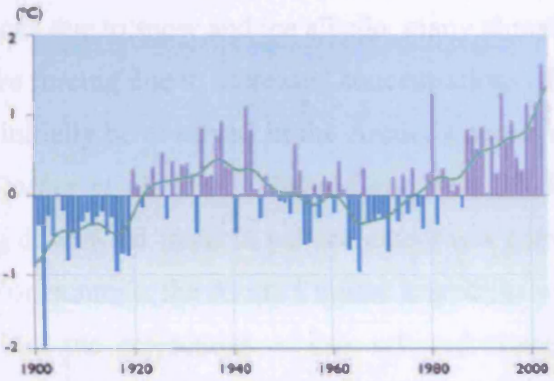

Figure 1.10 Annual anomalies of land-surface air temperature in the Arctic (above 60°N) calculated relative to the 1961–1990 average. The smoothed curve was created using a 21-point binomial filter, which approximates a 10-year running mean. From *ACIA* [2004].

One result of net surface warming is an extension of the length of the summer melt season in the Arctic, which has increased by 5.3 days per decade over sea ice [*Smith*, 1998]. Studies also suggest thawing permafrost [*Osterkamp and Romanovsky*, 1999], thinning ice sheets [*Krabill et al.*, 1999; *Zwally et al.*, 2002], changes to the melt regions of the Greenland ice sheet [*Comiso and Parkinson*, 2004], and Arctic surface water freshening and warming due to melting sea ice [*Semiletov et al.*, 2000], which are all consistent with large scale warming in the Arctic.

Probably the most striking environmental change in the Arctic is however the decreasing trend of 3% per decade in sea ice cover, based on satellite passive microwave observations between 1978 and 1996 [e.g. *Parkinson et al.*, 1999]. A more recent study by *Stroeve et al.* [2005] found that September ice extent has decreased by 7.7% per decade over the measurement period 1979-2004.

While consensus is growing that these changes in the Arctic are a direct result of increased radiative forcing due to anthropogenic greenhouse gas emissions (e.g. *ACIA*, 2004; *Overpeck et al.*, 2005), it remains unclear whether these changes truly represent a long-term trend or are part of the natural variability of the Arctic climate system [e.g. *Johannessen et al.*, 2004 and references therein].

1.3.3 Projections for the Future Arctic Climate System

As a result of feedbacks due to snow and ice albedo, many climate models predict that the effects of radiative forcing due to increased concentrations of greenhouse gases on the atmosphere will initially be observed in the Arctic, where warming is likely to be more pronounced [*Stocker et al.*, 2001; *Holland and Bitz*, 2003; *Johannessen et al.*, 2004]. A continuing downward trend in sea ice extent is a common feature of these model projections. For example, the Arctic Climate Impact Assessment (ACIA) study [*ACIA*, 2004] examines the projections of five selected climate models (CGCM2, CSM_1.4, ECHAM4/OPYC3, GFDL-R30_c, and HadCM3). Summer ice extent decreases in all five models, with one scenario (HadCM3) predicting a summertime ice-free Arctic Ocean by the middle of this century. Winter ice extent is projected to decrease less significantly with losses of 2-4 million km^2 predicted. The IPCC found that AOGCM simulations forced with the SRES emissions scenarios projected that Arctic warming will exceed global mean warming by more than 40% (1.3 to 6.3 °C for the range of models and scenarios considered) [*Giorgi et al.*, 2001].

In addition to changes in surface temperature and sea ice cover, there is suggestion (e.g. *Overpeck et al.*, [2005]) that the continued degradation of permafrost, northward advance of boreal forests, decrease in snow cover, melting of Arctic glaciers and the Greenland ice sheet, and the associated increased inflow of cold, fresh water to the Arctic Ocean are likely to move the Arctic to a new state. Although the retreat of summer sea ice is predicted to have economic benefits (Europe-Asia shipping routes could be diverted though navigable passages in the Arctic Ocean; oil, gas and mineral resources could be exploited), the environmental impact of these climate changes on indigenous peoples, Arctic mammals, marine-life, and Arctic ecology would likely be severe [*ACIA*, 2004].

1.4 Sea Ice and the Climate System

Sea ice is a key component of the Arctic climate system [*Lindsay and Zhang*, 2005], being one of the strongest drivers in this system [*Overpeck et al.*, 2005]. We have briefly introduced the idea that rapid changes in the state of the Arctic ice pack are occurring. We now describe the characteristics of sea ice and we discuss, in more detail, the role of sea ice in the climate system. We then move one to outline current understanding of the ice pack based on observational datasets, and future projections for changes in the thickness and extent of Arctic sea ice based on model simulations.

1.4.1 Characteristics of Sea Ice

The surface waters of the Arctic Ocean and the marginal seas of the Antarctic freeze to form a seasonally varying layer of sea ice which can be centimetres to metres thick. Sea ice is a complex material comprising a solid phase of ice crystals, a gaseous phase of air pockets, a liquid phase of brine solution in veins, and solid salt and contaminants within the ice matrix [*Wadhams*, 2000].

As temperatures drop below the freezing point of seawater (approximately –1.86 °C), millimetre-sized crystals, called frazil ice, form on the sea surface [*Eicken*, 2003]. Continued cooling, and the motion of waves, cause the frazil ice crystals to aggregate into grease ice and eventually small pancake-shaped ice floes. Surface winds and ocean swell force the small floes over each other, until they eventually freeze together and form a solid, thin ice cover called "new ice" (Figure 1.11a). New ice is mm to cm thick and its elevation is therefore very close to local sea level [*Eicken*, 2003]. As new ice floes consolidate and raft together, the temperature rises to that of the near-surface air. Additional growth then occurs mainly at the bottom of the ice by accretion processes. First-year ice (Figure 1.11b) is sea ice of not more than one winter's growth and represents up to 45% of the Arctic Ocean ice cover [*Comiso*, 2003]. It is between 30cm and 2m thick and its growth and decay in marginal seas is primarily responsible for the large seasonal variation in the total ice extent. Multiyear ice, or perennial ice, which is 3 to 5m thick, has survived one or more melting seasons. Multiyear ice has a rough surface with hummocks and ridges due to

deformation of the ice pack [*Warren et al.*, 1999]. Areas of very thin sea ice and open water, called leads, ranging from meters to kilometres in width, form when the ice pack diverges and fractures due to surface winds and ocean currents (Figure 1.11c). During the winter, sea ice is covered by a layer of snow, which may thaw during the summer melt season to form slush or melt ponds on top of the ice.

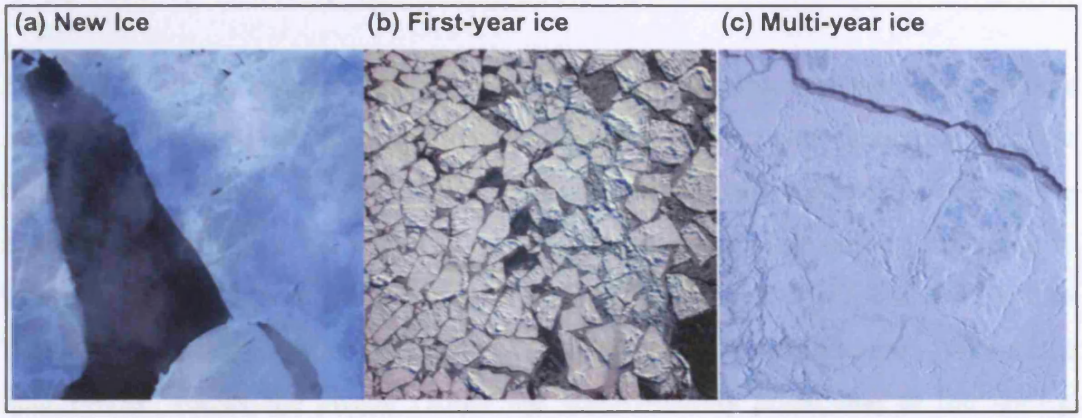

Figure 1.11 Aerial photography of Arctic sea ice in the Bering and Beaufort Seas from an altitude of approximately 1,300 m. (a) Evaporation from open water between thin, grey floes of new ice, has resulted in the formation of optically-thin clouds ("sea smoke"). (b) Medium and small white ice floes trapped in a matrix of newly frozen grey ice. The moderately deformed first-year ice surface is hummocky in appearance. (c) Fracturing in thicker multiyear ice floes due to differential motion within the ice pack, forms long leads often kilometres wide. These multi-year ice floes typically comprise rough surfaces, criss-crossed by pressure ridges, and areas of smoother bare ice.

1.4.2 Influence of Sea Ice on the Climate System

Sea ice thickness, roughness and albedo are important variables in the polar climate system, affecting both the overlying atmosphere and underlying ocean, by controlling the exchange of heat, moisture, momentum, and gases at the sea surface [*Dieckmann and Hellmer*, 2003]. Furthermore, sea ice provides a unique habitat for a range of organisms, from phytoplankton to polar marine mammals and birds [*Ainley et al.*, 2003]. There are three main processes through which Arctic sea ice interacts with the climate system and these are described below.

1.4.2.1 Ocean-ice-atmosphere Interactions

The energy balance at the ocean-atmosphere interface in the Arctic Ocean is determined by the absorbed incoming solar radiation, net long-wave radiation, sensible and latent heat fluxes, and heat conduction through sea ice, or the ocean heat flux in areas where there is no sea ice cover.

Sea ice is a strong insulator and its thickness therefore influences the Arctic climate system by acting as a barrier restricting sensible and latent heat fluxes between the ocean and atmosphere [*Tin and Jeffries*, 2001]. The thermal conductivity of sea ice is approximately 2 W m^{-1} K^{-1}, depending on its temperature and salinity, lowering to between 0.1 – 0.4 W m^{-1} K^{-1} in the presence of snow cover [*Eicken*, 2003], thus limiting the amount of heat transfer from the ocean into the atmosphere. Net surface heat fluxes[5] across the Arctic Ocean are comparatively small due to the strong, salinity-driven, stratification of the water column [*ACIA*, 2004]. The halocline, where salinity increases with depth, separates the surface layer of the Arctic Ocean from the relatively warmer intermediate "Atlantic layer" and the dense, salty deep water. The strong density gradient prevents vertical mixing, allowing sea ice to form in winter, and prevents melting during the summer [*Barry et al.*, 1993].

The interfaces between the air, snow, ice and ocean are modified by small-scale surface roughness which influences the turbulent transfer of heat, mass, and momentum between the ocean and the atmosphere [*Parkinson and Cavalieri*, 2002]. Since changes in ice thickness and lead fraction modify the heat transfer from the ocean to the atmosphere, an ice thickness feedback mechanism exists. A thinner ice pack with a higher lead fraction results in enhanced heat loss from the exposed ocean thus further warming the atmosphere [*Stocker et al.*, 2001]. However, increases in evaporation in such a system may lead to increased cloud cover and/or higher precipitation, resulting in increased snow cover on sea ice, and thus have a stabilising effect on this feedback.

[5] For example, the maximum flux over perennial sea ice is ~100 W m^{-2} in July [*Eicken*, 2003].

1.4.2.2 Radiation Balance of the Earth's Surface

Sea ice strongly influences the Earth's radiation balance since its high albedo[6] reflects solar radiation and decreases the level of absorption of short-wavelength energy at the surface [*Curry et al.*, 1995]. Short wavelength albedo increases from 0.06 for open water, to 0.52 for snow-free first-year ice, to 0.85 for thicker, snow-covered ice [*Eicken*, 2003]. The low temperatures of sea ice covered regions as a direct result of the high surface albedo, delay the onset of spring melt, and limit the decay of sea ice during the summer melt season.

The ice albedo feedback mechanism is one of the main mechanisms through which sea ice interacts with the global climate, contributing to polar amplification of global warming [*Stocker et al.*, 2001]. Rising surface temperatures result in a decrease of snow and ice cover, which results in the exposure of more open ocean and thus a decrease in surface albedo. The result of lower surface albedo is an increase in the absorption of incoming solar radiation and further surface warming [*Peixoto and Oort*, 1992].

1.4.2.3 Global Thermohaline Circulation

During formation, sea ice rejects brine which leads to a densification of the water column, while upon melting fresh water is released [*Wadhams*, 2000]. Sea ice therefore influences the freshwater balance of the polar oceans. The main export of sea ice (~14% of the total sea ice mass per year) from the Arctic Basin is through the Fram Strait [*Rothrock et al.*, 2000]. Best estimates of ice volume flux through the Fram Strait are between 2-3x10^3 km^3 yr^{-1} [*Barry et al.*, 1993], with maximum rates observed during the winter season [*Rothrock et al.*, 2000]. This sea ice export represents a major southward flux of fresh water, modulating sea surface salinity and deepwater formation in the Greenland Sea and northern North Atlantic [*Dickson et al.*, 1990]. Through its influence on the Atlantic thermohaline circulation, Arctic sea ice plays a critical role in driving the global thermohaline circulation [*Aagaard and Carmack*, 1989; *Rothrock et al.*, 2000]. Furthermore, it is likely (66-90% chance) that

[6] Albedo is defined as the fraction of incident irradiance reflected from the surface [*Eicken*, 2003].

sea ice has an effect on the stability of the global thermohaline circulation [*Stocker et al.*, 2001]. Figure 1.12 is a schematic diagram of the ocean thermohaline conveyor belt circulating in the world's ocean and indicates the North Atlantic as a region of ocean overturning. The current circulation is crucial to the redistribution of heat in the North Atlantic (e.g. the northerly component of the conveyor belt in the Atlantic Ocean), and is responsible for the mild climate of Western Europe [*Stocker et al.*, 2001].

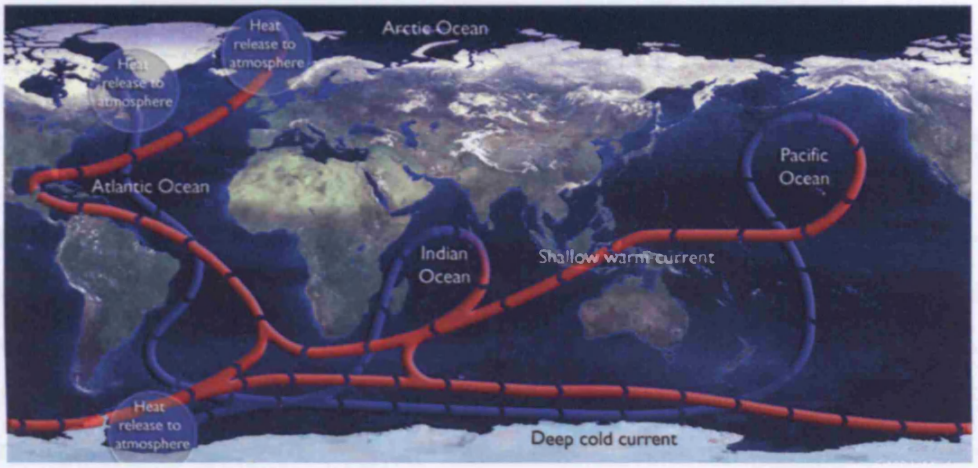

Figure 1.12 Schematic diagram of the global ocean thermohaline conveyor belt with warm surface currents (red) and cold, saline, deep currents (blue) connected in regions of deepwater formation in the northern North Atlantic and Antarctica. From *ACIA* [2004].

1.5 Observing and Modelling Arctic Sea Ice

1.5.1 Sea Ice Extent - Observations and Trends

Up to 7% of the Earth's surface can be covered in new, first-year and multi-year ice [*Dieckmann and Hellmer*, 2003]. The Arctic ice pack achieves its maximum extent in March when an area of around 15×10^6 km^2 is covered by sea ice [*Parkinson et al.*, 1999] (Figure 1.13a). During the summer melt season, the sea ice melts from the bottom and laterally, as well as from the top via the formation of melt ponds, until it reaches its minimum extent in September (Figure 1.13b), leaving only multiyear sea ice covering an area of $\sim 7 \times 10^6$ km^2, restricted to the central Arctic Ocean [*Warren et al.*, 1999].

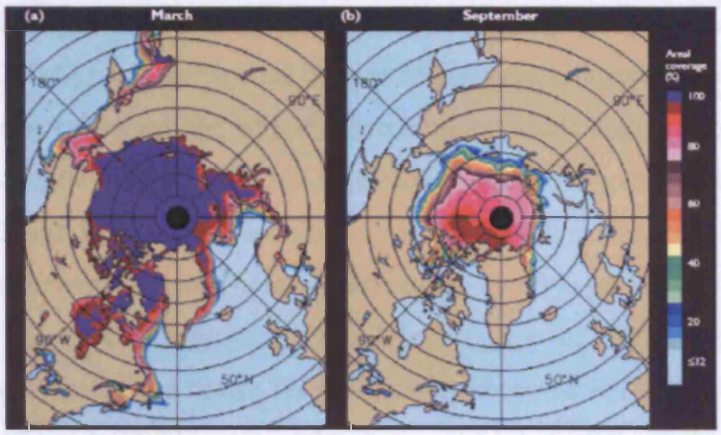

Figure 1.13 Seasonal variability of sea ice extent. Mean sea ice concentrations (1990-1999) in the Arctic Ocean from passive microwave satellite data for (a) March (maximum extent) and (b) September (minimum extent). From *ACIA* [2004].

Historically, the areal coverage of the ice pack, in particular measurements of sea ice extent[7], have been used to monitor the state of Arctic sea ice and calculate trends [*Comiso and Parkinson*, 2004]. *Vinje* [2001] analysed ships logs, which noted the location of the sea ice edge, and found that April ice extent in the Nordic Seas had decreased by ~33% over the past 135 years (Figure 1.14). The time series indicates that extreme events occur over decadal time scales and suggests that only time series of 30 years or more are sufficient to calculate trends in ice extent [*Vinje*, 2001]. Similarly, analysis of an historical sea ice dataset by *Divine and Dick* [2006] found oscillations with periods of 20-30 years and 60-80 years in the sea ice extent time series.

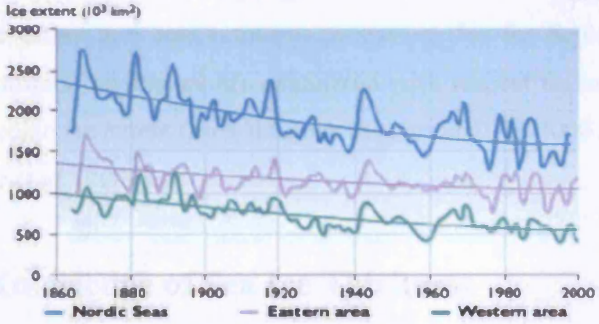

Figure 1.14 Historical record of sea-ice extent in April in the Nordic Seas calculated from data contained in ships logs. The time series for the eastern and western sub regions is included as well as the two-year running means for each time series. From *ACIA* [2004].

[7] Sea-ice extent is defined as the area of ocean with an ice concentration of at least 15%.

Satellite passive microwave imagery from the Scanning Multichannel Microwave Radiometer (SMMR) and the Special Sensor Microwave/Imager (SSM/I) sensors has successfully been used since the late 1970s to monitor Arctic sea ice extent [*Stroeve et al.*, 2005]. Satellite-derived time series of ice extent now span three decades and represent the longest continuous monitoring of sea ice [*Parkinson et al.*, 1999]. Sea ice cover over the Arctic as a whole has decreased by ~3% per decade over a period spanning the late 1970s to the late 1990s [*Parkinson et al.*, 1999; *Cavalieri et al.*, 2003], with the largest reductions (7% per decade) observed in summer [*Johannessen et al.*, 1999]. *Comiso* [2002] measured a downward trend of about -9% in the extent of perennial sea ice for the period 1978-2000. Arctic sea ice reached its lowest level in the satellite record at the end of the melt season in September 2002 [*Serreze et al.*, 2003]. Near record minimum conditions have been repeated in the subsequent two summers [*Stroeve et al.*, 2005] and the lowest recorded winter ice extent was recorded during the 2004-2005 winter season [*Meier*, 2005]. Figure 1.15 illustrates the latest observations of the summer extent of the ice pack.

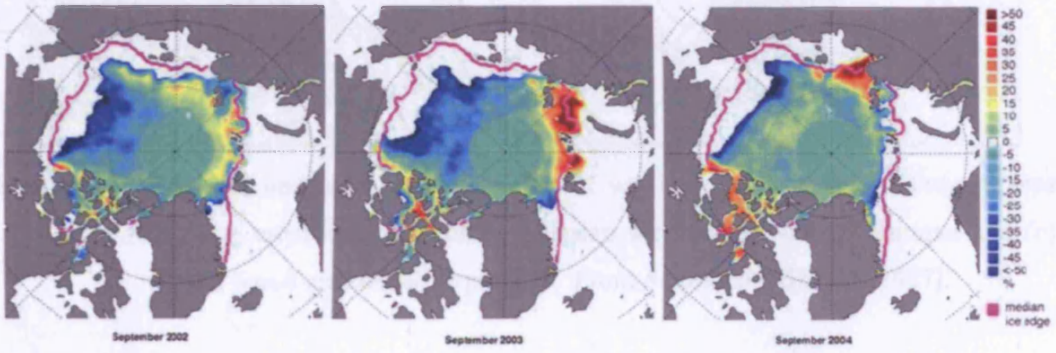

Figure 1.15 Sea ice extent and concentration anomalies (%) for September 2002 – 2004. Concentration anomalies are calculated with respect to the period 1979–2000. The median ice extent (pink line) for the period 1979-2000 is also shown. From *Stroeve et al.* [2005].

1.5.2 Current Knowledge of Sea Ice Thickness

Continuous monitoring of ice thickness has proved a more difficult task than measuring ice extent; while remote sensing techniques were available since the late 1970s to routinely map and monitor sea ice extent [e.g. *Parkinson et al.*, 1999], the first basin-wide estimates of sea ice thickness using satellite altimetry only became

available two decades later [e.g. *Laxon et al.*, 2003]. The first climatologies of Arctic sea ice thickness were produced using data collected during occasional and irregular submarine sonar measurements and from a few oceanographic moorings [e.g. *Bourke and Garrett*, 1987]. Typically, ice thickness gradually increases across the Arctic Basin from the Russian Arctic, across the North Pole towards the Canadian Arctic Archipelago and the northern coast of Greenland, with the distribution due mainly to the pattern of sea ice drift [*Wadhams*, 1995]. The regional and seasonal distribution of ice thickness, based on analysis of 17 submarine upward-looking sonar surveys, is illustrated in Figure 1.16.

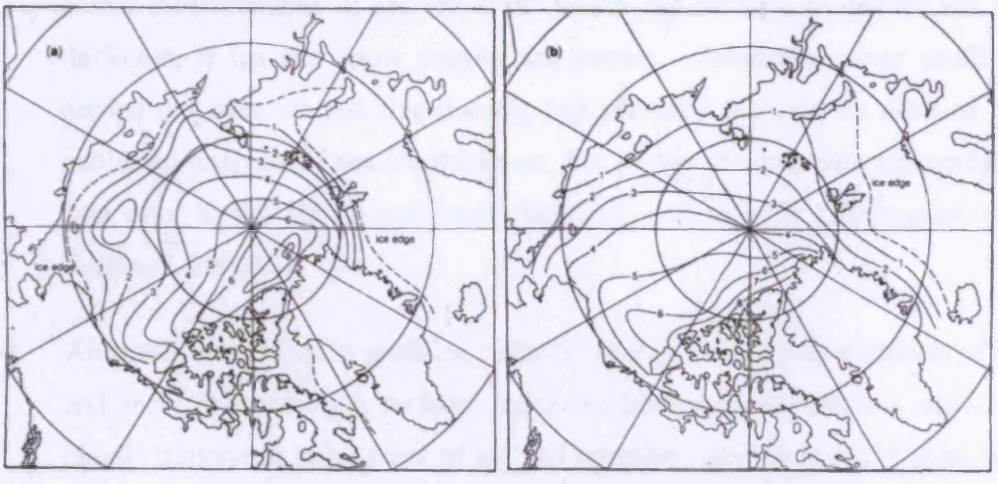

Figure 1.16 Regional and seasonal distribution of sea ice thickness (m). Contour maps showing estimated climatology of mean ice thickness for (a) summer and (b) winter, based on submarine profiles. From *Bourke and Garrett* [1987].

The seasonal and regional variability of Arctic sea ice thickness can be quantified via the following in situ, airborne and spaceborne techniques:

(i) In situ drilling is the traditional method of directly measuring sea ice thickness [*Wadhmas*, 2000]. Drilling is however time consuming and the harsh polar environment limits the time and area that can be surveyed. Nevertheless, in situ drilling has contributed significantly to knowledge of Antarctic sea ice thickness [*Haas*, 2003], and it is a useful validation tool for other measurement techniques [*Wadhams*, 2000].

(ii) Electromagnetic (EM) techniques utilise the difference in electrical conductivity between sea ice and cold seawater [*Haas*, 2003]. Ice thickness sounding can be achieved either by the use of an EM instrument installed on a sledge which is pulled across the sea ice surface, or a helicopter EM bird towed by a helicopter which flies at low altitude over the ice surface. This technique is limited by the area covered and is not suitable for surveying some terrain including deformed ice and pressure ridges [*Haas*, 2003].

(iii) Upward-looking sonar (ULS) mounted on submarines, autonomous underwater vehicles (AUVs), or as part of oceanographic moorings, is used to obtain measurements of sea ice draft[8] which can be used to deduce sea ice thickness, if ice and snow density are known. Submarine sonar profiling carried out over the last five decades has provided the data for most of the published analysis of sea ice thickness, but access to some data (particularly data prior to the 1990s) had been classified until recently [*Wensnahan and Rothrock*, 2005].

(iv) Airborne laser altimetry profiling (lidar) is used to measure the elevation of ice and snow above the sea surface. Airborne laser profiling offers a means of rapidly surveying large areas of ice and provides detailed maps of snow and ice elevation, but is limited by inaccurate knowledge of the geoid, and snow depth on sea ice [*Hvidegaard and Forsberg*, 2002].

(v) Satellite remote sensing techniques can overcome many of the disadvantages of other measurement techniques since they facilitate wide spatial and temporal coverage of the polar environment, even in harsh weather conditions and during polar darkness. Recently methods have been developed which use satellite radar altimetry to estimate sea ice thickness [*Laxon et al.*, 2003], but as with airborne laser altimetry, accuracy is also limited by knowledge of snow depth on sea ice.

In addition to the decreasing trend observed in measurements of sea ice extent which we have previously discussed, there are some indications of a reduction in sea ice thickness. Submarine-based sonar profiling has revealed reduced ice thickness in

[8] Sea ice draft is the portion of a sea ice floe below the water level.

parts of the Arctic since the 1970s: *Rothrock et al.* [1999] observed thinning of up to 42% by comparing sea ice draft measurements during two periods (1958-76 and 1993-97) and this result was corroborated by *Wadhams and Davis* [2000] who detected a 43% decline in ice thickness in the Eurasian Basin. Results from the *Rothrock et al.* [1999] study are shown in Figure 1.17, illustrating that the most significant change in ice draft occurred in the eastern and central Arctic Ocean. Examining the digitally recorded submarine data for 1987-1997 alone, *Rothrock et al.* [2003] find a steady decline of -0.16 m yr^{-1} and -0.11 m yr^{-1} in Arctic Ocean ice draft for winter and summer, respectively.

These results are however contested by others [e.g. *Holloway and Sou*, 2002] who argue that sea ice has thinned more slowly and that the proposed decrease of 40% is a result of undersampling the interannual variability and does not take account of wind-driven advection of sea ice in areas beyond the surveyed regions. In addition, a recent study by *Wensnahan and Rothrock* [2005] found a significant bias (~34 cm) between digitally recorded sonar data and an analogue sonar dataset (all submarine sonar datasets collected prior to 1976 are analogue), suggesting caution must be exercised when comparing recent sonar profiles with historical records.

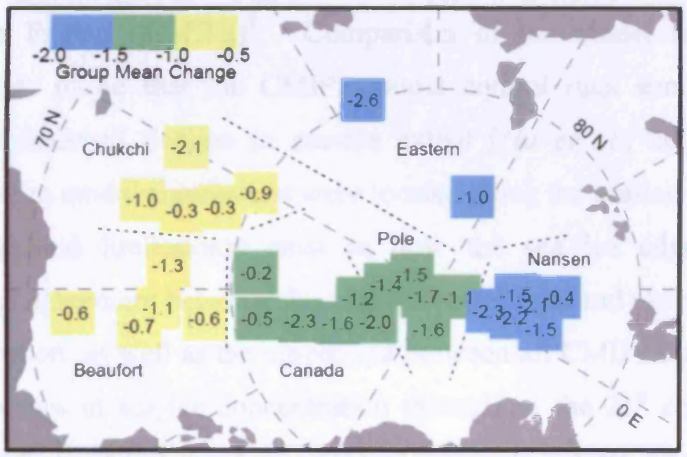

Figure 1.17 Changes in mean sea ice draft in the Arctic Ocean. Submarine sonar measurements collected between 1958 and 1976 are compared to data collected during the period 1993-1997. The change at each crossing is shown numerically (in meters) and the crossings within each regional group are given the same shading equivalent to their group mean. Each square covers about 150 km, the typical sample size. From *Rothrock et al.* [1999].

1.5.3 Model Projections of Arctic Sea Ice

If the apparent reductions in sea ice extent and increases in summer melt season are sustained, a very different ice regime will exist in the Arctic. This will contribute to major changes in ocean stratification and the exchange of heat and moisture in the region. Since sea ice is influenced by both the ocean and the atmosphere through complex physical processes, it is difficult to simulate sea ice in climate models [*Hu et al.*, 2004]. Furthermore these processes require high grid resolution and often must be parameterised [*Stocker et al.*, 2001]. Currently processes such as ice dynamics (ice motion and deformation), albedo variability due to changes in snow cover, multi-layer formulations of heat conduction through ice floes, and other thermodynamic processes, are being implemented in some coupled models [*Stocker et al.*, 2001]. Remaining problems in these models and a lack of observational data describing the ice pack limit the ability to project accurately future changes in Arctic sea ice [*Hu et al.*, 2004].

One test of the ability of a model to project future climate change is its ability to simulate the observed climate accurately [*ACIA,* 2004]. *Hu et al.* [2004] analysed integrations of fourteen models that are part of the second Coupled Model Intercomparison Project (CMIP2)[9]. Comparison of the model simulations with observational data found that the CMIP2 model control runs simulated the basic features of the observed decline in sea-ice extent [*Hu et al.*, 2004]. The main differences between model simulations were located along the sea-ice edge suggesting that differences (and limitations) exist in how the sea ice edge is simulated. Nevertheless, the agreement between the model control runs and observed changes in sea ice concentration, as well as the agreement between all CMIP2 model projections for further decreases in sea ice concentration throughout the 21st century (by more than 10% in most regions of the Arctic Ocean), suggests we can have confidence in predicted changes in ice extent [*Stocker et al.*, 2001].

On the other hand, projections of the future distribution of sea ice thickness differ quantitatively from one to another [*Cubash et al.*, 2001]. In terms of the CMIP2

[9] Further details about the models included in CMIP2 can be found in *Holland and Bitz* [2003] and at http://www-pcmdi.llnl.gov/cmip/.

models' ability to simulate present-day sea ice conditions, *Holland and Bitz* [2003] found that the spatial distribution of sea ice thickness across the Arctic Basin varied considerably, with particular differences in the location of maximum ice thickness. Similarly *Hu et al.* [2004] found various differences between the model simulations and the observed sea ice thickness climatology[10]: (i) the model mean sea ice thickness maximum is centred on the central Arctic Ocean, while the observed maximum is north of the Canadian Arctic Archipelago and (ii) the models produce sea ice that is too thick in the Barents Sea and Kara Sea regions. The basic features of sea-ice thickness climatology, as simulated by individual models, therefore needs further investigation [*Hu et al.*, 2004]. Figure 1.18 shows the simulated sea ice thickness and intermodel spread[11] and can be compared to the observed sea ice thickness climatology based on submarine sonar profiles (Figure 1.16).

The modelled changes in sea ice thickness given a doubling of CO_2 in the future global climate system are shown in Figure 1.19. *Hu et al.* [2004] found correlations between the mean and intermodel spread patterns for both the simulated Arctic surface air temperature changes and the changes in sea ice thickness. This implies that Arctic climate change, resulting from the increase in greenhouse-gas concentrations, is influenced by interaction between sea ice and the overlying atmosphere.

The discrepancies between the observed sea ice thickness climatology and the model simulations, as well as the intermodel variability limits our ability to accurately project the future distribution of Arctic sea ice thickness [*Hu et al.*, 2004]. Further improvements to the models are therefore required. A continuous and systematic dataset of sea ice thickness is required for model validation [*ACIA*, 2004]. Satellite altimetry data offers a means of gathering such data and techniques for measuring sea-ice thickness throughout the Arctic would be particularly valuable [*ACIA*, 2004].

[10] *Hu et al.* [2004] use an annual-mean sea ice thickness averaged over 1960–1982 as an estimate of the observed ice thickness climatology following *Bourke and Garrett* [1987] (see also section 1.5.2 and Figure 1.15).

[11] The intermodel spread is defined as the root-mean-square differences among the CMIP2 simulations [*Hu et al.*, 2004].

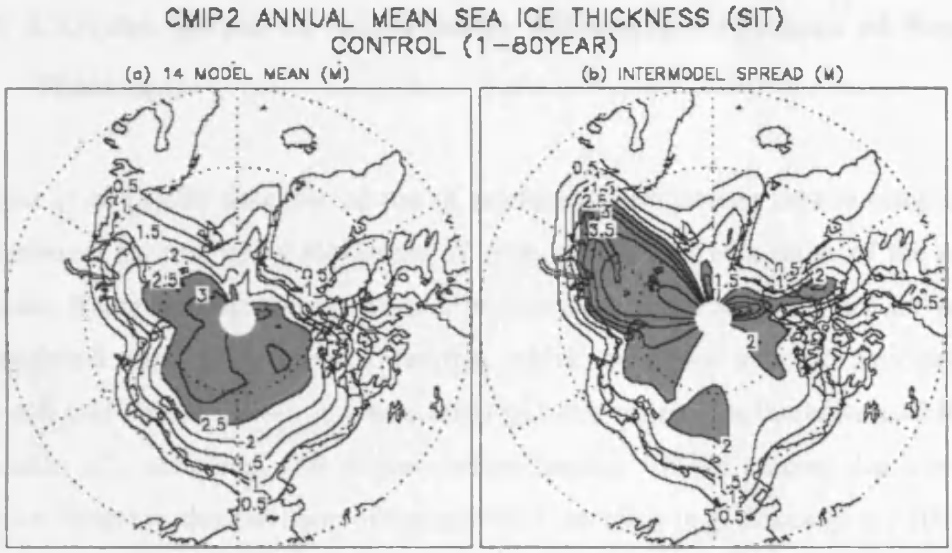

Figure 1.18 The (a) 14-model mean and (b) intermodel spread of annual sea ice thickness for the Arctic region north of 60°N averaged over the 80 years of the control runs. The contour interval is 0.5 m. Shading represents values larger than 2.5 m in Figure 1.18 (a) and larger than 2.0 m in Figure 1.18 (b). From *Hu et al.* [2004].

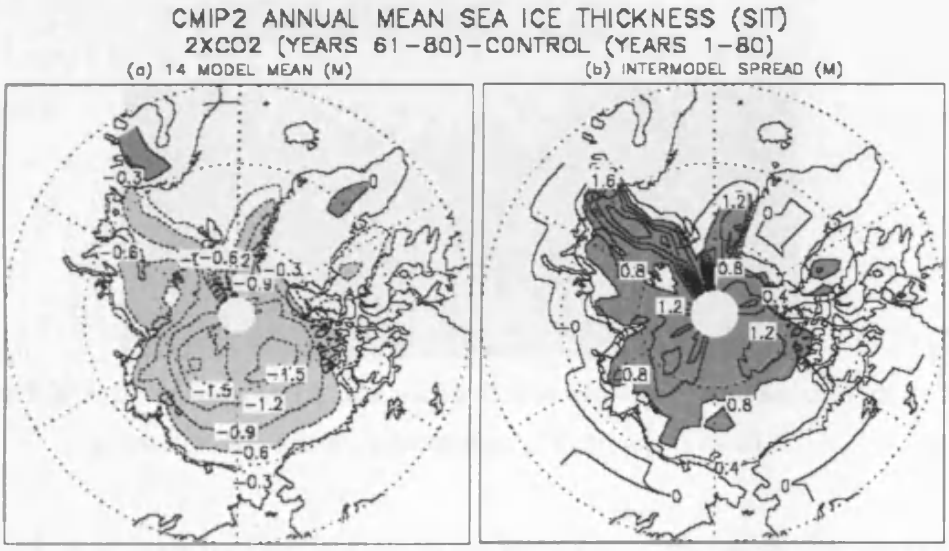

Figure 1.19 The (a) 14-model mean and (b) intermodel spread of annual sea ice thickness differences between CO^2 doubling (years 61–80) and the corresponding control runs (80 years). The contour interval (a) 0.3 m and (b) 0.4 m. Shading is used for values less than -0.6 m and larger than 0.0 m in Figure 1.19 (a) and larger than 0.8 m in Figure 1.19 (b). From *Hu et al.* [2004].

1.5.4 Current Status of Spaceborne Altimeter Estimates of Sea Ice Thickness

Peacock et al. [1998] describe the use of satellite radar altimeter data to estimate sea ice freeboard by comparing elevations of open water leads with those of the nearby ice floes. Radar returns over open water or thin ice are specular in nature and can be distinguished from diffuse radar returns, which originate over consolidated ice [*Peacock and Laxon*, 2004]. Classification of radar reflections therefore enables the generation of a reference grid of sea surface heights. If we assume that the radar altimeter ranges to the elevation of the snow/ice interface [e.g. *Laxon et al.*, 2003 and references therein], then knowledge of sea surface height can be used together with the altimetric measurements of sea ice elevation to deduce sea ice freeboard, h_f. Figure 1.20 illustrates the key measurements associated with a portion of sea ice. Note, sea ice freeboard, h_f, is defined here as the height of the ice above the local sea surface *excluding* the overlying snow layer.

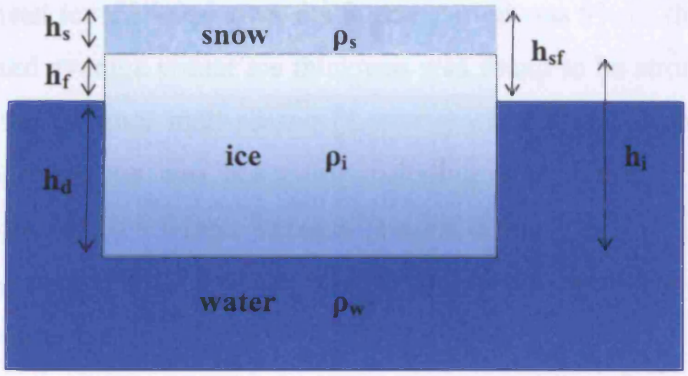

Figure 1.20 A schematic diagram of a sea ice floe in hydrostatic equilibrium with its related parameters (see text for a description of the symbols used).

Considering a single ice floe floating on the sea surface, we assume that the floe is in hydrostatic equilibrium; the balance in relative heights of the ice freeboard, h_f, ice draft, h_d, and snow load, h_s, is given by Archimedes' principle:

$$\rho_w h_d = \rho_s h_s + \rho_i h_f + \rho_i h_d \qquad (1.1)$$

where ρ_w, ρ_s, and ρ_i are the densities of near-surface sea water, snow, and sea ice respectively. Since the thickness of a sea ice floe, h_i, is the sum of h_f and h_d, rearranging Eqn. (1.1) yields

$$h_i = h_f\left(\frac{\rho_w}{\rho_w - \rho_i}\right) + h_s\left(\frac{\rho_s}{\rho_w - \rho_i}\right) \quad (1.2)$$

Uncertainties in (i) the scattering layer that the radar beam encounters and (ii) snow loading on sea ice, are the main sources of error in estimates of sea ice thickness using satellite radar altimetry [*Wingham et al.*, 2001].

Laxon et al. [2003] have described the use of ERS-1 and ERS-2 satellite radar altimetry data to determine sea ice freeboard, and by using auxiliary measurements of ice, water, and snow densities and snow depth, to estimate ice thickness in the Arctic. *Laxon et al.* [2003] analysed an eight-year satellite radar altimetry dataset, which represents the longest continual period of sea ice thickness monitoring. The standard deviation of mean ice thickness over the 8-year period was 9% of the overall average ice thickness and average winter ice thickness was found to be strongly correlated to the length of the summer melt season [*Laxon et al.*, 2003]. Significant variability between sea ice seasons was observed, including a 16% change in sea ice mass between two consecutive winter seasons [*Laxon et al.*, 2003]. Figure 1.21 shows average multi-year ice thickness derived for an 8-year period in the 1990s using satellite radar altimetry.

A major limitation of the satellite radar altimetry dataset is that only partial sea ice thickness data exists for the Central Arctic due to satellite orbit constraints which limit coverage to 81.5°N. Launched in 2003, NASA's ICESat mission presents a chance to study high-resolution satellite laser altimetry data with coverage of the Arctic up to 86°N. Figure 1.22 illustrates the latitudinal limit of coverage of satellite altimeters in the northern hemisphere. An additional area of sea ice, ~ 2 x 10^6 km^2 in size, is covered by the ICESat orbit configuration.

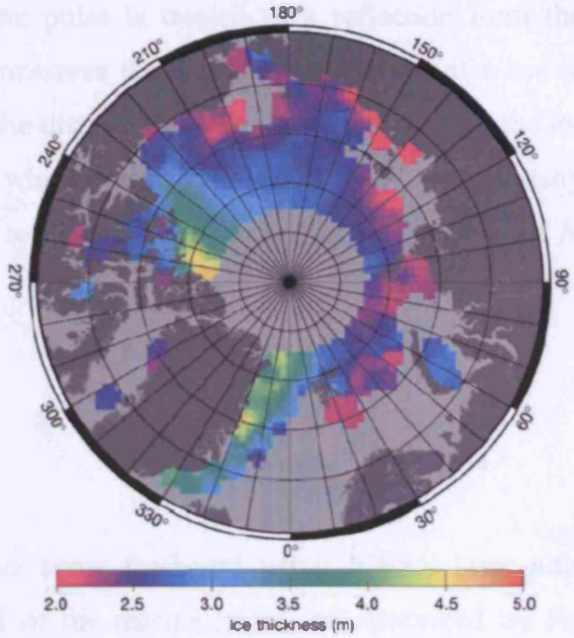

Figure 1.21 Mean winter sea ice thickness in the Arctic Ocean. Radar altimetry data was used to construct an eight-year average (1993-2001) sea ice thickness for the winter season (October to March). From *Laxon et al.* [2003].

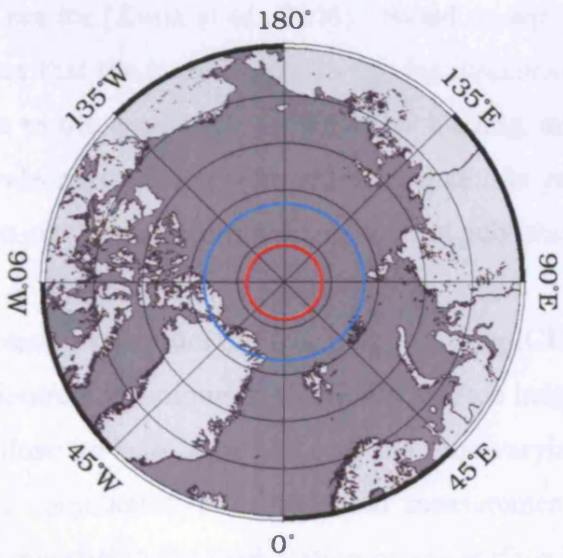

Figure 1.22 The latitudinal coverage of satellite radar altimeters (ERS-1, ERS-2, ENIVSAT), shown in blue, is 81.5°N, while the limit of the satellite laser altimeter (ICESat), shown in red, is 86°N. The proposed CryoSat mission will cover an area up to 88°N.

Since the return laser pulse is treated as a reflection from the air/snow interface, ICESat essentially measures the elevation of the top of a sea ice floe [*Kwok et al.*, 2004]. We refer to the distance between this elevation and the local sea surface as the snow freeboard, h_{sf}, which comprises h_f, and h_s. When analysing laser altimetry, it is therefore expedient to describe ice thickness, h_i, in terms of h_{sf} (rather than h_f) as follows,

$$h_i = h_{sf}\left(\frac{\rho_w}{\rho_w - \rho_i}\right) + h_s\left(\frac{\rho_s - \rho_w}{\rho_w - \rho_i}\right) \tag{1.3}$$

Techniques to derive snow freeboard using ICESat laser altimetry, based on the removal of a model of the marine geoid, are described by *Forsberg and Skourup* [2005] and *Kwok et al.* [2006]. These techniques are discussed further in Section 3.4. The published freeboards are however contaminated by geoidal errors, which illustrates that knowledge of the instantaneous sea surface height is required for direct retrieval of freeboard [*Kwok et al.*, 2006]. The largest uncertainties in estimating sea ice thickness from ICESat measurements are knowledge of (i) sea surface height and (ii) snow loading on sea ice [*Kwok et al.*, 2006]. Based on equations (1.2) and (1.3), *Giles* [2006] estimates that the largest error in sea ice thickness measurements from laser altimetry is due to the uncertainty in the snow loading, and is a factor of ~1.7 greater that the equivalent error using radar altimetry data. As yet, no estimates of sea ice thickness based on satellite laser altimetry have been published.

In the following chapters, we explore the feasibility of using ICESat data to determine ice elevation and describe a technique to locate sea surface height in the presence of sea ice cover. We illustrate how knowledge of the time-varying sea surface height can then be used in conjunction with elevation measurements to estimate snow freeboard. We also investigate the exploitation of sea surface height measurements for oceanographic and geodetic applications, specifically the determination of mean dynamic topography and the mapping of marine gravity anomalies.

1.6 Summary

The primary aim of the work presented in this thesis is the exploitation of ICESat satellite laser altimetry of the Arctic Ocean for the measurement of parameters associated with the Arctic climate system. We now summarise the main conclusions we can draw regarding the state of the climate system and the role of sea ice in this system.

- Since instrumental records began in 1861, global average surface temperature has increased by 0.6 ±0.2 °C. Most of the observed warming can be attributed to anthropogenic causes, namely an increase in greenhouse gas concentrations.

- Amplification of global average climate change occurs in the Arctic.

- Sea ice influences the global climate system mainly through the ice albedo feedback, and the role of sea ice in thermohaline circulation.

- In situ, airborne and spaceborne techniques are used to monitor the extent and thickness of sea ice, parameters of fundamental importance in monitoring the Arctic climate system.

- Observations of the Arctic sea-ice pack, since satellite records began in the late 1970s, show that sea ice extent has decreased by ~3% per decade.

- It remains unclear whether simultaneous reductions in Arctic sea ice thickness have occurred. Observational records, collected during field and ship expeditions and from submarines and drifting buoys, exist for the last few decades but vary in time-span and region surveyed. About a decade of satellite altimetry-derived sea ice thickness data has been analysed so far.

- Satellites offer the best means to monitor the circumpolar region systematically.

- Satellite altimetry can be used to map the interannual and regional variability of Arctic sea ice thickness.

- Simulations of sea ice extent using coupled atmosphere ocean global climate models are promising – good agreement exists between the observed climatology and modelled data. Modelling sea ice thickness remains difficult and model errors exist due to the inadequate treatment of the complex processes governing sea ice.

- Continued satellite-based monitoring of sea ice should provide a sea ice thickness time series that can be used to better understand the changes in sea ice thickness and improve model projections of the Arctic sea ice pack.

2 Satellite Laser Altimetry

2.1 Introduction

As stated in Chapter 1, the primary aim of the work presented in this thesis is the exploitation of ICESat laser altimetry data collected over the sea-ice covered Arctic Ocean. In Chapter 2 we introduce the concept of satellite laser altimetry. We first discuss the advantages and limitations associated with both satellite radar altimetry and satellite laser altimetry. The ICESat mission is introduced, including a brief description of the Geoscience Laser Altimeter System (GLAS) instrument, as well as an outline of the spatial coverage of the ICESat ground tracks. The principles of satellite laser altimetry are described, together with the corrections applied to laser altimetry data to account for generic range errors. We discuss the geophysical effects that act on sea surface topography and outline methods to account for these effects when analysing satellite altimetry measurements. The ICESat single shot measurement error budget is also presented.

2.2 Overview of Satellite Altimetry

Altimetry is an active remote sensing tool that measures the distance between the Earth's surface and the instrument [*Bufton*, 1989]. Satellite radar altimeters have greatly advanced polar mass balance studies [*Brenner et al.*, 1983; *Zwally et al.*, 1989; *Yi et al.*, 1997] since they are capable of obtaining extensive, densely distributed elevation profiles in all weather conditions. This gives satellite radar altimeters a major advantage over many other remote sensing instruments. Spaceborne radar altimeters can acquire topographic datasets of numerous remote and inaccessible regions such as the Earth's poles. Furthermore, they are particularly suited to monitoring flat surfaces, such as the ocean and sea ice, due to the ability of the onboard waveform trackers to keep the leading edge of the waveform centred at the tracking point [*Ekholm et al.*, 2002].

However certain limitations exist while using satellite radar altimetry over certain surfaces. The radar footprint is large (kilometres to tens-of-kilometres) and increases

with surface slope. Radar altimeters are best suited to surfaces with slopes $<1^{o}$, since surface undulations and sloping terrain introduce errors within the beam-limited radar footprint. Over sea ice, further uncertainties arise from microwave penetration of the pulse into the surface snow layer [*Wingham*, 1995]; this process remains poorly understood and further analysis is required to determine the depth of penetration of the radar pulse [*Wingham et al.*, 2001].

The technique of laser altimetry can be used to determine the topography of the sea ice and ocean surfaces at high resolution [*Bufton*, 1989]. The key difference between laser and radar altimeters is the wavelength at which the instruments operate. Microwave radar pulses have wavelengths of ~2-10 cm, while laser altimeters usually emit visible or near infra-red pulses at wavelengths of ~1 μm. Figure 2.1 illustrates this contrast for a 1 μm laser wavelength and a 2 cm radar wavelength. The pulse wavelength governs (i) pulse transmission through the atmosphere and (ii) the magnitude of pulse penetration of the surface snow layer, if present. A further difference between laser and radar altimeters is the order of magnitude smaller footprint (~100 m compared to kilometres) that results from the narrow beam of the pulse produced by the laser [*Bufton*, 1989]. Analysis by *Zwally et al.* [1981] suggests the smaller laser altimeter footprint size could be optimal for surveying sea ice since it would average over small-scale ice roughness while fully resolving the major components of surface height variability.

Unlike radar altimetry, which requires pulse averaging to obtain accurate range measurements, each individual laser pulse is not only capable of acquiring unique high-quality elevation measurements, but has the potential to detect the height distribution and the slope of the surface illuminated by the laser beam [*Bufton*, 1989]. Surface reflectivity may also be inferred since the total area under the received pulse is proportional to the transmitted pulse energy and this is a measure of surface albedo at the monochromatic laser wavelength [*Bufton*, 1989].

Satellite laser altimetry therefore overcomes some of the problems associated with radar altimetry. For example, the 40Hz pulses from the operating laser aboard ICESat facilitate single-shot elevation measurement precision over smooth, flat surfaces of

around 3 cm [*Fricker et al.*, 2005], high mapping density (successive spots on the Earth's surface, around 65 m in diameter, are illuminated every ~172 m), and almost global coverage (to ±86°). Whereas radar returns are contaminated by land near coastlines, satellite laser altimetry is unique in that both shallow waters in coastal areas, and high latitude regions, may be surveyed [*Urban and Schutz*, 2005].

There are nonetheless some notable disadvantages associated with laser altimetry. Scattering of the laser pulse in the presence of thick cloud can result in range biases or even signal loss. As with radar altimetry, penetration of the laser beam into surface snow cover on sea ice remains poorly understood. The absorption coefficient of sea ice is such that at near-infrared wavelengths light penetration into the sea ice itself is negligible [*Perovich*, 1996]. In previous studies received pulses are treated as returns from the highly reflective air/snow interface, penetration of the laser beam into snow having been assumed negligible and thus disregarded [*Thomas et al.*, 1999; *Kwok et al.*, 2006]. Furthermore, in order to obtain high precision altimetry data, accurate beam pointing control is necessary to maintain near nadir alignment of the laser beam [*Bufton*, 1989], and knowledge of beam pointing angle uncertainty is required to determine the associated range error [*Lisano and Schutz*, 2001]. The later has proven problematic in the case of ICESat [*Luthcke et al.*, 2005].

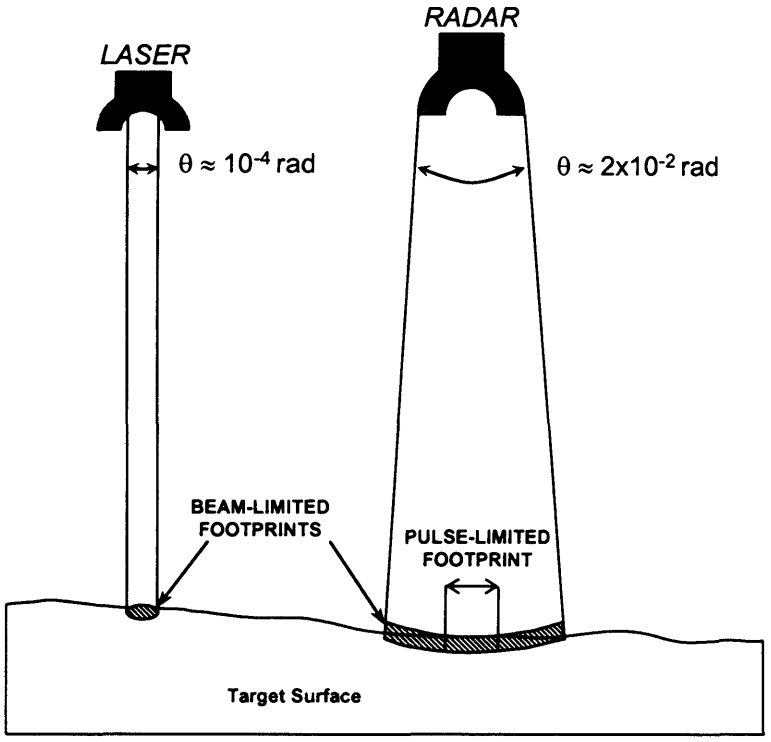

Figure 2.1 Comparison of laser and radar altimetry. Adapted from *Bufton* [1989].

2.3 ICESat Mission Overview

The ICESat mission is one of a series of NASA Earth Observing System (EOS) of satellites that were launched between 1999 and 2003. These missions form an integral part of an international effort to monitor changes in the Earth's atmosphere, oceans and ecosystems [*Lisano and Schutz*, 2001]. The primary aim of the ICESat mission is to obtain precise measurements of elevation change on the Greenland and Antarctic ice sheets with sufficient accuracy, spatial density, and temporal coverage to derive interannual and decadal scale trends [*Zwally et al.*, 2002]. In addition to this, ICESat gathers measurements of sea ice elevation and roughness, ocean and land surface elevation, surface reflectivity, and measurements of cloud height and vertical structure [*Zwally et al.*, 2002]. The satellite was initially designed to operate for a minimum of 3 years, with a five-year goal [*Zwally et al.*, 2002]. However problems with laser lifetime prompted a revised mission plan that resulted in reduced laser operations (~33-day operations periods, three times per year) while maintaining the ability to monitor intra- and inter-annual changes in polar ice cover [*Schutz et al.*, 2005].

The Geoscience Laser Altimeter System (GLAS) is carried onboard ICESat. This is the first Earth-orbiting satellite laser altimeter and first space-borne altimeter specifically designed to study polar ice sheets [*Lisano and Schutz*, 2001]. The Mars Orbiting Laser Altimeter (MOLA), flown on the Mars Global Surveyor mission, and the Shuttle Laser Altimeter, were the predecessors of GLAS [*Brenner et al.*, 2003]. These missions demonstrated the feasibility of using a spaceborne laser to map the topography of a planetary surface and, in the case of the SLA, to characterise ocean, land and cloud elevations [*Brenner et al.*, 2003].

GLAS has three lasers (designated Laser 1, 2, and 3) which are frequency-doubled, diode pumped, solid state Nd:YAG (neodymium-yttrium-aluminium-garnet) lasers with a pulse repetition rate of 40 Hz [*Duda et al.*, 2001]. A laser channel operating with an energy level of 74 mJ at a wavelength of 1064 nm obtains the altimeter measurements, while a 532 nm lidar channel operating at 36 mJ provides atmospheric backscatter measurements that can be used to describe the vertical distribution of clouds and aerosols [*Zwally et al.*, 2002]. The laser pointing direction is titled forward slightly ("pitched-up") and has an off-nadir angle of 0.3° to mitigate damage

to the detector by specular echoes reflected from mirror-like surfaces (e.g. standing surface water) [*Schutz et al.*, 2005]. Laser divergence angle and altimeter platform height determine the laser footprint size. The GLAS laser beam divergence is approximately 110 μrad [*Zwally et al.*, 2002] resulting in laser footprints approximately 65 m in diameter (depending on the precise altitude of the instrument) at the Earth's surface [*Zwally et al.*, 2002]. The pulse repetition rate and altimeter platform velocity determine the separation between the footprints [*Bufton*, 1989]. GLAS has a pulse repetition rate of 40 Hz and the laser illuminates a spot every 172 m along the Earth's surface [*Schutz et al.*, 2005]. The mission specifications are outlined in Table 2.1.

ICESat has an orbital altitude of around 600 km (with respect to mean sea level) and an inclination of 94°, providing global coverage to a maximum latitude of ±86° [*Schutz*, 2002]. The ICESat orbit is a non sun-synchronous, near circular, frozen orbit[12]. The orbit characteristics are such that satellite altitude is a function of latitude: orbit perigee is 597 km and remains fixed (i.e. perigee does not circulate) at the northernmost latitude of 86°N; orbit apogee is 626 km at 86°S [*Zwally et al.*, 2002]. For the science phase of the mission, the initial plan for the satellite ground-track was a 183-day repeat period with a near-repeat subcycle of 25 days [*Lisano and Schutz*, 2001]. However, due to the revised mission plan, a 91-day exact repeat orbit (with a 33-day subcycle) was chosen for the science phase of the mission (see Figure 2.2). This orbit results in ground-tracks with a 30 km cross-track separation at the equator and a 5 km separation at ±80° [*Fricker et al.*, 2005].

The post-launch calibration and validation (cal/val) phase lasted approximately 38 days during February and March 2003. The performance of the onboard laser altimeter was verified and the instrument and spacecraft orientation were calibrated. During this phase of the mission an 8-day exact repeat orbit was maintained (Figure 2.2). Although this orbit configuration did not support high-density coverage (track separation of 337 km at the equator), it provided for several repeat-tracks over ground

[12] The ICESat orbit characteristics (i.e. inclination and eccentricity) are chosen so that a frozen orbit is maintained and the mean perigee is stationary. This configuration results in ground tracks that exactly repeat each other. The orbit is corrected by drag-compensation manoeuvres so that pointing to reference ground tracks is preserved [*Schutz*, 2002]. Refer to Ice, Clouds and Land Elevation Satellite (ICESat) http://science.hq.nasa.gov/missions/satellite_20.htm for more details.

calibration sites (e.g. the salt flats of the salar de Uyuni, Bolivia), which enabled validation of the mission data products [*Schutz et al.*, 2005]. The dates and laser campaigns associated with the cal/val and science phases of the ICESat mission are outlined in Table 3.1.

Launch date	January 13 2003
Planned Mission duration	3 years (with a 5 year goal)
Mean orbital altitude	600 km
Orbit inclination	94°
Orbit eccentricity (frozen orbit)	0.0013
Ground-track repeat period (science phase)	91 days
Orbit determination	
- radial accuracy	<5 cm RMS
- horizontal accuracy	<20 cm RMS
Laser pulse sample rate	40 Hz
Laser wavelength	1064 nm (near-infrared) 532 nm (green)
Number of lasers	3 (operating alternately)
Height measurement precision requirement (1σ)	15cm
Laser pointing knowledge requirement (1σ)	1.5 arcsec

Table 2.1 ICESat mission specifications. From *Lisano and Schutz* [2001].

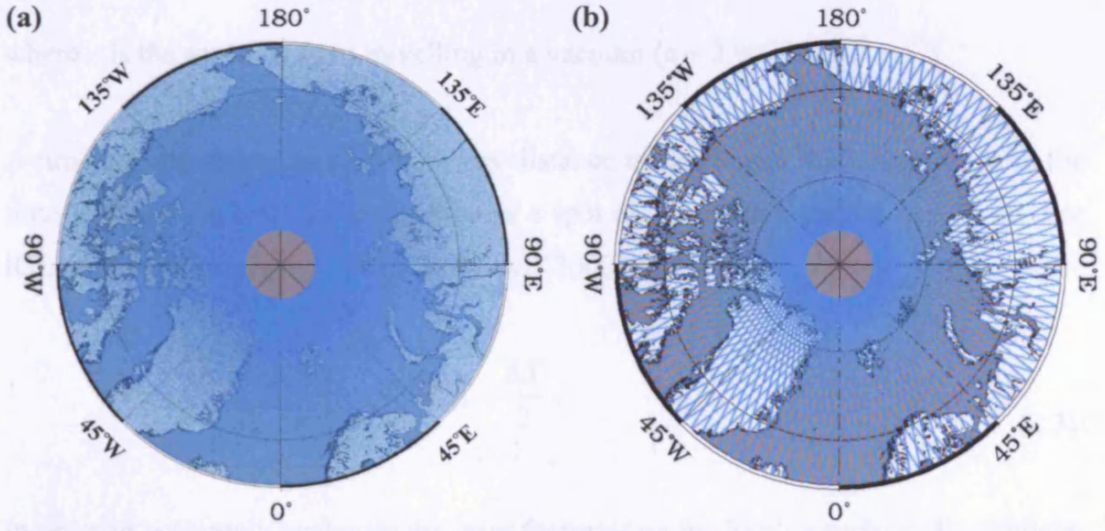

Figure 2.2 Spatial coverage of ICESat ground tracks over the Arctic. Coverage for (a) 91-day exact repeat orbit and (b) 8-day exact repeat orbit. The instrument currently operates in a 91-day repeat orbit.

2.4 Principles of Satellite Laser Altimetry

The range measurement produced by a laser altimeter is based on the round trip time of flight of a short laser pulse (~6 ns duration), propagating at the speed of light, between the spacecraft and a target surface [*Bufton*, 1989]. The round trip travel time, ΔT, is defined as

$$\Delta T = T_R - T_0 \tag{2.1}$$

where T_0 is the laser transmit time and T_R is the received pulse time. Both times are measured with the same clock and it is assumed that clock drift over the time interval ΔT is small [*Schutz*, 2002].

The time interval, ΔT, is subsequently converted into distance by multiplying by the speed of light to obtain the two-way range. Ignoring atmospheric refraction, one-way distance or the (uncorrected) altimeter range measurement, R_{alt}, can be represented by

$$R_{alt} = \frac{c\,\Delta T}{2} \tag{2.2}$$

where c is the speed of light travelling in a vacuum ($c = 2.99793 \times 10^8$ ms^{-1}).

A time tag is assigned to each one-way distance measurement that corresponds to the time at which the laser pulse illuminates a spot on the Earth's surface or a cloud. For ICESat the time tag, T_m, is given in *Schutz* [2002] as

$$T_m = T_0 + \frac{\Delta T}{2} \tag{2.3}$$

In order to accurately geolocate the laser footprint on the Earth's surface, the altimeter measurement must be treated as a vector quantity. The magnitude of the altimeter measurement vector, $\bar{r}_h$, is simply R_{alt} and the direction of this vector is obtained from the pointing instrumentation (i.e. the Stellar Reference System (SRS), star

camera and gyroscope) onboard ICESat. The ICESat position vector, $\bar{r}_{ref}$, of a suitable reference point in the laser altimeter instrument is calculated with respect to a common geodetic coordinate system (i.e. the IERS Terrestrial Reference Frame (ITRF)). The magnitude of the ICESat position vector, H_{sat}, represents the altitude of the satellite above the reference ellipsoid.

The vector sum

$$\bar{r}_{ref} + \bar{r}_h = \bar{r}_{spot} \tag{2.4}$$

provides the geocentric coordinates of the laser footprint on the Earth's surface (i.e. the laser footprint location), $\bar{r}_{spot}$, with respect to the ITRF [*Schutz*, 2002]. This concept is illustrated in Figure 2.3.

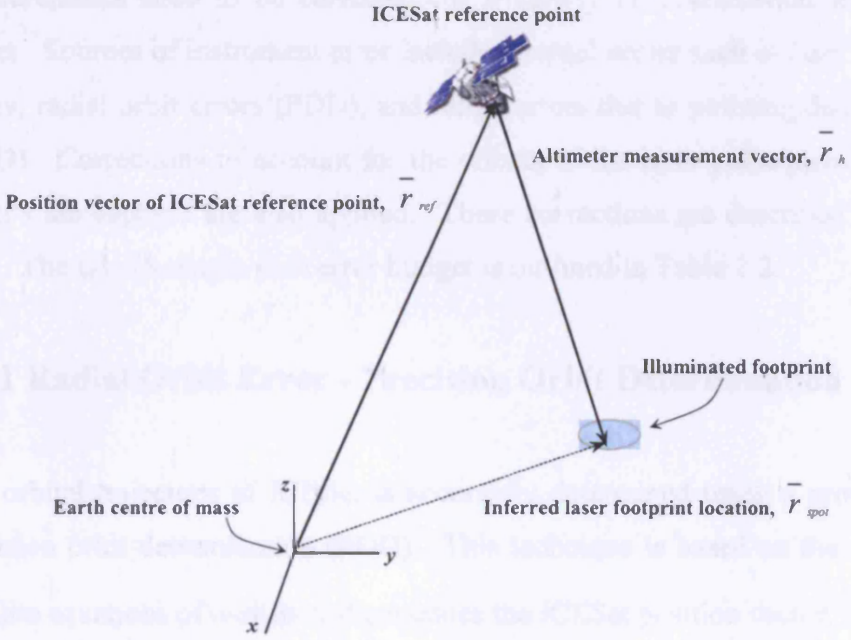

Figure 2.3 Satellite laser altimetry concept. Adapted from *Schutz* [2002].

The spot coordinates in the ITRF can be converted into geodetic latitude, longitude and ellipsoidal height [*Schutz*, 2002]. This is the primary altimeter data product and a

series of spot coordinates enables a profile of the Earth's surface, with respect to the ellipsoid[13], to be obtained [*Schutz*, 2002].

The surface elevation as measured by ICESat, h_{alt}, is determined from the altitude of the satellite orbit (above the reference ellipsoid), minus the slant range to the surface

$$h_{alt} = H_{sat} - R_{alt} - R_{cor} \tag{2.5}$$

where, R_{cor}, are range corrections for propagation delays which, if not properly accounted for, would lead to overestimates of the range. These are described in detail in the following section.

2.5 Range Corrections

Regardless of the surface (ice sheets, sea ice, land or ocean), all GLAS range measurements need to be corrected for a variety of instrumental and geophysical errors. Sources of instrument error include internal errors such as laser bias, boresight errors, radial orbit errors (POD), and range errors due to pointing determination bias (PAD). Corrections to account for the effects of the laser pulse passing through the Earth's atmosphere are also applied. These corrections are described in some detail here. The GLAS single-shot error budget is outlined in Table 2.2.

2.5.1 Radial Orbit Error - Precision Orbit Determination

The orbital trajectory of ICESat is accurately determined using a process known as precision orbit determination (POD). This technique is based on the solution of the satellite equations of motion and generates the ICESat position vector, $\bar{r}_{ref}$ (see Figure 2.2). The exact position of the GLAS instrument in space is determined using data from the on-board Global Positioning System (GPS) receivers [*Schutz et al.*, 2005]. In addition, laser ranging data from ground-based satellite laser ranging (SLR) stations collaborating in the International Laser Ranging Service is gathered via the use of a

[13] In the case of ICESat, surface height measurements are measured relative to the TOPEX/Poseidon reference ellipsoid (a_e = 6378136.3 m, $1/f$ = 298.257).

laser retroreflector array on ICESat [*Schutz et al.*, 2005]. While this data is not utilised by the POD procedure, it is used to test the accuracy of the POD derived from the GPS data [*Schutz et al.*, 2005]. Based on such tests, the current radial orbit accuracy is ~ 2 cm [*Schutz et al.*, 2005], which is a significant improvement on the figure provided in the pre-launch error budget (see Table 2.2).

2.5.2 Pointing Determination – Precision Attitude Determination

In order to obtain high resolution altimetry data, accurate pointing control is necessary to maintain near nadir alignment of the laser beam, since deviations in laser pointing angle can map directly into significant range biases [*Bufton*, 1989]. To meet the ICESat mission requirements and measure surface elevation to centimetre-level accuracy, it is necessary to measure the GLAS beam pointing angle to arcsecond-level accuracy [*Lisano and Schutz*, 2001]. The precision attitude determination (PAD) process is used to calculate the direction in which the laser beam is pointing and the position of the footprint on the Earth's surface [*Zwally et al.*, 2002]. This process generates a laser pointing vector, $\bar{r}_h$ (see Figure 2.2). The laser pointing direction is calculated for each shot using data from the stellar-reference system (SRS) as described by *Sirota et al.* [2005].

The range error, ΔR_{alt}, which is a result of beam pointing angle uncertainty and surface slope, is approximated in *Harding et al.* [1994] as

$$\Delta R_{alt} = R_{alt}\, \Delta\alpha \tan(\theta + \alpha_{est}) \tag{2.6}$$

where, R_{alt} is the one-way range (magnitude of the laser pointing vector), θ is the local ground slope, α_{est} is the estimated altimeter beam pointing angle[14], and $\Delta\alpha$ is the pointing determination error. This concept is illustrated in Figure 2.4; note the surface profile is greatly exaggerated. Over sea ice, assuming a negligible ground slope, and estimated beam pointing angle of 0.3°, a one arc second ($\Delta\alpha$ = 1 arcsec) error in the laser pointing direction produces a 1.5 cm range measurement error from a spacecraft altitude of ~600 km.

[14] For ICESat, the off-nadir laser pointing angle, α_{est}, is 0.3° [*Schutz et al.*, 2005].

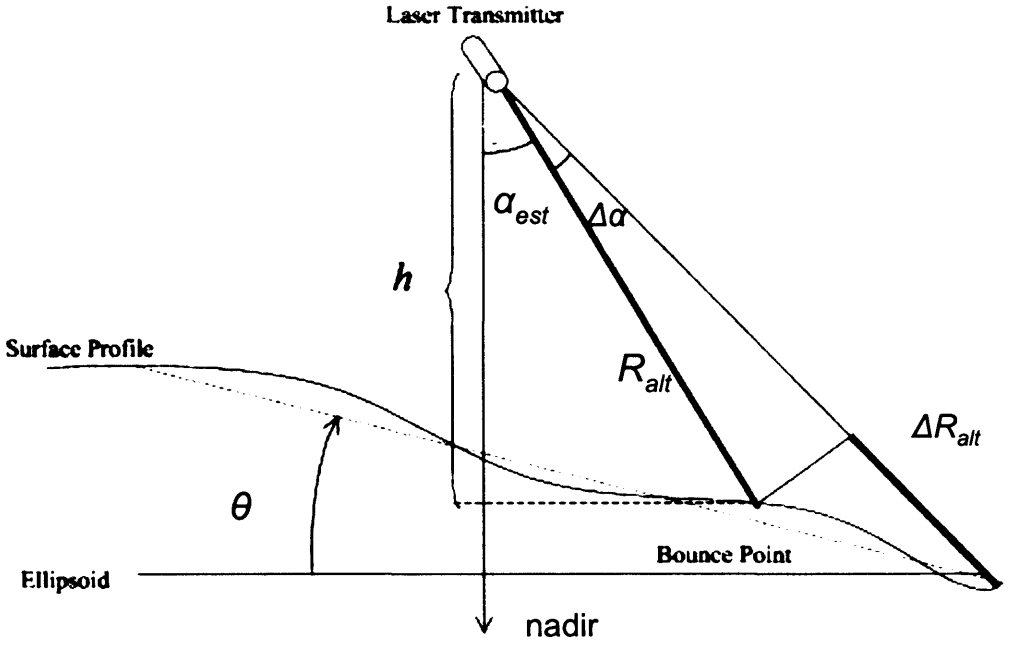

Figure 2.4 Concept of the laser altimetry range error (ΔR_{alt}) due to off-nadir pointing angle uncertainty ($\Delta\alpha$) and surface slope (θ). Note that (i) scale is greatly exaggerated for illustration purposes and (ii) over sea ice, the surface profile would be almost flat with respect to the ellipsoid (i.e. $\theta \approx 0°$). Adapted from *Bufton* [1989].

Since launch, it has been found that thermally-driven systematic pointing errors (SPE) can seriously compromise the elevation accuracy of the GLAS laser data [*Luthcke et al.*, 2005]. SPE are a result of transmit path pointing errors and/or field of view (FOV) shadowing of the received pulse in the receiver telescope [*Luthcke et al.*, 2005]. Correcting these SPE is dependent on both the laser operations period and thorough understanding of the instrumental corrections [*Schutz et al.*, 2005]. Through spacecraft attitude manoeuvres, known as Scan Manoeuvre Calibrations (SMC), *Luthcke et al.* [2005] have devised a method to calibrate the SPE for each laser operations period to sub-arcsecond precision. So far these corrections have been applied to the L2a, L2b and L3a datasets. L2a data have a pointing knowledge accuracy of ~2 arcsec, which results in a surface horizontal geolocation accuracy of ~6 m and 3 cm vertical elevation accuracy for small surface slopes [*Schutz et al.*, 2005]. Current pointing knowledge is at the 15 - 20 arcsec level (equivalent to 22.5 – 30 cm vertical accuracy) for the datasets that have not had the SMC corrections applied.

2.5.3 Tropospheric Delay

Both the transmitted and received laser pulses are delayed as they travel through the troposphere. This effect is called the tropospheric delay and requires a further correction to the range measurement. For nadir-pointing ray paths the tropospheric delay is almost directly related to surface pressure and total column precipitable water vapour, with some variations due to the height of the laser footprint location, changes in gravity with respect to height and the effects of non-hydrostatic forces acting in the atmosphere [*Herring and Quinn, 2001*]. It is calculated by integrating the atmospheric refractivity, as a function of pressure, temperature and relative humidity along a ray path [*Herring and Quinn, 2001*].

The full zenith tropospheric delay, ΔL_Z, at the laser wavelength, is given in *Herring and Quinn* [2001] as

$$\begin{aligned} \Delta L_Z &= \Delta L_D + \Delta L_W \\ \Delta L_D &= \left(2.2582 m^2 s^2 / Pa\right) g_m^{-1} P_S \\ \Delta L_W &= \left(8.0834 x 10^{-5} m / mm\right) PW \end{aligned} \tag{2.7}$$

where, ΔL_D is the dry (hydrostatic) component of the tropospheric range delay, ΔL_W is the wet component of the tropospheric range delay, g_m is the mean value of gravity in the column of the atmosphere, P_S is surface pressure, PW is precipitable water vapour.

For an average surface pressure of 1000 hPa, and an approximate value of 9.8 ms^{-2} for the mean gravity, the zenith dry tropospheric delay is approximately 2.3 m and is the main component of total tropospheric delay [*Herring and Quinn, 2001*]. The zenith wet delay is much smaller in magnitude but varies globally. Given precipitable water vapour values of less than 1 cm in the polar regions, the wet tropospheric delay is approximately 0.1 cm. The dry troposphere correction and the wet troposphere correction are calculated separately once per measurement [*Brenner et al.*, 2003].

The tropospheric range correction depends on accurate knowledge of surface pressure along ICESat ground tracks [*Schutz*, 2002]. The National Centre for Environmental Prediction (NCEP) provides a global analyses (a blend of observational and model data), which is a dataset of atmospheric variables (temperature, geopotential height and relative humidity at standard upper atmospheric pressure levels). An investigation of the use of the NCEP global analyses to model surface pressure shows that an accuracy of 5 mb or better can be achieved, corresponding to an accuracy of 1 cm or better for the tropospheric delay calculation [*Schutz*, 2002]. The atmospheric fields are six-hourly and are interpolated to coincide with the time tag and location of each GLAS footprint so as to enable the calculation of surface pressure and precipitable water vapour. Due to the additional errors involved in the interpolation process, a 10 mb error in the surface pressure is assumed. The total error associated with the tropospheric delay correction is therefore estimated to be 2 cm (Table 2.2).

2.5.4 Forward Scattering due to Clouds

Cloud area, thickness, height and water content all have an effect on the propagation of the GLAS laser beam as it travels through a cloudy atmosphere. Despite the fact that the Arctic and Antarctic are classified as desert regions, clouds and aerosols are common [*Duda et al.*, 2001]. The GLAS laser pulse is of sufficient power to penetrate a large fraction of polar clouds, so that even when a region is classified as cloud covered, surface elevation measurements can be obtained [*Schutz et al.*, 2005].

Nevertheless, if a laser pulse is transmitted through thick clouds or an aerosol layer, atmospheric multiple scattering effects will lengthen the path taken by the photons to return to the GLAS telescope. Attenuation of the laser pulse energy is primarily caused by photon scattering since atmospheric absorption is small at 1064nm [*Duda et al.*, 2001]. Consequently, the return pulse is broadened due to the forward scattering of light, which causes the signal for the delayed photons to appear at a later time in the received waveform. The resultant waveform is asymmetric with a long "tail" at the end of the echo waveform [*Fricker et al.*, 2005]. The effects of atmospheric forward scattering due to the presence of thick cirrus clouds over the salar de Uyuni included high noise on the received echo and anomalously low elevation estimates which were ~16 cm below the true elevation of the surveyed

terrain; up to 13% of the GLAS laser pulses could not penetrates the thick cloud cover [*Fricker et al.*, 2005]. An example of the effects of forward scattering on a GLAS waveform is displayed in Figure 2.5.

Duda et al. [2001] and *Mahesh et al.* [2002] investigated the impact of multiple scattering on satellite laser altimetry and the magnitude of this error source on range measurements. *Duda et al.* [2001] found that low altitude clouds and cloud particles with radii in the range 3 – 20 μm will cause the largest delays. The persistent haze of the Arctic region contains particle radii typically 0.1 μm in size and therefore has little effect on the path delay since the mean particle size is smaller than the wavelength of the laser pulse [*Duda et al.*, 2001].

The ICESat Science Team is continuing research into the detection of, and possible correction for, forward scattering. However only the trailing edge of echo waveforms is affected by forward scattering, and the standard Gaussian fit method used for estimating elevation (see Figure 3.4) is specifically designed with this in mind, so as to lessen the effects of atmospheric multiple scattering and reduce path delays [*Duda et al.*, 2001].

2.6 GLAS Error Budget

The range error combined with the best estimates for all the other anticipated error sources can be used to derive the accuracy of individual elevation measurements [*Harding et al.*, 1994]. *Zwally et al.* [2002] predicted the GLAS elevation measurement accuracy to be approximately 15 cm and their pre-launch error budget is outlined in Table 2.2. The budget is based on two assumptions: i) the GLAS laser pointing angle is determined with an accuracy of 1.5 arc seconds and ii) a sloping surface of 1° (typical slope of the West Antarctic ice streams) [*Schutz*, 2002]. However, for clear sky conditions with atmospheric transmission at or above 50%, the range error is expected to be less than 10 cm [*Zwally et al.*, 2002]. The errors in the budget are a combination of random and systematic errors and, while some are correlated on successive pulses, the errors for a specific location on the surface will tend to be random and uncorrelated [*Zwally et al.*, 2002].

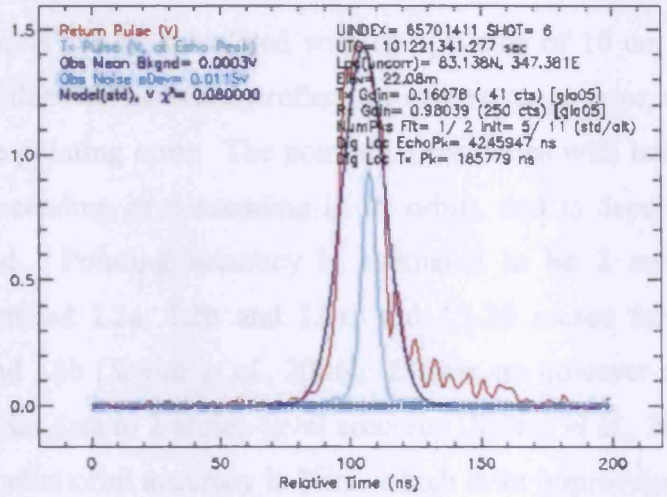

Figure 2.5 An example of the effect of forward scattering on a GLAS waveforms. This waveform was acquired on 18th March 2003 over the Arctic Ocean. The image illustrates that the received pulse (red) is much broader than the transmit pulse (green). The elongated tail segment of the pulse is clearly visible and is likely due to the transmission of the laser pulse through polar clouds where forward scattering of photons within a cloud has resulted in their delayed return to the detector. This plot was generated using software available at the GLAS Science Computing Facility (SCF) at Goddard Space Flight Centre.

Source	Budgeted 1-σ error (cm)	Typical error over sea ice (cm)
GLAS range measurement precision	10	2 *
Precision orbit determination (POD)	5	2 +
Laser pointing determination (PAD)	7.5	3 $
Tropospheric delay	2	2 #
Atmospheric forward scattering	2	2 #
Other (mass-centre location, tides, etc.)	1	1 #
Ocean tide elevation error (Arctic Ocean)	N/A	7 §
Uncertainty in Inverse Barometer correction	N/A	4 ¶
Root-sum-squared (RSS) error	13.8	9.5

Table 2.2 Single-shot error budget for ICESat elevation measurements. Pre-launch error budget (first column) [*Zwally et al.*, 2002], assumes a 1° surface slope and 1.5 arcsec pointing accuracy. Typical error budget for elevation measurements over sea ice (second column), where the error sources are based on **Kwok et al.*, [2004], *+Schutz et al.*, [2005], $Eqn. (2.6) for a measurement over sea ice with 0° surface slope, 2-arcsec pointing knowledge accuracy consistent with L2a data, and satellite altitude of 600km, #as for error budget given in *Zwally et al.*, [2002], §*Peacock and Laxon* [2004] (see Section 2.7.3),¶ *Chelton et al.*, [2001], (Figure 25).

In order to meet the scientific requirements of the ICESat mission, it is necessary that range measurements can be calculated with an accuracy of 10 cm for a single laser pulse. This value does not accurately reflect the current range error, which is primarily dependent on the pointing error. The pointing error varies with latitude (i.e. whether the satellite is ascending or descending in its orbit), and is dependent on the laser operations period. Pointing accuracy is estimated to be 2 arcsec for the laser campaigns designated L2a, L2b and L3a, and 15-20 arcsec for laser campaigns designated L1 and L3b [*Schutz et al.*, 2005]. Efforts are however underway to bring all available ICESat data to 2 arcsec-level accuracy [*Schutz et al.*, 2005]. Conversely, the actual POD radial orbit accuracy is 2 cm, which is an improvement over the value estimated in the pre-launch error budget [*Schutz et al.*, 2005].

An estimate of the total error on a single-shot range measurement over sea ice is also presented in Table 2.2. The estimate is based on the following assumptions: (i) elevation measurements are over smooth, flat, sea ice surfaces with zero surface slope, (ii) measurements are part of the L2a dataset which has a 2 arcsec pointing knowledge accuracy [*Schutz et al.*, 2005], and (iii) the range measurement precision is 2 cm, as estimated by *Kwok et al.* [2004]. We have also included estimates of the errors in the ocean tidal model and the inverse barometer correction, since we expect these to be two major sources of error on the range measurements over sea ice in the Arctic Ocean. *Peacock and Laxon* [2004] compared three ocean tidal models of the Arctic Ocean and found that they differed by ~6-8 cm (see Section 2.7.3). The inverse barometer correction, which takes account of the effects of atmospheric pressure loading on the sea surface, is based on knowledge of sea level pressure (see Section 2.7.4). The accuracy of the inverse barometer correction is therefore limited by the uncertainty in the actual sea level pressure. A study comparing NCEP and European Centre for Medium-Range Weather Forecast (ECMWF) sea level pressure fields showed that uncertainties in these fields could be up to 4 mb at high northern latitudes [*Chelton et al.*, 2001]. This corresponds to an uncertainty in the inverse barometer correction of approximately 4 cm (see Section 2.7.4 for further details). Overall, the total error on a single-shot range measurement over sea ice is estimated to be approximately 9.5 cm.

2.7 Geophysical Effects on the Sea Surface Topography

Over the ice-covered oceans, the altimetric surface elevation measurement can be described as

$$h_{alt} = h_{sf} + h_{ssh} \tag{2.8}$$

where, h_{sf} is the snow freeboard (the height of the air/snow interface above the local sea surface – see Figure 1.20), and h_{ssh} is the sea surface height relative to the reference ellipsoid.

Over scales of centimetres to a few hundred metres the sea surface is roughened by waves and ocean swell. However, over larger distances of many kilometres, the sea surface is approximately flat with some long-wavelength undulations due to ocean currents, changes to atmospheric pressure loading, and variations in the Earth's gravity field associated with features such as seamounts and ocean trenches. The sea surface height is composed of the geoid height, dynamic ocean topography (DOT), tidal height and variations in surface elevation due to the inverse barometer effect. These components are illustrated in Figure 2.6.

Thus the basic equation for sea surface height, h_{ssh}, is

$$h_{ssh} = h_g + h_{DOT} + h_T + h_{IB} \tag{2.9}$$

where h_g is the geoid height above the reference ellipsoid, h_{DOT} is the dynamic topography, h_T is the tidal elevation, and h_{IB} is the inverse barometer effect. The terms in Eqn (2.9), and their magnitude, are discussed in more detail in the following sections. The altimetric sea surface height measurement clearly has a number of geophysical applications, since any of the elements of Eqn. (2.9) may be derived if all other elements are known or can be modelled or eliminated [*Chelton et al.*, 2001].

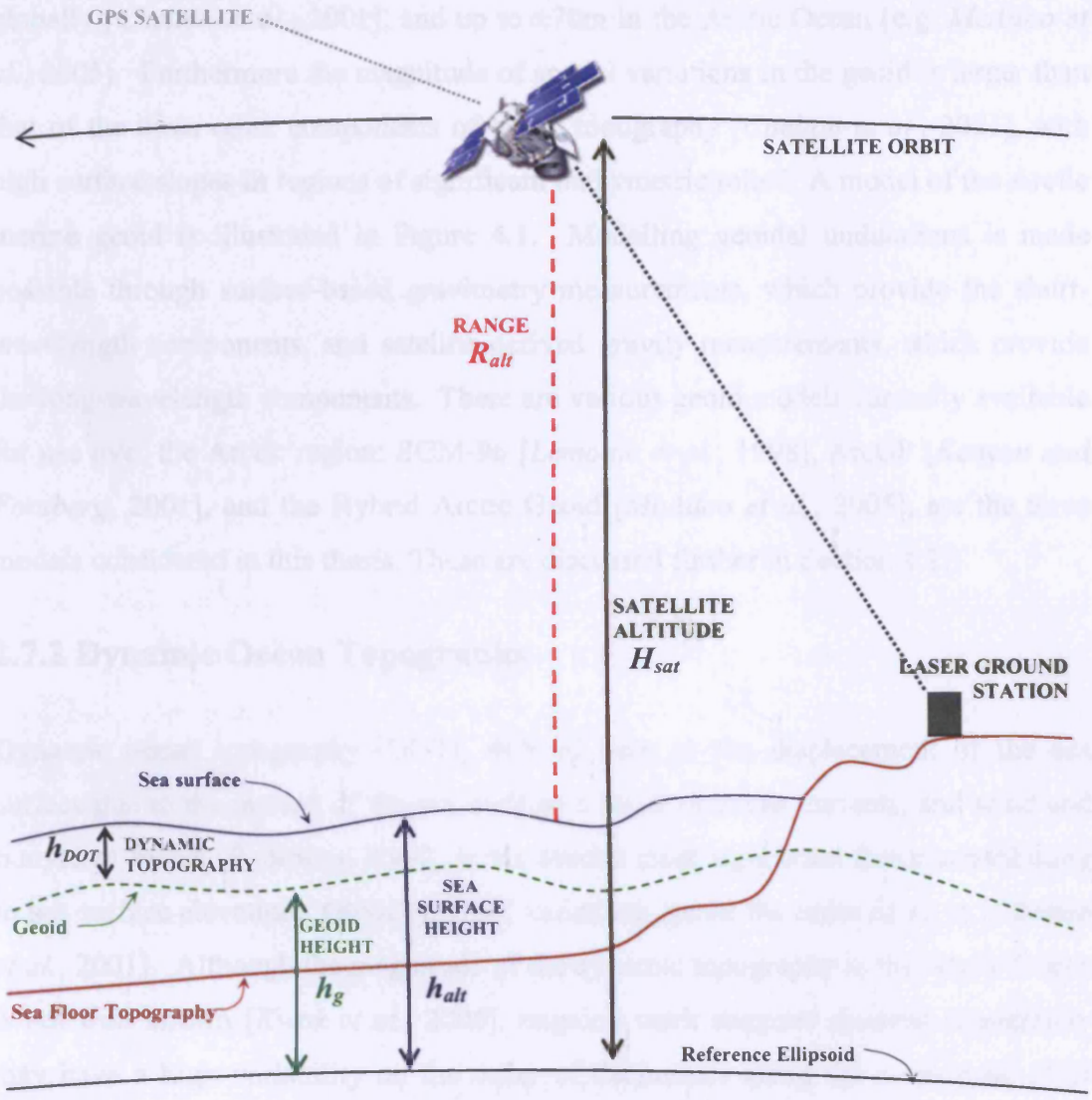

Figure 2.6 Schematic diagram illustrating satellite altimetric measurement of sea surface height in relation to the reference ellipsoid. Note topography is not to scale and the vertical scale is greatly exaggerated for illustration purposes. Adapted from *Robinson* [2004].

2.7.1 The Geoid

The geoid represents the theoretical shape of the ocean surface at rest were there no oceanic or atmospheric circulation. At short wavelengths, the marine geoid reflects sea floor bathymetry, while at longer wavelengths it reflects variations in the Earth's gravitational field, due to density changes in the Earth's interior [*Chelton et al.*, 2001]. As illustrated in Figure 2.6, the main component of sea surface height is geoidal height, which can deviate by approximately ±100m from the reference ellipsoid

globally [*Chelton et al.*, 2001], and up to ±70m in the Arctic Ocean [e.g. *McAdoo et al.*, 2005]. Furthermore the magnitude of spatial variations in the geoid is larger than that of the three other components of ocean topography [*Chelton et al.*, 2001], with high surface slopes in regions of significant bathymetric relief. A model of the Arctic marine geoid is illustrated in Figure 4.1. Modelling geoidal undulations is made possible through surface-based gravimetry measurements, which provide the short-wavelength components, and satellite-derived gravity measurements, which provide the long-wavelength components. There are various geoid models currently available for use over the Arctic region; EGM-96 [*Lemoine et al.*, 1998], ArcGP [*Kenyon and Forsberg*, 2001], and the Hybrid Arctic Geoid [*McAdoo et al.*, 2005], are the three models considered in this thesis. These are discussed further in Section 4.2.1.

2.7.2 Dynamic Ocean Topography

Dynamic ocean topography (DOT), defined here as the displacement of the sea surface due to the motion of the sea itself as a result of ocean currents, and wind and buoyancy forces [*Robinson*, 2004], is the second most significant factor contributing to sea surface elevation. Globally, DOT variations are on the order of ±2 m [*Chelton et al.*, 2001]. Although the magnitude of the dynamic topography in the Arctic Ocean is not well known [*Kwok et al.*, 2006], ongoing work suggests dynamic topography may have a high variability on the order of decimeters along the continental shelf regions of the Arctic Ocean [*McAdoo et al.*, in preparation]. Current ocean models likely underestimate the variability of Arctic DOT [*Kwok et al.*, 2006], but there is general agreement between the spatial patterns found in the oceanographic models with those exhibited in the available observational datasets [*McAdoo et al.*, in preparation].

DOT can be decomposed into a further two components: long-period mean dynamic topography (MDT), and fluctuating, time variant topography. MDT is mainly due to large-scale mean oceanic circulation. For instance, it may be estimated from satellite altimetry data, by subtracting the geoid from a mean sea surface (MSS), which has been calculated by averaging sea surface height measurements ($\bar{h}_{ssh}$) over a specific observational time period:

$$MDT = \bar{h}_{ssh} - h_g \tag{2.10}$$

Time variant topography, due to meso-scale ocean circulation (ocean eddies, etc.) as well as the effects of wind, changes in atmospheric pressure, and density variations in the ocean, varies over a range of spatial and temporal scales. We define sea level anomalies, "SLA", as the difference between the altimeter-derived, instantaneous sea surface elevations and the long-term MSS:

$$SLA = h_{ssh} - \bar{h}_{ssh} \quad (2.11).$$

2.7.3 Tidal Corrections

Appropriate tidal elevations must be applied to altimetry data to remove any time-varying tidal effects. Algorithms for correcting ICESat elevations for tidal effects have been generated and are used to calculate the main tide components: ocean tide, solid Earth tide, ocean loading tide, and the pole tide [*Phillips et al.*, 1999]. The ocean tide and solid Earth tide are caused by the gravitational force exerted by the Sun and the Moon on the oceans and the solid Earth, respectively [*Chelton et al.*, 2001]. The ocean loading tide and the pole tide are much smaller in magnitude, and are a result of crustal loading due to the weight of the ocean tide, and the motions of the ellipsoid due to polar motion, respectively [*Phillips et al.*, 2001].

The magnitude of each tidal component is estimated using tidal prediction models and these quantities are subtracted from the elevation data [*Brenner et al.*, 2003]. The corrections that take account of the solid Earth tide, long period tides and the pole tide are consistent with those used for previous radar altimetry missions, such as TOPEX-Poseidon [*Phillips et al.*, 1999; *Zwally et al.*, 2002]. The ocean tide and ocean loading tide corrections are based on the GOT99.2 global ocean model [*Padman and Fricker*, 2005], which is described in *Ray* [1999].

Estimates of the magnitude of the main tidal components are given in Table 2.3 with the uncertainties associated with these estimates (i.e. residual error after tidal correction has been calculated). The ocean loading tide causes displacements of several tens of millimetres in polar regions and *Phillips et al.* [1999] have calculated that the highest amplitudes of the ocean load tide are along the coast. Notably, the magnitudes of the ocean loading tide, and the solid Earth tide, included in the ICESat

data products over the Arctic, are much smaller than the global averages presented in Table 2.3, both quantities having values around 2 cm [*Kwok et al.*, 2006].

Component	Magnitude	Uncertainty
Ocean Tide (open ocean)	± 50 cm	± 10 cm
Ocean Tide (coasts)	± 2 m	± 10 cm
Long Period Ocean Tide	± 1 m	few cm
Pole Tide	< 2 cm	few mm
Ocean Loading Tide	± 10 cm	< 0.5 cm
Solid Earth Tide	± 30 cm	± 0.5 cm

Table 2.3 Approximate magnitudes of the components of the ICESat tide correction with their associated uncertainties. From *Phillips et al.* [1999].

Errors in ocean tide models are believed to be significant in the Arctic, since there is a relative lack of observational data [*Wingham et al.*, 2001] and the inclination of oceanographic satellites is such that it limits coverage of the Arctic region (e.g. ERS surveys to ±81.5°). A comparison of three ocean tidal models by *Peacock and Laxon* [2004] found that they differed by ~6-8 cm in the Arctic Ocean. The ocean tide includes diurnal, semi-diurnal, and long period components; the major components being the semidiurnal constituents M_2 and S_2, and the diurnal constituents K_1 and O_1 [*Le Provost*, 2001]. The amplitude of these constituents, based on a tidal model devised by *Kowalik and Proshutinsky* [1994], is illustrated in Figure 2.7.

Proper simulation of the ocean tide, particularly in continental shelf regions of the Arctic Ocean, such as the Canadian Arctic Archipelago and Baffin Bay, is challenging and remains a possible source of error in satellite altimetric measurements of sea surface height which would mask actual sea surface variability [*Kwok et al.*, 2006].

2.7.4 Atmospheric Pressure Loading

The local response of the ocean to changes in the atmospheric pressure distribution across the ocean surface also contributes to the surface elevation, and is known as the "inverse barometer effect" (IBE). This is usually taken into account by applying an inverse barometer correction. Assuming an isostatic response by the ocean to atmospheric pressure loading, an increase in atmospheric pressure of 1 mb will decrease the sea surface elevation by ~ 1 cm [*Chelton et al.*, 2001].

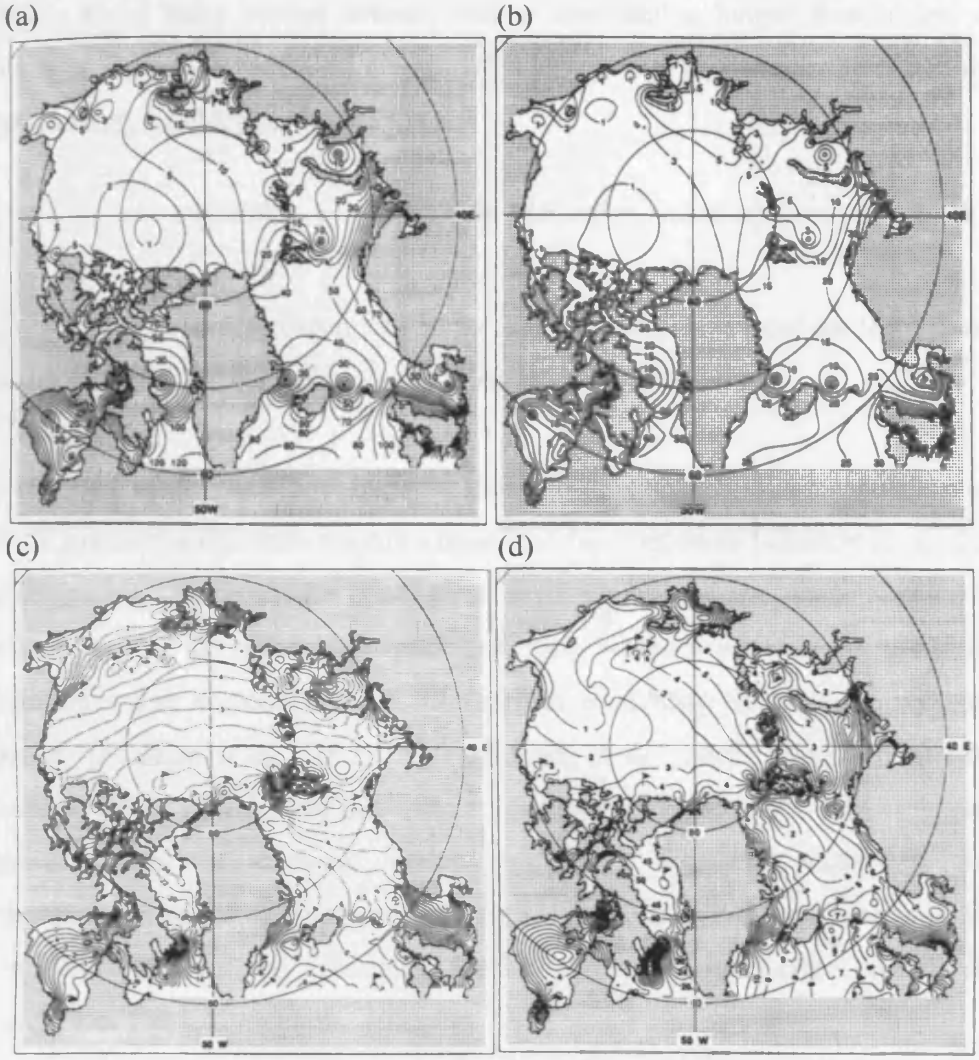

Figure 2.7 The amplitude (cm) of the contribution to surface elevation due to the main ocean tide constituents, (a) M_2, (b) S_2, (c) O_1 and (d) K_1. Flags denote shelf wave regions. From *Kowalik and Proshutinsky* [1994].

Recent work by *Kwok et al.* [2006] found pressure variations of up to 70 mb over a 16-day period across the Arctic Ocean. This variation is equivalent to a variation of ~ 70 cm in sea surface elevation, illustrating the impact of this effect. Including an inverse barometer correction in the calculation of sea surface height from altimetry data significantly reduces the variance of the sea surface height estimate [*Kwok et al.*, 2006].

The first approximation when accounting for atmospheric pressure loading is to apply the isostatic inverse barometer correction, since it is accurate at middle and high

latitudes, away from coastal effects, and at time-scales longer than a few days [*Chelton et al.*, 2001]. Following *Gill* [1982], the isostatic inverse barometer correction may be calculated as follows:

$$IBc = -0.009948 * (P - P_0) \quad (2.12)$$

where, *IBc*, is the inverse barometer correction in meters, P is local sea level pressure in millibars, and P_0 is the reference sea level pressure (1013.3 mb).

However, the ocean does not simply respond to atmospheric pressure loading in an isostatic manner; a dynamic response must also be considered [*Chelton et al.*, 2001]. In shallow seas (such as the continental shelf regions of the Arctic Ocean) near coastlines, where the effects of wind stress may be more pronounced, the isostatic inverse barometer correction is not expected to adequately describe the sea surface response [*Padman et al.*, 2003]. Indeed *Kwok et al.* [2006] calculated an inverse barometer effect of 1.12 cm mb^{-1} for a 16-day Arctic dataset, which is higher in magnitude than the classical inverse barometer correction described above. Furthermore, in terms of cross-comparing satellite radar and laser altimetry data, we are interested in accurately accounting for the inverse barometer effect on time-scales ranging from 1 day to 1 month.

In order to account for the response of the ocean to atmospheric pressure loading accurately, we should therefore combine the classical isostatic inverse barometer correction with a second component based on wind stress [*Carrere and Lyard*, 2003; *Kwok et al.*, 2006]. A global model, called MOG2D-G, which simulates the ocean response to atmospheric wind and pressure forcing, has been constructed by *Carrere and Lyard* [2003]. When the MOG2D-G solutions were applied to TOPEX/Poseidon altimetry data *Carrere and Lyard* [2003] found that high latitudes, continental shelf areas, and shallow waters, were the locations of the most significant reduction in sea level variance. Furthermore the RMS variance of ENVISAT sea level estimates at crossover locations was lower when the MOG2D-G solution was used in place of the classical IBc (A. Ridout, *personal communication*). We will apply the solutions derived from the MOG2D-G model to the altimetry data considered in this thesis to correct for the dynamic response of the ocean to atmospheric pressure loading.

2.8 Summary

The ICESat/GLAS mission, launched in January 2003, is the first Earth-orbiting satellite laser altimeter and the first space-borne altimeter specifically designed to study the Earth's polar regions. Satellite laser altimeters have some advantages over satellite radar altimeters, notably an order of magnitude smaller footprint. Individual laser pulses present the opportunity to acquire not only high-quality elevation measurements, but also information regarding surface height distribution, slope, roughness and reflectivity. ICESat provides high mapping density and almost global coverage (up to 86°). The pre-launch plan for the science phase of the ICESat mission included a ground-track with a 183-day repeat period. Due to a revised mission plan, ICESat now utilises a 91-day exact repeat orbit with a 33-day subcycle. The GLAS laser operates for one 33-day subcycle every ~3 months, typically during the months: February-March, May-June, and October-November.

Standard corrections for satellite orbit, tides, and atmospheric delay are applied to the laser data. The accuracy of ICESat elevation measurements are compromised by inadequate knowledge of beam pointing and the lack of a range correction for forward scattering of the laser pulse in the presence of cloud cover. Under favourable instrument operation conditions the total measurement error for a single laser pulse is estimated to be on the order of 9.5 cm over sea ice with negligible surface slope.

In order to accurately determine sea surface height using altimetric data, corrections for geoidal undulations, dynamic ocean topography, tidal elevation, and atmospheric pressure loading must be applied to the data. Over the global oceans, the approximate magnitudes of these components of sea surface height are as follows: geoid height ± 100 m, dynamic topography ± 2 m, ocean tide ± 50 cm, inverse barometer effect ± 10cm. A lack of observational data over the Arctic limits our ability to adequately account for these effects in some regions. Shallow seas around the continental shelf regions of the Arctic Ocean are likely to be the sites of the highest ocean tide amplitudes, dynamic topography and elevation variation due to atmospheric wind and pressure loading. The accuracy of our method to determine sea surface height in these particular regions may therefore be compromised.

3 Exploitation of ICESat Data over Sea Ice

3.1 Introduction

In Chapter 2 we gave a brief introduction to satellite altimetry and the errors associated with altimetry measurements over sea ice. In this chapter we describe (i) the altimetric datasets used in the analysis presented in this thesis and (ii) other complementary satellite data which is integral to our analysis. We briefly introduce the ICESat dataset, paying particular attention to data collected over sea-ice covered oceans. We describe the radar altimetry data which we use for comparison with our ICESat results. We provide a detailed description of the parameters that are relevant to the analysis of ICESat data over sea ice, noting the limitations associated with each parameter. Although much of this information is already available in the literature, Algorithm Theoretical Basis Documents (ATBDs), and the GLAS Release Notes, we have collated the information pertinent to the analysis of ICESat data over sea ice and it is this that we present here. We review the results of analysis of ICESat data for various oceanographic investigations carried out to date, and the outstanding issues that need to be addressed for the successful analysis of ICESat data over sea ice. We conclude with an overview of the aims of the work presented in this thesis.

3.2 Data Description

3.2.1 ICESat Data

The first ICESat laser, designated Laser 1 (or L1), began operations on February 20, 2003 and continued gathering data until the end of March 2003 as part of the first laser campaign. After the failure of L1, the second GLAS laser was utilized for the first of three campaigns in a period during September and November 2003. During this laser campaign (designated L2a) all ICESat instrumentation operated with near expected performance under optimal conditions [*Schutz et al.*, 2005]. Since this period represents the best performance of ICESat, major efforts were employed to correct the data for systematic pointing errors [*Luthcke et al.*, 2005]. Pointing knowledge accuracy is ~2 arcsec for L2a data [*Schutz et al.*, 2005].

The GLAS Software Development Team generates a new data release every time changes have been made to the algorithms used to generate the data products. Data from previous laser campaigns may be reprocessed under a new release. The first public release of data was Release 12. Although the highest available release is currently Release 26, data from each laser operations period are in different post-processing states at the time of writing. There are therefore limitations associated with some of the available data. Table 3.1 describes the relationship between laser operations periods and data releases, and highlights those datasets we consider in the analysis presented here.

Laser Operations Period	Data start date	Data stop date	Days in Operation	Orbit Repeat (days) *	Product Release #
L1	20/02/2003	20/03/2003	29	8	18
L2a	04/10/2003	18/11/2003	45	91/33	26
L2b	17/02/2004	21/03/2004	34	91/33	26
L3a	03/10/2004	08/11/2004	37	91/33	23
L3b	17/02/2005	24/03/2005	36	91/33	19

Table 3.1 Description of ICESat data releases. The laser operations periods included in this table represent the datasets considered in analysis presented in this thesis. * A 91-day repeat orbit, with a 33-day near-repeat subcycle, was implemented on 4th Oct, 2003.

One of the major differences between successive releases of data collected during a particular laser campaign is the improved treatment of instrument pointing biases [see *Luthcke et al.*, 2005]. Ongoing efforts by the ICESat science team are expected to improve all ICESat datasets, bringing them to the 2 arcsec level of pointing accuracy achieved with L2a data [*Fricker at al.*, 2005]. For each operations period that we consider in our analysis, we use the latest available release at the time of writing.

3.2.2 Other Data Sets

In order to assess the ability of our processing schemes to identify sea surface height, and the accuracy of our results from ICESat data over Arctic sea ice, we compare our data to a number of independent datasets. We briefly describe these datasets here. In

addition we use sea ice drift vector data and sea ice concentrations as part of our analysis and a short description of these datasets is also provided.

3.2.2.1 Satellite Radar Altimetry

We analyse SSH and sea ice freeboard measurements derived from ENVISAT satellite radar altimetry (RA-2) data which are coincident with the ICESat dataset. ENVISAT, launched in March 2002, facilitates coverage of the Arctic region to 81.5°N and follows a similar orbit to the ERS-2 satellite. RA-2 is a nadir-looking, pulse limited radar operating at two frequencies: 13.575 GHz (Ku Band) and 3.2 GHz (S band) [*Baker et al.*, 2002]. ENVISAT utilises a 35-day repeat orbit and data can therefore be used for direct comparison with ICESat. The altimetry science products have been derived from SGDR data acquired from the European Space Agency (ESA) (*A. Ridout*, personal communication).

The identification of the sea surface is possible through analysis of the received waveform echo shape. Radar returns over open water or thin ice are specular in nature due to scattering from the smooth surface. These can be distinguished from diffuse radar returns which originate over rough, consolidated ice [*Peacock and Laxon*, 2004]. An example of specular and diffuse radar echo waveform shapes is illustrated in Figure 3.1. The procedure for deriving elevations from the two sets of waveforms is beyond the scope of this thesis, but it is described in detail in *Peacock and Laxon* [2004]. An example of an along-track surface height profile over the ice pack is illustrated in Figure 3.2. The sharp jump in elevation is due to the elevation change between the sea surface and a sea ice floe.

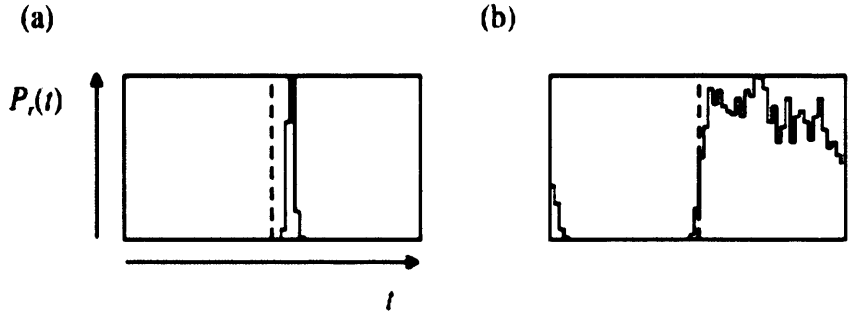

Figure 3.1 Typical radar altimeter return waveforms over Arctic sea ice. (a) A sharp, bright specular echo reflected from the smooth sea surface within a lead, (b) a diffuse echo reflected from rough sea ice. From *Peacock and Laxon* [2001].

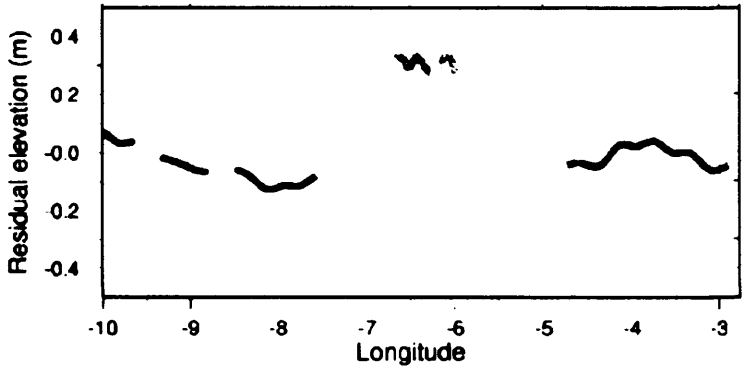

Figure 3.2 An along-track elevation profile over Arctic sea ice derived from radar altimetry data. The jump in elevation is due to the elevation difference between the sea surface and the top of an ice floe. From *Wingham et al.* [2001].

3.2.2.2 Satellite Imagery

The Moderate Resolution Imaging Spectroradiometer (MODIS) imagery presented in this thesis was acquired from the National Snow and Ice Data Centre (NSIDC). MODIS is one of the instruments on board the NASA satellites AQUA and TERRA. Terra MODIS and Aqua MODIS illuminate swaths of the Earth's surface 2330km by 10km in size and cover the entire globe every 1 to 2 days. Data is acquired in 36 spectral bands ranging in wavelength from 0.4 μm to 14.4 μm. Here we use the MODIS Calibrated Radiances product, which provides visible imagery (bands 1 and 2) with a resolution of 250 m. We utilise an IDL software tool called simap.pro[15], which was developed by the Goddard DAAC MODIS Data Support Team to process the MODIS data acquired from NSIDC, and to overlay ICESat science products onto the visible imagery.

The Advanced Along-Track Scanning Radiometer (AATSR) imagery was acquired from the EOLI-SA online catalogue at ESA[16]. AATSR is an imaging radiometer which acquires images of the Earth's surface at a range of infrared and visible wavelengths. We utilise the AATSR TOA Radiance product, which provides visible imagery at a resolution of 1000 m. As with the MODIS imagery we use IDL-based software to analyse the AATSR imagery and overlay ICESat science products.

[15] Simap.pro and associated documentation is available at http://daac.gsfc.nasa.gov/MODIS/simap/
[16] EOLI-SA catalogue available at http://eoli.esa.int

3.2.2.3 Sea Ice Drift Data

We utilise 3-day, merged datasets which combine QuikSCAT and SSM/I sea ice drift vector data, acquired from the French Ifremer website[17]. Data is available for all ICESat time periods and is presented in the form of browse images which illustrate the direction and speed of sea ice drift over 3-day periods.

3.2.2.4 Sea Ice Concentration Data

As part of our analysis we require a sea ice mask to enable selection of ICESat altimetry data over the sea-ice covered regions of the Arctic Ocean (see Section 4.3). For this purpose we use Special Sensor Microwave/Imager (SSM/I) sea ice concentrations which are computed from the Defence Meteorological Satellite Program (DMSP) F-13 SSM/I Daily Polar Gridded Brightness Temperatures. These data are available at the NSIDC website[18].

3.3 Characteristics of ICESat Data

We now provide a detailed description of the parameters that are relevant to the analysis of ICESat data over sea ice (Section 3.3.1), and the limitations associated with each parameter (Section 3.3.1). Although much of this information is already available in the literature, Algorithm Theoretical Basis Documents (ATBDs), and the GLAS Release Notes, we present a collated set of information pertinent to the analysis of ICESat sea ice data.

3.3.1 Parameters used in Geophysical Analysis of ICESat Data over Sea Ice

Raw data are telemetered from ICESat to the ICESat-Science Investigator-led Processing System (I-SIPS), the ground-based data processing system, at the Goddard Space Flight Centre (GSFC). I-SIPS generates fifteen separate data products from the

[17] Data is available at ftp://ftp.ifremer.fr/ifremer/cersat/products/gridded/psi-drift/quicklooks/
[18] Data and further information is available at http://nsidc.org/data/nsidc-0001.html

ICESat measurements labelled GLAxy, where xy denotes a two-digit number. We make use of geolocated footprint locations and elevations from the GLA06 Global Elevation Data Product and, for each footprint, we obtain a record of the transmitted and received waveforms from the GLA01 Global Altimetry Data Product.

The key products derived in the GLAS sea ice algorithm for pulses reflected from sea ice are: the average elevation of sea ice or open water, and the average reflectance of the sea ice within the footprint [*Brenner et al.*, 2003]. Other parameters relevant to our analysis of ICESat data over sea ice include the shapes of the transmitted and received laser pulses themselves, and the energy and gain associated with the return laser pulse. A full list of parameters used in our forthcoming analysis of ICESat data over sea ice is presented in Table 3.2.

3.3.1.1 Transmitted and Received Pulse Waveforms (*i_tx_wf, i_rng_wf*)

The concept of range measurement by a laser altimeter is illustrated in Figure 3.3, where signal strength or power, P, is plotted against time, T. The initial transmitted laser pulse has maximum signal strength, P_0, a duration or pulse width, ΔT_0, at a signal strength of one-half the maximum, and a total energy, E_0. The reflected laser energy, in the form of scattered light, is focused by a telescope onto a silicon avalanche photodiode detector [*Bufton*, 1989].

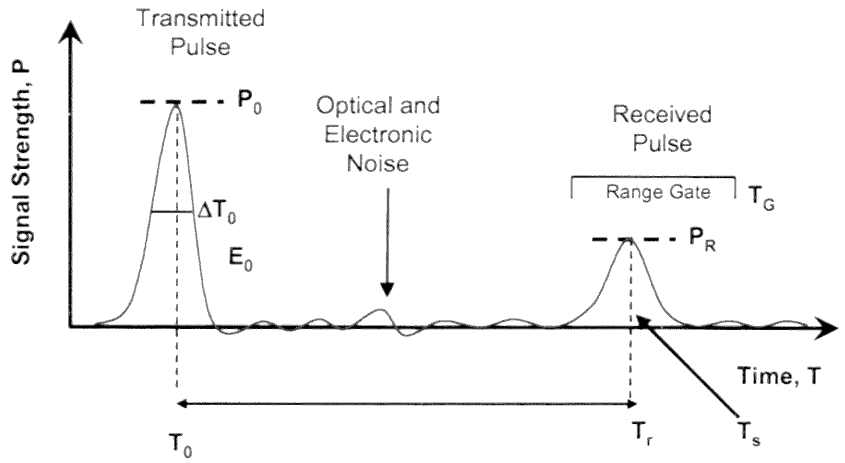

Figure 3.3 Schematic illustrating the concept of range to surface measurement for a transmitted and received laser pulse. T_0 is the transmitted pulse time, T_r is the received pulse time, P_0 is the transmitted pulse power and P_r is the received pulse power. From *Bufton* [1989].

Product Variable Name	Short Description	Product Data Frequency (Hz)	Algorithm Units	Long Description
GLA01				
i_tx_wf	Sampled Transmit Pulse Waveform	40	counts	Transmit Pulse; 48 bytes of raw data samples.
i_rng_wf	1064 nm Laser Received Pulse Waveform	40	counts	The 1064 nm echo waveform digitizer sample output, at 544 samples per shot over land and ice sheets, and at 200 samples per shot over sea ice and oceans. The surface type is determined by the instrument from the on-board DEM. This has no calibration applied. The calibration is applied internally during ground science algorithm processing. The calibration constants are available in the ANC07 file.
i_RecNrgLast_EU	1064 nm Laser Received Pulse Energy	40	fJoules	This is the energy in the 1064 nm laser pulse between the threshold crossings before and after the maximum amplitude in energy units.
i_gainSet1064	Gain value used for Received Pulse	40	counts	The receiver gain; Gain value used is uncalibrated and is in counts. Before calculating energy from this gain value, it needs to be calibrated.
GLA06				
i_UTCTime	Transmit Time of First Shot in frame	1	seconds	The transmit time in UTC of the 1st shot in the 1 second frame referenced to noon on Jan 1, 2000 (J2000). This is not the ground bounce time, but the transmit time.
i_lat	Latitude Corrected	40	Degrees	The geodetic latitude of the 40 laser spots in the 1 second time frame, computed from the precision orbit, precision attitude, and ice-sheet specific range, after instrument corrections, atmospheric delays and tides have been applied. The values are in degrees North.
i_lon	Longitude Corrected	40	Degrees	The longitude of the 40 laser spots in the 1 second time frame, computed from the precision orbit, precision attitude, and ice-sheet specific range, after instrument corrections, atmospheric delays and tides have been applied. The values are in degrees East.
i_elev	Surface Elevation	40	Meters	Surface elevation with respect to the ellipsoid at the spot location determined by the ice-sheet specific range, after instrument corrections, atmospheric delays and tides have been applied.
i_gdHt	Geoid	2	Meters	The height of the geoid above the ellipsoid for the first and last shot in the record, based on the NASA/NIMA Earth Gravity Model, EGM-96 geoid.
i_dTrop	Range Correction, Dry Troposphere	1	Meters	The range correction due to the dry troposphere; one correction for each shot.
i_reflctUncorr	Reflectivity not corrected for Atmospheric Effects	40	Unitless	The reflectance (not corrected for atmospheric effects) is calculated as the ratio of the received energy after it has been scaled for range, and the transmitted energy. This uses all signal between signal begin and signal end.
Release 24+	**(new parameters)**			
i_satRngCorr	Saturation Range Correction	40	meters	The saturation range correction.
i_satCorrFlg	Saturation Correction Flag	40	NA	This is a flag indicating when i_satRngCorr should be applied.

Table 3.2 Description of ICESat parameters used in analysis presented in this thesis[19].

Over the polar ice pack the received pulse, which corresponds to a reflection from the surface, is assumed to be a single Gaussian similar in shape to the transmitted pulse [*Zwally et al.*, 2002]. The received pulse is however spread and distorted due to interaction with the target surface and the atmosphere [*Bufton*, 1989]. Many factors, including impulse response, surface roughness due to ridges, hummocks, and rafts,

[19] GLAS Altimetry Data Dictionary available at http://nsidc.org/data/docs/daac/glas_altimetry/data_dictionary.html

beam curvature, and a geometric component dependent on the off-nadir pointing angle of the laser beam, affect the spreading of the pulse in time. Pulse spreading directly affects data quality since it causes pulse energy to be redistributed into a larger time interval [*Bufton*, 1989]. This reduces the peak-power signal to noise ratio (SNR) and therefore increases the probability of errors in the determination of range to the surface [*Harding et al.*, 1994].

The received pulse is selected by an instrument algorithm and digitised in 1ns (15cm) range bins by GLAS and subsequently analysed by I-SIPS. From a total of 1000 selected range bins, the 200 samples around the detected pulse are selected and telemetered to the ground. The corresponding width of the telemetered range window is 30m over sea ice and ocean [*Brenner et al.*, 2003]. The width of the transmitted pulse is 6ns and is digitised in the same manner as the received pulse in 1ns (15cm) range bins (*X. Sun*, personal communication).

3.3.1.2 Procedure to Calculate Elevation and Geolocate Footprint (*i_lat, i_lon, i_elev*)

The GLAS sea ice footprint will usually contain smooth ice, rough ice, open water or a mixture of these units. Surface elevations in the GLA06 product are estimated using the "standard fit" Gaussian-fitting procedure for land and ice sheets [*Brenner et al.*, 2003], which is appropriate for a flat, smooth surface such as sea ice. In this procedure, the average elevation will be represented by the centroid of the best-fit Gaussian curve associated with the maximum peak in the received waveform [*Brenner et al.*, 2003] as outlined in Eqn. 3.1 and illustrated in Figure 3.4.

The modelled waveform is defined by *Brenner et al.*, [2003] as

$$w(t) = \varepsilon + \sum_{m=1}^{N_p} W_m \quad , \quad W_m = A_m e^{\frac{-(t-t_m)^2}{2\sigma_m^2}} \tag{3.1}$$

where $w(t)$ is the amplitude of the waveform at time t, W_m is the contribution from the m^{th} Gaussian, N_p is the number of Gaussian peaks found in the waveform, A_m is the

amplitude of mth Gaussian, ε is the bias (noise level) of the waveform, t_m is the temporal centre of the modelled Gaussian, σ_m is the standard deviation of the mth Gaussian peak. Nonlinear least squares fitting is used to compute the model parameters (ε, A_m, t_m, and σ_m) by fitting the theoretical model to the observed received waveform [*Brenner et al.*, 2003]. The maximum number of peaks (N_p) calculated is usually six [*Zwally et al.*, 2002], although over sea ice it is usually one single peak.

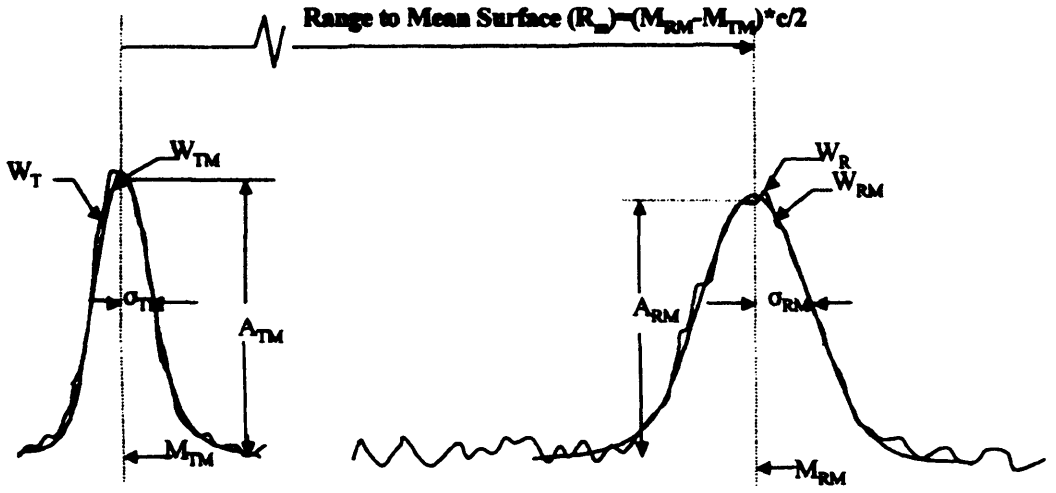

Figure 3.4 Schematic illustrating the waveform fitting procedure used for calculating the range and elevation distribution from a typical set of transmitted and received GLAS pulses. *W* indicates the waveform, *A* indicates the amplitude of the waveform, *M* indicates the waveform mid-point, σ indicates the standard deviation of the waveform, and *c* indicates the speed of light. The subscript *T* indicates the transmitted pulse, subscript *R* indicates the received pulse, subscript *M* indicates the Gaussian model fitted to the waveform. From *Zwally et al.* [2002].

A limitation of this fitting technique is that it may not be valid when applied over very rough sea ice (e.g. sea ice ridges or rubble fields), since the best-fit curve associated with the return pulse may be asymmetric and non-Gaussian [*Brenner et al.*, 2003]. Furthermore, occasionally all, or part, of the footprint can be occupied by an iceberg, a glacier, land ice, or land. These surfaces will usually have shorter ranges (higher elevations) and their effect on return-pulse shape will be determined primarily by their surface height distribution [*Brenner et al.*, 2003].

The following procedure, as outlined in *Brenner et al.* [2003], is implemented to geolocate the GLAS footprint and determine surface elevation. The surface elevation data products are referenced to the TOPEX/Poseidon reference ellipsoid [*Schutz et al.*, 2005].

a. Transmitted pulse is characterised. Time for beginning of range calculation is identified.
b. The received waveform is characterised to determine if there is a signal. The point on the waveform to be used to estimate slant range is determined. The mean range, POD and PAD are used to derive the preliminary footprint geolocation.
c. The database is interrogated to determine type of surface at footprint location.
d. Waveform smoothing is performed and initial estimates for waveform parameters are estimated.
e. A best-fit Gaussian curve is fitted to waveform using the procedure outlined in Eqn. (3.1).
f. The slant range to mean surface and surface elevation distribution are calculated.
g. This data, together with time and meteorological data, are used to calculate atmospheric delay due to the interaction of the laser pulse with the atmosphere. The tidal values for the ocean, load and solid earth tides are also calculated at this stage. A polar tide correction is not included in the PAD, but is accounted for in the orbit determination (*A. Brenner*, personal communication). See Figure 3.5.
h. The range to the mean surface is recalculated ("corrected range") with atmospheric and tidal corrections applied.
i. The time tag is corrected, with travel time taken into account.
j. Precise footprint geolocation and mean surface elevation are calculated. The value of the geoid is interpolated (once per second) at this stage. See Figure 3.6.
k. Region specific parameters are calculated.

3.3.1.3 Footprint Time Tag (*i_UTCTime*)

The footprint time tag is computed using two-way travel time to the surface. It is calculated as the time between the centroid of the transmitted pulse and the centre of the Gaussian fitted to the received pulse [*Zwally et al.*, 2002]. The time tag associated with the received pulse is calculated using Eqn. (2.3) (see section 2.4).

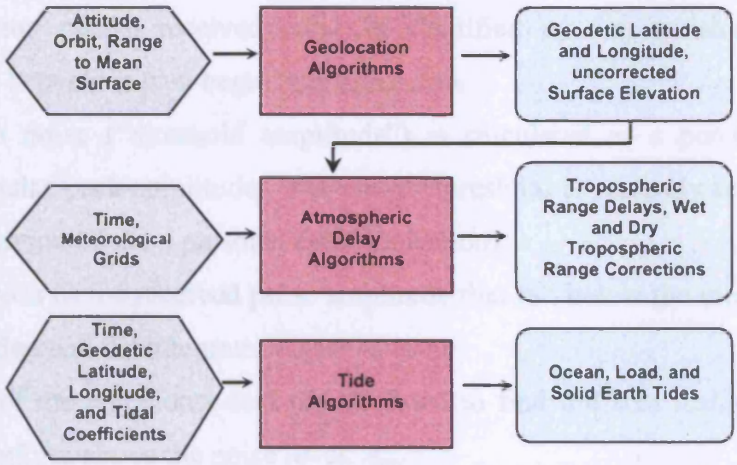

Figure 3.5 Flow diagram describing the calculation of range corrections showing the order in which the parameters are computed. Steps a-g, which are described in Section 3.3.1.2, are illustrated in this diagram. From *Brenner et al.,* [2003].

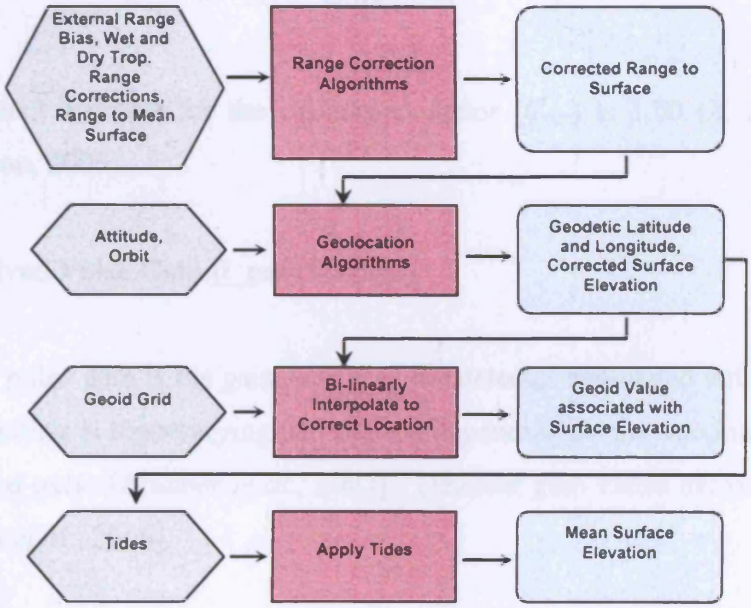

Figure 3.6 Flow diagram outlining the order in which range measurements are corrected, footprint geolocation calculated, and surface elevation estimated. Steps h-j, which are described in Section 3.3.1.2, are illustrated in this diagram. From *Brenner et al.,* [2003].

3.3.1.4 Received Energy (*i_RecNrgLastEU*)

The received pulse energy is calculated using the following procedure, as outlined in *Brenner et al.*, [2003]:

a. The position of the received pulse is identified by distinguishing maximum amplitude between signal begin and signal end.
b. The mean noise ("threshold amplitude") is calculated as a percentage of the received pulse peak amplitude. The cut-off threshold is currently set at 3% of the peak amplitude (*X. Sun*, personal communication).
c. The locations of the received pulse amplitude that fall below the mean noise level are identified and the integration interval is set.
d. The sum of the waveform data is calculated to find the area under the received pulse waveform above the noise level, A_{rec}.
e. The received pulse energy, E_{rec}, is calculated as the product of the pulse area, the received pulse gain, $Gain_{rec}$, and a calibration coefficient, C_{rec},

$$E_{rec} = A_{rec} * Gain_{rec} * C_{rec} \quad (3.2)$$

The most recent estimate for the calibration factor (C_{rec}) is 1.00 (*X. Sun*, personal communication, 2005).

3.3.1.5 Received Pulse Gain (*i_gainSet1064*)

The received pulse gain is the gain setting of the detector associated with the received pulse. The setting is time-varying and adjusts depending on the maximum amplitude of the received pulse [*Brenner et al.*, 2003]. Detector gain varies between 7 and 250 counts [*Kwok et al.*, 2006].

3.3.1.6 Reflectivity (*i_reflctUncorr*)

The total energy in the received pulse is used to infer the average reflectivity of the sea ice within the footprint. This procedure takes factors such as the transmitted energy, spacecraft altitude, and the characteristics of the receiver optics into account. The surface reflectivity of sea ice is dependent on two factors: surface roughness and the dielectric properties of sea ice (e.g. albedo).

Reflectivity is calculated as the ratio of the received pulse energy (after it is scaled for range) to the transmitted pulse energy. The unscaled received pulse energy is calculated as the area under the received pulse waveform above the noise level combined with the received pulse gain and the optical to detector volt efficiency for the received pulse [*Brenner et al.*, 2003]. The transmitted pulse energy is calculated as the area under the transmitted pulse waveform combined with the transmitted pulse gain and the optical to detector volt efficiency for the transmitted pulse [*Brenner et al.*, 2003].

Surface reflectivity, ρ_{surf}, is defined by *Brenner et al.*, [2003] as

$$\rho_{surf} = \frac{\rho_{surf\_uncor}}{\tau_{RTatm}},$$

$$\rho_{surf\_uncor} = \frac{\pi E_{rec} R^2}{E_{trans} A_{telescope} \tau_{opt}},$$

$$\tau_{RTatm} = e^{-2(\tau_c+\tau_a+\tau_m)} \tag{3.3}$$

where, ρ_{surf_uncor} is the uncorrected surface reflectivity, E_{trans} is the transmitted pulse energy, R is the range (in meters), $A_{telescope}$ is the telescope area (0.709 m^2), τ_{opt} is the optics transmission (67%), τ_{RTatm} is the roundtrip atmospheric transmissivity, τ_c is the cloud (column) integrated optical depth, τ_a is the aerosol (column) integrated optical depth, τ_m is the molecular optical depth.

3.3.1.7 Geoid Height (*i_gdHt*)

The height of the geoid above the reference ellipsoid is calculated for the first and last shot in each 1-second record. The geoid included in the product is based on the NASA/NIMA Earth Gravity Model EGM-96 geoid.

3.3.1.8 Dry Tropospheric Range Correction (*i_dTrop*)

The range correction to account for the dry troposphere is calculated at a frequency of 1Hz (i.e. once per 40 pulses). Section 2.5.5 outlines the procedure for calculating the dry tropospheric range correction and accounting for tropospheric delay.

3.3.1.9 Saturation Range Correction (*i_satRngCorr*)

The accuracy of ICESat elevations is compromised by factors affecting the range measured by the instrument. Detector saturation, due to the nonlinear response of the detector to the high incident energy of a received pulse, has been detected over ice and other surfaces [*Schutz et al.*, 2005] and reduces the performance of the instrument. Detector saturation is governed by at least four factors: transmit and received pulse energies, atmospheric attenuation, surface reflectivity (and abrupt changes thereof), and surface slope (*D. Yi*, personal communication). Atmospheric transmission of the GLAS 1064nm pulse is higher than expected; furthermore surface reflectance of the laser beam is approximately two times stronger than anticipated for a Lambertian surface (*X. Sun*, personal communication). In the clearest atmospheric conditions, and at strong laser energies (>13 fJ), over flat surfaces (<0.5° slope), received pulses can be up to two times over the receiver saturation threshold [*Abshire et al.*, 2005; *X. Sun*, personal communication]. Rapid variations in pulse energy, combined with the inability of the automatic gain control loop to adjust below its preset lower limit, cause the detector to overload and become saturated [*Fricker et al.*, 2005 and references contained therein].

The result of such detector saturation is distorted received pulse echoes which are artificially wide and have clipped peak amplitudes. Figure 3.7 shows a typical waveform stack over the salar de Uyuni salt flats, which contains various types of GLAS waveform. A particular group of echoes with very high received-pulse energy, known as "super saturated echoes", originate over still, flat water surfaces. Return echoes from smooth water surfaces tend to be specular in nature and have a narrow, highly peaked backscatter function. Ripples on the water surface are believed to produce a wider angular spread of the backscatter distribution (*J. Abshire*, personal communication). The standard Gaussian fit to saturated echoes is unsuitable for

accurate detection of the true surface elevation, since the broad Gaussian function manifests itself as a considerable range delay and hence produces poor estimates of surface elevation. *Fricker et al.* [2005] have found that the Gaussian fit is biased towards longer ranges (e.g. biases of -1 m over flooded regions of the salar due to super saturated echoes) and thus results in elevation estimates that fall below the true surface. As illustrated in Figure 3.7, there is an anti-correlation between ICESat elevations and received pulse energy, which is the expected effect from saturation [*Abshire et al.*, 2005]. Since the area under the return waveform is reduced through pulse saturation, the reflectivity measurement is also compromised and is effectively underestimated [*X. Sun*, personal communication].

Work by the ICESat science team to develop corrections for saturated waveforms is ongoing [*Schutz et al.*, 2005]. An empirical correction to be applied to the two-way travel time for pulses suffering from saturation was derived from laboratory experiments using the GLAS flight spare detector. The saturation correction, Δt, is valid for all gains and can be applied to returns originating over flat or gently sloping surfaces. It is given in *Kwok et al.* [2006] as:

$$\Delta t\ (ns) = \begin{cases} 0 & for\ E_r < 9fJ \\ 0.68706 - 0.30919E_r + 4.9006\times10^{-2}E_r^2 - 3.2897\times10^{-3}E_r^3 & \\ \quad +8.5389\times10^{-5}E_r^4 & for\ 9fJ \le E_r < 16fJ \\ -1.9426 + 0.14868E_r & for\ E_r \ge 16fJ \end{cases} \tag{3.4}$$

where E_r is received pulse energy in femtojoules (fJ). This correction became available with the Release 26 datasets. For data prior to Release 26 (i.e. L1, L3a, L3b) we applied the correction manually. When an echo fulfils one of the saturation criteria, the range correction is added to the elevation value to correct for the effects of saturation (*J. DiMarzio*, personal communication). Table 3.3 describes the criteria used to indicate "low-gain" and "high-gain" saturation. *Fricker et al.* [2005] demonstrate that the saturation correction reduced the elevation bias as measured over the salar from ~-10 cm to ~-2 cm.

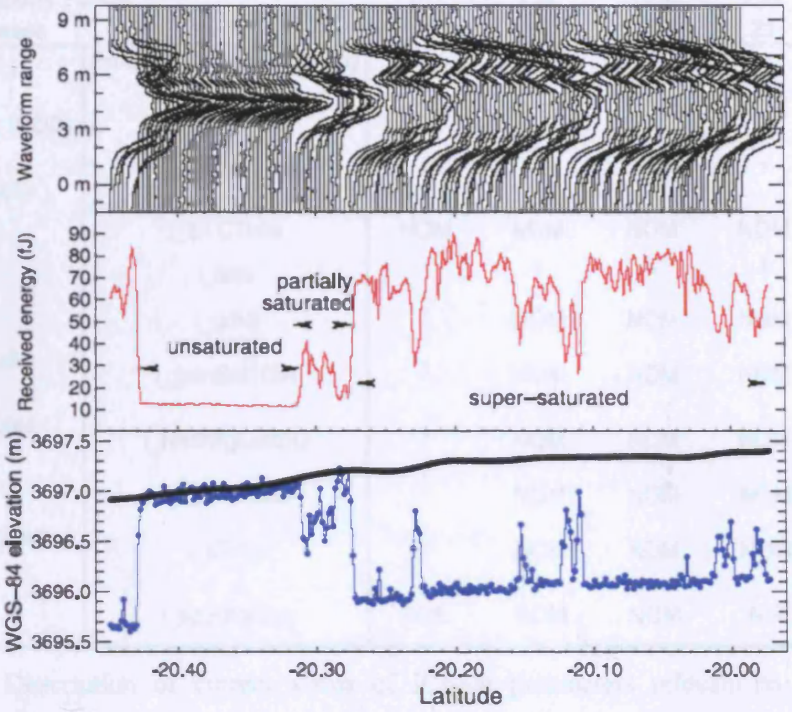

Figure 3.7 The effects of saturation on GLAS received pulses that were acquired over the salar de Uyuni while it was partially flooded. (Top) waveform stack; (Middle) received pulse energy; (Bottom) ICESat (blue) versus GPS elevations (black). From *Fricker et al.*, [2005].

	Low Gain Saturation	High Gain Saturation
Received Pulse Gain (counts)	≤ 13	≥ 250
Received Pulse Energy (fJ)	> 15	< 10
Received Pulse Amplitude (counts)	> 220	N/A

Table 3.3 Criteria for identifying low gain and high gain pulse saturation. From *Brenner et al.*, [2003].

3.3.2 Status of Selected ICESat Parameters

Due to the complicated nature of the processing applied to various GLAS data releases and individual parameters, we now discuss the impacts of such processing on the parameters relevant to this work. Table 3.4 describes the limitations associated with these parameters.

Laser Operations Period		**L1**	**L2a**	**L2b**	**L3a**	**L3b**
Product Release		**18**	**26**	**26**	**23**	**19**
Parameter	***Product Variable Name(s)***					
Footprint Geolocation (POD)	i_lat, i_lon	NOM	NOM	NOM	NOM	NOM
Instrument Pointing (PAD)	i_lat, i_lon, i_elev	[1]	[3]	[3]	[3]	[2]
Time Tag	i_UTCTime	NOM	NOM	NOM	NOM	NOM
Elevation	i_elev	[4]	[6]	[6]	[6]	[5]
Geoid	i_gdHt	[7]	NOM	NOM	NOM	NOM
Received Pulse Gain	i_gainSet1064	[8]	NOM	NOM	NOM	NOM
Received Pulse Energy	i_RecNrgLastEU	[9]	NOM	NOM	NOM	[10]
Reflectivity	i_reflctUncorr	[11]	NOM	NOM	NOM	[12]
Dry Troposphere Correction	i_dTrop	[13]	NOM	NOM	NOM	[13]
Saturation Correction	i_satRngCorr	N/A	NOM	NOM	N/A	N/A

Table 3.4 Description of current status of ICESat parameters relevant to the analysis presented in this thesis. Refer to text for footnote descriptions. "NOM" indicates the measurement of the parameter is nominal under a particular data release and in line with the GLAS error budget described in Section 2.6. "N/A" denotes parameter is "not applicable" under a particular data release.

[1] The version of Precision Attitude Determination (PAD) (PAD Release #12), used in this release does not include Laser Reference Sensor (LRS) corrections due problems with the green laser. The data is therefore compromised by pointing errors that reduce the accuracy of elevations reported in this dataset [*Schutz et al.*, 2005]. Pointing knowledge accuracy is estimated to be at the 15 – 20 arcsec level [*Schutz et al.*, 2005].

[2] The version of PAD (PAD Release #16), used in this release does not include pointing corrections [*GSAS v4.1 Release Notes*, 2004]. Pointing knowledge accuracy is estimated to be at the 15 – 20 arcsec level [*Schutz et al.*, 2005].

[3] Data from this operations period benefit predominantly from PAD improvements. LRS corrections, Instrument Star Tracker (IST) distortion corrections, and Scan Manoeuvre Calibration (SMC) corrections, reducing the effects of pointing errors and improving elevation measurement accuracy [*Luthcke et al.*, 2005]. Pointing knowledge accuracy is estimated to be at the ~ 2 arcsec level [*Schutz et al.*, 2005].

[4] Corrections to the waveform fitting procedure were included in this release and should improve elevation measurements [*GSAS v4.0 Release Notes*, 2004]. However,

the lack of pointing corrections (see [1]) results in range errors that seriously compromise the accuracy of elevations reported in the Release 18 dataset. Using Eqn. (2.6) and assuming flat sea ice, we calculate the range error associated with the error in pointing knowledge accuracy can be up to ~ 0.3 m.

[5] The version of PAD used in this release (see [2]) does not include pointing corrections, which results in range errors of up to ~ 0.3 m.

[6] Data from this operations period benefit predominantly from PAD improvements and the application of pointing corrections (see [3]). Pointing knowledge accuracy for this dataset is ~2 arcsec [*Schutz et al.*, 2005], which corresponds to a range error of 0.03 m. An absolute accuracy (range bias) of <2 cm has been derived for L2a Release 21 (and higher) elevations over the salar de Uyuni salt flats [see *Fricker et al.*, 2005].

[7] Errors exist in the EGM96 geoid reported in the product. EGM96 geoid heights are referenced to the WGS-84 reference ellipsoid in the tide-free system, making them incompatible for direct comparison with GLAS elevations, which are referenced to the TOPEX/Poseidon reference ellipsoid in the mean-tide system [*NSIDC*, 2006].

[8] The 40Hz received gain values are offset from the shot to which they pertain by one shot. The gain used onboard for shot N is contained in the record for shot N-1. The gain reported in this release of the data was not shifted and therefore all parameters that are calculated using the gain (e.g. reflectivity, received pulse energy) have some error associated with them. This gain offset does not however cause any errors in the elevation measurements themselves [*NSIDC*, 2006].

[9] The received pulse energy is calculated using knowledge of the received pulse gain. Due to the problems associated with the received pulse gain measurement (see [8]) the error on this measurement is proportional to the change in gain between shots [*NSIDC*, 2006]. In addition, there is a problem associated with the algorithm used to calculate the received pulse energy [*NSIDC*, 2006].

[10] A 1-shot gain shift algorithm included in Release 19 helped to improve the calculation of the received pulse energy parameter [*GSAS v4.1 Release Notes*, 2004]. However, further errors associated with the received energy in this data release exist [see *Fricker et al.*, 2005].

[11] The reflectivity associated with the received pulse is calculated using the value of received pulse gain. Due to the problems associated with the received pulse gain measurement (see [8]) the error on this measurement is proportional to the change in gain between shots [*NSIDC*, 2006]. Additional problems associated with the

algorithm used to compute reflectivity were discovered subsequent to this data release; the reflectivity algorithm uses an estimate of atmospheric transmissivity rather than the actual atmospheric transmissivity.

[12] A 1-shot gain shift algorithm included in Release 19 helped to improve the calculation of surface reflectivity [*GSAS v4.1 Release Notes*, 2004]. There is however a further problem associated with the reflectivity calculation: the reflectivity algorithm uses an estimate of atmospheric transmissivity rather than the actual transmissivity [*GSAS v4.1 Release Notes*, 2004].

[13] The dry troposphere correction occasionally includes sporadic offsets (or "blips") where the recorded value is offset from the expected value [*GSAS v4.3 Release Notes*, 2005].

In summary, we conclude that the L2a, L2b, L3a datasets should contain the best available data in terms of elevation measurement accuracy, since all known instrument and pointing corrections have been applied to these data. Based on Table 2.2, we can expect the RSS error on a single GLAS pulse to be ~5 cm for the L2a, L2b, and L3a datasets. L1 and L3b data could be compromised by pointing errors and possible problems with the recorded received pulse energy and surface reflectivity. Furthermore in terms of saturation effects, the L2b data period has the highest quality with the lowest number of saturated echoes [*Kwok et al.*, 2006]. Where possible we will therefore use the L2a, L2b, and L3a data in our analysis.

3.4 Applications of ICESat Altimetry in the Arctic – Review of Recent Results and Current Status

In this section we review the recently published results of the exploitation of ICESat data in the Arctic.

3.4.1 Deriving Sea Ice Freeboard Distributions from ICESat Data

The first investigation of ICESat data over Arctic sea ice was performed by *Zwally et al.* [2003]. The ArcGP geoid height was removed from the individual laser measurements and the distribution of ~ 300 along-track sea ice heights within running

50 km arc segments was calculated. The open-water/thin ice level was estimated by selecting the elevation corresponding to lowest 2% of each distribution. An example of this method is shown over Antarctic sea ice in Figure 3.8. Mean sea ice freeboard is calculated from the distribution of points above the local sea level. This method assumes some open water or thin ice is sampled by GLAS in each 50 km segment. Preliminary sea ice freeboard results, derived using this technique, are illustrated in Figure 3.9. Comparison of these ICESat-derived freeboards with temporally coincident sea ice freeboard measurements from ERS-2 radar altimetry data were favourable [*Farrell et al.*, 2003] with the decimetre differences attributable to a combination of snow loading on sea ice and residual errors in the two independent freeboard measurements.

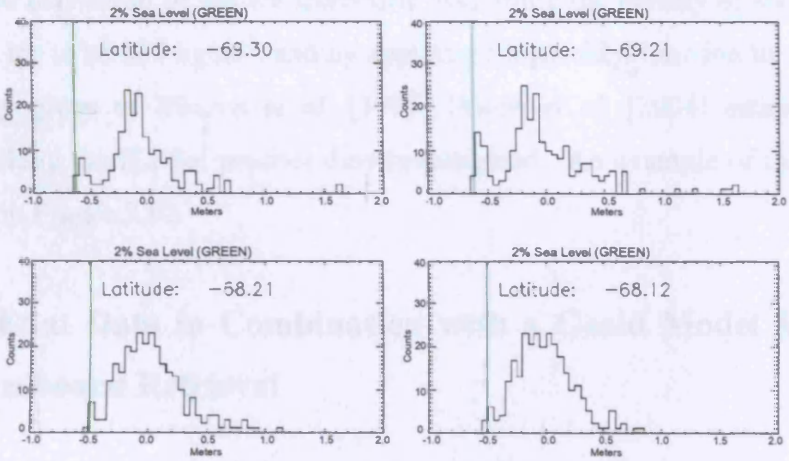

Figure 3.8 Estimating sea level from ICESat altimetry data by computing a histogram of surface elevations along a 50 km track segment. Local sea level is defined as the elevation corresponding to the lowest 2% of the distribution (green line). Figure courtesy of *D. Yi and J. Zwally*.

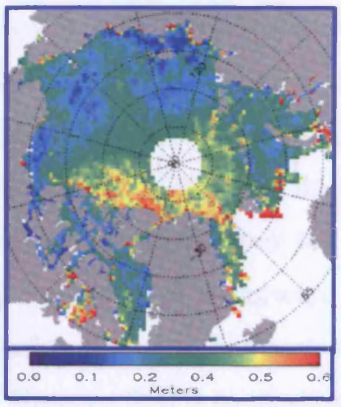

Figure 3.9 The first Arctic sea ice freeboard results derived from ICESat altimetry data collected during the L1 campaign in March 2003. From *Zwally et al.*, [2003].

3.4.2 Analysis of ICESat Data and RADARSAT Imagery

Kwok et al. [2004] have shown that the small diameter of the ICESat footprint allows for the resolution of thin ice, areas of open water and leads between ice floes, and larger, multi-year sea ice floes in the Arctic Ocean. By identifying relatively flat regions in along-track profiles, which had associated low values of reflectivity, and using coincident RADARSAT imagery, *Kwok et al.* [2004] identified leads and thin ice in the ICESat elevation data over sea ice in specific regions of the Arctic (Figure 3.10). This approach demonstrated that determination of sea surface topography, from direct measurements of open water and thin ice using ICESat data was possible. *Kwok et al.* [2004] used this direct measurement of sea level as a reference surface that enabled derivation of sea ice freeboard. Assuming the density of snow to be 300 kg m^{-3} and ice to be 928 kg m^{-3}, and by applying a sigmoidal function to a snow depth climatology given in *Warren et al.* [1999], *Kwok et al.* [2004] estimated sea ice thickness along the ICESat profiles they investigated. An example of these results is illustrated in Figure 3.10.

3.4.3 ICESat Data in Combination with a Geoid Model for Sea Ice Freeboard Retrieval

Forsberg and Skourup [2005] continued the analysis of ICESat data for the application of determining sea ice freeboard across the Arctic Ocean. They employed a "lowest-level" filtering scheme, similar in theory to that described by *Zwally et al.* [2003], to analyse L1 and L2a data. *Forsberg and Skourup* [2005] also begin by removing the ArcGP geoid model from ICESat measurements over the ice pack and make the assumption that the lowest geoid-reduced elevations within 10km areas describe local sea level. As *Forsberg and Skourup* [2005] acknowledge, this assumption may not be valid in areas with very thick, densely packed ice floes, introducing a bias of approximately 25 cm to their sea level elevation estimates. In addition, the affects of pulse saturation, pulse forward scattering due to clouds and elevation errors due to systematic pointing errors, have not been taken into account in their analysis [*Forsberg and Skourup*, 2005] suggesting that further elevation biases may also exist within their dataset.

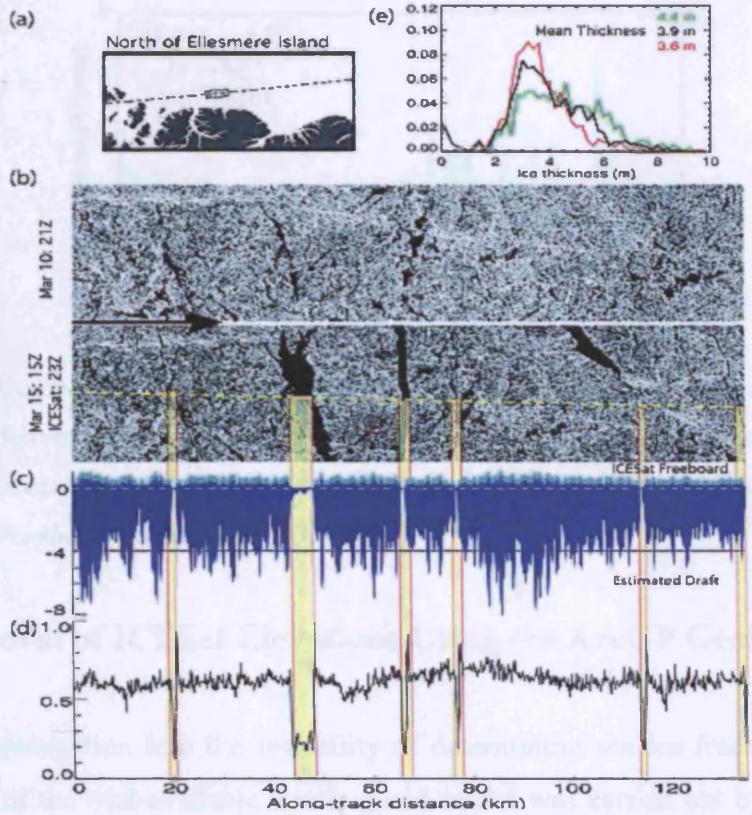

Figure 3.10 A comparison of near-coincident RADARSAT and ICESat data. (a) Geographic location of data. (b) ICESat track (dashed yellow line) and new leads/openings seen in time-separated RADARSAT image over the same area in the ice pack. (c) ICESat freeboard profile and estimated ice draft (snow: light blue; ice: dark blue). (d) Uncorrected reflectivity along ICESat track. (e) The sea ice thickness distribution with three superimposed snow covers (red: climatological mean+10 cm; black: mean; green: mean−10 cm). From *Kwok et al.*, [2004].

Independent verification of the sea surface elevation estimates presented in *Forsberg and Skourup* [2005] was not provided. While a comparison of sea ice freeboards from a segment of ICESat data with those estimated from an airborne laser altimeter utilised spatially coincident data (Figure 3.11), the data was not temporally coincident with an 8-hour offset between the two datasets. We estimate sea ice drift in the region surveyed[20] (north of Greenland) could have been up to 0.3 km hr^{-1} at the time of the survey, and the comparison cannot therefore be used as a robust verification of the ICESat freeboard estimates presented.

[20] Sea ice drift estimated using 3-day map for 23-26 May 2004 available at ftp://ftp.ifremer.fr/ifremer/cersat/products/gridded/psi-drift/quicklooks/arctic/merged/3-daily

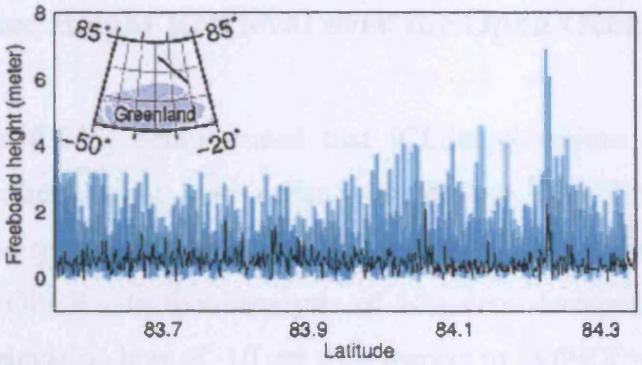

Figure 3.11 Comparison of ICESat sea ice freeboards (black) with freeboard estimates derived from airborne laser altimetry (blue) collected over the ice pack north of Greenland in May 2004. The inset map shows the location of the track. From *Forsberg and Skourup*, [2005].

3.4.4 Retrieval of ICESat Elevations Using the ArcGP Geoid

A second investigation into the feasibility of determining sea ice freeboard through the removal of the best-available Arctic geoid model was carried out by *Kwok et al.* [2006]. In addition to removing the ArcGP geoid from ICESat elevations, *Kwok et al.* [2006] accounted for the effects of atmospheric pressure loading by applying an inverse barometer correction to the data. Nevertheless, the largest signals in the derived surface elevation fields were spatially coincident with bathymetric topography and therefore attributable to remaining errors in the current state-of-the-art geoid models [*Kwok et al.*, 2006]. An example of surface elevation derived in this manner is illustrated in Figure 3.12

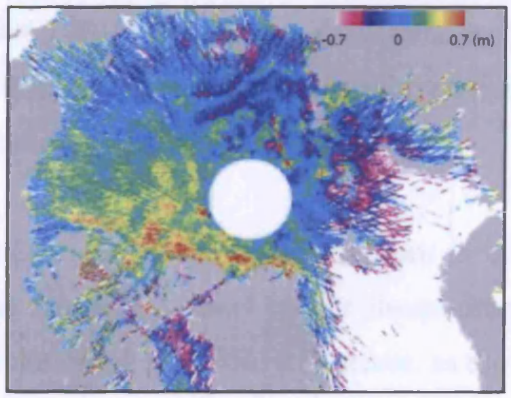

Figure 3.12 An example of ICESat elevations after the removal of a state-of-the-art geoid model, and application of tidal and inverse barometer corrections. The elevations for the L2b dataset are illustrated here. From *Kwok et al.* [2006].

3.4.5 Sea Surface Height Retrieval over the Open Ocean

Urban and Schutz [2005] demonstrated that ICESat elevations could be used to determine sea surface height over ocean-wide scales. They investigated ICESat elevation estimates over the open ocean and verified their results with sea surface elevations from TOPEX. In their analysis of L2a data, *Urban and Schutz* [2005] detected a global elevation bias of -10 cm with respect to TOPEX sea surface heights. Nevertheless they demonstrated that detection of the major components of sea level anomaly and mesoscale oceanographic features is possible with ICESat.

3.4.6 Reflectivity as an Indicator of Newly Formed Sea Ice and Leads

As noted in Section 3.4.2, relatively flat regions in along-track profiles of ICESat elevation were often associated with low values of reflectivity. *Kwok et al.* [2004] interpreted these regions to be leads and/or thin ice and verified this using coincident RADARSAT imagery (e.g. Figure 3.10). We now discuss the use of reflectivity measurements for the identification of leads and open water within the ice pack, in more detail. We explore whether the reflectivity parameter is useful for discriminating pulse returns from the sea surface.

The spectral albedo of leads which contain open water, or a thin ($\leq$ 3 cm) cover of new ice, is between 0 and 0.1 at GLAS laser wavelengths. For thicker sea ice, or sea ice covered with snow, the spectral albedo is significantly higher at ~ 0.8. [c.f. Figure 11 in *Kwok et al.*, 2006.] Therefore dips in along-track profiles of reflectivity over the sea-ice pack could indicate the presence of leads, particularly so if the dips were associated with coincident dips in local elevation.

However, over leads in sea ice we note that there is often a peak in reflectivity associated with pulse saturation caused by the abrupt change in albedo between the dark open water and the bright snow/sea ice surface, as the satellite crosses from lead to pack ice, or vice-versa. Once the onboard gain control loop adjusts to the darker surface of the lead, lower reflectivity values associated with ripples on the surface of the lead or thin frazil ice, etc. are recorded. This phenomenon can be identified in

Figure 3.10 where each instance of a lead or open water within the ice pack (highlighted in yellow) is associated with a spike (i.e. anomalously high value) in reflectivity at the lead/sea ice boundary.

Analysis of ICESat data collected over the salar de Uyuni revealed that reflections from ponds of still standing water on the salar resulted in super saturated waveforms (see Figure 3.7). These data had high values of received energy and thus high reflectivity (c.f. Eqn. 3.3). Reflections from very still, calm water within leads, or a calm lead surface with a thin, frazil-ice skim, could therefore also suffer from such pulse saturation, and anomalously high values of reflectivity. Furthermore, pulse saturation acts to broaden return waveforms resulting in anomalously low elevation measurements.

In addition, we note that prior to Release 22 data, there were problems with the calculation of reflectivity (c.f. Table 3.4), and thus the accuracy of the L1 and L3b reflectivity datasets may be compromised.

Although we would expect minimum values of reflectivity to be associated with GLAS returns from leads in the ice pack, pulse saturation due to high levels of received energy over still, standing water surfaces, and the failure of the gain control loop to adjust to abrupt changes in albedo, can result in anomalously high values of reflectivity over leads. We therefore conclude that (i) caution should be employed when interpreting reflectivity data over the sea ice pack and (ii) the reflectivity parameter alone cannot be used to accurately distinguish leads and/or thin sea ice floes in ICESat data. Nevertheless, reflectivity in association with other parameters, including elevation, could be used together to discriminate thin sea ice and leads. This idea is developed further in Chapter 4.

3.5 Aims of this Study

In Chapter 1 we stated that the primary goal of the work presented in this thesis is the exploitation of data collected by ICESat over the sea-ice covered regions of the Arctic Ocean. Bearing in mind the limitations associated with the ICESat data (Section 3.3),

and based on the current state of analysis of ICESat altimetry data over sea ice (Section 3.4), we now set out the aims of the work presented in this thesis in detail:

- To understand further the origins of ICESat laser pulse returns from sea ice covered regions to enable identification of returns from leads and thin ice.

- To assess existing methods for determination of sea surface height in the presence of sea ice over the Arctic Ocean.

- To improve current techniques through the development of a new algorithmic-based method for sea surface height estimation over Arctic sea ice.

- To investigate the ability of algorithmic-based methods to identify openings within the ice pack (e.g. leads) using spatially and temporally coincident satellite imagery from MODIS and AATSR.

- To map sea surface height in the Arctic Ocean during ICESat operation periods.

- To compare sea surface height measurements derived from ICESat data with coincident measurements from ENVISAT RA-2 altimeter data.

- To use knowledge of the sea surface in conjunction with an accurate geoid model to map dynamic ocean topography.

- To investigate the potential for using sea surface height measurements collected throughout various ICESat laser campaigns to map gravity anomalies in the Arctic Ocean up to the limit of coverage at 86°N.

- To examine the use of ICESat data in conjunction with sea level estimates derived from satellite altimetry data to measure snow ice freeboard, from which sea ice thickness can be deduced, and to compare these measurements with contemporaneous radar altimetric estimates of ice freeboard.

- To investigate the feasibility of combining satellite laser and radar altimetric measurements of sea ice freeboard to measure snow loading on sea ice.

3.6 Summary

We have described the various data products that are relevant to the exploitation of ICESat data over sea ice. The ICESat dataset is limited as a result of systematic pointing errors and pulse saturation, which degrade measurement accuracy. The quality of each available dataset is governed by the ground-segment processing. We expect elevation measurements from operations periods L2a, L2b, and L3a to be of the highest quality since these have been corrected for systematic pointing errors. We will therefore use these datasets were possible, recalling the limitations associated with the L1 and L3b data.

Although the use of RADARSAT imagery as a means of identifying (and verifying) areas of open water in ICESat data, and hence provide estimates of sea surface thickness, is robust [*Kwok et al.*, 2004], the published literature contains application of this method to only two individual ICESat tracks. To achieve the goal of analysing ICESat data over sea ice at large spatial scales such as that of the Arctic Ocean, examining individual ICESat profiles in combination with RADARSAT imagery would be time consuming and possibly even unfeasible; an algorithmic-based method, based on ICESat data alone, would appear to be more efficient [*Kwok et al.*, 2006].

Initial attempts to derive sea ice freeboard on Arctic-wide scales were based on removing a geoid model from ICESat measurements [*Forsberg and Skourup*, 2005; *Kwok et al.*, 2006]. The largest signals in the resultant elevation fields were however attributable to remaining errors in the current geoid models [*Kwok et al.*, 2006]. This demonstrates that knowledge of the time-varying sea surface height is required for direct retrieval of freeboard [*Kwok et al.*, 2006]. A robust method for identifying local sea surface height in the ICESat dataset is therefore required for accurate derivation of sea ice freeboard [*Kwok et al.*, 2006]. A method for identifying local sea surface by calculating the lowest 2% of elevations in 50 km along-track segments has been proposed by *Zwally et al.* [2003]. However investigation of the validity of this method has thus far not been carried out.

Since (i) the reflectivity parameter was first corrected for the affects of atmospheric attenuation under Release 22 and, (ii) errors in reflectivity measurements due to detector saturation have been reported [*Kwok et al.*, 2004], we suggest that reflectivity alone cannot be used to accurately distinguish leads and/or thin sea ice floes.

We concluded the chapter by defining the aims of the research presented in this thesis.

4 Retrieval of Altimetric Sea Surface Height Measurements in Ice Covered Seas

4.1 Introduction

In Chapter 4 we introduce three methods for the retrieval of altimetric sea surface height (SSH) in the Arctic Ocean. We begin by first discussing the reference surfaces that are employed in our analysis: the mean sea surface (MSS) and the Arctic geoid. We then move on to describe the filtering we apply to ICESat elevation data prior to processing. The aim of the filtering scheme is to improve the overall accuracy of the dataset. It is specifically designed to remove returns over the open ocean along the sea ice edge, as well as returns affected by pulse saturation, atmospheric forward scattering, and other invalid returns. We describe two alternative algorithms for identifying sea surface height in the ice covered Arctic Ocean. Method 1 follows initial work carried out by *Zwally et al.* [2003]. Method 2 is a new method for determining sea surface height based on analysis of (i) the relationship between ICESat elevations and surface reflectivity and (ii) ICESat waveforms. We also describe a third algorithm that identifies large leads (greater than ~5 km wide), which will be useful for deriving a baseline reference set of SSH measurements against which the first two methods can be verified. We conclude the chapter with a qualitative assessment of Methods 1 and 2 by investigating their ability to pick out small-scale features identified in satellite imagery.

4.2 Auxiliary Data

In order to estimate dynamic ocean topography and sea ice freeboard, it is useful to remove the largest component of the sea surface height signal; as discussed in Section 2.7 the geoid is the main component of sea surface height.

4.2.1 The Arctic Geoid

There remain uncertainties in some publicly available geoid models at high latitudes [e.g. see *McAdoo et al.*, 2004] and the EGM-96 geoid (*i_gdHt*) included in the ICESat product is too coarse in the polar regions to be suitable for sea ice analysis[21]. Here we have chosen to use two geoids specifically developed for geodetic, gravimetric, altimetric and oceanographic studies of the Arctic.

4.2.1.1 ArcGP

The Arctic Gravity Project (ArcGP) geoid model [*Kenyon and Forsberg*, 2001] was developed as part of an international initiative of the International Association of Geodesy and combined all available surface, airborne, and submarine gravity data in the Arctic region. Satellite-derived gravity (from ERS-2) was also used as part of the ArcGP but only in limited areas of the eastern sector of the Arctic, north of Siberia [*Forsberg and Skourup*, 2005]. The resolution of the ArcGP geoid model is 5° x 10° (latitude by longitude). A limitation of the ArcGP geoid model is that it does not sufficiently model long wavelength geoidal features [*Kwok et al.*, 2006; *McAdoo et al.*, 2006].

4.2.1.2 Hybrid Geoid

We also use an Arctic geoid model recently developed by *McAdoo et al.* [2006] comprising satellite and ground-based gravimetric data known as the "hybrid geoid". The hybrid geoid model is illustrated in Figure 4.1. The data is provided by D. McAdoo, at the National Oceanographic and Atmospheric Administration (NOAA), in a gridded format and with a longitude spacing of $1/8^{\circ}$ and a latitude spacing of $1/40^{\circ}$. Observations by the twin satellites of the Gravity Recovery and Climate Experiment (GRACE) mission [*Tapley et al.*, 2004] provide, for the first time, global coverage of the Earth's gravity field every 30 days from a single source. The hybrid geoid model is a high-resolution geoid constructed using an optimal combination of the long wavelength components (> 600 km) of the GRACE satellite-only GGM02S

[21] *i_gdHt* is calculated at a frequency of 2Hz, which, given the velocity of the spacecraft, is equivalent to once per 3.5km [*NSIDC*, 2006].

geoid, and the short wavelength components of the ArcGP geoid. The GRACE GGM02S data provides high precision at long wavelengths; long-wavelength errors in the hybrid geoid are less than 1 cm [*McAdoo et al.*, 2006]. *Kwok et al.* [2006] found that subtraction of the ArcGP geoid, updated with GRACE observations, from ICESat elevations significantly reduced the variance of the ICESat elevation field, as compared to using the ArcGP model alone. We assume that the same would be true in the case of the hybrid geoid.

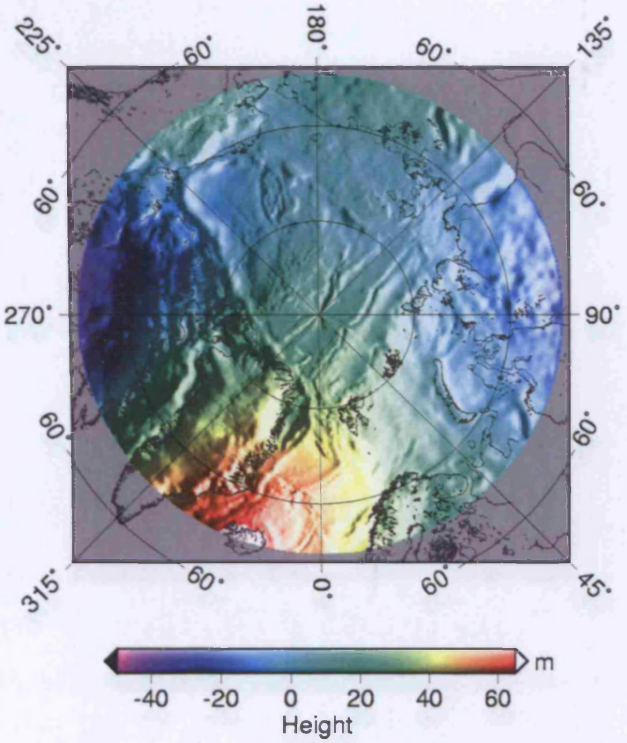

Figure 4.1 The Arctic hybrid geoid. The hybrid geoid is derived by combining GRACE GGM02S data with an updated ArcGP geoid model [*McAdoo et al.*, 2006]. Artificial illumination from the east has been added. Figure courtesy of *D. McAdoo*.

4.2.2 The Arctic Mean Sea Surface

4.2.2.1 ERS-2 Mean Sea Surface

Peacock and Laxon [2004] have described a technique utilising satellite radar altimetry data to discriminate sea surface elevations and determine sea surface height in the Arctic Ocean (see Section 3.2.2 for methodology). A map of the MSS is illustrated in Figure 4.2. This map was generated by plotting 35-day repeat mean

profiles onto a reference grid and using bilinear interpolation to estimate the MSS for each point along the individual tracks of the geodetic phases of the ERS-2 satellite between May 1995 and June 1999. Once the MSS height at each reference location was calculated, the heights were interpolated onto a grid with a longitude spacing of 1/8° and a latitude spacing of 1/40°. The ERS-2 sea surface height estimates are accurate to ≤ 9 cm in ice-covered seas between the latitudes of 60°N and 81.5°N [*Peacock and Laxon*, 2004]. This MSS is hereinafter referred to as the ERS-2 MSS.

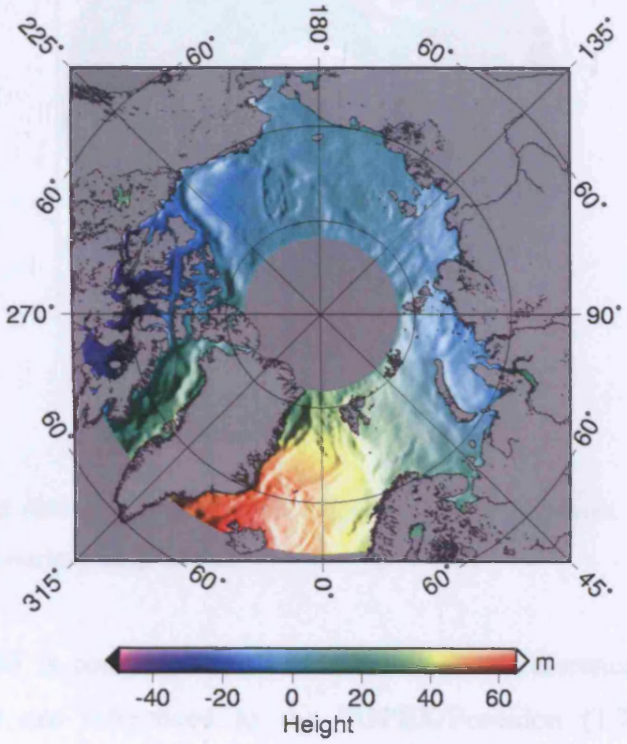

Figure 4.2 The ERS-2 Arctic mean sea surface (ERS-2 MSS). The ERS-2 MSS was derived using four years (1995-1999) of ERS-2 radar altimetry [*Peacock and Laxon*, 2004]. Artificial illumination from the east has been added. Figure courtesy of *D. McAdoo*.

An update to the ERS-2 MSS, the ArcGICE MSS, has been generated using 8 years of ERS-2 radar altimetry data for the period between May 1995 and June 2003 (*A. Ridout*, personal communication). We use the ArcGICE MSS, provided by A. Ridout, as a baseline to compute sea level anomalies (SLA) which are the difference between the altimeter-derived instantaneous sea surface heights and the long-term MSS (Eqn. 2.11). The standard deviation of sea surface heights used to construct the ArcGICE MSS is illustrated in Figure 4.3. The standard deviations indicate (i) that the error in

the ArcGICE MSS is ~ 12 -15 cm and (ii) regions of the Arctic Ocean where the error in the MSS is high (e.g. around 72°N 165°E) are due to the high variability of the instantaneous sea surface heights due to, for example, river run-off, etc. (*A. Ridout*, personal communication).

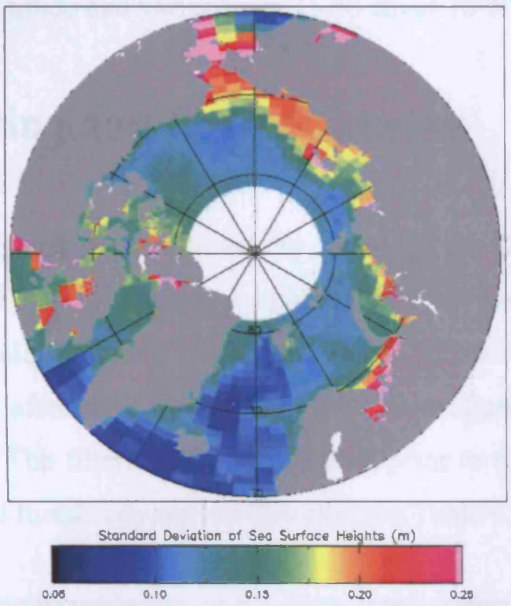

Figure 4.3 Standard deviation of sea surface heights used to construct the ArcGICE MSS. Figure courtesy of *A. Ridout*.

The ArcGICE MSS is computed relative to the WGS84 reference ellipsoid. Since ICESat elevations are referenced to the TOPEX/Poseidon (T/P) ellipsoid, it is necessary to apply a correction to the ArcGICE MSS data so that is it consistent with the ICESat dataset.

The Earth's radius, R, at a given geographic latitude, φ, is

$$R = A\left(1 - F\left(\sin^2(\varphi) - F\sin^2(2\varphi)\right)\right) \tag{4.1}$$

where A is the equatorial radius and F is Earth's flattening. For the WGS-84 reference ellipsoid, A_{WGS} is 6378137 m and F_{WGS} is 1/298.2572236. For the T/P reference ellipsoid, A_{TP} is 6378136.3 m and F_{TP} is 1/298.2570000.

The correction applied to the ArcGICE MSS (R_{DIFF}), to transform the MSS into the T/P reference frame, is calculated as follows

$$R_{DIFF} = R_{WGS} - R_{TP} \tag{4.2}$$

R_{DIFF} is a function of latitude and varies from 71.20 cm at 70°N to 71.34 cm at 82°N.

4.3 Data Filtering and Pre-processing

Based on the filtering scheme employed by *Kwok et al.* [2006] and the scheme recommended by D. Yi (*D. Yi*, personal communication), we developed a filtering scheme that is specifically designed for the analysis of ICESat data over sea ice. This removed most returns affected by saturation, forward scattering due to clouds, and other invalid returns. The filters applied to ICESat prior to processing are based on empirically determined thresholds and are described in Table 4.1.

Filter	Criteria for removal of received echo
Sea Ice Concentration	SSMI sea ice concentration <35 %
Elevation	-5 m < (*i_elev* - Hybrid Geoid) > 5 m
Waveform Filter*	*Rx_max_binpos* ≤ 9 OR *Rx_max_binpos* ≥ 191 OR *Rx_nTH* ≥ 35 OR *Rx_fwhm* = 30 m
High Gain#	*i_gainSet1064* > 30 counts
Reflectivity$	*i_reflctUncorr* > 1

Table 4.1 Description of filters applied to ICESat data prior to processing. *Refer to Table 4.2 for a description of the parameters utilised in this filter. #(*D. Yi*, personal communication). $[*Kwok et al.*, 2006].

4.3.1 Sea Ice Concentration Filter

In order to exclude from our analysis regions of open ocean near the sea ice edge, we only considered areas of the ice pack were the SSM/I sea ice concentration is ≥ 35%.

4.3.2 Elevation Filter

We performed coarse editing of the dataset to remove any anomalous elevations which deviate by more than 5 m from the Arctic hybrid geoid.

4.3.3 Waveform Filter

We analysed the characteristics of the received pulse to exclude anomalous (i.e. unusually shaped) waveforms from our analysis. Waveforms with maximum amplitudes, *Rx_max_binpos* (see Table 4.2), recorded in the first or last 5% of the range window were removed. These are instances where the surface reflection is partially or completely lost from the range window. In addition, waveforms with a higher than usual noise level, *Rx_nTH*, were removed. Although the gain control can adjust to waveforms with low pulse energies, both the signal and the noise are amplified. *Fricker et al.* [2005] have recorded large values of the standard deviation of elevation for such high-noise pulses. Received pulses with no discernible signal above the background noise level (i.e. *Rx_fwhm* = 30 m) were also removed. Transmission of the laser pulse through thick polar clouds could give rise to a received pulse which fits any of the criteria outlined in this filter.

4.3.4 High Gain Filter

High values of *i_gainSet1064* indicate a low signal-to-noise ratio as a result of atmospheric scattering due to clouds, water vapour, etc. [*Kwok et al.*, 2006]. Following the filtering scheme proposed by D. Yi (personal communication), we eliminated any received pulses with *i_gainSet1064* > 30 counts from our analysis. This is a more conservative level than that employed by *Kwok et al.* [2006], who removed received pulses with *i_gainSet1064* > 50 counts. Figure 4.4 illustrates the effects of an along-track transition from clear to cloudy conditions on received pulse gain and received pulse energy. Analysis of measurements from Antarctica suggests that low received pulse energies ($\leq$ 8 fJ) as well as high values of gain ($\geq$ 30 counts) may indicate echoes which suffer from forward scattering (*C. Shuman*, personal communication).

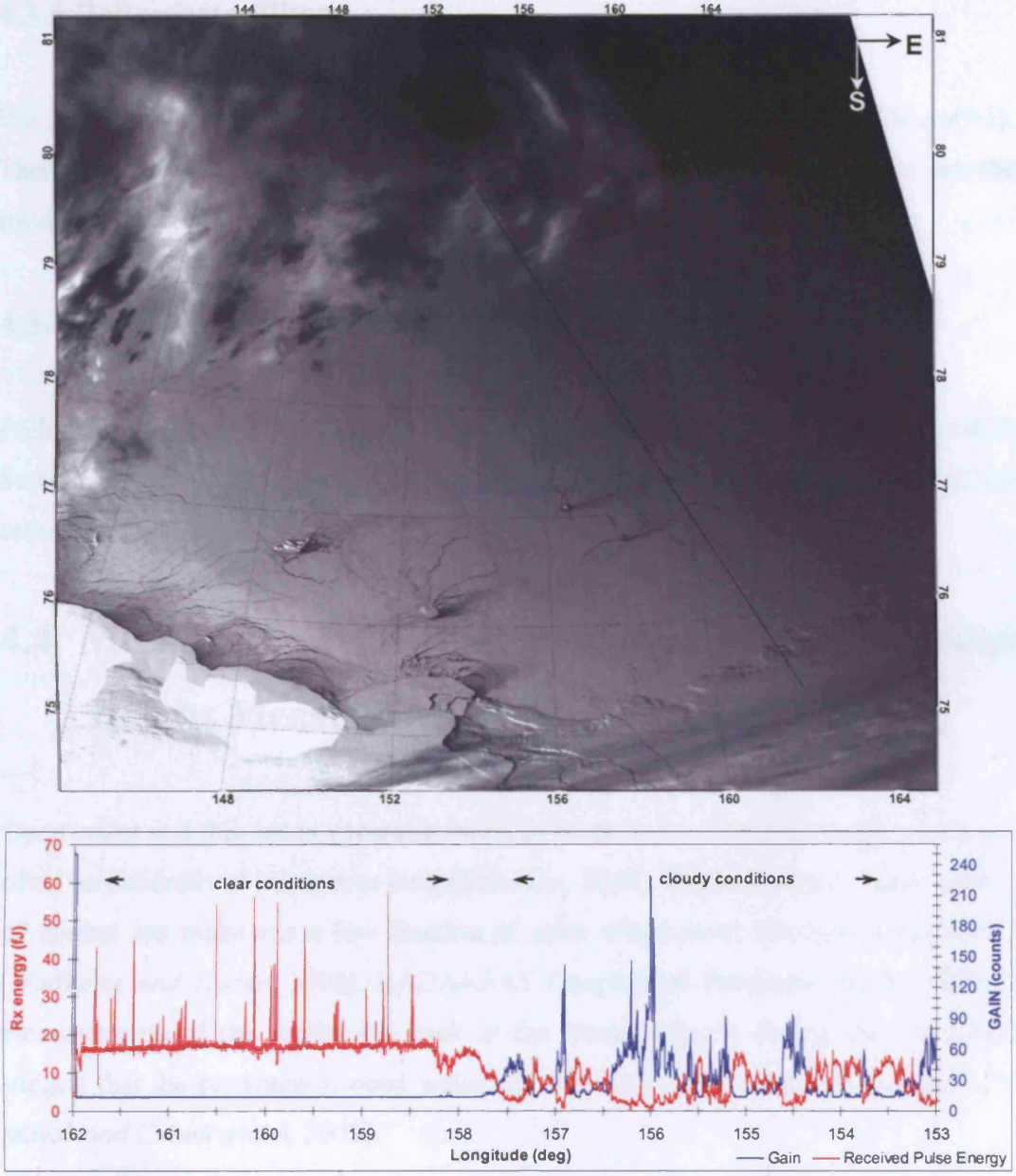

Figure 4.4 Illustration of the along-track transition between clear and cloudy conditions over Arctic sea ice. (Top) 250m-resolution MODIS image with geolocation of GLAS satellite track overlaid. (Bottom) Gain (blue) and received laser energy (red) for segment of L1, cycle 4, track 38. Note that the MODIS image was acquired on 14 Mar 2003 at 05:25 while the ascending ICESat overpass occurred at 14:50 on the same day. Evidence from additional MODIS imagery acquired over the region on the same day suggests that the cloud formation was moving in a southeasterly direction.

4.3.5 Reflectivity Filter

We filtered out anomalous echoes with an unphysical reflectivity (*i_reflctUncorr* >1). These are likely to be associated with distorted (saturated) waveforms that are the result of detector saturation [*Kwok et al.*, 2006].

4.3.6 Low Gain Saturation Correction

Following *Kwok et al.* [2006], we applied the saturation correction as outlined in Section 3.3.1.9 to the elevation estimates whose associated waveforms fulfilled the saturation criteria.

4.4 Methodology for the Retrieval of Sea Surface Height Measurements

Open water and thin ice is generally found in leads in the Arctic ice pack, which can often be hundreds of kilometres long [*Schulson*, 2004]. Rapid thermodynamic growth of thinner ice maintains a low fraction of open water cover throughout the winter [*Wadhams and Horne*, 1980]. RADARSAT Geophysical Processor System (RGPS) measurements of the winter ice pack in the western Arctic during the late 1990s suggest that the coverage of open water and thin ice (< 20cm thick) is less than 2% [*Kwok and Cunningham*, 2002].

We now present two alterative methods for SSH retrieval from ICESat in the presence of a sea ice cover. The advantage of the first algorithm is the selection of a constant number of data points from which local SSH is calculated. The downfall of the algorithm is a higher number of so-called "false alarms" (i.e. inclusion of elevation measurements from sea ice floes rather than from leads and open water only). The second algorithm aims to unambiguously identify regions of open water and leads within the ice pack, giving rise to fewer false alarms. The disadvantage of this method is that there are often few data points from which to derive the local SSH estimate and hence it may provide a noisier SSH dataset than the first algorithm.

4.4.1 Method 1: GSFC Algorithm

This method follows initial work by *Zwally et al.* [2003] and was developed by Dr. J. Zwally and Dr. D. Yi of the NASA Goddard Space Flight Centre (GSFC). This method is hereinafter referred to as the "GSFC Algorithm" and is essentially the same as that described in the first paragraph of Section 3.4. The GSFC algorithm is based on the assumption that at least 2 % of ICESat elevation measurements over the ice pack are those of open water or thin ice.

First we obtained surface height anomalies by subtracting the hybrid geoid model from ICESat elevations. Removal of the geoidal signal from the ICESat measurements before further analysis reduces the risk of contamination of ice elevation estimates by short wavelength geoidal features. For each GLAS received pulse, we computed a distribution of ICESat surface height anomalies for ~ 300 measurements along a 50 km segment centred on the local anomaly. The mean of the 2% of the lowest points in each distribution was classified as local sea level (see Figure 3.8). The geoidal component of the local sea level was subsequently restored to the elevation measurement. The resultant ICESat SSH data extend across the ice-covered regions of the Arctic Ocean and are referenced to the ICESat reference ellipsoid.

A limitation of this method is the variable coverage of open water throughout the sea ice season. Evidence exists to suggest that the percentage cover of leads and open water within the ice pack varies regionally (sea ice edge compared to multi-year ice pack), as well as seasonally (first year ice formation in October compared to maximum ice extent in March) [e.g. *Laxon et al.*, 2003 and references therein]. Measurements of open water fraction within the ice pack vary and a complex story emerges. *Laxon et al.* [2003] analysed submarine measurements of sea ice draft gathered in different years during the 1990s and calculated that the fraction of thin ice and open water ranges from 20 ± 8.2 % in September – October, to 3.2 ± 1.4 % in March and early April. Using infrared satellite imagery collected during one sea ice season, *Lindsay and Rothrock* [1995] estimated that the thin ice fraction decreased from 33 % in September, to 13 % in October, and to ~ 6 % between January and

April. *Kwok* [2002] analysed RGPS measurements of openings in perennial sea ice during the winter of 1998 (January – April) and found an even lower open-water coverage of ~ 0.3 %. While it is clear that lead percentage is dependent on season and region observed, an overall estimate of lead percentage in the Arctic Ocean remains unclear. We suggest therefore that any method to determine sea surface height in ice-covered regions using ICESat data which depends on a fixed threshold for the percentage of leads within the ice pack will provide SSH estimates that suffer inaccuracies. That is to say either some SSH data will be contaminated with elevation measurements from sea ice floes, or data points which could potentially be used in the derivation of the SSH measurement are excluded from the calculation.

4.4.2 Method 2: UCL Algorithm

An alternative method for discriminating returns from leads and thus determining SSH is based on knowledge of (i) the relationship between ICESat elevations and surface reflectivity, and (ii) the characteristics of ICESat pulses. The technique is intended to directly distinguish echoes originating over sea ice from those reflected from leads or thin ice. This method is hereinafter referred to as the "UCL Algorithm".

4.4.2.1 Parameters to Describe the Shape of a GLAS Pulse

In addition to the parameters outlined in Table 3.2, we derived a number of additional parameters associated with the shape of the transmitted (Tx) and received (Rx) pulses. These parameters are outlined in Table 4.2 and are described below.

We extracted the maximum amplitude (*Tx_max*, *Rx_max*), as well as the bin position of the maximum amplitude (*Tx_max_binpos*, *Rx_max_binpos*), of *i_tx_wf* and *i_rng_wf* as follows:

$$Tx\_\max = \max\left(i\_tx\_wf_{i=start} : i\_tx\_wf_{i=end}\right) \quad (4.3)$$

$$Tx\_\max\_binpos = i, \quad where\ i\_tx\_wf_i = Tx\_\max \quad (4.4)$$

where *start* and *end* refer to the bin at the start and end of the signal in the waveform. *Rx_max*, and *Rx_max_binpos* were calculated similarly.

Variable Name	Short Description	Data Frequency (Hz)	Units	Long Description
Tx_max	Max Amplitude Transmitted Pulse	40	counts	Maximum recorded amplitude of transmitted pulse signal.
Rx_max	Max Amplitude Received Pulse	40	counts	Maximum recorded amplitude of received pulse signal.
Tx_max_binpos	Position of Tx_max	40	bin number	Bin position in range window of maximum amplitude of the transmitted pulse echo.
Rx_max_binpos	Position of Rx_max	40	bin number	Bin position in range window of maximum amplitude of the received pulse echo.
Tx_nTH	Tx noise threshold	40	counts	The average amplitude of the first eight range bins is calculated. The noise threshold for the transmit pulse is defined as the average amplitude plus one standard deviation
Rx_nTH	Rx noise threshold	40	counts	The average amplitude of the first eight range bins is calculated. The noise threshold for the received pulse is defined as the average amplitude plus one standard deviation
Tx_fwhm	Tx full width half maximum	40	m	The full width half maximum of the transmit pulse is calculated first in terms of bin width and can then be multiplied by 0.15m to convert to width in meters.
Rx_fwhm	Rx full width half maximum	40	m	The full width half maximum of the received pulse is calculated first in terms of bin width and can then be multiplied by 0.15m to convert to width in meters.
Xcorrel_max	Maximum value of cross correlation	40	unitless	The maximum value of the cross correlation between the transmit pulse and the received pulse.
Tx_skew	Skewness of the Transmitted echo	40	unitless	The skewness of the transmit echo.
Rx_skew	Skewness of the Received echo	40	unitless	The skewness of the received echo.

Table 4.2 Description of parameters associated with the transmitted and received waveforms, which we have derived for use in the development of the UCL Algorithm.

For each individual waveform, we calculated the mean noise level:

$$Tx\_nTH = \left(\overline{N} + \sigma N\right)$$

where

$$\overline{N} = \frac{\sum_{j=1}^{k} i\_tx\_wf_j}{k}$$

$$\sigma N = \sqrt{\frac{\sum_{j=1}^{k}\left(i\_tx\_wf_j - \overline{N}\right)^2}{k}}$$

$$k = 8$$

and similarly for *Rx_nTH*. (4.5)

We also recorded the full-width half-maximum value of the signal in the waveform:

$$Tx\_fwhm = |i2 - i1|$$

where

$$i\_tx\_wf_{i1} = i\_tx\_wf_{i2} = \frac{Tx\_\max}{2}$$

and similarly for *Rx_fwhm.* (4.6)

Following *Box and Jenkins* [1976], we derived the cross correlation between the Tx and Rx pulses as follows: given two series $x_1, x_2, ..., x_n$ and $y_1, y_2, ..., y_n$, of length n, the cross correlations, for a maximum lag L, between x_t and the lagged values of y_t, are calculated by

$$r_{xy}(l) = \frac{\sum_{t=1}^{n-l}(x_t - \bar{x})(y_{t+l} - \bar{y})}{n\, s_x\, s_y}, \quad l = 0, 1, ..., L$$

where

$$\bar{x} = \frac{\sum_{t=1}^{n} x_t}{n},$$

$$S_x^{\,2} = \frac{\sum_{t=1}^{n}(x_t - \bar{x})^2}{n}$$

and similarly for y. (4.7)

We define *Xcorrel_max* as the maximum value of $r_{xy}(l)$. *Xcorrel_max* is an indication of the similarity of the Rx pulse to the Tx pulse; for perfectly Gaussian Tx and Rx pulses, or for a waveform crossed with itself, *Xcorrel_max* would be 1.

We also calculated the skewness of Tx and Rx (*Tx_skew*, *Rx_skew*). Skewness describes the degree of asymmetry of the pulse about the mean distribution. Following *Brenner et al.* [2003], we define skewness as:

$$skewness = \frac{1}{\sigma^3} \frac{\sum_{i=start}^{i=end} (i - mean)^3 \, w(i)}{\sum_{i=start}^{i=end} w(i)},$$

$$mean = \frac{\sum_{i=start}^{i=end} i \, w(i)}{\sum_{i=start}^{i=end} w(i)},$$

$$\sigma^2 = \frac{\sum_{i=start}^{i=end} (i - mean)^2 \, w(i)}{\sum_{i=start}^{i=end} w(i)} \tag{4.8}$$

where $w(i)$ is the power of the i^{th} bin of the waveform. *Start* and *end* refer to the bin at the start and end of the signal in the waveform.

4.4.2.2 Development of UCL Algorithm

It is possible to distinguish returns that originate over leads in radar altimetric data due to the distinct, specular shape of the echo (see Figure 3.1). Distinguishing returns from open water or leads in laser altimetric data is more complex since returns from both smooth water surfaces and smooth snow/ice surfaces are expected to be specular.

To identify GLAS echoes that originate over flat-water surfaces such as leads, we derived a set of criteria based on the characteristics of the Rx pulse. In clear, calm conditions, for a reflection from a lead, we expect the shape of the GLAS Rx pulse to be near-specular in shape and highly correlated with the shape of the Tx pulse. We also expect the reflectivity associated with the Rx pulse to be low (see Section 3.4.6) and the elevation to be low relative to the surrounding surfaces. Analysis of a set of five ICESat profiles of elevation, reflectivity, and the parameters describing pulse shape, in combination with near-coincident imagery, allowed us to derive parameter thresholds that indicate laser returns from flat, water surfaces. This analysis is included as supplementary material in Appendix B. Based on these parameter

thresholds, we developed a set of criteria for discriminating returns over leads within the ice pack. These criteria are described in Table 4.3. All criteria must be satisfied for a pulse to be classified as a return from open water.

Criterion	Threshold
Cross-correlation	$Xcorrel\_max \geq 0.975$
Reflectivity	$0 \leq i\_reflctUncorr \leq 0.5$
Received pulse FWHM	$5.5 \leq Rx\_fwhm \leq 8.5$
FWHM deviation	$-0.1 \leq (Rx\_fwhm - Tx\_fwhm) \leq 2.0$
Skewness deviation	$-0.3 \leq (Rx\_skew - Tx\_skew) \leq 0.3$

Table 4.3 Criteria for discriminating open water within the ice pack. Parameter thresholds are empirically determined and are based on comparisons of ICESat parameters with near coincident satellite imagery. All criteria must be met for a pulse to be classified as a return from open water.

An example of this analysis is illustrated in Figure 4.5. Figure 4.5(a) shows an AATSR image acquired on 12th March 2003, at 22:01, north of the Queen Elizabeth Islands, with the geolocation of the ICESat track overlaid on the image. The linear black feature crossing the centre of the image, represents a region of low backscatter, and can be identified as a large lead. Figure 4.5(b) illustrates the method used to identify this lead in the ICESat data.

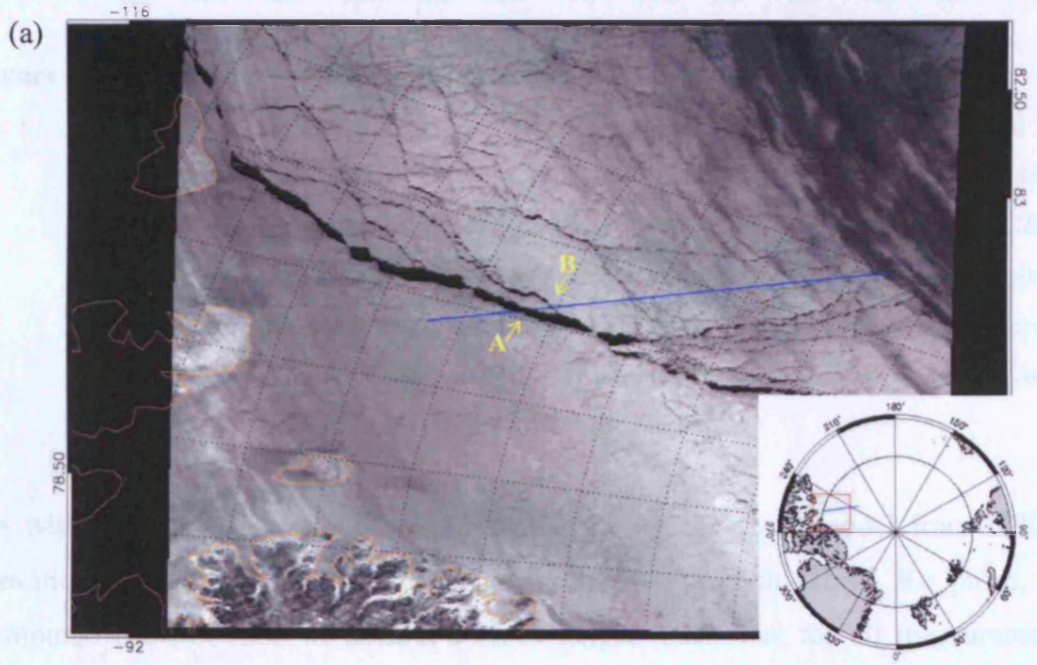

Figure 4.5 Continued overleaf.

(b)

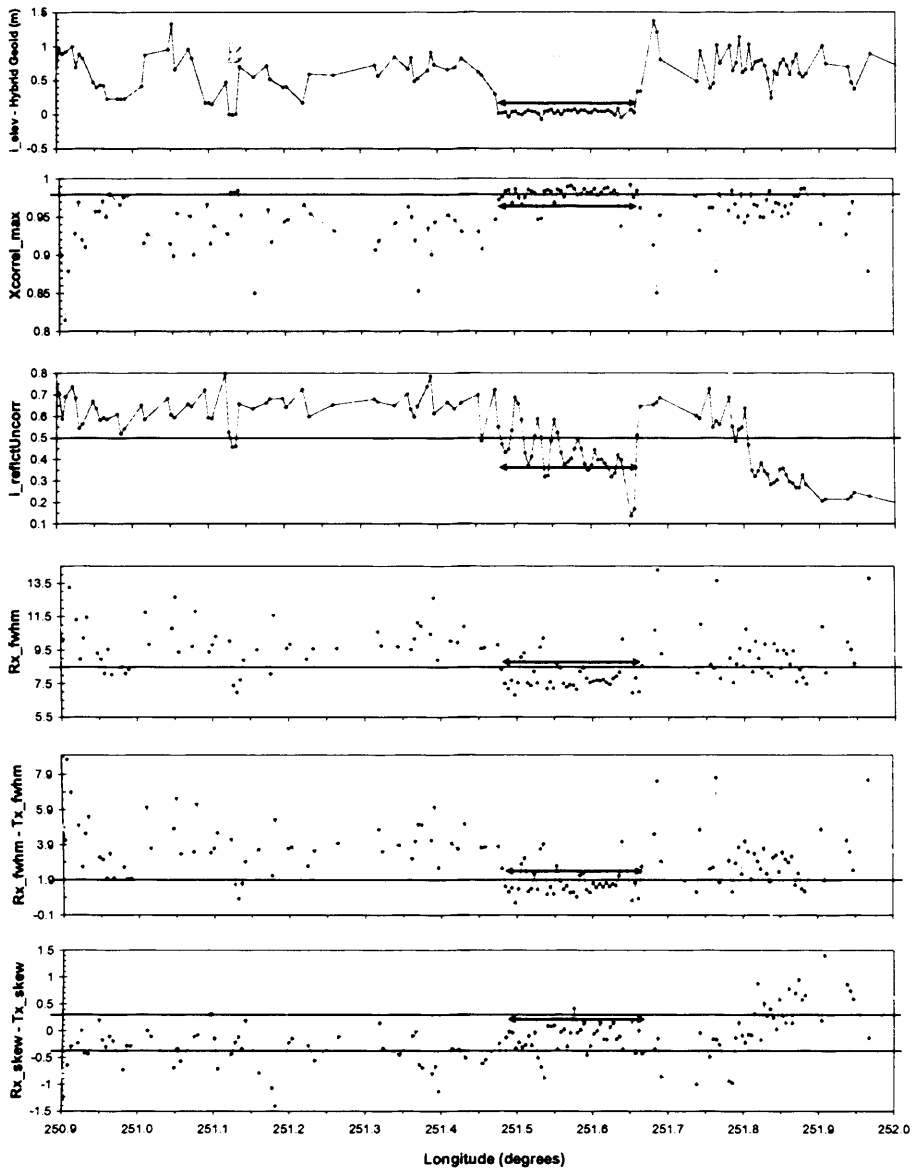

Figure 4.5 Comparison of satellite imagery with a near-coincident ICESat overpass. (a) AATSR image of the ice pack north of Queen Elizabeth Islands acquired on 12th March 2003, at 22:01, with the geolocation of an ICESat track overlaid in blue. Inset shows the geographic location of the comparison. (b) Distribution of ICESat elevations, reflectivity, and pulse shape parameters within the track segment associated with the near-coincident AATSR image. The ICESat ascending overpass occurred on 13th March 2003, at 08:14. The major lead is indicated by blue arrows, while green lines indicate the parameter thresholds.

As with the GSFC algorithm, we subtracted the hybrid geoid model from ICESat elevations to obtain surface elevation anomalies. For each GLAS Rx pulse, we computed a distribution of ICESat surface height anomalies for all measurements within a 100 km segment centred on the local point. We identified the lowest 2% of

elevation anomalies in each distribution. From these elevation anomalies, we then selected only those pulses which fit all the open water criteria outlined in Table 4.3. Local sea level was defined as the average elevation of those pulses which fit the criteria. The geoidal component of the local sea level was subsequently restored to the elevation measurement. The final sea surface data are thus in the form of an ICESat SSH measurement, referenced to the ICESat reference ellipsoid.

4.4.3 Identification of Large Leads

To estimate the accuracy of the GSFC and UCL algorithms to estimate sea surface height, we have developed an additional method, which discriminates large leads. By large lead, we refer to leads that are greater than 5 km wide. The choice of lead size is based on the large leads identified by *Kwok et al.* [2006] (see Figure 12 in *Kwok et al.* [2006]) and should provide for unambiguous identification of the sea surface. Although coverage of the Arctic will be limited, we use the sea surface height measurements from large leads as a baseline against which to assess the GSFC and UCL algorithms.

Development of the method to identify large leads in ICESat profiles is based on the characteristics of large leads. We expect large leads to be associated with (i) a dip in local elevation, (ii) low standard deviation of elevation across the lead, and (iii) low reflectivity. The criteria for identifying large leads are outlined in Table 4.4. The parameter thresholds were defined based on analysis of comparisons each parameter with coincident satellite imagery. All criteria must be fulfilled for a pulse to be classified as a return from a large lead.

Criterion	Threshold
Standard deviation elevation	$SD \leq 0.035$ m
Number data points	$sum \geq 15$
Reflectivity	$0 \leq i\_reflctUncorr \leq 0.5$

Table 4.4 Criteria for discriminating large leads within the ice pack. Parameter thresholds are empirically determined and are based on comparisons of ICESat parameters with near coincident satellite imagery. All criteria must be satisfied for a pulse to be classified as a return from a large lead.

We subtracted the hybrid geoid model from ICESat elevations to obtain surface elevation anomalies as before. For each Rx pulse, we computed the standard deviation of elevation anomalies for 15 points, centred on the local point. We define the standard deviation as follows

$$SD = \sqrt{\frac{\sum_{j=1}^{n} \left(\left(i\_elev - Hybrid\ Geoid \right)_j - mean \right)^2}{n}},$$

$$mean = \frac{\sum_{j=1}^{n} \left(i\_elev - Hybrid\ Geoid \right)_j}{n}$$

where n is 15. (4.9).

For each individual Rx pulse, we then doubled the search range and identified the 15 data points either side of the local point (i.e. 30 data points in total). We computed *sum*, which we define as the cumulative sum of the elevation anomalies within the search range with SD $\leq$ 0.035 m (i.e. with a standard deviation that fulfils the *SD* criterion outlined in Table 4.4).

Finally, for each pulse, we generated a distribution of ICESat surface height anomalies for all measurements within a 100 km segment centred on the local point. We selected only those pulses which fit all the criteria outlined in Table 4.4. Local sea level was defined as the average elevation of those pulses which fit the large lead criteria. The geoidal component of the local sea level was subsequently restored to the elevation measurement, so that the data are in the form of an ICESat SSH measurement referenced to the ICESat reference ellipsoid.

We compared the algorithm for identifying large leads to the analysis carried out by *Kwok et al.* [2006]. In March 2004, a large lead, approximately 6 km wide, developed just north of Ellesmere Island (refer to Figure 12 and accompanying text in *Kwok et al.*, [2006]). Figure 4.6 illustrates the elevation, standard deviation of elevation, and reflectivity profiles across this large lead on two separate occasions.

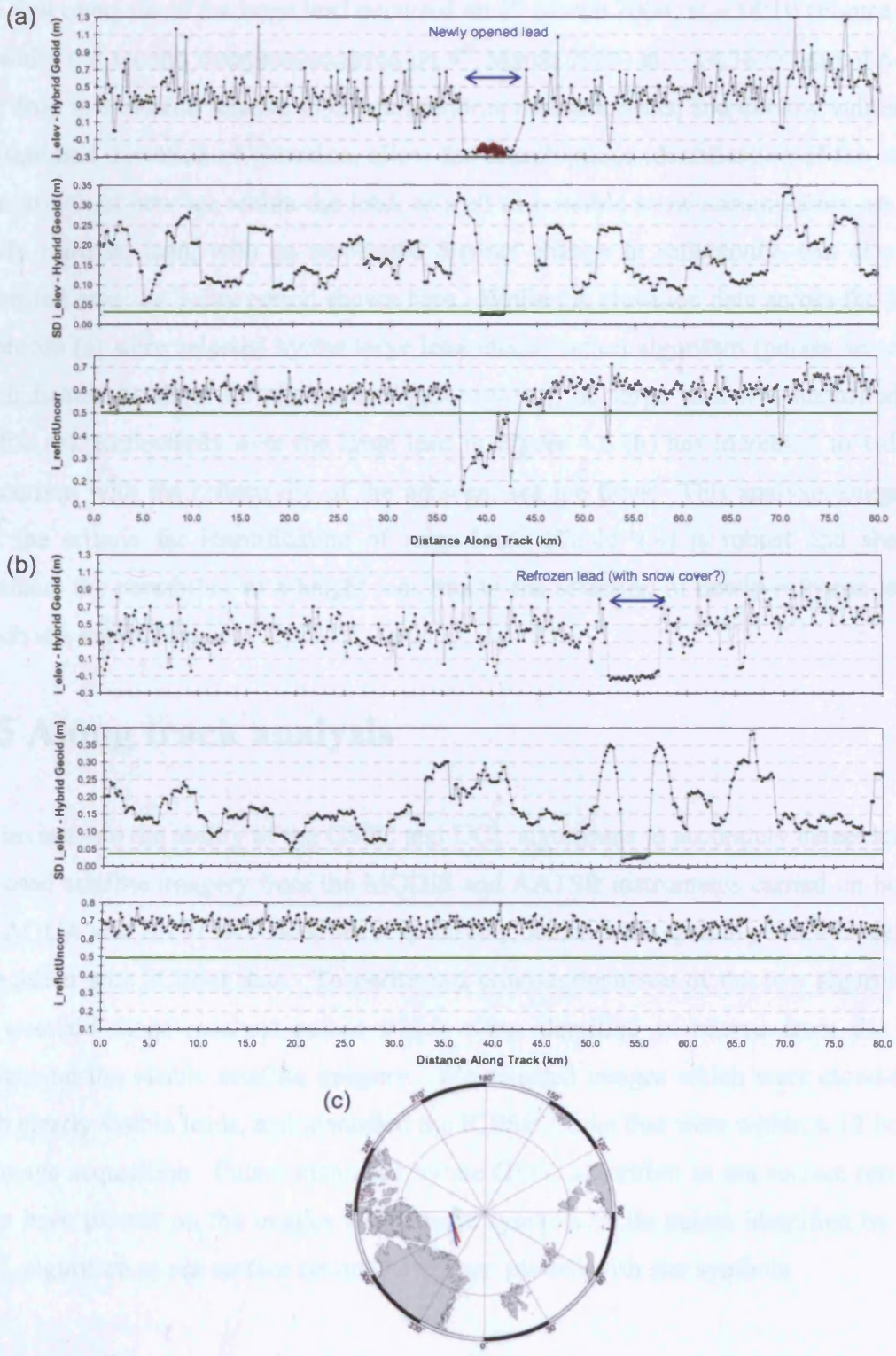

Figure 4.6 Profiles of elevation, standard deviation of elevation, and reflectivity across a large lead acquired on (a) 1st March 2004 and (b) 4th March 2004. Dark red circles indicate those pulses identified as reflections from a large lead and green lines indicate the parameter thresholds. (c) The geographic location of the ICESat tracks: the blue track indicates the geolocation of overpass (a) while the red track pertains to overpass (b).

The first overpass of the large lead occurred on 1st March 2004, at ~ 14:10 (Figure 4.6 a), while the second overpass occurred on 4th March 2004, at ~ 14:38 (Figure 4.6 b). The drop in elevation relative to the surrounding measurements, and the low values of the standard deviation of elevation, allow for unambiguous identification of the lead. The growth of new ice within the lead, as well as possible snow accumulation on the newly refrozen lead, with an associated distinct change in reflectivity, can also be identified over the 3-day period shown here. While the elevation data across the lead in profile (a) were selected by the large lead identification algorithm (pulses selected are indicated by dark red circles in Figure 4.6 (a)), no large lead was identified in profile (b). Reflectivity over the large lead in Figure 4.6 (b) has increased to values concurrent with the reflectivity of the adjacent sea ice floes. This analysis suggests that the criteria for identification of large leads (Table 4.4) is robust and should eliminate the possibility of a height bias due to the selection of newly-refrozen leads which are snow covered.

4.5 Along track analysis

To investigate the ability of the GSFC and UCL algorithms to accurately detect leads, we used satellite imagery from the MODIS and AATSR instruments carried on board the AQUA and ENVISAT satellites respectively, which were spatially and temporally coincident with ICESat data. To perform a cross-comparison of the two algorithms we overlaid those received pulses which were identified as returns from the sea surface on the visible satellite imagery. We selected images which were cloud-free with clearly visible leads, and identified the ICESat tracks that were within ± 12 hours of image acquisition. Pulses identified by the GSFC algorithm as sea surface returns have been plotted on the images with square symbols while pulses identified by the UCL algorithm as sea surface returns have been plotted with star symbols.

4.5.1. Results

4.5.1.1 Analysis of MODIS image acquired 13th March 2003, 00:05

The first satellite image analysed was a MODIS image acquired over the East Siberian Sea on the 13th March 2003 at 00:05. A cross-comparison with ICESat data is shown

in Figure 4.7. The ICESat elevation profile was recorded approximately 5 hours after the image retrieval at 05:05 on 13th March 2003. A large area of open water, clearly visible at the centre of the image (74.4°N 158.45°E), as well as numerous large leads which cross the image, make this particular image ideal for unambiguous investigation of the sea surface algorithms. Furthermore, using sea ice drift data (see Section 3.2.2.3 for details), we estimated that the ice had moved between 0 – 1 km northwards in the 5 hours difference between acquisition of the image and the ICESat profile (Figure 4.9). Sea ice drift of ~ 1 km is equivalent to ~ 0.01° latitude and is thus negligible in terms of this cross-comparison.

The analysis demonstrates that both algorithms accurately identified leads along the ICESat track (Figure 4.7a), particularly those near the bottom of the image (72.5°N 156.5°E, and 72.3°N 156.4°E) where leads have formed between the pack ice (grey ice floes) and land fast ice (smooth, white ice). The UCL algorithm also distinctly identified the large area of open water at 74.4°N 158.5°E; a large concentration of sea surface returns were recorded at this location (crosses near the centre of Figure 4.7a). Both algorithms identified other lead locations along the ICESat track, and while some coincide with lead locations in the imagery, it is harder to verify others.

The ICESat elevation profile (Figure 4.8) illustrates the surface elevation across the centre of the MODIS image (from 73.25°N 157.2°E to 74.6°N 158.6°E). The features of the ice pack in this region are highlighted in Figure 4.7b. The high number of sea surface returns identified by the UCL algorithm (blue stars) over the area of open water is again evident. Furthermore the algorithm can distinguish between open water and two distinct ice floes within the open water region. The elevation profile also illustrates the methodology employed by the GSFC algorithm, namely that the lowest 2% of elevations within 50 km segments are identified as open water. Only one pulse over the large area of open water was identified as a sea surface return by the GSFC algorithm, whereas the UCL algorithm identified ~24 pulses over the same area.

Selected ICESat waveforms are illustrated in Figures 4.8b and 4.8c. Waveforms identified as sea surface returns by the GSFC algorithm are bounded by a red box, while those identified by the UCL algorithm are bounded by a blue box. Waveforms bounded by a green box indicate waveforms that were discounted from our analysis based on the filtering scheme described in Section 4.3.

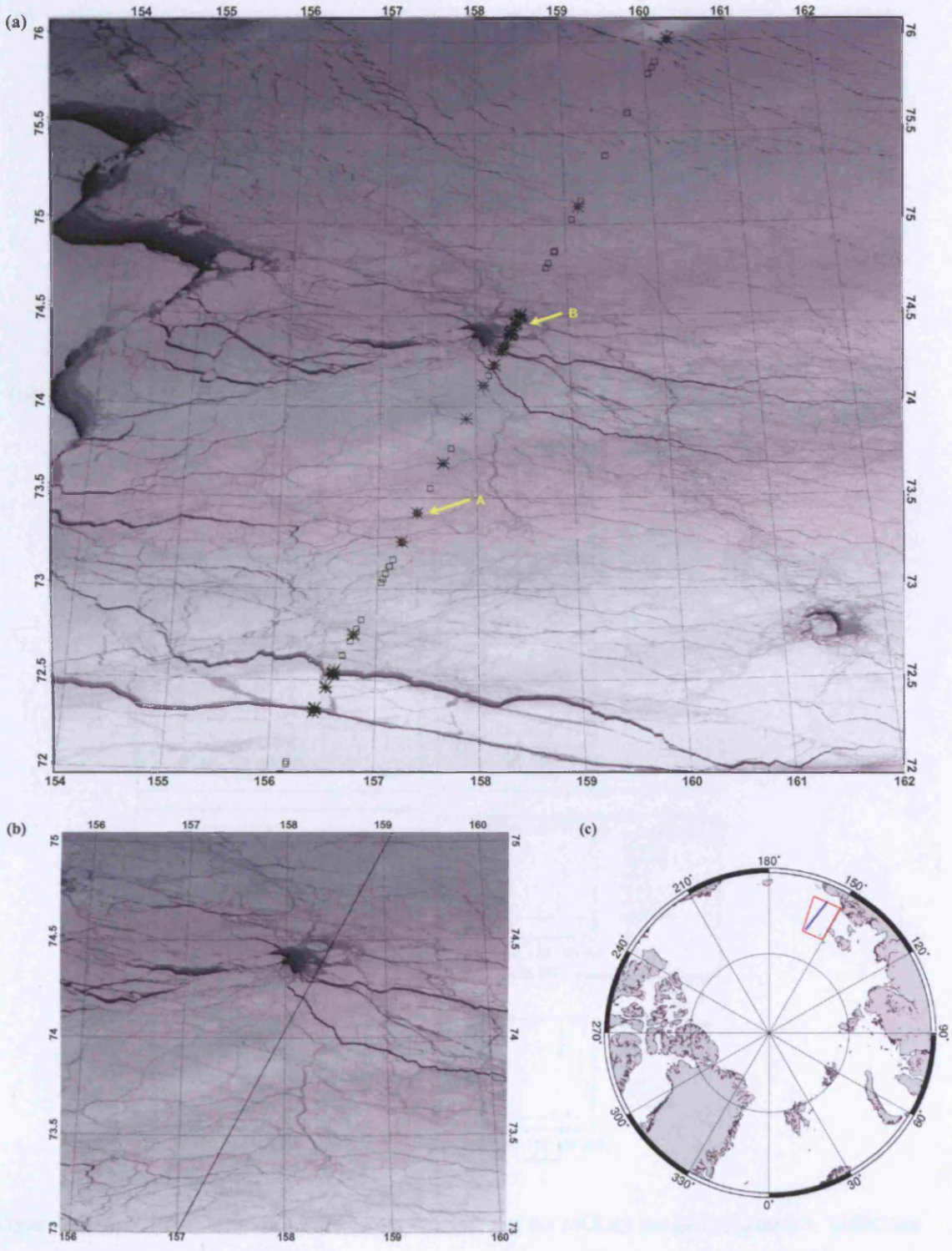

Figure 4.7 Comparison of the UCL and GSFC algorithms with a near coincident MODIS image acquired on the 13th March 2003 at 00:05. (a) The GSFC Method (*boxes*) and UCL Method (*stars*) discrimination of sea surface returns. (b) Geolocation of the ICESat overpass in the region of interest. (c) The geographic location of the cross-comparison in the East Siberian Sea.

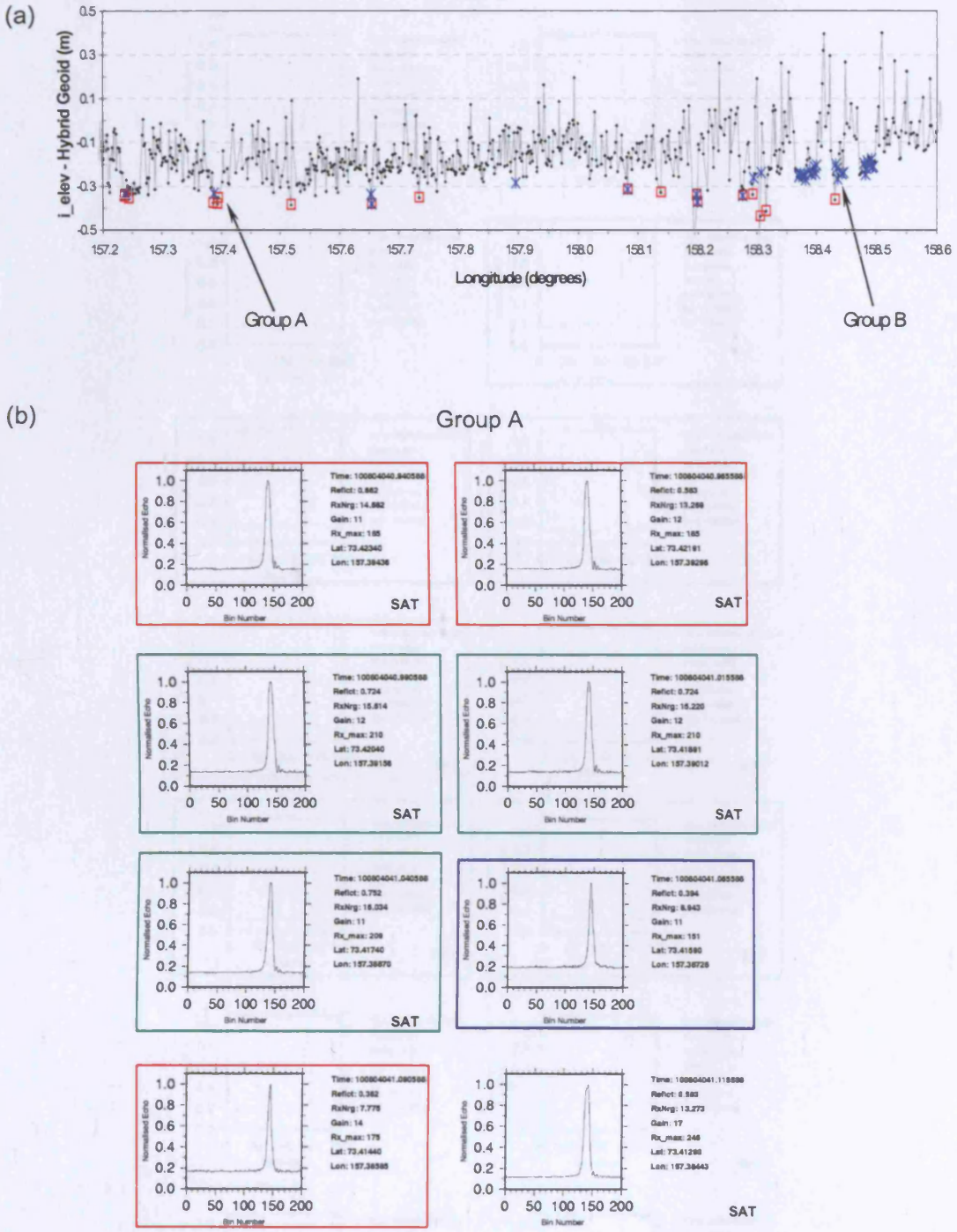

Figure 4.8 (a) ICESat elevation profile across the centre of the MODIS image in Figure 4.7. GSFC sea surface returns are illustrated by red squares, while blue stars indicate UCL sea surface returns. (b, c) Selected ICESat waveforms for two waveform groups identified by the arrows in the elevation profile. Green boxes indicate waveforms removed by the filtering scheme, red boxes mark waveforms identified as sea surface returns by the GSFC algorithm, and blue boxes mark those identified by the UCL algorithm. Saturated waveforms are indicated by the word "SAT". (Figure continued overleaf)

(c)

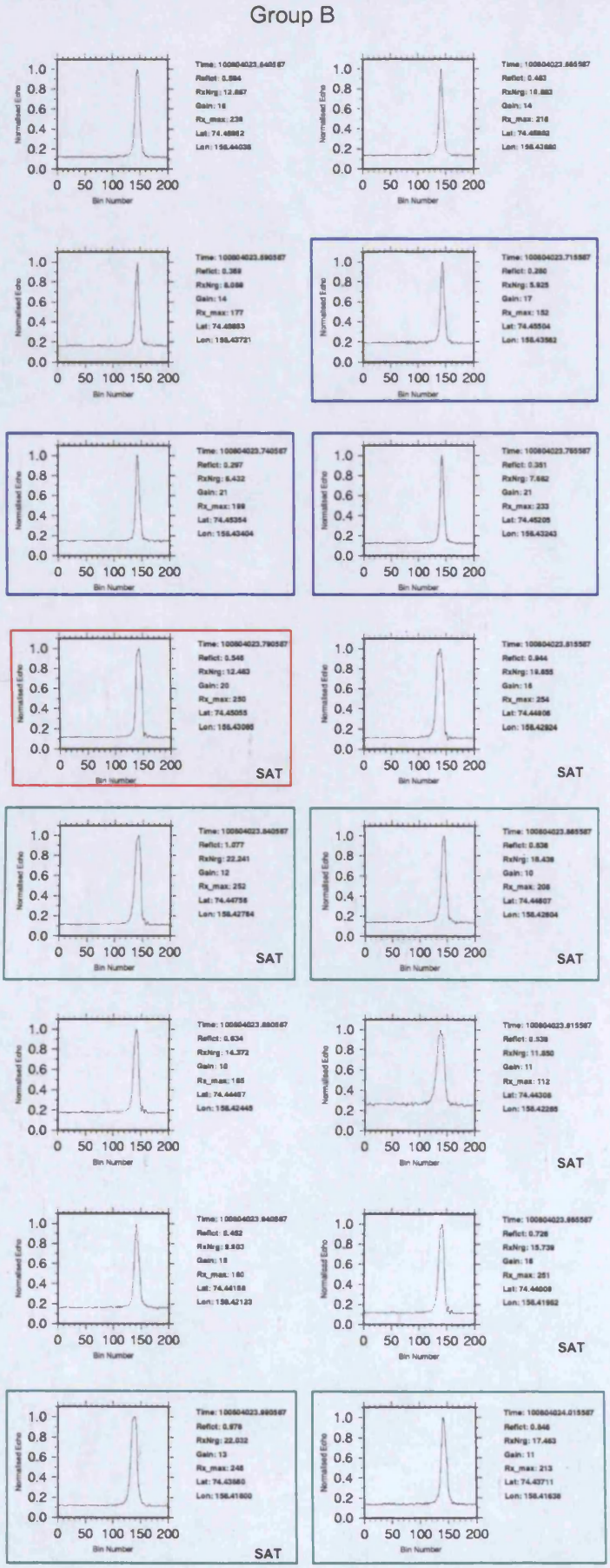

Figure 4.8 Caption on previous page.

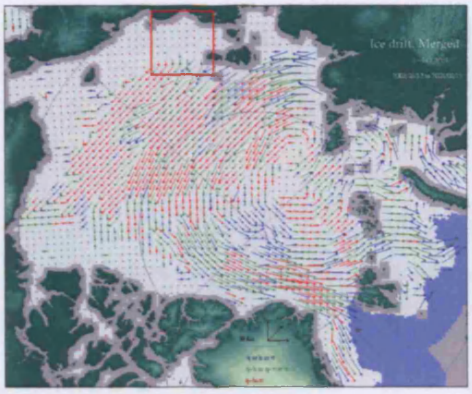

Figure 4.9 Arctic sea ice drift map. The merged, 3-day ice drift data set for 12 – 15th March 2003 illustrates that the sea ice moved a maximum of ~ 14.3 km over three days in the region of interest outlined by the red box.

Saturated echoes are distinguished by their distorted shape which includes slightly flatter peaks and pulse ringing on the tail of the waveform. Although the filtering scheme removes a number of saturated echoes (waveforms bounded by green boxes) not all saturated echoes were removed. The GSFC algorithm has selected some of the remaining saturated echoes (red boxes) as sea surface pulses; as discussed in Section 3.3.1.9, saturated echoes are associated with erroneous elevation measurements which manifest themselves as anomalously low elevation measurements. The waveforms identified by the UCL algorithm as sea surface returns (blue boxes) are almost perfectly specular, demonstrating that the algorithm is functioning as desired.

4.5.1.2 Analysis of AATSR image acquired 7th March 2005, 08:14

Further analysis of the GSFC and UCL algorithms was achieved by comparison with two AATSR images acquired over the East Siberian Sea on 7th March 2005 at 08:14. Figure 4.10 illustrates: (a) and (b) the satellite images and the discrimination of sea surface returns by both algorithms, (c) the geolocation of the overpasses, and (d) the sea ice drift vector data for the regions of interest. The number of leads identified by the GSFC algorithm as compared to the UCL algorithm is summarised in Table 7.5.

	GSFC Algorithm	UCL Algorithm
Track A	176	3
Track B	188	12
Track C	127	39

Table 4.5 Number of leads identified by the GSFC and the UCL algorithms for the ICESat-AATSR comparison of the 7th March 2005.

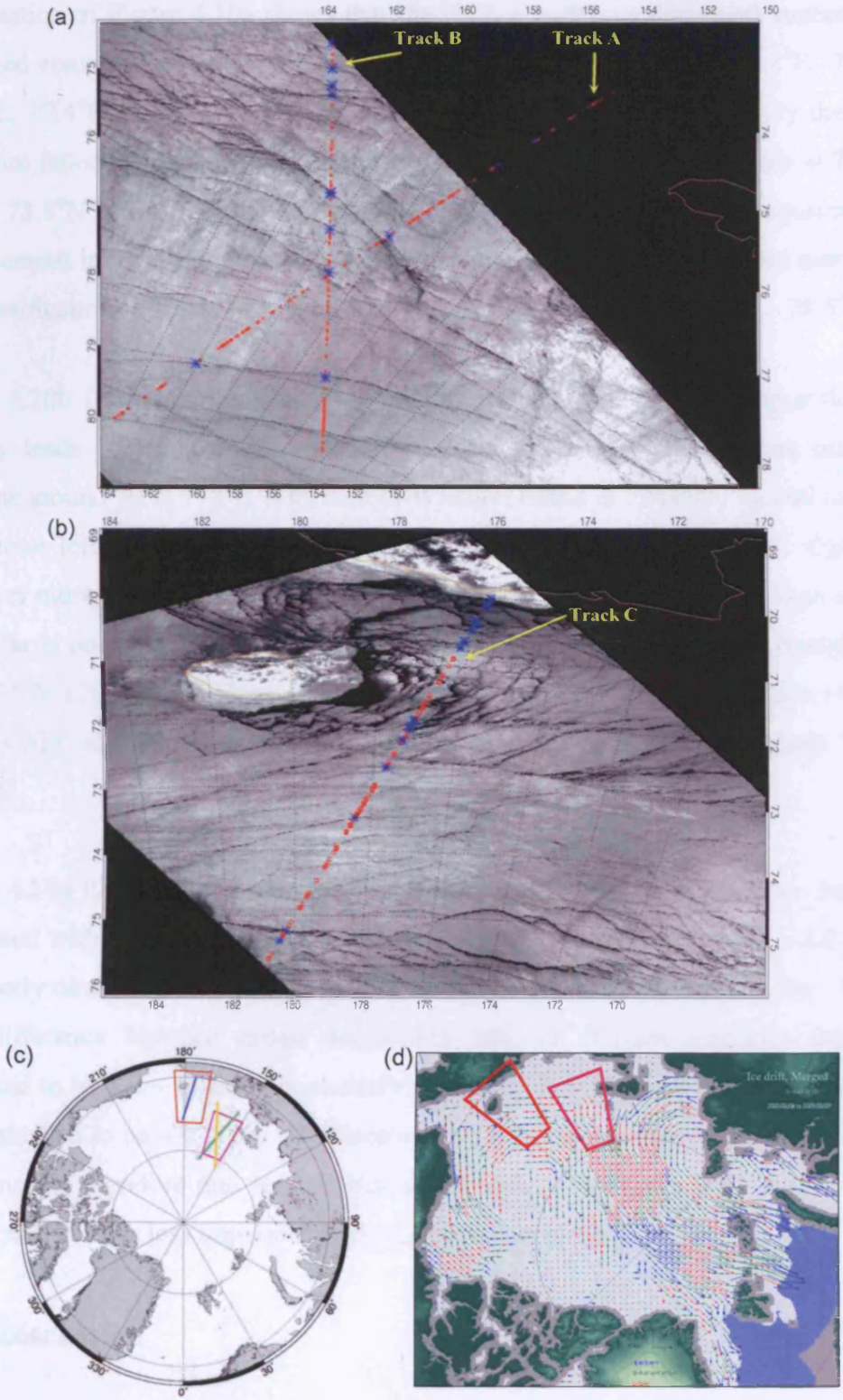

Figure 4.10 (a) AATSR image acquired on 7th March 2005 at 08:14 with two ICESat overpasses occurring 2 hours earlier at 06:12 (*Track A*) and 8 hours later at 16:18 (*Track B*). (b) AATSR image acquired on 7th March 2005 at 08:14 with the ICESat overpass occurring ~ 3.5 hours earlier at ~ 04:36 (*Track C*). (c) Geolocation of AATSR images and ICESat tracks. (d) Sea ice drift vector map with boxes illustrating the regions of interest.

Examination of Figure 4.10a shows that the UCL algorithm (blue stars) successfully identified returns over leads (e.g. leads at 75°N 162.5°E, 76.3°N 160.8°E, 76.7°N 160.1°E, 77.4°N 159.2°E, 78.8°N 156.6°E, and 79°N 162°E). Occasionally the UCL algorithm failed to pick sea surface returns from some large leads (e.g. leads at 75.4°N 162°E, 75.8°N 161.4°E, and 79.6°N 155°E). The GSFC algorithm (red squares) had some success in identifying leads, but the signal is apparently dominated by numerous misidentifications of leads (e.g. near 75.6°N 161.5°E and in the region 78 – 78.5°N).

Figure 4.10b illustrates the ability of both the GSFC and the UCL algorithms to identify leads. Particular examples of successful lead identification are near the coastline around 70°N 175°E, northeast of Wrangel Island at 72°N 177°E, and towards the bottom left of the image at 75.2°N 179.7°W. In general, the GSFC algorithm identifies more leads than the UCL algorithm (Table 7.5), and the UCL algorithm in particular is poor at identifying smaller leads, for example in the region bounded by 73°N–75°N 178–180°E. There is some evidence to suggest misidentification of leads by the GSFC algorithm, for example near 73.6°N 178.6°E, 74°N 178.9°E, and 74.5°N 179.3°E.

Figure 4.10d illustrates the ice drift vector data for the regions of interest. Ice drift associated with track A in Figure 4.10a was estimated to be between 0.2 – 1.0 km in an easterly direction. Ice drift along track B was more significant (due to the ~ 8 hour time difference between image acquisition and the ICESat overpass) and was estimated to be 1.4 – 4 km in an easterly direction. Ice drift associated with track C was estimated to be ~ 0.7 km. Displacement of 1 km represents about 0.01° latitude. We conclude therefore that sea ice drift along track B in Figure 4.10a is potentially significant, but it is less important along the two other tracks.

4.5.2 Discussion

The GSFC algorithm identified significantly more along-track returns as reflections from leads and open water than the UCL algorithm (Table 7.5). The UCL algorithm appears to be more conservative in lead identification than the GSFC algorithm. The GSFC algorithm apparently misidentified leads on several occasions (Figure 4.10a in the region 78 – 78.5°N), and is thus associated with frequent "false alarms". The

resolution of the MODIS image (Figure 4.7) is 250 m, while the resolution of the AATSR images (Figure 4.10) is 1 km, and the ICESat footprint resolution is ~170 m. It is therefore possible that both algorithms have identified sub-pixel leads, i.e. leads that are narrower than the resolution of the imagery and therefore invisible to the eye.

As discussed in Section 3.3.1.9, pulses reflected from open water are often saturated and the elevation measurements are therefore inaccurate and anomalously low [*Kwok et al.* 2006]. Although we have tried to eliminate saturated echoes from the dataset, some remain (Figures 4.8b and 4.8c). The GSFC algorithm is susceptible to identifying saturated echoes as returns from the sea surface, since these have the lowest elevations in along-track segments.

The UCL algorithm detects fewer leads than the GSFC algorithm (Table 7.5 and Figures 4.7a and 4.10a). Most of the returns identified as sea surface returns were however accurate, since they coincided with leads and open water in the visible imagery (e.g. Figure 4.7a at 74.4°N 158.5°E; Figure 4.10a at 76.3°N 160.8°E, and 76.7°N 160.1°E). Some large leads were not picked out by the UCL algorithm (e.g. Figure 4.10a at 79.6°N 155°E; Figure 4.10b at 74.2°N 179.2°E), but this may be due to the laser footprint either partly sampling the lead or missing it entirely. Analysis of some waveforms (Figures 4.8b and 4.8c) that were identified as sea surface returns confirmed that the UCL algorithm selects near specular echoes and the data is not affected by saturated pulses.

4.6 Summary

We have described a reference MSS computed from eight years of ERS-2 radar altimetry data which extends to 81.5°N. We have also discussed two currently available state-of-the-art Arctic geoid models, the ArcGP, derived mainly from terrestrial gravimetry, and the hybrid geoid, derived from an optimal combination of satellite gravimetry from the GRACE satellites and terrestrial gravimetry from ArcGP.

We have described the filtering scheme which we have applied to ICESat elevation data prior to processing to remove returns over the open ocean along the sea ice edge, as well as most returns affected by pulse saturation and atmospheric forward scattering. We have described the existing method (the GSFC algorithm) for identifying sea surface height in the ice-covered Arctic Ocean. In addition we have described two new algorithms: the UCL algorithm, also designed to measure sea surface height, and the large lead algorithm that identifies leads greater than ~ 5 km wide. We will use the large lead algorithm to obtain a baseline reference set of SSH measurements, against which we can verify the accuracy of the GSFC and UCL algorithms.

Finally, we have assessed the GSFC and UCL algorithms by investigating their ability to pick out lead features identified in visible satellite imagery. We found that the UCL algorithm picked out less sea surface returns than the GSFC algorithm, but a high proportion of those returns identified were associated with leads in the visible imagery. The UCL algorithm is apparently inefficient at identifying small leads. The GSFC algorithm successfully identified some leads in the visible imagery; many returns identified as sea surface returns were however "false alarms" associated with sea ice floes in the imagery. Analysis of selected waveforms suggests that a further limitation of the GSFC algorithm is that it often identifies saturated echoes as sea surface returns since these pulses are associated with locally-low elevations. Both algorithms therefore have advantages and limitations. The GSFC algorithm works to identify more leads than the UCL algorithm, thus providing more data points for the calculation of local SSH. However the GSFC algorithm is also associated with more false alarms than the UCL algorithm, so that SSH estimates derived using the GSFC algorithm may be contaminated with elevations from sea ice floes. We suggest that the development of an optimised algorithm comprising aspects of all three methods for detecting SSH in the Arctic Ocean would be a reasonable next step.

In the following chapter we provide a quantitative assessment of the three techniques for the retrieval of SSH in the ice-covered Arctic Ocean which we have described here. We will investigate the extent to which the algorithms provide accurate SSH measurements and we will compare SSH estimates derived from ICESat laser altimetry with contemporaneous measurements derived from satellite radar altimetry.

5 Assessment of Altimetric Sea Surface Height Measurements in Ice Covered Seas

5.1 Introduction

In Chapter 4 we described three techniques for the retrieval of sea surface height (SSH) measurements in the Arctic Ocean using ICESat data, and we presented a qualitative evaluation of these techniques. The purpose of Chapter 5 is to provide a quantitative assessment of the three techniques with the aim of investigating whether they provide accurate SSH measurements. The assessment is based on comparisons of ICESat data with spatially and temporally coincident radar altimetric measurements of sea surface height from ENVISAT. The ENVISAT radar altimetry SSH measurements were provided courtesy of A. L. Ridout, C.P.O.M.

We present the SSH measurements in terms of sea level anomalies (SLA) with respect to the ArcGICE mean sea surface (MSS). The ArcGICE MSS was derived from ERS-2 altimetric data. We evaluate and compare the performance of each of the three techniques described previously in Chapter 4. To facilitate this we first investigated the accuracy of the SLA estimates derived from the individual ENVISAT, ICESat GSFC algorithm, ICESat UCL algorithm SSH datasets using single-satellite crossovers. Second we compare monthly average SLA estimates from ICESat and ENVISAT and discuss the overall biases associated with each of the ICESat laser campaigns. Third we compare 3-day SSH estimates from ICESat and ENVISAT via a comparison of mean SLA signals and dual satellite crossovers. Fourth we assess the ability of the GSFC and UCL algorithms to measure SSH, is via the comparison of freeboard estimates based on these SSH measurements.

We discuss the accuracy of the ICESat SSH retrievals and explore their usefulness for further geophysical investigations. We identify periods when direct comparisons of geophysical data from ICESat and ENVISAT are possible. These periods are instances where (i) we observe low variability of the sea level anomaly signal and (ii) the difference in SSH signal from the two satellites, at dual satellite crossover

locations, is small. We can exploit both the laser and radar altimetry data during these time periods for the retrieval of additional geophysical parameters such as sea ice freeboard. We conclude the chapter with a summary of our findings.

5.2 Sea Level Anomalies

To obtain an indication of the accuracy of the ICESat SSH measurements using the three algorithms which were described in detail in Section 4.4 (the GSFC algorithm, the UCL algorithm, and the large lead algorithm), we derive estimates of ICESat SLA. We compare ICESat SLA estimates to an independent dataset of SLA estimates derived from coincident ENVISAT SSH data. The SLA are computed as the altimetric measurement of SSH minus the long-term reference MSS. Both the ENVISAT and ICESat SLA estimates, SLA_{ENV} and SLA_{ICE} respectively, are calculated similarly following Eqn. 2.11,

$$\begin{aligned} SLA_{ENV} &= h_{ssh\_RA} - \bar{h}_{ssh} \\ SLA_{ICE} &= h_{ssh\_LA} - \bar{h}_{ssh} \end{aligned} \tag{5.1}$$

where h_{ssh_RA} is an ENVISAT SSH measurement calculated as described in Section 3.2.2.1, h_{ssh_LA} is an ICESat SSH measurement calculated using one of the algorithms described in Section 4.4, and $\bar{h}_{ssh}$ is the ArcGICE MSS.

Using each of the three ICESat SSH retrieval algorithms we generated a dataset of ICESat SLA for each laser campaign. The SLA estimates are valid for all ice-covered ocean areas between the latitudes of 65°N and 81.5°N (bounded by the limit of coverage of the ArcGICE MSS). SLA derived from ENIVSAT SSH data we computed for 35-day periods (one complete orbital cycle) which coincided with ICESat operation periods.

The atmospheric corrections applied to both the ICESat and ENVISAT elevation data are the same, and the MOG2D-G inverse barometer correction (see Section 2.7.4) was applied to both datasets. The tidal corrections were however not consistent between the two datasets: the ICESat data had an ocean tide correction based on the GOT99.2

tidal model [*Padman and Fricker*, 2005], while the ENVISAT tidal corrections were based on the FES2004 ocean tide model (*S. Baker*, personal communication). This is likely to be a source of difference in the SSH signal in the two datasets and is explored further in Section 5.4.4. Time constraints prevented us from applying consistent tidal corrections to both datasets, but we suggest this should be considered as a "next step" in future analysis (Section 5.4.4).

5.3 Single Satellite Crossover Analysis

We computed 3-day SLA estimates for both the ICESat and ENVISAT datasets over the ice-covered regions of the Arctic Ocean. Although ENVISAT is in a 35-day repeat orbit, analysis of ENVISAT SLA over 3-day periods is convenient since there is a 3-day sub-cycle. The Arctic-wide coverage of ICESat over 3-day periods is limited as compared to ENVISAT. The spatial coverage of Arctic sea ice by ICESat and ENVISAT ground tracks over a 3-day period is illustrated in Figure 5.1.

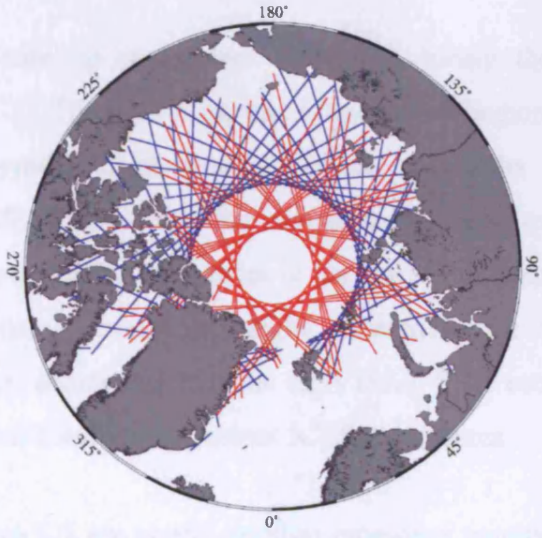

Figure 5.1 Illustration of the spatial coverage of ICESat ground tracks (red) and ENVISAT ground tracks (blue) over Arctic sea ice for a 3-day period.

To investigate the accuracy of the SLA estimates derived from the individual algorithms, single-satellite crossovers were computed using ENVISAT SLA, ICESat GSFC algorithm SSH data, and ICESat UCL algorithm SSH data. At crossover locations, two measurements of SSH are available, usually in the form of an ascending-pass measurement and a descending-pass measurement.

Single-satellite crossovers were calculated as follows: The along-track data from ascending passes and descending passes were separated and these along-track profiles were subsequently split into smaller arc segments. The maximum distance between successive along-track data points for an arc to be considered continuous was defined; if the distance between data points exceeded this value then a new arc segment was established[22]. The arc segments from the ascending and descending passes were cross-referenced and arcs that crossed each other were selected. SSH estimates at the crossover points were interpolated using the SSH values of the two data points either side of the crossover location. Finally, the two SSH estimates at each crossover location were differenced, giving rise to the single-satellite crossover height difference. The crossover height differences were calculated as the ascending-pass measurement minus the descending-pass measurement. Crossover height differences were constrained so that the maximum time difference between the acquisitions of the two height estimates was 3 days. To maximise the number of measurements included in the ICESat single satellite crossover calculations, we included all SSH measurements up to the limit of coverage of ICESat at 86°N.

Examples of single satellite crossovers computed during the L2a campaign are presented in Figure 5.2. The data from the 3-day period beginning 6th Nov 2003 are illustrative of the typical single-satellite crossover results throughout the L2a campaign. The ENVISAT single satellite crossovers are close to a 0 cm mean and the distribution of crossover height differences is narrow with a standard deviation of ~ 7 cm. The distributions of crossover height differences for the GSFC and UCL algorithms are broader, indicating that the ENVISAT SSH estimates are less noisy and more self-consistent than the equivalent ICESat estimates.

Also included in Figure 5.2 are single satellite crossover results for the 3-day period beginning 28th Oct 2003. While the results for the 6th Nov 2003 are representative of the other 3-day periods during the L2a campaign, the single-satellite results for the 3-day period beginning 28th Oct 2003 were the one exception. Large variations in SSH measurements were recorded during this period resulting in wide distributions with large standard deviations.

[22] In our analysis, the maximum distance between successive data points for an arc to be considered continuous was set at 100 km.

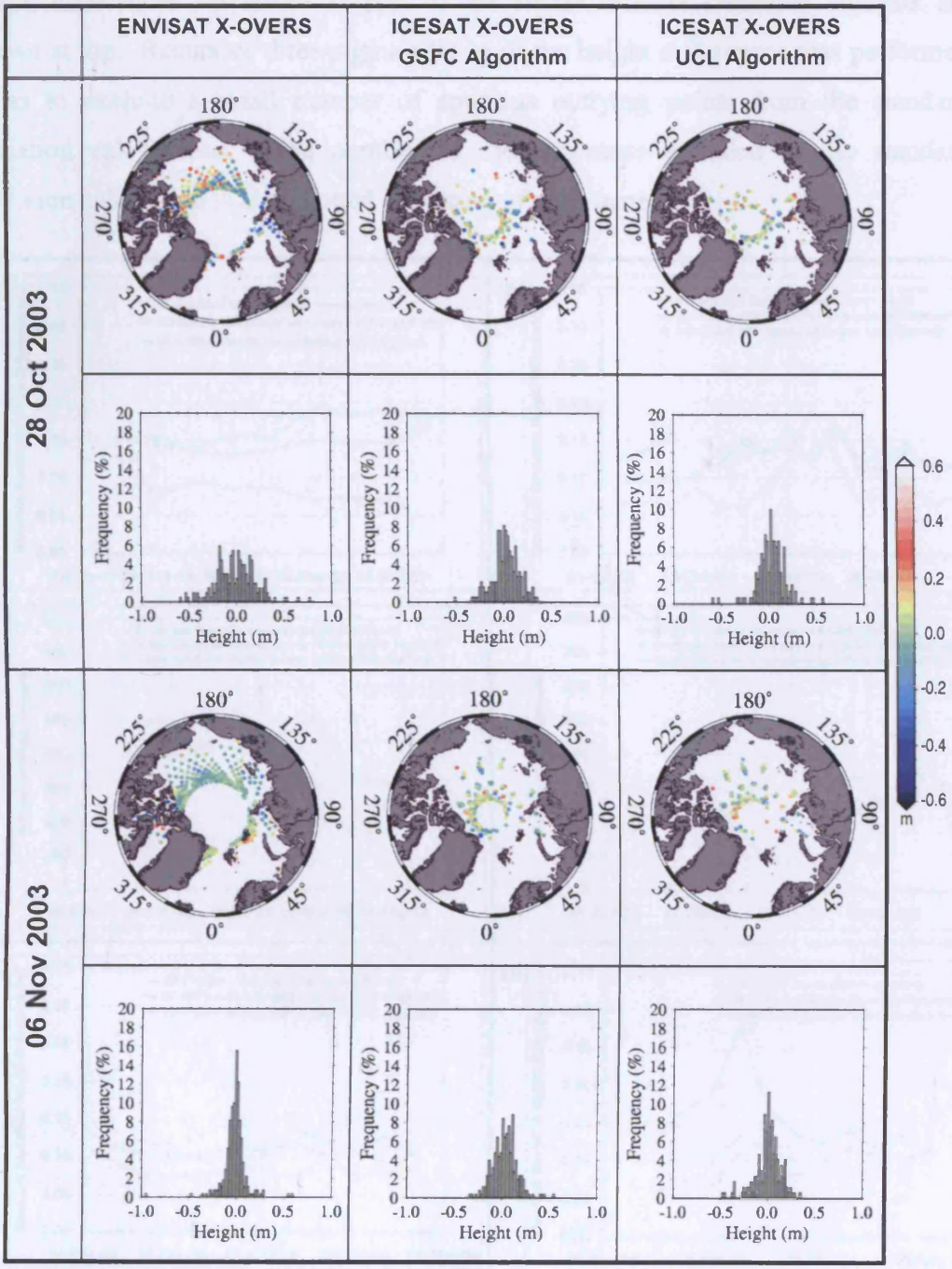

Figure 5.2 Single satellite crossovers. The 3-day mean SSH crossover differences along with the distribution of height differences for the ENVISAT and ICESat SSH datasets are shown for two occasions during the L2a campaign. The dates given in the left-hand column indicate start date of the two 3-day periods.

The single-satellite crossover analysis was carried out for each of the five ICESat laser campaigns based on sets of 3-day SSH estimates. The results of this analysis are summarised in Figure 5.3. For each panel the standard deviations of sea surface

height differences calculated as part of the single satellite crossover analysis are shown at top. Recursive three-sigma editing of the height differences was performed so as to exclude a small number of spurious outlying points from the standard deviation calculations. The number of measurements included in the standard deviation calculation is also plotted at bottom of each panel.

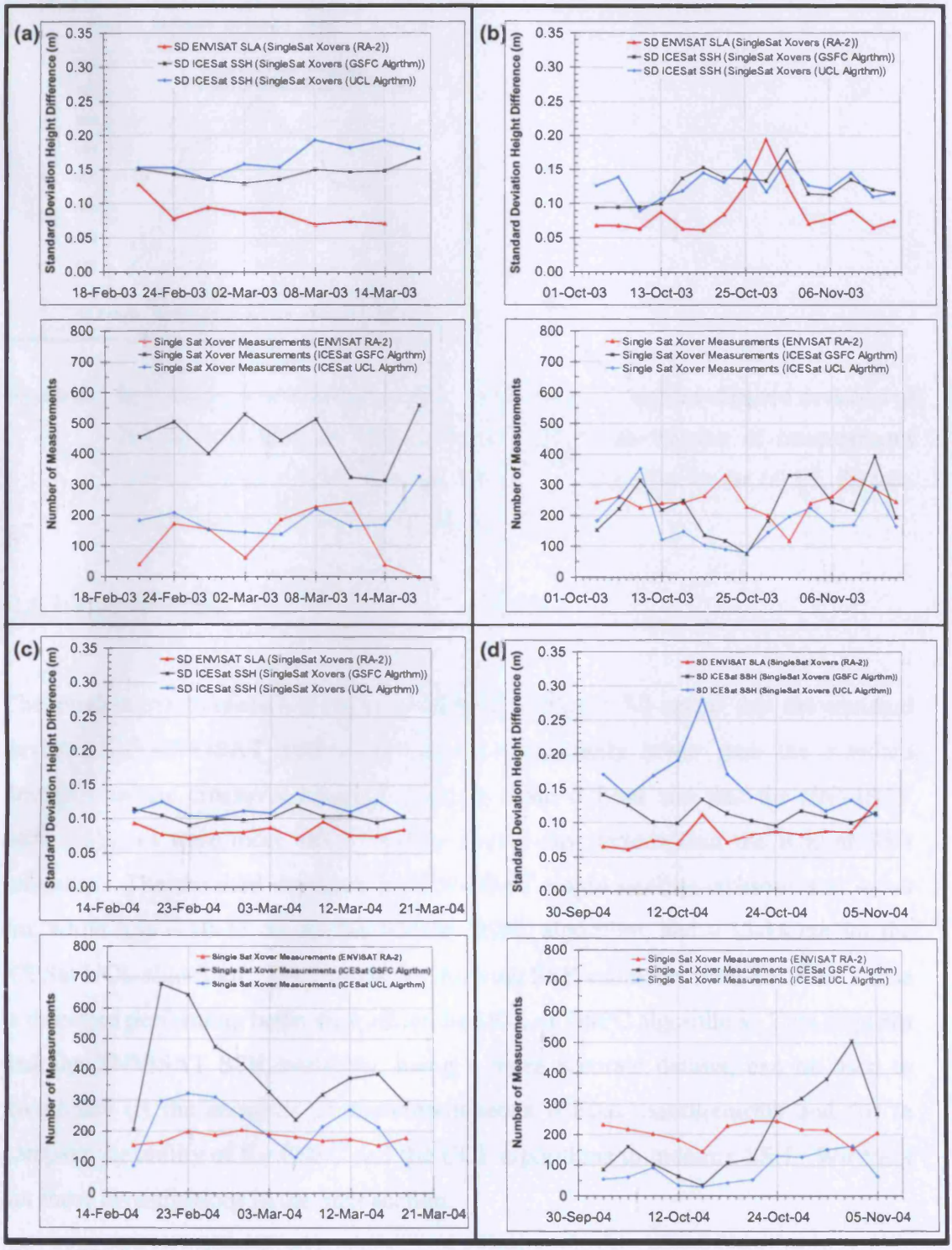

Figure 5.3 Continued overleaf.

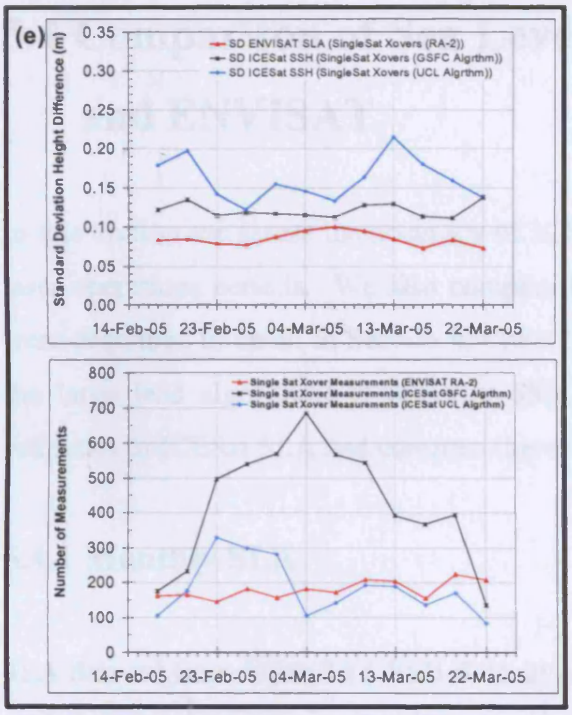

Figure 5.3 Single satellite crossover statistics. For each panel, (top) the standard deviation of height differences for 3-day periods, (bottom) the number of measurements included in the standard deviation calculation. Statistics for the (a) L1, (b) L2a, (c) L2b, (d) L3a, (e) L3b campaigns are illustrated.

5.3.1 Key Results

The single satellite crossover results presented in Figure 5.3 reveal that the standard deviation of ENVISAT SSH crossovers is consistently lower than the standard deviation of the crossover height differences from ICESat and that the ENVISAT SSH estimates were more self-consistent over 3-day periods than the ICESat SSH estimates. The standard deviation for ENVISAT single satellite crossovers is ~ 7-9 cm, while it is ~ 10-15 cm for the ICESat GSFC algorithm, and ~ 13-18 cm for the ICESat UCL algorithm. The method for deriving SSH estimates from ENVISAT data is therefore performing better than either the UCL or GSFC algorithms. This suggests that the ENVISAT SSH retrievals, being a more accurate dataset, can be used to investigate (i) the accuracy of contemporaneous ICESat measurements and (ii) to compare the ability of the GSFC and the UCL algorithms to measure SSH. We carry out these investigations in the next section.

5.4 Comparison of Sea Level Anomalies from ICESat and ENVISAT

In this section we assess the accuracy of ICESat SSH measurements during different laser operations periods. We also compare the ability of the three algorithms which were described in detail in Section 4.4 (the GSFC algorithm, the UCL algorithm, and the large lead algorithm) to measure SSH. To facilitate this analysis we derive estimates of ICESat SLA and compare these to coincident ENVISAT SLA estimates.

5.4.1 Monthly SLA

SLA derived from ENIVSAT SSH data, averaged over 35-day periods (one complete orbital cycle) coinciding with ICESat operation periods were interpolated onto a grid with longitude spacing of 1/8° and latitude spacing of 1/40°. The ENVISAT SLA values were then subtracted from the ICESat SLA estimates. We re-interpolated the resultant SLA difference data onto a grid with a 2° by 1° longitude by latitude spacing.

The differences between coincident radar and laser estimates of SLA for each ICESat laser campaign are plotted in Figure 5.4. The results of the three independent algorithms for the retrieval of ICESat SSH in ice-covered oceans are also illustrated in Figure 5.4. Frequency distributions describing the difference between ICESat and ENVISAT SLA estimates are outlined in Figure 5.5.

ICESat Laser Operations Period	Coincident ENVISAT data period	GSFC Algorithm SLA Diff		UCL Algorithm SLA Diff		Large Lead Algorithm SLA Diff		Laser Operations Period Average	
		Mean	Standard Deviation	Mean	Standard Deviation	Mean	Standard Deviation	Mean	Standard Deviation
L1 (20 Feb - 20 Mar 2003)	17 Feb - 23 Mar 2003	-5.49	13.39	-0.86	13.21	-0.41	12.76	-2.25	13.12
L2a (04 Oct - 18 Nov 2003)	10 Oct - 13 Nov 2003	-1.05	13.82	-0.49	13.38	2.40	14.00	0.28	13.73
L2b (17 Feb - 21 Mar 2004)	16 Feb - 22 Mar 2004	12.35	12.41	8.71	12.14	9.49	11.88	10.18	12.14
L3a (03 Oct - 08 Nov 2004)	04 Oct - 07 Nov 2004	-6.59	19.36	0.09	14.87	2.38	12.71	-1.37	15.65
L3b (18 Feb - 24 Mar 2004)	18 Feb - 24 Mar 2004	-14.97	15.49	-8.55	15.67	-10.98	14.87	-11.50	15.34

Table 5.1 The mean and the standard deviation of ICESat SLA minus ENVISAT SLA ('SLA Diff') for five ICESat laser campaigns. Statistics for the three algorithms described in Section 4.4 are presented. Units are cm.

The mean of SLA differences, averaged over the ice-covered regions of the Arctic Ocean between 65°N and 81.5°N, and over each laser operations period, is presented in Table 5.1. The standard deviation of SLA differences for each laser campaign is also included in Table 5.1. These measurements describe the mean, and the spread (standard deviation), of the distributions presented in Figure 5.5.

5.4.1.1 Key Results

We find that the lowest bias between ICESat-derived SLA and the equivalent ENVISAT-derived SLA is obtained during the Laser 2a campaign. SLA differences across all regions of the Arctic Basin are on the order of 0 – 2 cm (Table 5.1) for this laser operations campaign, and there is agreement across the data derived from all three ICESat algorithms (Figure 5.5). Some larger differences (20 – 25 cm) exist in areas close the North American and Siberian coasts, in the Beaufort and East Siberian Seas respectively (apparent as red grid-cells in Figure 5.4). Due to the different orbital patterns of the ICESat and ENVISAT satellites, the temporal sampling of the ocean differs between the altimetric datasets. Differences between the average (~ monthly) SLA estimates may therefore be affected by differing ocean tide corrections, particularly in shelf regions where the amplitude of the main tidal constituents is large (see Section 2.7.3 for further discussion).

There is also agreement between the ICESat SLA data from the L1 and L3a campaigns and the contemporaneous ENVISAT measurements. On a basin-wide scale, SLA differences are ~ 0 - 6 cm (Table 5.1). On a regional scale however, large differences of up to ~ 30 cm are visible near the Queen Elizabeth Islands (~ 80°N 250°E in Figure 5.4). These positive biases in the ICESat data are possibly due to contamination of the SSH measurements by inadequate performance of the algorithm resulting in the inclusion of retrievals from ice floes rather than from open water or leads only. Although we do not have direct evidence to support this assertion, we do expect this region to be the site of the thickest sea ice floes and deformed pressure ridges (see Figures 1.16 and 1.21).

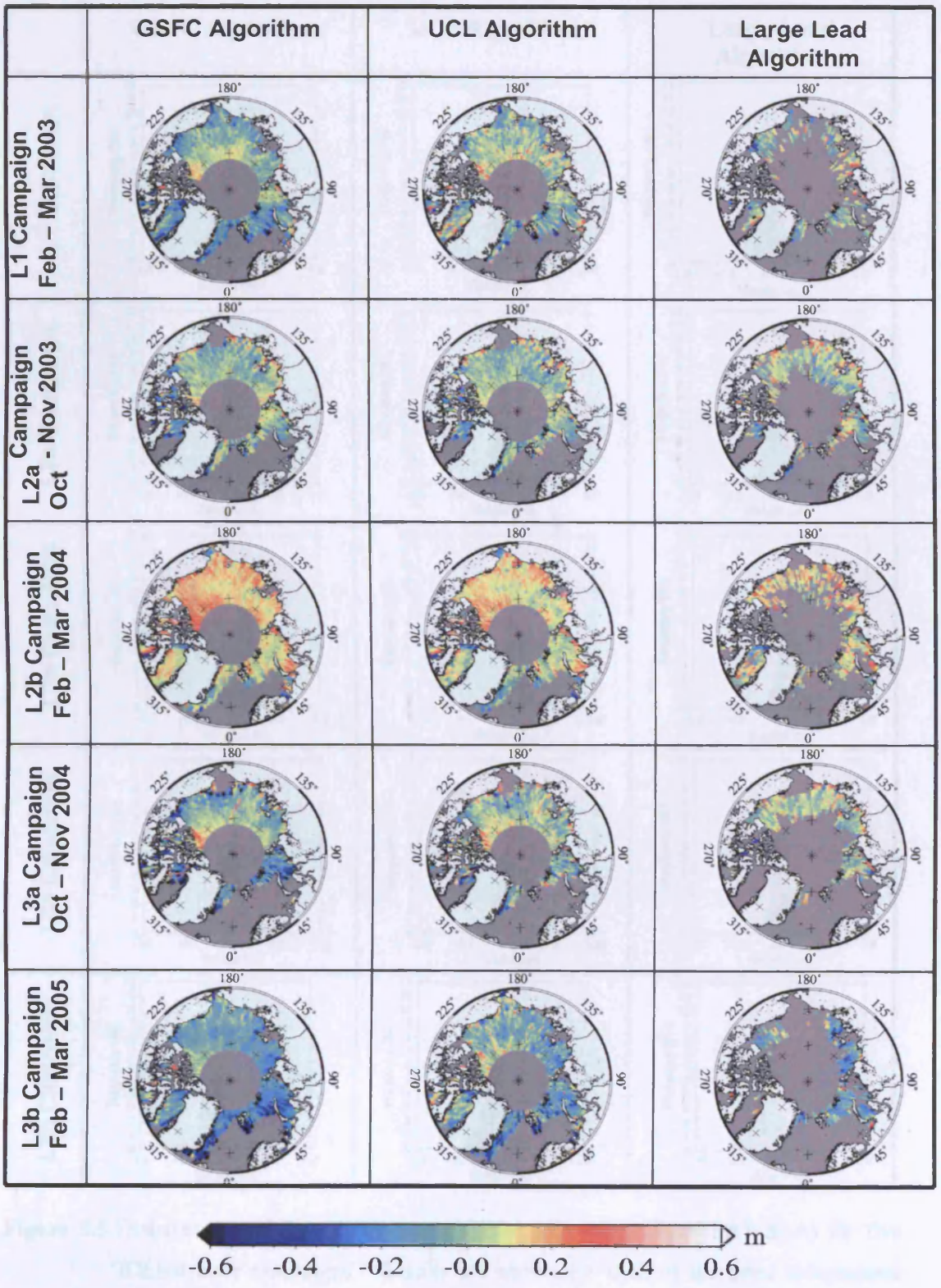

Figure 5.4 ICESat SLA minus ENVISAT SLA for five ICESat laser campaigns. Results are shown for each of the three independent algorithms described in Section 4.4.

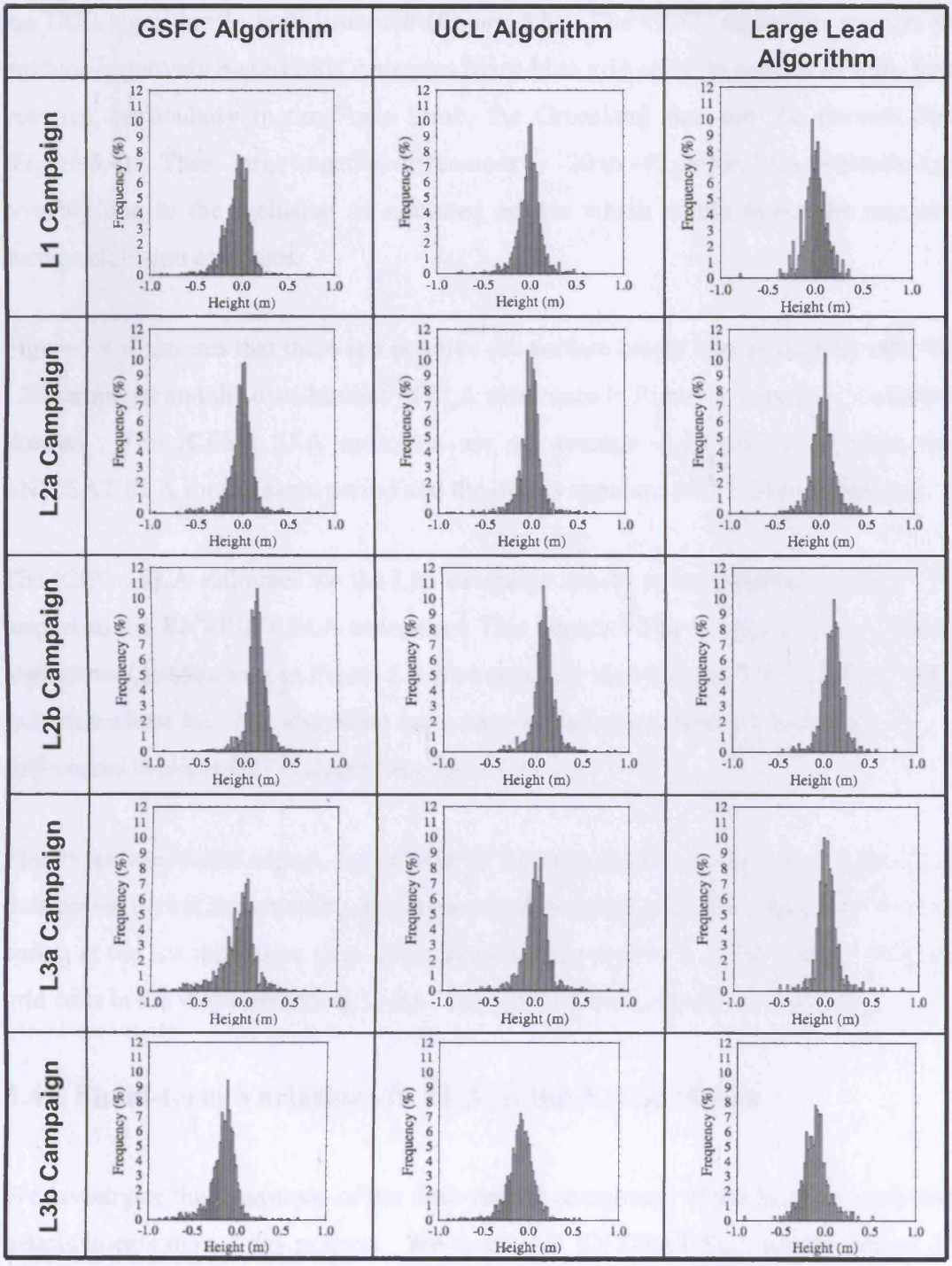

Figure 5.5 Distributions of SLA differences (ICESat SLA minus ENVISAT SLA) for five ICESat laser campaigns. Results are shown for each of the three independent algorithms described in Section 4.4.

The UCL algorithm appears to perform better than the GSFC algorithm for both the L1 and L3a campaigns, and the standard deviation of height differences is lower for

the UCL algorithm in both instances (Figure 5.5). The GSFC algorithm appears to produce negatively biased SSH estimates (dark-blue grid cells) in regions of thin, first year ice, particularly in the Fram Strait, the Greenland Sea and the Barents Sea (Figure 5.4). These large negative differences (~ -20 to -40 cm) in SLA estimates are possibly due to the inclusion of saturated echoes which would lower the true sea surface elevation estimates.

Figure 5.4 illustrates that there is a positive sea surface height bias associated with the L2b campaign and the distributions of SLA difference in Figure 5.2 are also positively skewed. The ICESat SLA estimates are on average ~ 10 cm higher than the ENVISAT SLA for the same period and the bias is apparent for all three algorithms.

The ICESat SLA estimates for the L3b campaign appear to be negatively biased with respect to the ENVISAT SLA estimates. This negative bias is apparent for all three algorithms (distributions in Figure 5.5 are negatively skewed) and this campaign is the only one where the UCL algorithm has a marginally higher standard deviation of SLA differences than the GSFC algorithm (Table 5.1).

Finally as one would expect, in the case of the large lead algorithm, we obtain more data points during the autumn just after sea ice minimum (e.g. L3a), than we do in the spring at sea ice maximum (e.g. L1). This is illustrated by a lower number of filled grid cells in the maps pertaining to the large lead algorithm results in Figure 5.4.

5.4.2 Short-term Variations in SLA in the Arctic Ocean

We investigate the magnitude of the time-variant component of the SLA by analysing measurements over 3-day periods. We calculated ENVISAT SLA for the period 4th Oct – 18th Nov 2003 (corresponding to the ICESat L2a campaign) over the ice-covered regions of the Arctic Ocean and divided the data into 3-day intervals. The results are plotted in Figure 5.6.

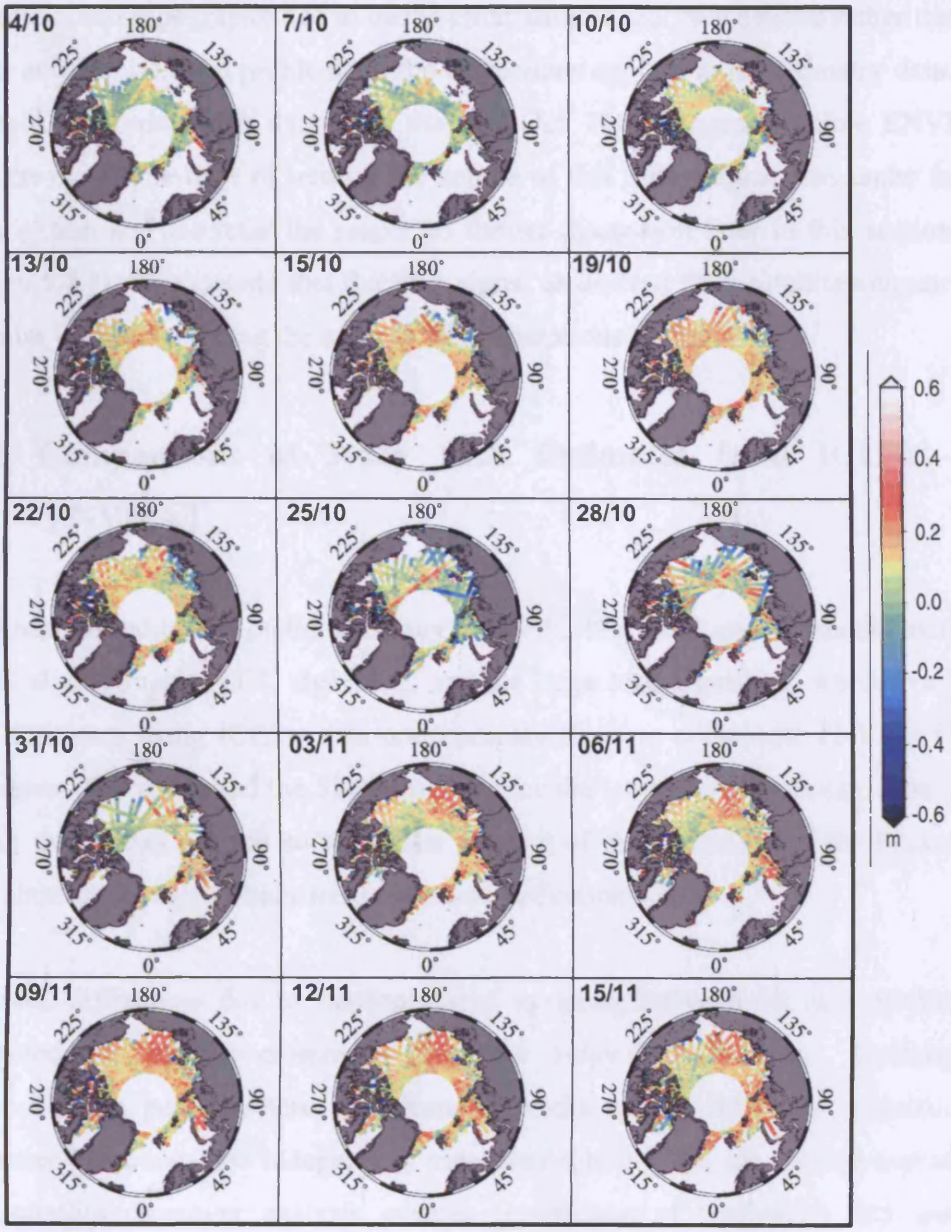

Figure 5.6 Mean 3-day ENVISAT SLA for the period 04 Oct – 15 Nov 2003. The dates given in each panel indicate the start date of each 3-day observation period.

5.4.2.1 Key Results

The 3-day SLA estimates reflect the variations of the sea surface over a period of ~1 month. Figure 5.6 indicates that the sea surface topography signal as measured by satellite altimetry varies substantially (by up to 10 cm) during the L2a campaign. The magnitude of the SLA variability over such short time-scales was unexpected and we believe it unlikely that the signal accurately represents the time-variant component of

dynamic ocean topography due to ocean circulation alone. We believe rather that this signal may be linked to problems in the corrections applied to the altimetry data. For example, the 3-day SLA data from the 25th Oct. 2003 suggest possible ENVISAT orbit error. At the time of writing the source of this 3-day signal was under further investigation and we refer the reader to further discussion later in this section (see Section 5.4.4). We assume that the SLA signal as derived from satellite altimetry has a similar variability during the other ICESat operations periods.

5.4.3 Comparisons of 3-day SLA Estimates from ICESat and ENVISAT

To obtain an indication of the accuracy of the ICESat SSH measurements using the GSFC algorithm, the UCL algorithm, and the large lead algorithm, we derive 3-day SLA estimates using ICESat data and compare these to coincident ENVISAT SLA estimates. We computed the SLA estimates for the ice-covered regions of the Arctic Ocean over 3-day periods so as to take account of the variability of the SLA signal over short time-scales which were discussed in Section 5.4.2.

To avoid differences due to varying spatial sampling between the two satellites we computed dual-satellite crossovers using the 3-day SLA datasets. Dual-satellite crossovers are points where the altimeter tracks of two satellites coincide. At crossover locations, two independent measurements of SSH are therefore available. Dual-satellite crossover analysis ensures comparison of temporally and spatially coincident data from two satellite datasets. Crossover height differences were calculated in a similar manner to the single-satellite crossovers (see Section 5.3) but with the crossover height difference calculated ICESat SLA minus ENVISAT SLA.

To demonstrate the dual satellite crossover analysis an example is plotted in Figure 5.7; the results for the L2a ICESat SLA (UCL algorithm) minus ENVISAT SLA are shown. Overall during this campaign there is excellent agreement between the radar altimetric and laser altimetric estimates of sea surface height over 3-day periods; the crossover height differences are typically ~ ±5 cm. However some larger crossover height differences of ~ ±15 cm were recorded on occasion. The distributions of

crossover height differences were also calculated; the distributions for L2a ICESat SLA (UCL algorithm) minus ENVISAT SLA are plotted in Figure 5.8.

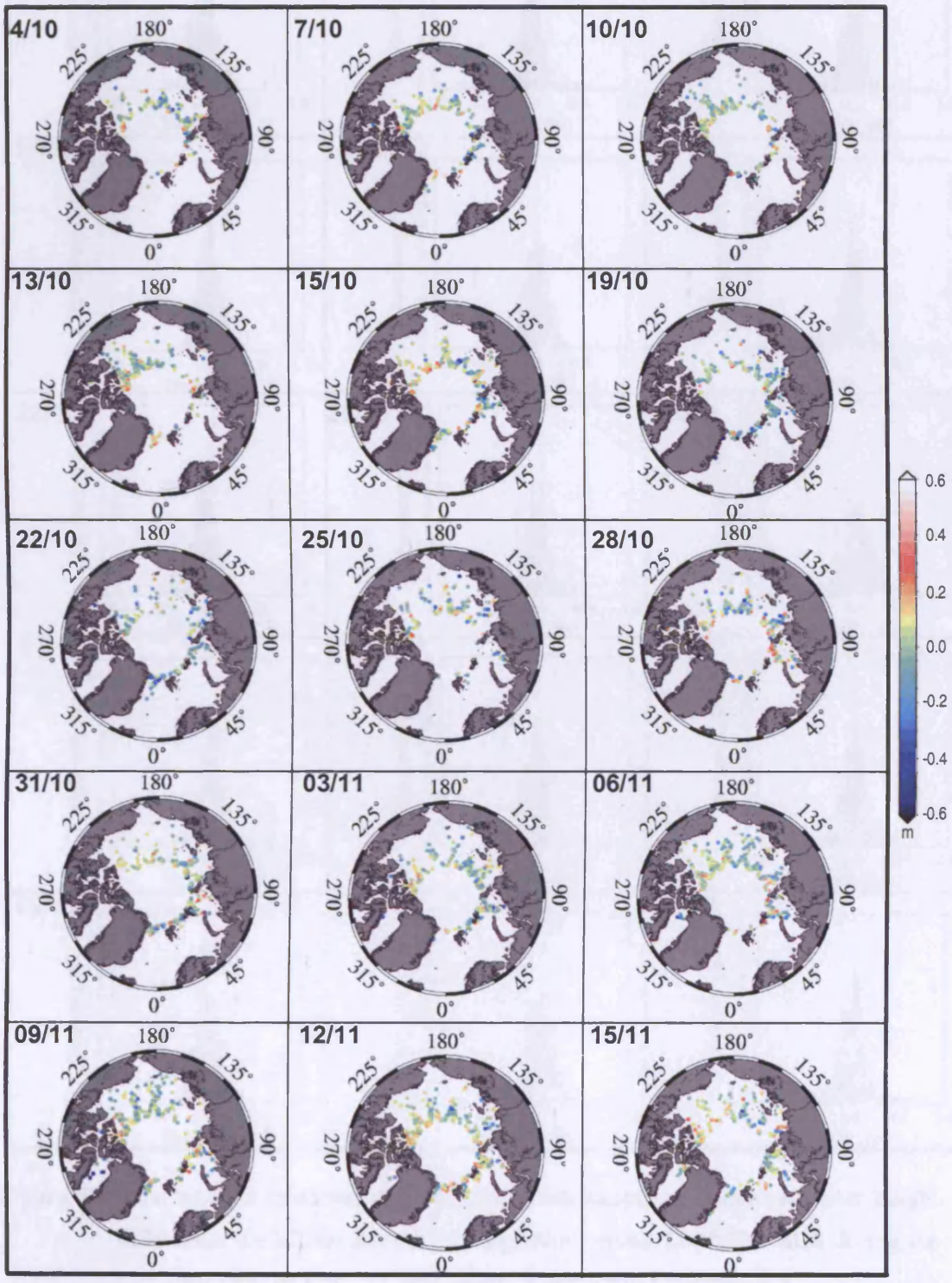

Figure 5.7 Dual satellite crossovers. 3-day crossover height differences for ICESat SLA (UCL Algorithm) minus ENVISAT SLA during the L2a campaign (04 Oct – 15 Nov 2003). Labelling as for Figure 5.3.

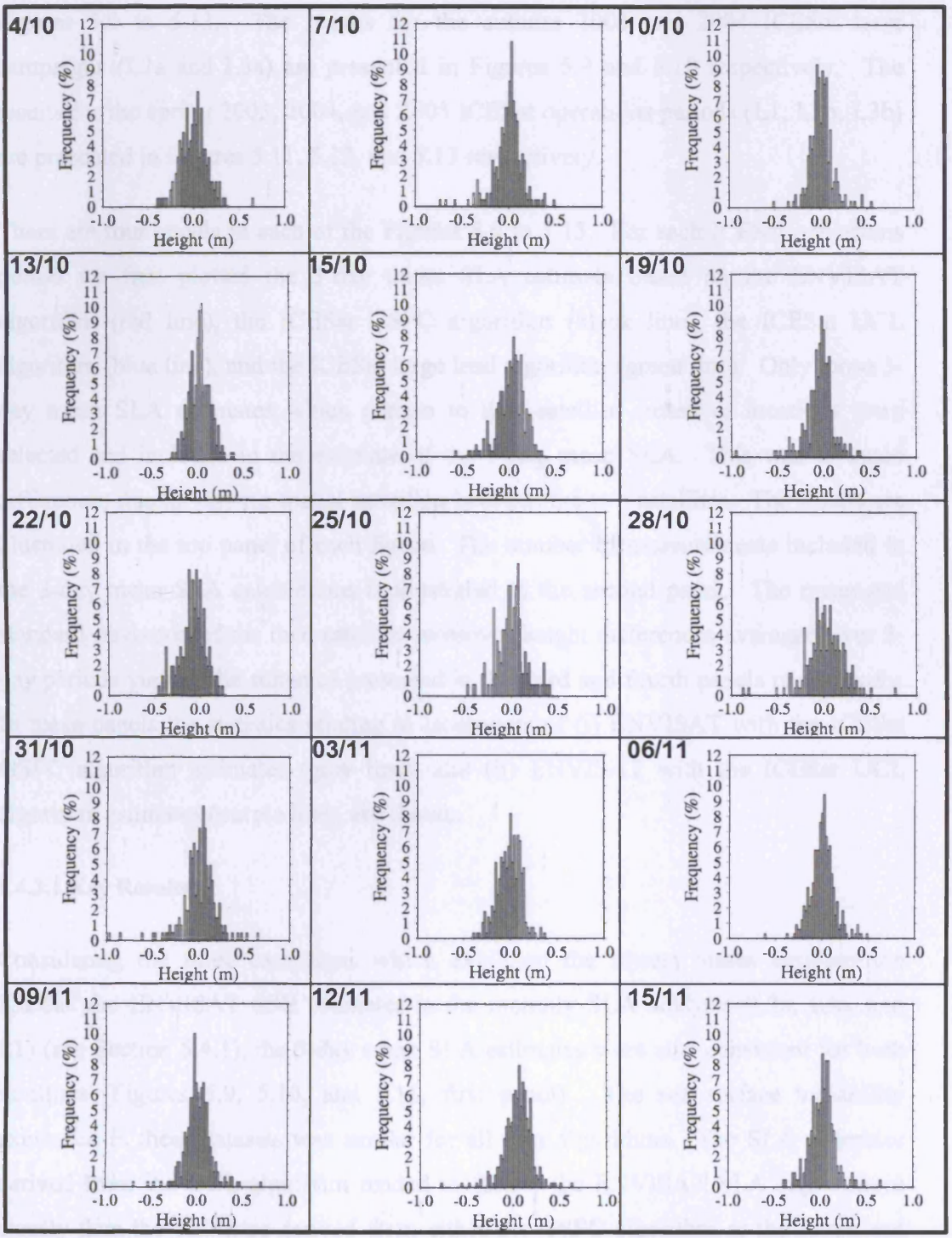

Figure 5.8 Dual satellite crossover distributions. Distributions of 3-day crossover height differences for ICESat SLA (UCL Algorithm) minus ENVISAT SLA during the L2a campaign (04 Oct – 15 Nov 2003). Labelling as for Figure 5.3.

Dual-satellite crossovers were computed for each of the five ICESat laser campaigns based on sets of 3-day SLA estimates. The results of this analysis are summarised in

Figures 5.9 to 5.13. The results for the autumn 2003 and 2004 ICESat laser campaigns (L2a and L3a) are presented in Figures 5.9 and 5.10 respectively. The results for the spring 2003, 2004, and 2005 ICESat operations periods (L1, L2b, L3b) are presented in Figures 5.11, 5.12, and 5.13 respectively.

There are four panels in each of the Figures 5.9 to 5.13. For each ICESat operations period we first plotted the 3-day mean SLA estimate based on the ENVISAT algorithm (red line), the ICESat GSFC algorithm (black line), the ICESat UCL algorithm (blue line), and the ICESat large lead algorithm (green line). Only those 3-day mean SLA estimates which pertain to dual-satellite crossover locations were selected and included in the estimate of the 3-day mean SLA. This was to avoid differences due to varying spatial sampling between the two satellites. The results are illustrated in the top panel of each figure. The number of measurements included in the 3-day mean SLA calculations is illustrated in the second panel. The mean and standard deviation of the dual satellite crossover height differences averaged over 3-day periods yielded the statistics presented in the third and fourth panels respectively. In these panels the statistics relating to crossovers of (i) ENVISAT with the ICESat GSFC algorithm estimates (grey line), and (ii) ENVISAT with the ICESat UCL algorithm estimates (purple line), are shown.

5.4.3.1 Key Results

Considering the three campaigns which exhibited the lowest biases between the ICESat and ENVISAT SSH estimates in the monthly SLA analysis (L2a, L3a, and L1) (see Section 5.4.1), the 3-day mean SLA estimates were also consistent for both satellites (Figures 5.9, 5.10, and 5.11, first panel). The sea surface variability expressed in these datasets was similar for all four algorithms. The SLA estimates derived from the UCL algorithm tended to follow the ENVISAT SLA signal more closely than the estimates derived from either the GSFC algorithm or the large lead algorithm. Biases between the ICESat and ENVISAT SLA estimates were low with dual satellite crossover differences of ~ 5 - 10 cm (Figures 5.9, 5.10, and 5.11, third panel). The number of measurements included in the 3-day mean calculations for the large lead algorithm was low (< 50). Hence the estimates of 3-day mean SLA derived using the large lead algorithm tended to be noisier than the SLA estimates derived from the other three algorithms.

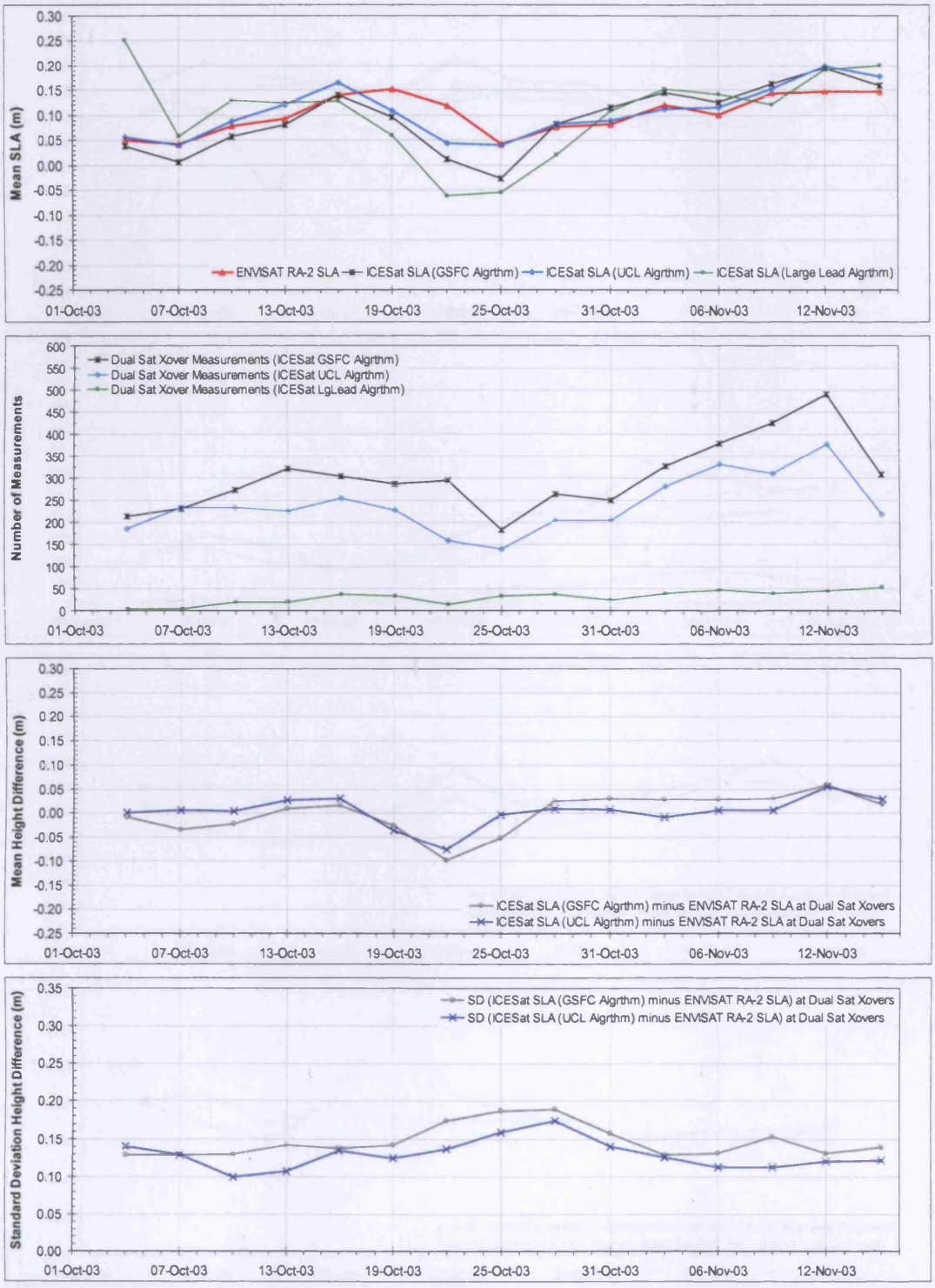

Figure 5.9 L2a campaign 3-day SLA dual-satellite crossover statistics. (First panel) 3-day mean SLA at dual-satellite crossover locations. (Second panel) Number of measurements included in the 3-day mean SLA calculations. (Third panel) 3-day mean crossover height difference (ICESat - ENVISAT) at dual-satellite crossover locations. (Fourth panel) Standard deviation of dual-satellite crossover height differences for each 3-day period.

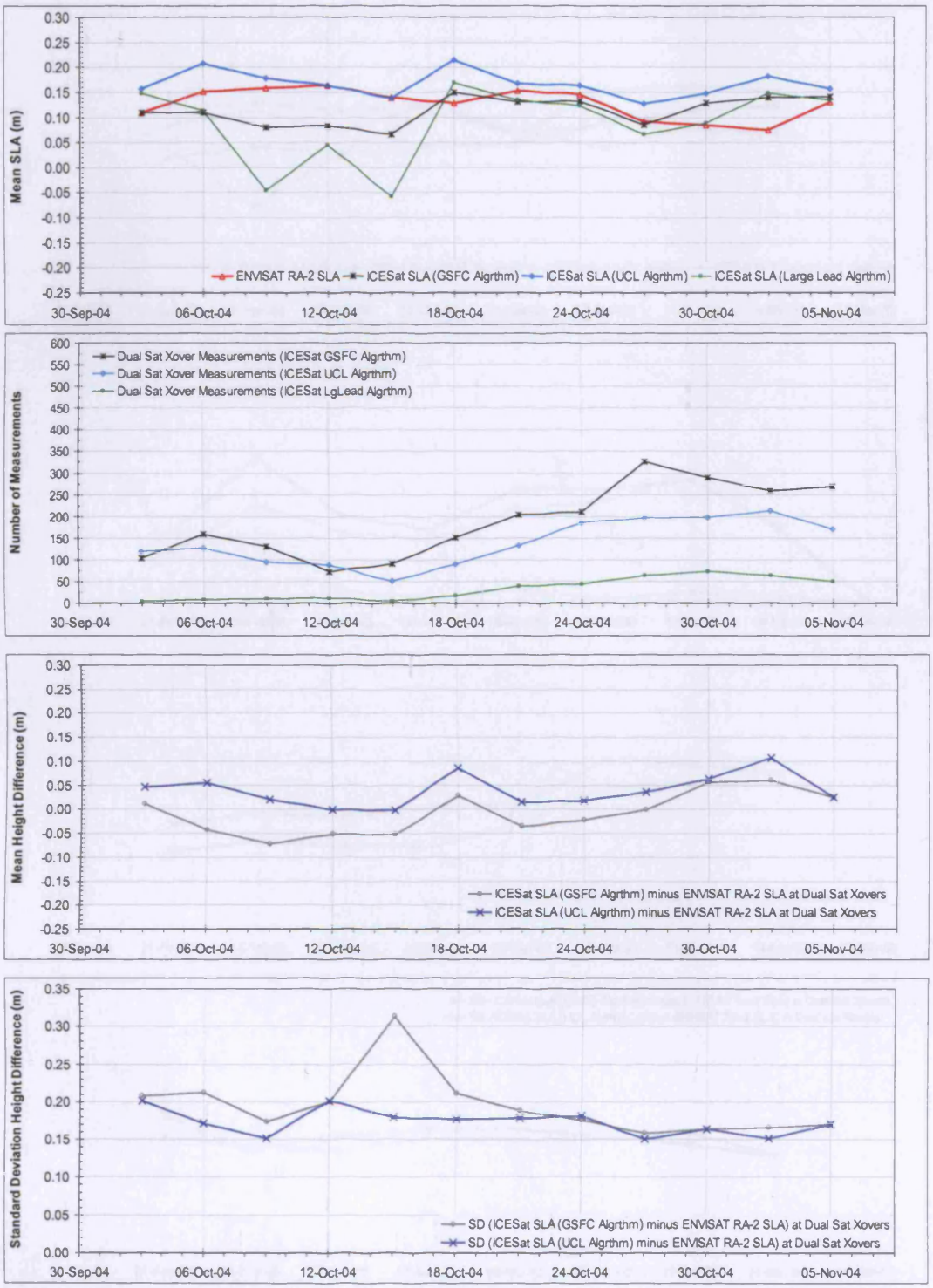

Figure 5.10 L3a campaign 3-day SLA dual-satellite crossover statistics. (First panel) 3-day mean SLA at dual-satellite crossover locations. (Second panel) Number of measurements included in the 3-day mean SLA calculations. (Third panel) 3-day mean crossover height difference (ICESat - ENVISAT) at dual-satellite crossover locations. (Fourth panel) Standard deviation of dual-satellite crossover height differences for each 3-day period.

Figure 5.11 L1 campaign 3-day SLA dual-satellite crossover statistics. (First panel) 3-day mean SLA at dual-satellite crossover locations. (Second panel) Number of measurements included in the 3-day mean SLA calculations. (Third panel) 3-day mean crossover height difference (ICESat - ENVISAT) at dual-satellite crossover locations. (Fourth panel) Standard deviation of dual-satellite crossover height differences for each 3-day period.

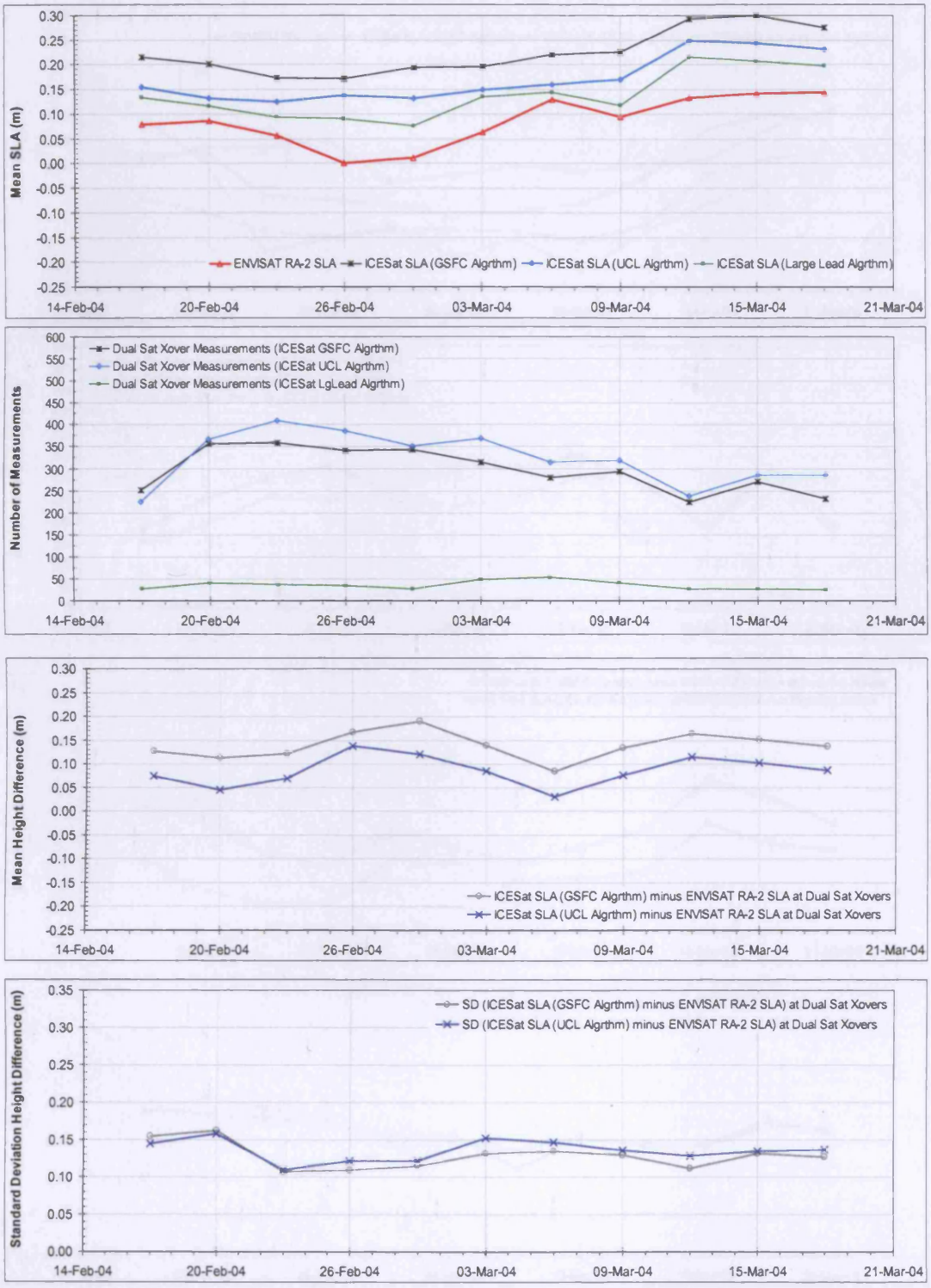

Figure 5.12 L2b campaign 3-day SLA dual-satellite crossover statistics. (First panel) 3-day mean SLA at dual-satellite crossover locations. (Second panel) Number of measurements included in the 3-day mean SLA calculations. (Third panel) 3-day mean crossover height difference (ICESat - ENVISAT) at dual-satellite crossover locations. (Fourth panel) Standard deviation of dual-satellite crossover height differences for each 3-day period.

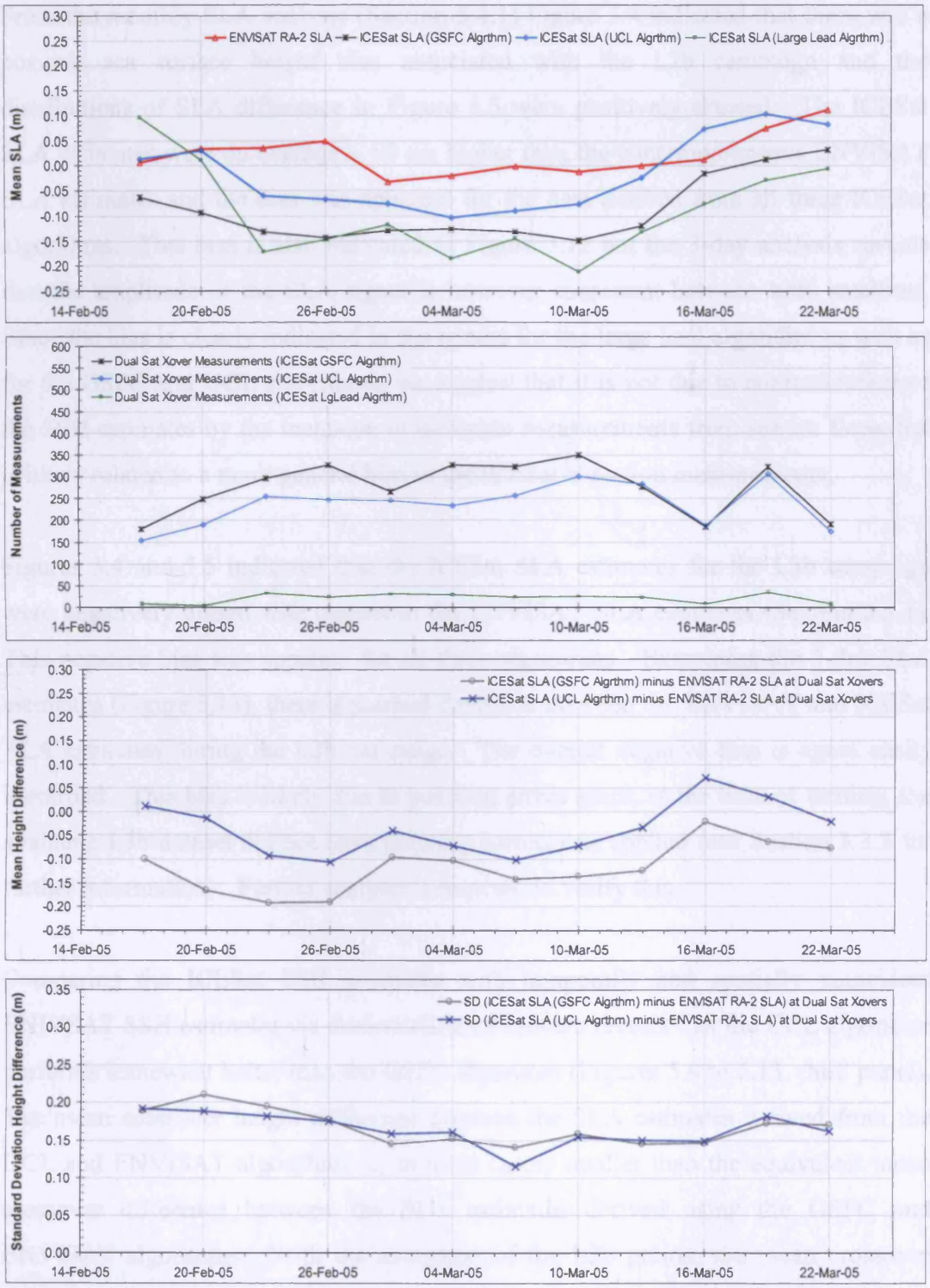

Figure 5.13 L3b campaign 3-day SLA dual-satellite crossover statistics. (First panel) 3-day mean SLA at dual-satellite crossover locations. (Second panel) Number of measurements included in the 3-day mean SLA calculations. (Third panel) 3-day mean crossover height difference (ICESat - ENVISAT) at dual-satellite crossover locations. (Fourth panel) Standard deviation of dual-satellite crossover height differences for each 3-day period.

From the monthly SLA analysis (Section 5.4.1) Figure 5.4 indicated that there was a positive sea surface height bias associated with the L2b campaign and the distributions of SLA difference in Figure 5.5 were positively skewed. The ICESat SLA estimates were on average ~ 10 cm higher than the contemporaneous ENVISAT SLA estimates and the bias was apparent for the data derived from all three ICESat algorithms. This bias is also indicated in Figure 5.12 but the 3-day analysis reveals that the amplitude of the SLA signal is however consistent between both satellites. Since the bias is clearly indicated in the results for the large lead algorithm as well as for the GSFC and UCL algorithms, we suggest that it is not due to contamination of the SSH estimates by the inclusion of elevation measurements from sea ice floes, but is likely related to a more general bias in the ICESat elevation measurements.

Figures 5.4 and 5.5 indicated that the ICESat SLA estimates for the L3b campaign were negatively biased with respect to the ENVISAT SLA estimates (Section 5.2.1). This negative bias was apparent for all three algorithms. Examining the 3-day SLA estimates (Figure 5.13), there is marked deviation between the ENVISAT and ICESat SLA estimates during the L3b campaign. The overall negative bias is again easily identified. This bias is likely due to pointing errors since, at the time of writing, the available L3b dataset did not have pointing corrections applied (see Section 3.3.2 for further information). Further analysis is required to verify this.

Comparing the ICESat SSH estimates with temporally and spatially coincident ENIVSAT SSH estimates via dual-satellite crossovers reveals that the UCL algorithm performs somewhat better than the GSFC algorithm (Figures 5.9 to 5.13, third panel). The mean crossover height difference between the SLA estimates derived from the UCL and ENVISAT algorithms is, in most cases, smaller than the equivalent mean crossover difference between the SLA estimates derived using the GSFC and ENVISAT algorithms. With the exception of the L2b period, the mean crossover differences based on the GSFC algorithm are negatively biased with respect to the UCL algorithm data. This indicates that the GSFC algorithm SSH estimates are lower than the equivalent measurements derived using the UCL algorithm. This is further evidence that the GSFC algorithm acts to include saturated echoes which effectively lowers the sea surface height estimates below their true level.

The standard deviation of crossover height differences is lower for the UCL algorithm comparisons than for the GSFC algorithm comparisons during the autumn campaigns (fourth panel, Figures 5.9 and 5.10). During the spring campaigns (fourth panel, Figures 5.11 to 5.13) the standard deviation results for both algorithms are not markedly different. This suggests that the UCL algorithm performs better than the GSFC algorithm during the autumn season, but the algorithms produce similar SLA estimates during the spring campaigns.

Using the dual-satellite crossover analysis, we can identify time periods when crossover height differences are small (i.e. between ±3 cm) and the SSH estimates from ICESat and ENVISAT are therefore directly comparable. For example, during the periods 4th – 18th Oct 2003, and 25th Oct – 11th Nov 2003, the mean crossover height difference between the ICESat UCL algorithm data and the ENVISAT data is close to 0 cm (Figure 5.9, third panel). Other time periods when mean dual-satellite crossover differences are constrained to ±3 cm are 9th - 15th Oct 2004 and 21st - 26th Oct 2004, during the L3a campaign (Figure 5.10, third panel), and 21st Feb – 7th Mar 2003, during the L1 campaign (Figure 5.11, third panel). During these time periods, the SSH estimates are consistent between ICESat and ENVISAT, suggesting that comparisons of geophysical data such as sea ice freeboard should be possible. Furthermore since we have identified periods during the autumn 2003 and 2004 campaigns as well as a period during spring 2003, we should be able to detect interannual and seasonal variability in sea ice freeboard. This opportunity is explored further in Chapter 7.

5.4.4 Discussion

There are some cases of large deviations in dual satellite crossover differences (e.g. 19th – 22nd Oct 2003, Figure 5.9, third panel) where the data derived either from the ICESat algorithm, or the ENVISAT data, or both, fail to characterise the true sea surface height. Since the atmospheric corrections applied to both satellite datasets are consistent, we explored the possibility that the deviation was due to differences in the tidal corrections between the datasets. The ocean tide correction applied to the ICESat data is based on the GOT99.2 tidal model [*Padman and Fricker*, 2005], while

the ENVISAT tidal corrections use the FES2004 ocean tide model (*S. Baker*, personal communication).

Figure 5.14 illustrates the 3-day mean ocean tide corrections which were applied to the ICESat and ENVISAT data during the L2a campaign. In general, the tidal corrections appear consistent between the two satellite datasets although some small deviations are evident. The periods of the largest deviations in the mean tidal correction, for example on the 13th Oct 2003, do not however coincide with the largest dual satellite crossover differences on the 19th Oct, 22nd Oct, and 12th Nov 2003 (Figure 5.9). Furthermore the amplitude of the largest differences between the tidal corrections is ~ 5 cm, which is lower than the amplitude of the largest dual-satellite crossover height differences at ~ 8 – 10 cm.

Before eliminating differences in tidal corrections as a source of the deviations in SSH estimates between ICESat and ENVISAT, a more thorough investigation is necessary. Ideally the tidal corrections for one of the altimetric datasets should be reprocessed using tidal corrections which are consistent with the other dataset. With this in mind, we propose that the ENVISAT ocean tide corrections be recalculated using the GOT99.2 tide model. At the time of writing such data was not available for analysis.

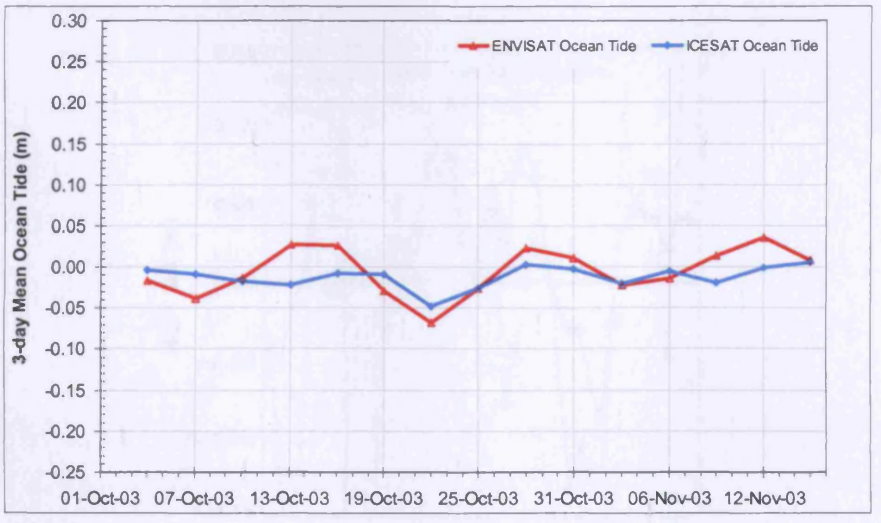

Figure 5.14 L2a campaign 3-day mean ocean tide correction applied to ICESat data (blue line) and to ENVISAT data (red). Corrections were averaged over the ice-covered regions of the Arctic Ocean.

Deviations between the ICESat and ENVISAT SSH estimates may also be due in part to time-varying geophysical effects. It is conceivable that the presence of thick clouds could adversely affect the accuracy of the laser altimetric data, while heavy precipitation could influence the accuracy of the radar data. Furthermore the effect of wind forcing on the distribution and size of leads within the ice pack should be considered, since this will influence the number of sea surface returns the algorithms can detect and hence the accuracy of the SSH estimates. Further analysis is required to investigate these geophysical effects and their influence on the data.

The possibility also exists that the MOG2D-G inverse barometer (IB) correction does not fully account for atmospheric pressure loading and/or wind effects. If this were true the altimetric SSH estimates would not be adequately corrected for atmospheric effects. The 3-day dual-satellite crossover analysis would therefore be compromised. This idea is currently being explored in collaboration with colleagues at CPOM. A positive correlation between SLA and the IB correction has been identified. An example based on a comparison of the ENVISAT SLA estimates with the corresponding IB correction is illustrated in Figure 5.15. Furthermore analysis of the various geophysical corrections applied to the altimetry data (e.g. tidal corrections, wet and dry tropospheric corrections, etc.) shows that the SLA signal is most significantly influenced by the IB correction (*A. Ridout*, personal communication).

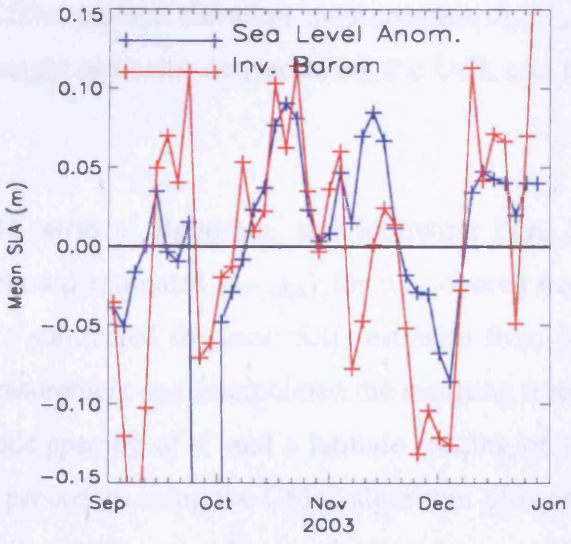

Figure 5.15 Comparison of ENVISAT SLA and the MOG2D-G inverse barometer correction. 3-day averages were calculated for both variables and results for the Sep – Dec 2003 period are illustrated. Figure courtesy of *A. Ridout*.

5.5 Comparison of Arctic Freeboard using the GSFC and UCL algorithms

An alternative method to the analysis presented in Section 5.4 to assess the ability of the GSFC and UCL algorithms to estimate SSH, is via the comparison of freeboard estimates. Derivation of sea ice freeboard using satellite altimetry is possible if estimates of both sea ice and sea surface topography are known (Eqn. 2.8). Laser altimetric freeboard measurements define the snow freeboard (h_{sf}), or the height of the air/snow interface of a sea ice floe above the water surface (i.e. comprising both the sea ice freeboard and any overlying snow).

Following Eqn. 2.8 we use ICESat surface elevation measurements over the Arctic Ocean in conjunction with along-track SSH measurements estimated using (i) the UCL algorithm and (ii) the GSFC algorithm, to derive two different estimates of snow freeboard, h_{sf}:

$$h_{sf\_UCL} = h_{alt} - h_{ssh\_LA\_UCL} \tag{5.2}$$

$$h_{sf\_GSFC} = h_{alt} - h_{ssh\_LA\_GSFC} \tag{5.3}$$

where, h_{alt} is the ICESat surface elevation measurement, $h_{ssh\_LA\_UCL}$ and $h_{ssh\_LA\_GSFC}$ are the sea surface height estimates derived using the UCL and the GSFC algorithms respectively.

Using the UCL SSH retrieval algorithm, and following Eqn. 5.2, we calculated a dataset of snow freeboard estimates (h_{sf_UCL}) for ice-covered ocean regions between 65°N and 86°N. We subtracted the local SSH estimate from its associated ICESat surface elevation measurement and interpolated the resulting freeboard estimates onto a grid with a longitude spacing of 4° and a latitude spacing of 1°. We subsequently carried out the same procedure using the GSFC algorithm SSH estimates (Eqn. 5.3) to generate a second, alternative map of snow freeboard (h_{sf_GSFC}). This analysis was performed for the autumn 2003 and 2004 laser campaigns as well as the spring 2004 and 2005 campaigns.

In the absence of Arctic-wide *in situ* estimates of sea ice freeboard that coincide with the dates of acquisition of ICESat data, against which we could compare the altimetry freeboard estimates, we developed a method to investigate the internal consistency of each snow freeboard dataset. For each of the four laser operations periods we split the dataset in half and defined two observation periods. The dates of these observation periods are given in Table 5.2. We expect ice advection and ice growth to be the sources of differences in freeboard estimates throughout a particular observation period. Nevertheless, since we are analysing data which has been interpolated onto 4° by 1° grid, we expect a strong relationship between the snow freeboard results from the first half of a given laser campaign with those from the second half of the campaign. Indeed analysis carried out by *Perovich et al.* [2003] of changes in ice thickness during the SHEBA study suggest that we should expect growth of approximately 12 cm or less during our selected laser operations periods[23].

Laser Campaign	Observation Period	
	I	II
L2A	04 Oct 13:38 - 27 Oct 02:52 2003	27 Oct 02:53 - 18 Nov 22:34 2003
L2B	17 Feb 21:18 - 04 Mar 23:55 2004	05 Mar 01:31 - 21 Mar 18:38 2004
L3A	03 Oct 21:53 - 21 Oct 12:00 2004	21 Oct 13:32 - 08 Nov 13:15 2004
L3B	17 Feb 20:33 - 06 Mar 10:26 2005	06 Mar 12:02 - 24 Mar 16:35 2005

Table 5.2 Dates of observation periods I and II during four ICESat laser campaigns.

Using both the h_{sf_UCL} and h_{sf_GSFC} snow freeboard estimates, we compared results from period I with those from period II checking for consistency between estimates. The results are illustrated in Figures 5.16 to 5.23. In each figure there are three panels: the left panel describes the snow freeboard estimates averaged over observation period I with the freeboard map at top and the distribution of freeboard heights at bottom, similarly the right panel describes the estimates pertaining to observation period II, while the bottom panel contains a scatter plot of freeboard estimates for observation period II versus freeboard estimates for period I. The black line in each scatter plot indicates the line of best fit through the data. The number of points in each scatter plot as well as the correlation coefficient (R^2) for a linear relationship of the form $y = ax + b$ are also shown in each scatter plot.

[23] Refer to Figure 5 in *Perovich et al.* [2003].

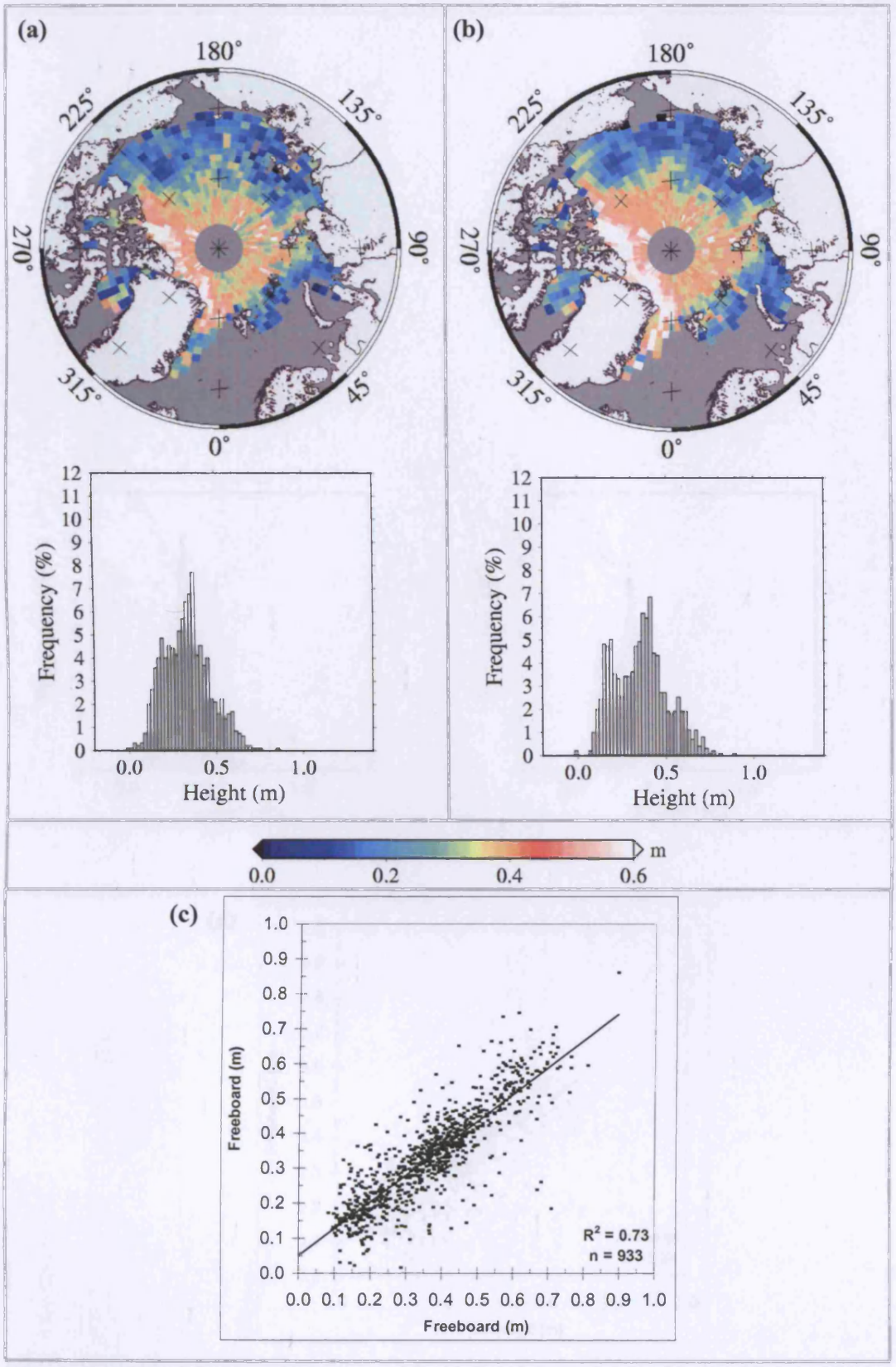

Figure 5.16 Snow freeboard, h_{sf_UCL}, during autumn 2003 derived from ICESat elevations measured with respect to the UCL algorithm SSH measurements for (a) observation period I and (b) observation period II. (c) Scatter plot of snow freeboard between 65°N and 86°N for period II (*x-axis*) versus period I (*y-axis*). See Table 5.2 for the dates of each observation period.

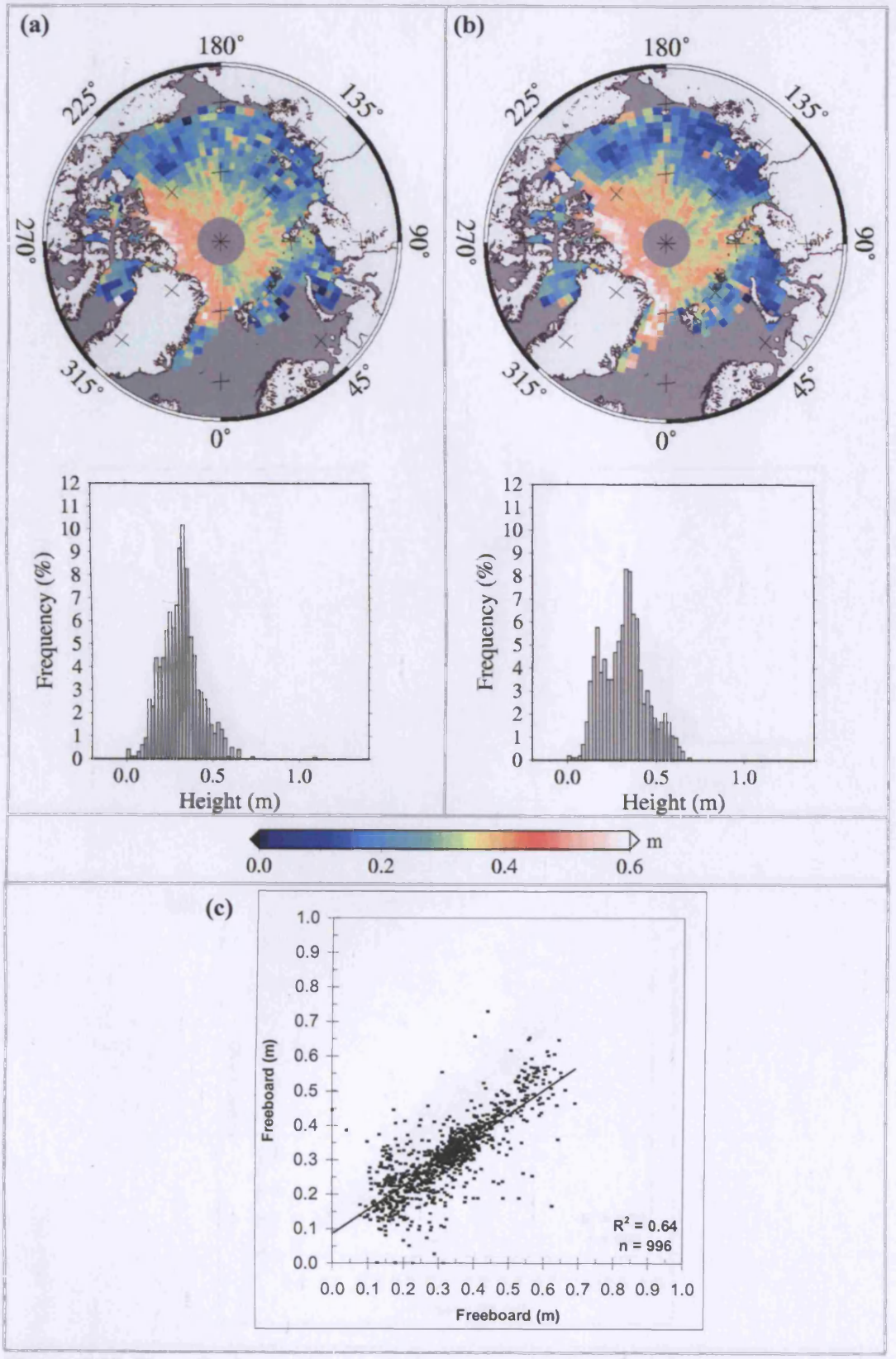

Figure 5.17 Snow freeboard, h_{sf_GSFC}, during autumn 2003 derived from ICESat elevations measured with respect to the GSFC algorithm SSH measurements. Labelling as for Figure 5.16.

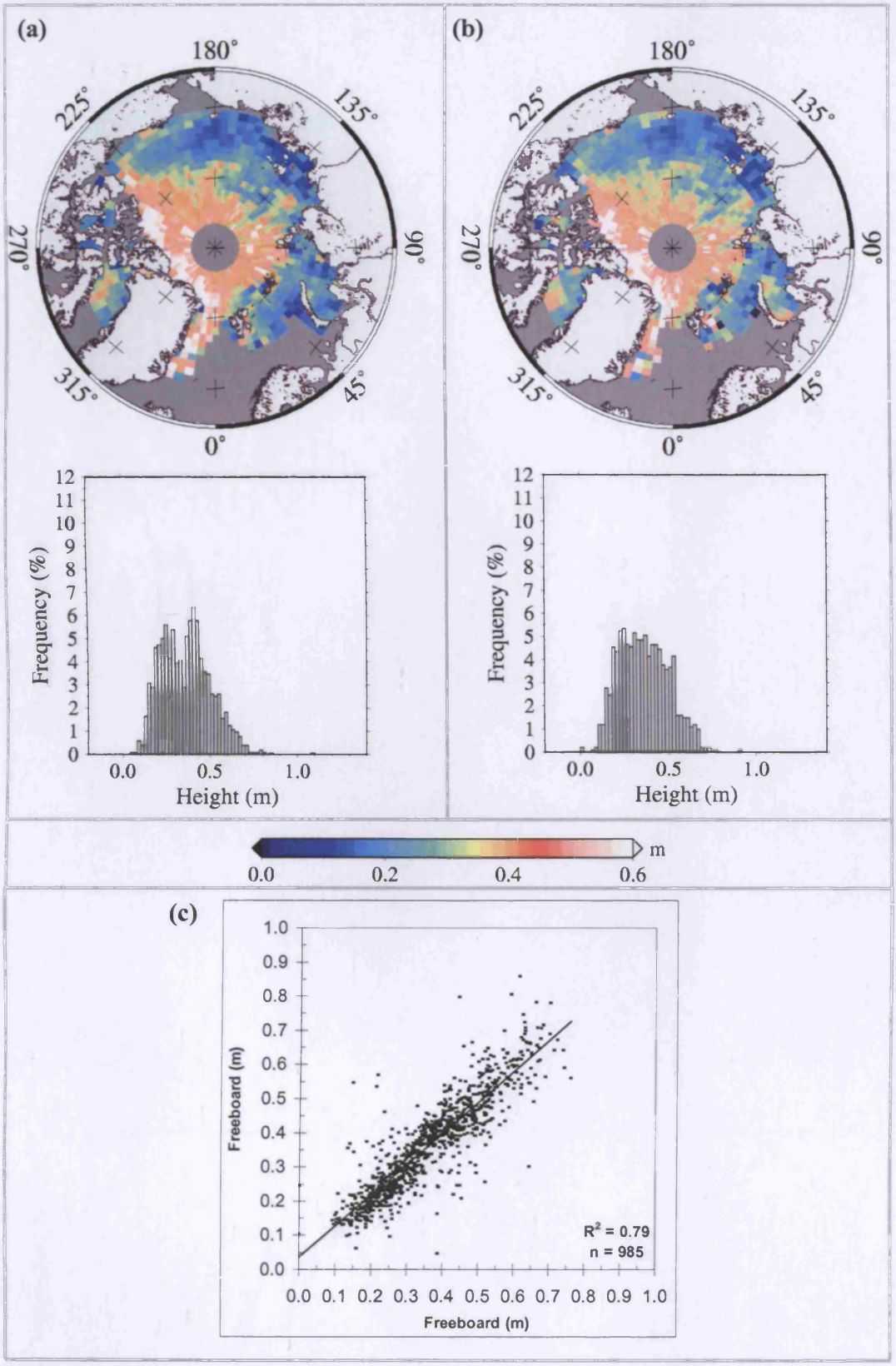

Figure 5.18 Snow freeboard, h_{sf_UCL}, during spring 2004 derived from ICESat elevations measured with respect to the UCL algorithm SSH measurements. Labelling as for Figure 5.16.

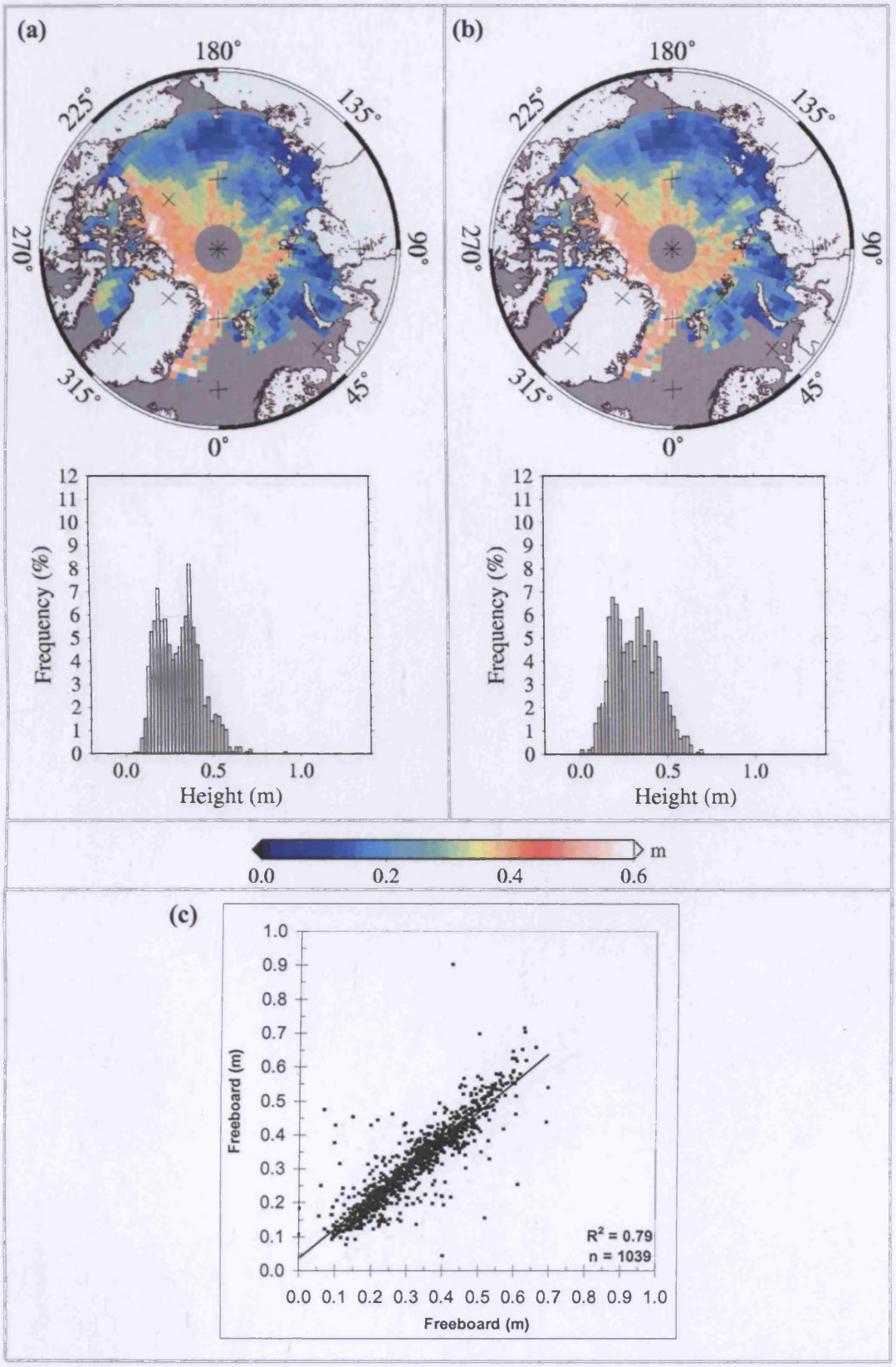

Figure 5.19 Snow freeboard, h_{sf_GSFC}, during spring 2004 derived from ICESat elevations measured with respect to the GSFC algorithm SSH measurements. Labelling as for Figure 5.16.

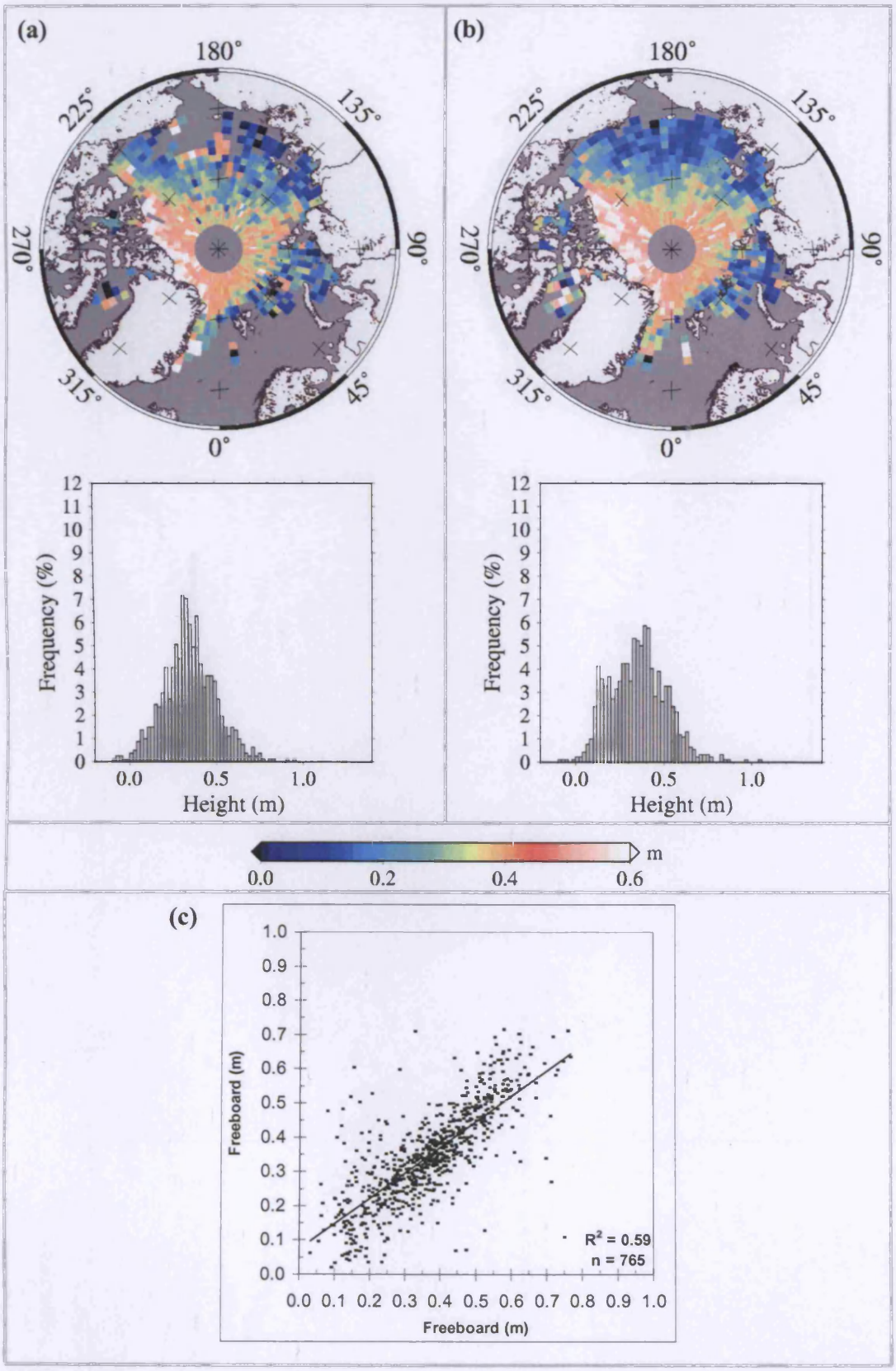

Figure 5.20 Snow freeboard, h_{sf_UCL}, during autumn 2004 derived from ICESat elevations measured with respect to the UCL algorithm SSH measurements. Labelling as for Figure 5.16.

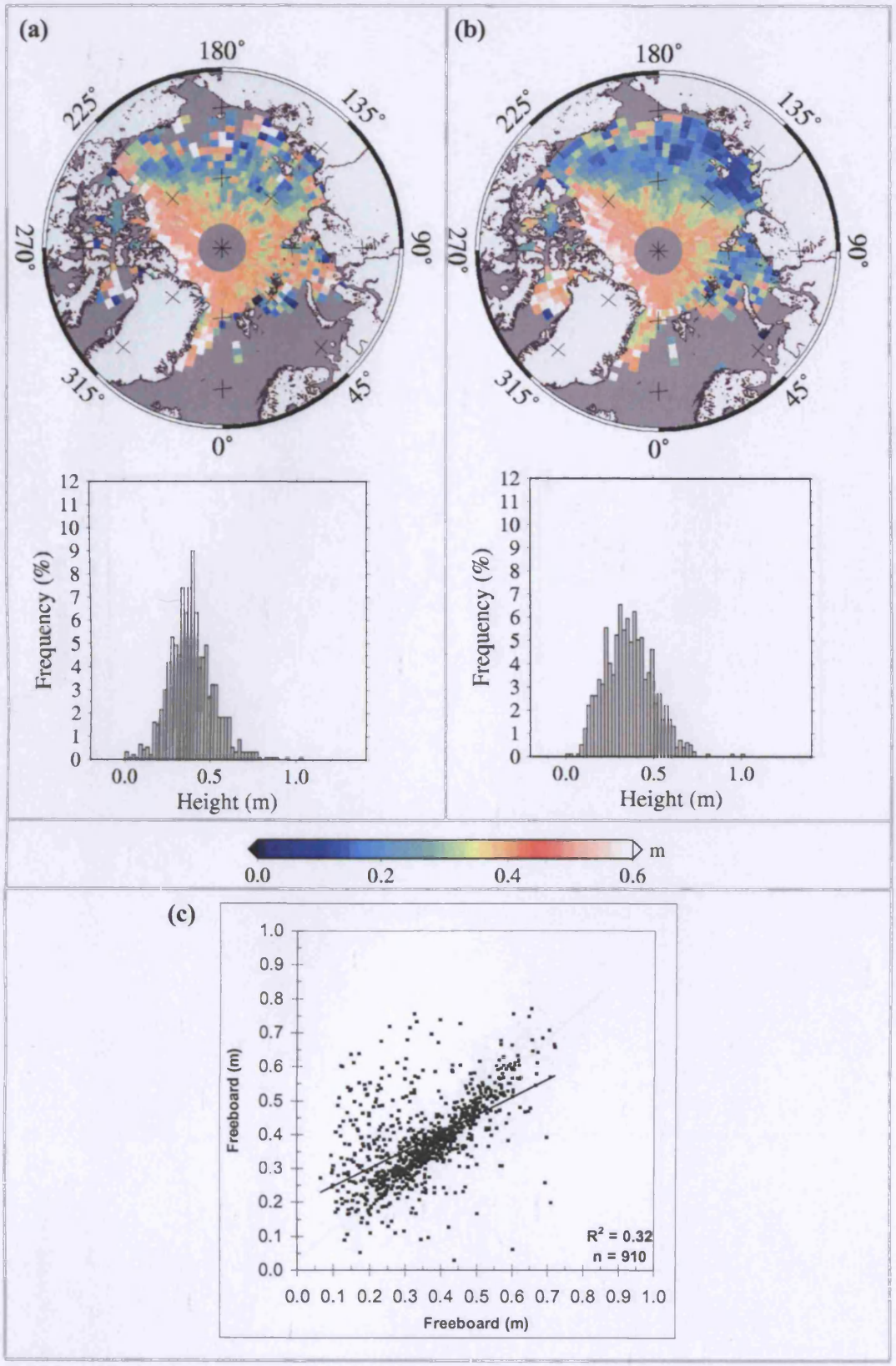

Figure 5.21 Snow freeboard, h_{sf_GSFC}, during autumn 2004 derived from ICESat elevations measured with respect to the GSFC algorithm SSH measurements. Labelling as for Figure 5.16.

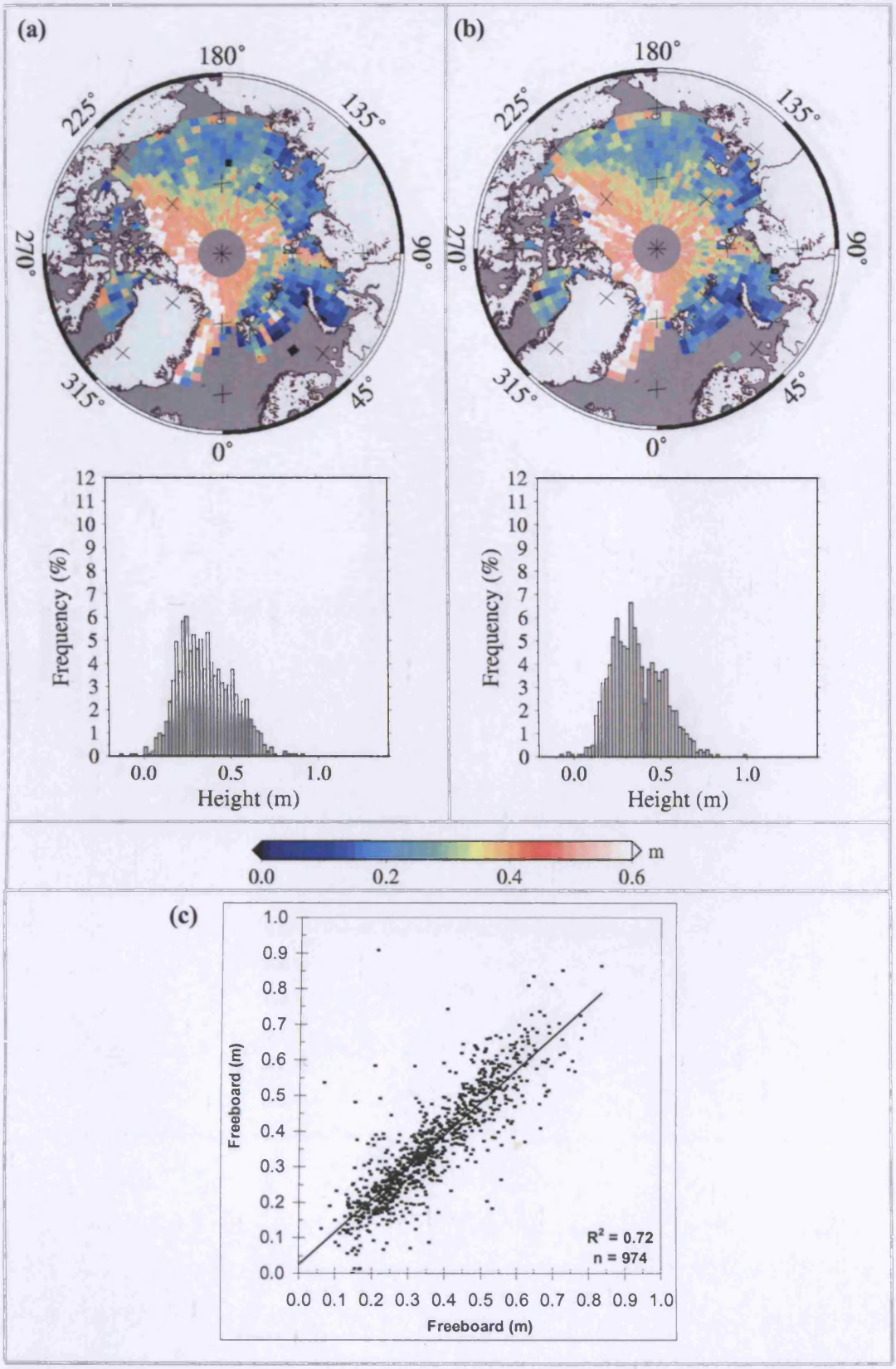

Figure 5.22 Snow freeboard, h_{sf_UCL}, during spring 2005 derived from ICESat elevations measured with respect to the UCL algorithm SSH measurements. Labelling as for Figure 5.16.

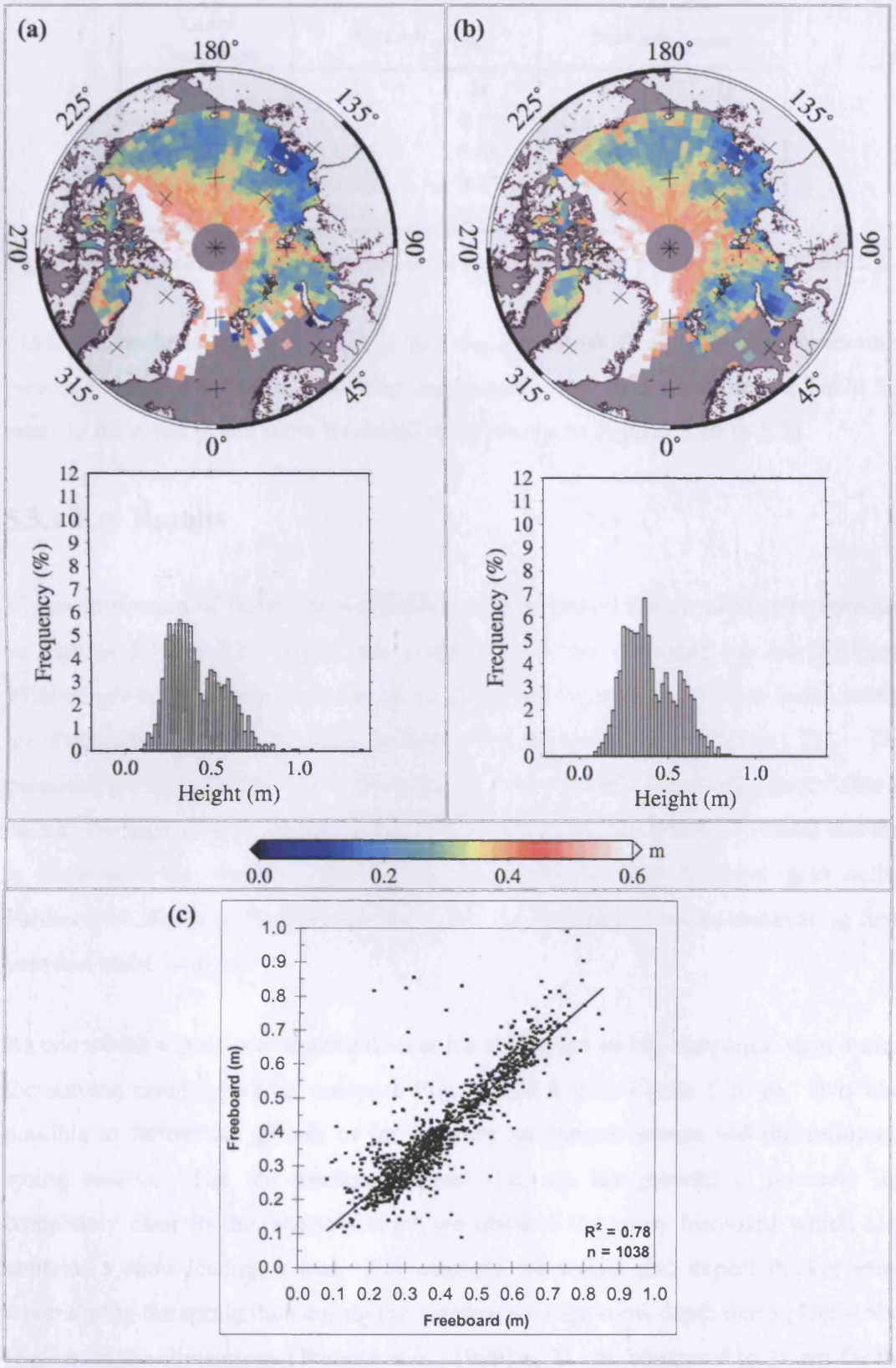

Figure 5.23 Snow freeboard, h_{sf_GSFC}, during spring 2005 derived from ICESat elevations measured with respect to the GSFC algorithm SSH measurements. Labelling as for Figure 5.16.

Laser Campaign	Mean h_{sf_UCL}		Mean h_{sf_GSFC}	
	I	II	I	II
L2A	0.33	0.37	0.31	0.33
L2B	0.36	0.36	0.31	0.31
L3A	0.35	0.37	0.39	0.36
L3B	0.35	0.37	0.40	0.40

Table 5.3 Mean snow freeboard derived for the eight observation periods given in Table 5.2.

Table 5.3 outlines the mean h_{sf_UCL} and h_{sf_GSFC} snow freeboards for observation periods I and II for four ICESat laser campaigns. The values outlined in Table 5.3 relate to the mean of the snow freeboard distributions in Figures 5.16 to 5.23.

5.5.1 Key Results

Visual inspection of the regional distribution of freeboard height estimates presented in Figures 5.16 to 5.23 shows that it agrees with the estimated sea ice thickness climatology based on submarine sonar profiles (see Figure 1.16) and the mean winter ice thickness as observed from satellite radar altimetry (see Figure 1.21). The perennial ice zone (region of multiyear ice in the high Arctic) is clearly identifiable in each of the figures as having thicker snow freeboard (red and white grid cells) and this is surrounded by thinner, first-year ice (depicted by blue or green grid cells). Furthermore the snow freeboard distributions are typically bi-modal delineating first-year and multi-year ice.

As one would expect, we observe thicker ice during the spring campaigns than during the autumn campaigns (e.g. compare Figure 5.22 b with Figure 5.20 b). It is also possible to follow the growth of ice between an autumn season and the following spring season. The ice freeboard signal (i.e. sea ice growth) is however not completely clear in this analysis since we observe the snow freeboard which also contains a snow-loading signal. For example we would also expect thicker snow cover during the spring than during the autumn; average snow depth during Oct – Nov is given in the climatology [*Warren et al.*, 1999] as 21 cm, compared to 31 cm for the average snow depth in Feb - Mar.

A comparison of snow freeboard estimates from observation period I with those from observation period II gives an indication of the consistency of the results. As noted earlier, we expect a strong relationship, and hence a high correlation, between the snow freeboard results from the first half of a given laser campaign with those from the second half of the campaign. Indeed the mean snow freeboards for observation period II are either equal to, or higher than, those associated with observation period I, representing overall growth of the ice pack throughout the period of analysis and/or accumulation of snow on sea ice surfaces (Table 5.3). The exception to this is the mean h_{sf_GSFC} estimate during the L3A laser campaign; we attribute a decrease in mean snow freeboard to inaccuracies in the retrieval process. There are likely to be some fluctuations in snow accumulation and ice growth during the two observation periods. However, since we compute the correlation coefficients for the h_{sf_UCL} and h_{sf_GSFC} estimates over the same observation periods, we account for such fluctuations since they would have equal effects on the correlation coefficients of both datasets.

This freeboard analysis reveals that for the autumn laser campaigns, the UCL SSH algorithm produced more consistent freeboard retrievals than the GSFC SSH algorithm. The correlation coefficients for autumn 2003 and 2004 were 0.73 and 0.59 respectively, for freeboards derived using the UCL algorithm, while they were 0.64 and 0.32 respectively, for freeboards derived using the GSFC algorithm.

During the spring periods there was strong correlation between estimates from the two observation periods with less scatter than during the autumn periods. The UCL and GSFC SSH algorithms produced equally consistent freeboard estimates: the correlation coefficients for spring 2004 and 2005 were 0.79 and 0.72 respectively for the h_{sf_UCL} freeboard estimates, and 0.79 and 0.78 respectively for the h_{sf_GSFC} freeboards. The mean snow freeboard for observation periods I and II also show good agreement (Table 5.3).

This result is consistent with one of the key findings of Section 5.4.3.1 where the dual-satellite crossover height differences between the SSH estimates from ENVISAT and the UCL algorithm were smaller than those between the SSH estimates from ENVISAT and the GSFC algorithm during the autumn campaigns. During the spring campaigns the UCL and the GSFC compared equally to the ENVISAT SSH estimates.

5.6 Conclusions

We have provided the first maps of comparisons between ICESat and ENVISAT estimates of the sea surface topography in the Earth's ice-covered polar regions. We presented our comparison of sea surface height estimates in terms of SLA differences, where SLA were calculated with respect to the long term MSS and extends to 81.5°N. We generated results for five ICESat laser operations periods and we compared monthly average SSH estimates from the UCL, GSFC, and large lead algorithms, which were described previously in Chapter 4. We derived 3-day Arctic-wide averages of SLA to investigate further the source of differences between the ICESat and ENVISAT SLA estimates. Comparisons of spatially and temporally coincident data, through crossover analysis, minimised differences due to varied sampling (as a result of different satellite orbit patterns) of the natural variability of the sea surface topography (i.e. the time-variant component of dynamic ocean topography).

As discussed in Section 3.3.2, we expected the L2a, L2b, and L3a datasets to contain the best quality elevation measurements as a consequence of the ground-segment processing. Indeed we found that the L2a SLA data compared best with coincident ENVISAT SLA, and the difference in SLA estimates was on the order of 1-2 cm for all three algorithms. Both the monthly and 3-day mean SLA signals were consistent between all algorithms. This suggests that the GSFC algorithm for determining SSH from ICESat altimetry over sea ice, which is based on the assumption that 2% of the winter sea ice pack contains areas of open water and leads, is suitable as a preliminary approach. The SLA estimates derived using the UCL algorithm were however closer to the ENVISAT estimates than those derived using the GSFC algorithm.

The L2b dataset contained a significant positive bias (~10 cm average bias) as compared to the ENVISAT measurements. This bias was apparent in the data derived from all three ICESat algorithms in both the monthly and 3-day analysis. In addition to the close agreement between the L2a data and the ENVISAT data, L1 and L3a SLA estimates also compared well to contemporaneous ENVISAT estimates. During the L3b campaign, ICESat SLA estimates were negatively biased with respect to the equivalent ENVISAT measurements.

We present a summary of our key findings:

- Based on the single-satellite crossover analysis, the ENVISAT SSH estimates were more self-consistent over 3-day periods than the ICESat SSH estimates. This suggests that the ENVISAT SSH retrievals are more accurate than contemporaneous ICESat measurements, and can therefore be used to validate the ICESat SSH estimates.

- We have compared retrievals based on ICESat SSH estimates derived using the UCL algorithm with those derived using the GSFC algorithm. During the autumn campaigns the UCL algorithm performs better than the GSFC algorithm, while during the spring campaigns the two algorithms produce very similar SSH estimates.

- During the autumn laser campaigns the snow freeboard retrievals based on the UCL algorithm SSH estimates had higher correlation coefficients than those based on the GSFC algorithm SSH estimates. The correlation coefficients associated with the spring-time snow freeboards using the two alternative ICESat SSH estimates were similar. These results verify the previous key finding.

- As predicted in Chapter 3, the L2a and L3a campaigns provide data which compares best to contemporaneous ENVISAT data. The L1 SSH data also compared well to the ENVISAT SSH measurements and the difference in monthly averaged SLA estimates was ≤ 5 cm.

- Estimates of 3-day mean SLA derived from all four methods (ENVISAT RA-2 algorithm, ICESat UCL algorithm, ICESat GSFC algorithm, and ICESat large lead algorithm) were consistent in the cases of the best available ICESat data (i.e. the L2a and L3a datasets).

- There remain systematic biases in the ICESat laser elevation data. Biases of up to ± 10 cm with respect to coincident ENVISAT data were recorded.

- There is a large variability in the SLA signal over short timescales, which can be up to ~ ±10 cm. We believe that there may be errors associated with this signal possibly as a result of problems in the corrections applied to the altimetry data and this finding therefore requires further investigation.

- Large dual-satellite crossover differences exist in all datasets, where one or both of the SSH estimates are incorrect. These differences could be due in part to errors in the SSH retrieval process (i.e. poor performance of one or both of the algorithms), errors in orbit corrections, and a time-dependent error in the retrieval process remains a possibility. Crossover differences may also be due to geophysical effects, for example due to (i) the application of inconsistent ocean tide corrections between the two satellite datasets, or (ii) remaining errors in the inverse barometer correction. Further investigation is required to explore these possibilities.

- We have successfully identified five periods in the datasets when dual-satellite crossover height differences are small (i.e. $\leq \pm 3$ cm). During these time periods, the SSH estimates are consistent between ICESat and ENVISAT, suggesting that comparisons of geophysical data such as sea ice freeboard should be possible.

The close agreement between the SSH estimates identified during five particular observation periods will enable us to cross-compare satellite laser and radar altimetric estimates of sea ice freeboard as well as allow us to investigate the seasonal and interannual variability in sea ice freeboard; we will explore this further in Chapter 7. In addition in Chapter 6, we will investigate the use of ICESat SSH measurements to map mean Arctic dynamic topography as well as gravity anomalies up to the limit of coverage of ICESat at 86°N.

6 Applications of ICESat Altimetry for Arctic Oceanography and Marine Geophysics

6.1 Introduction

In the previous two chapters we described methods for the retrieval of altimetric sea surface height measurements from ICESat data and provided an assessment of these measurements. In Chapter 6 we discuss how knowledge of sea surface height (SSH) can be exploited for oceanographic and geodetic applications. The work presented in Chapter 6 has been carried out in collaboration with Dr. D. McAdoo of the National Oceanographic and Atmospheric Administration (NOAA). In particular, work to derive the Arctic Ocean gravity field using ICESat SSH data (Section 6.3) was conducted exclusively by D. McAdoo. It is included here to demonstrate the usefulness of Arctic-Ocean ICESat SSH data for marine geophysics applications.

First we derive a mean sea surface (MSS) based on UCL algorithm estimates of SSH throughout five ICESat laser campaigns between 2003 and 2005. We discuss how the combination of this MSS with an accurate geoid model can be used to map the mean dynamic topography (MDT) of the Arctic Ocean. We compare our data with (i) equivalent data based on eight year's of ERS-2 SSH measurements (the ArcGICE MSS) and (ii) the Ocean Circulation and Climate Advanced Modelling (OCCAM) numerical model of MDT.

Second we investigate the use of ICESat SSH measurements to map marine gravity anomalies up to the limit of coverage of ICESat at 86°N. We compare the gravity field estimates from ICESat with those derived previously from ERS radar altimetry. We briefly discuss the new tectonic information provided by the ICESat gravity field above the limit of coverage of the ERS satellites, in the high Arctic (81.5°N to 86°N).

We demonstrate that although the ICESat MSS is preliminary in nature and should benefit from additional data from future laser operations periods, the potential exists to use satellite laser altimetry for geodetic and oceanographic investigations of the polar oceans.

6.2 Ocean Circulation Studies and Model Comparison

6.2.1 Extension of the Mean Sea Surface beyond 81.5°N

The inclination of ICESat at 94° extends the coverage of satellite altimeters in the Arctic beyond 81.5°N, to 86°N, for the first time (see Figure 1.22). The potential to derive an estimate of MSS topography above the limit of the ERS and ENVISAT satellites therefore exists.

We have generated a map of MSS height in the Arctic Ocean using estimates of sea surface topography derived from the UCL algorithm (see Section 4.4.2). The SSH data are derived from altimetry measurements gathered over the sea ice pack up to 86°N. The ICESat MSS has been calculated using L1, L2a, L2b, L3a, and L3b SSH data, and therefore includes data gathered over a two-year period between February 2003 and March 2005. Individual height measurements from each of the five ICESat laser campaigns were interpolated onto a grid with a longitude spacing of 1/8° and a latitude spacing of 1/20°. The time-averaged MSS for each grid cell was computed.

Figure 6.1 illustrates two, time-averaged estimates of the Arctic mean sea surface (MSS) computed with respect to the reference ellipsoid. The ICESat MSS above 74°N is illustrated in Figure 6.1 (b) and the ArcGICE MSS[24] is shown in Figure 6.1 (a) for comparison. The black circle indicates the limit of coverage of satellite altimeters in the Arctic prior to the launch of ICESat.

The ICESat MSS presented here is preliminary: it is based on data from five different campaigns and hence different data releases (see Table 3.1). The dataset includes measurements recorded during the L1 and L3b laser campaigns which have not yet been fully corrected for systematic pointing errors (see Section 3.3.2). Furthermore an apparent positive elevation bias in the L2b dataset (see Figure 5.1) has yet to be accounted for and thus requires further investigation. Reprocessing of ICESat data by the ICESat science team is expected to improve the accuracy of the data for each operations period. Such data should help to improve the ICESat MSS in the future.

[24] The ArcGICE MSS was constructed using eight years of ERS-2 data (1995 – 2003) and is provided courtesy of *A. Ridout* (see Section 4.2.2.1 for further details).

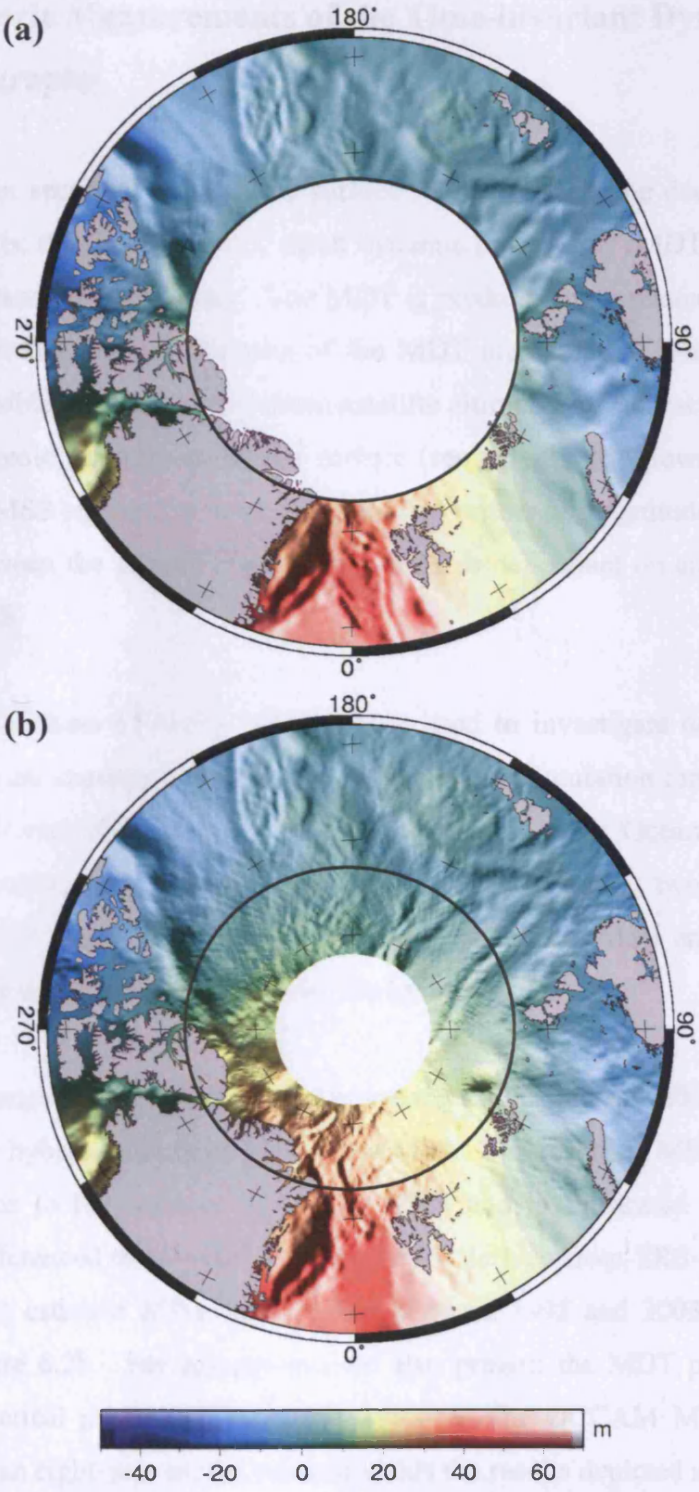

Figure 6.1 Arctic Ocean mean sea surface height. (a) The ArcGICE MSS derived from eight years of ERS-2 altimetry (1995 – 2003) and (b) the ICESat MSS derived from five months of ICESat altimetry gathered over two years (2003-2005). The black circle indicates the limit of coverage of ERS-2 at 81.5°N. Artificial illumination from the east has been added. Data for the top figure was provided courtesy of *A. Ridout*.

6.2.2 Altimetric Measurements of the Time-invariant Dynamic Ocean Topography

As discussed in section 2.7.2 the sea surface topography can be deconstructed into two components: the time-invariant, mean dynamic topography (MDT), and the time-variant, instantaneous topography. The MDT is predominantly related to large-scale, mean ocean circulation, and features of the MDT are therefore relatively stable in time. It is possible to deduce MDT from satellite altimetry by subtracting an accurate model of the geoid from the mean sea surface (see eqn. 2.10). However, since both the geoid and MSS signals are similar and are two orders of magnitude larger than the difference between the signals[25], extracting MDT is dependent on an accurate geoid model and MSS.

Observational datasets of Arctic MDT can be used to investigate ocean circulation patterns and ocean currents as well as to validate ocean circulation models. However, due to a lack of such observational data the MDT of the Arctic Ocean remains poorly constrained. Here we investigate Arctic MDT by differencing two, independently derived altimetric estimates of the Arctic MSS, the ICESat MSS and the ArcGICE MSS, with a state-of-the-art geoid model, the hybrid geoid[26].

First we estimated Arctic MDT for a two-year period between 2003 and 2005 by subtracting the hybrid geoid from the ICESat MSS. The resulting MDT spans all ice-covered regions to the limit of ICESat at 86°N and is illustrated in Figure 6.2a. Second we differenced the 8-year ArcGICE MSS, derived from ERS-2 data, with the hybrid geoid to estimate MDT for a period between 1995 and 2003. The result is shown in Figure 6.2b. For comparison we also present the MDT predicted by the OCCAM numerical model [*Webb et al.*, 1998]. The OCCAM MDT output was averaged over an eight-year model run and yields the results depicted in Figure 6.2c.

[25] In the absence of atmospheric and oceanic circulation, the geoid and mean sea surface would coincide. The geoid and MSS signals are of order 10 m, while the difference between signals (i.e. the MDT) is of order 10 cm.

[26] See Section 4.2.1.2 for further details of the hybrid geoid

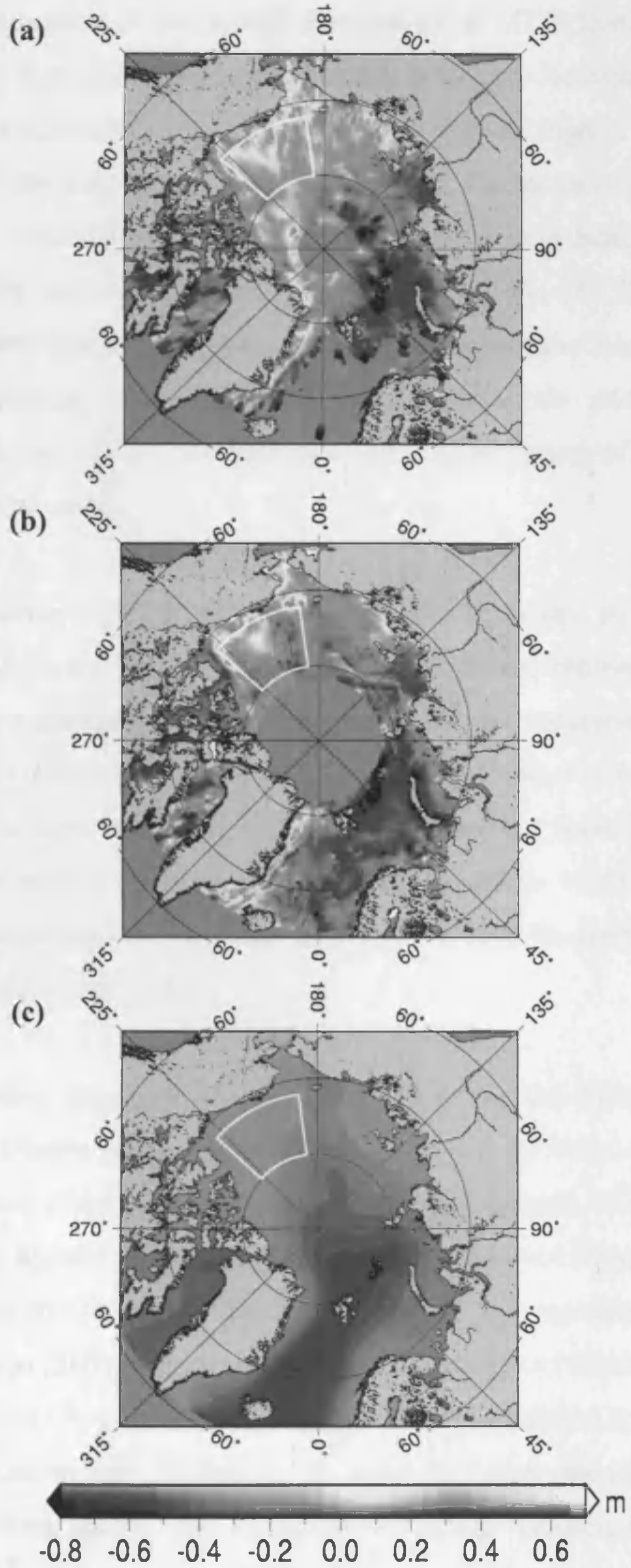

Figure 6.2 Estimates of the mean dynamic topography (MDT) of the Arctic Ocean. MDT derived from (a) the ICESat MSS minus the hybrid geoid, (b) the ArcGICE MSS minus the hybrid geoid, and (c) the OCCAM model of MDT. The solid white box is described in the text.

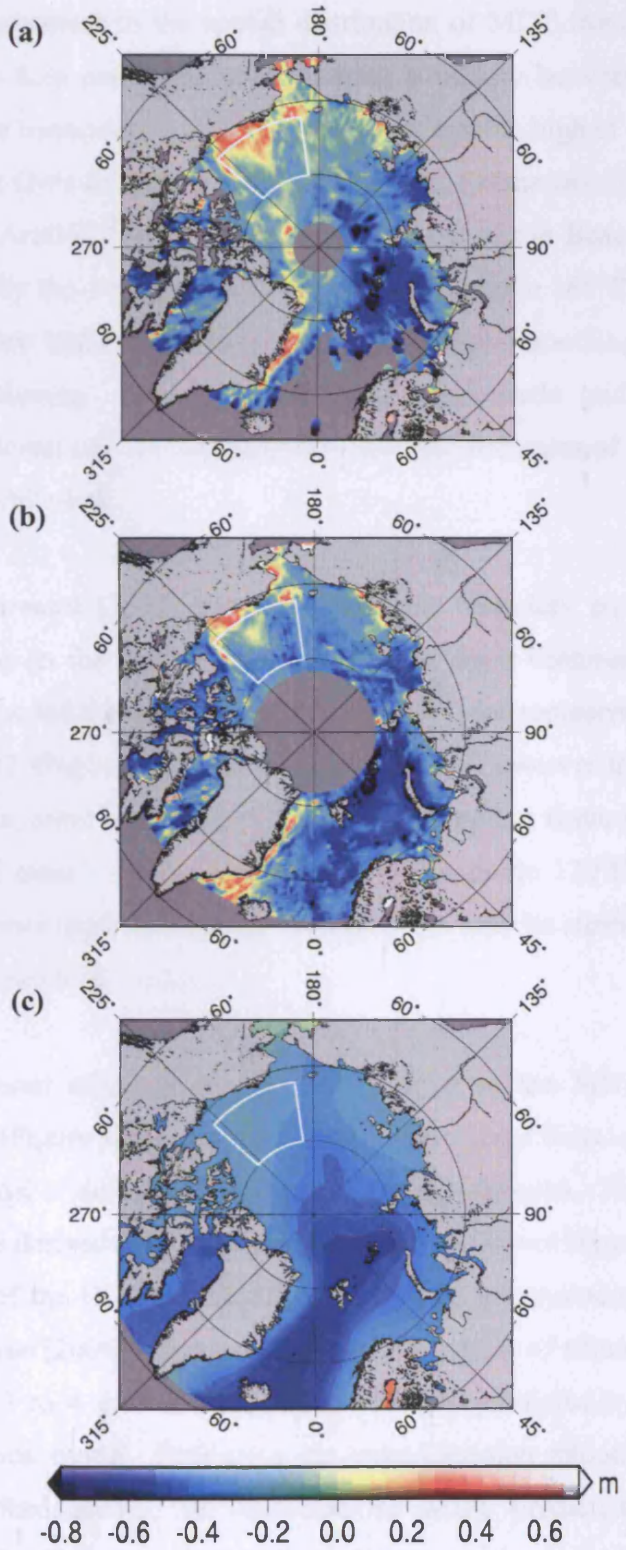

Figure 6.2 Estimates of the mean dynamic topography (MDT) of the Arctic Ocean. MDT derived from (a) the ICESat MSS minus the hybrid geoid, (b) the ArcGICE MSS minus the hybrid geoid, and (c) the OCCAM model of MDT. The solid white box is described in the text.

There is good agreement in the spatial distribution of MDT from the two altimetric datasets (Figures 6.2a and 6.2b) with a strong similarity between features at long-wavelengths. For example at ~ 210°E 74°N, a topographic high of ~ 15 cm associated with the Beaufort Gyre features in both MDT maps. Estimates of MDT, derived from the ICESat and ArcGICE MSS data, in the vicinity of the Beaufort Gyre within a region bounded by the white box in Figure 6.2 (longitude 188°E to 228°E; latitude 72°N to 80°N) are highly correlated. After Gaussian smoothing (using a 120 km radius) and re-binning into 1° by 0.5° longitude-latitude grid, we calculated a correlation coefficient of 0.90 between the altimetric estimates of MDT in the region bounded by the white-box.

Aagaard and Carmack [1994] hypothesise marine boundary currents along all the major topography in the Arctic Ocean. Some of these features, such as the East Greenland Current and the Alaskan Coastal Current[27], are represented in the altimetric estimates of MDT (Figures 6.2a and 6.2 b). We note however that interpretation of the MDT maps in some regions is difficult; for example a feature which follows the continental shelf margin off the Siberian coast (longitude 120°E to 180°E, latitude 79°N) could be associated with a boundary current or may be attributable to remaining errors in the marine geoid model.

The altimetric-based estimates of MDT are similar to the MDT predicted by the OCCAM model (Figure 6.2c) and there is some agreement between the observational data and the model at decimetre level over long wavelengths. The amplitude of the apparent MDT as derived from the altimetric data is however larger, by nearly a factor of 2, than that of the OCCAM model. This result is consistent with the work of *Peacock and Laxon* [2004] which revealed that variability of altimetric SSH estimates was a factor of 3 to 4 greater than SSH variability predicted by the NPS coupled ocean-ice numerical model. Following the same Gaussian smoothing and re-binning procedure described above, we find that the MDT predicted by the OCCAM numerical model within the white box region is poorly correlated with the MDT derived from the ICESat MSS (correlation coefficient of 0.28). Furthermore there is

[27] Refer to Figure 1.8 for the location of the surface currents of the Arctic Ocean.

also poor correlation between the OCCAM model of MDT and that derived from the ArcGICE MSS (correlation coefficient of 0.39) within the white box region.

The differences between the model predictions of MDT and the altimetric estimates may be due to a lack of bathymetric detail in the OCCAM model. Further errors in the altimetric estimates of MDT are likely to be due to small-scale, regional errors remaining in the hybrid geoid (e.g. a topographic high near 230°E 85°N in Figure 6.2a). Indeed some of the high correlation between the two altimetric estimates of MDT may be attributable to common, small-scale geoid errors. Residual errors in the ICESat MSS, due to the inclusion of data that has not been fully corrected for pointing errors (see Section 6.2.1 above), could also be the source of some anomalous topographic elevation estimates.

6.3 Measurement of the Marine Gravity Field of the Arctic Ocean from ICESat

As we have previously discussed in Section 2.7, the SSH signal, as measured by satellite altimeters, is composed of contributions from dynamic ocean topography and the marine geoid. Since the marine geoid is the largest component of the SSH signal, altimetric measurements contain information regarding the geoid and hence reflect variations in the gravity field. Short wavelength (< 250 km) features of the gravity field reflect sea floor bathymetry and the density variations of the oceanic crust and lithosphere, while longer wavelength variations reveal details of the mass anomalies in the Earth's mantle [*Laxon and McAdoo*, 1994]. Accurate knowledge of the marine gravity field of the Arctic Ocean is critical for mapping the geologic structure and tectonic fabric of the seafloor, including fracture zones, spreading ridges, and seamounts. Furthermore, Arctic marine gravity is of importance for marine and submarine navigation, global gravity field modeling, and satellite orbit determination.

The use of altimetric SSH measurements in the ice-covered Arctic Ocean for mapping marine gravity was first demonstrated by *Laxon and McAdoo* [1994]. ERS-1 radar altimetry measurements were used to derive a marine gravity field covering all ocean areas between 61°N and 81.5°N. The gravity field map provided details of several

important tectonic features and revealed new geophysical information regarding a linear feature at the centre of the Canada Basin thought to be an extinct spreading centre. ICESat extends the domain of satellite altimetry in the Arctic beyond 81.5°N to 86°N and could provide new insights on the tectonic fabric of the Arctic seafloor.

ICESat SSH height data (see Section 6.2.1) were provided to D. McAdoo at NOAA. First along-track slopes were computed and, following the method of *McAdoo and Marks* [1992], these were further processed to yield marine gravity anomalies spanning the ice-covered regions of the Arctic Ocean (*D. McAdoo*, personal communication). The ICESat gravity field, as derived by D. McAdoo, covering the region 74°N to 86°N, is illustrated in Figure 6.3. Also included in Figure 6.3 is the ERS-1 gravity field generated by *Laxon and McAdoo* [1998]. Note that ICESat SSH data has been derived over the ice pack only, and the (long-wavelength) gravity field data in the region of the Greenland Sea, south of the sea ice edge, in Figure 6.3b was derived from GRACE data (*D. McAdoo*, personal communication).

Overall there is close agreement between the ERS-1 and ICESat gravity field data. Although the ICESat data is apparently noisier than the ERS data, and long wavelength errors are visible (e.g. in the Canada Basin at ~225°E), short wavelength gravity anomalies are consistent between the datasets. The ICESat gravity map depicts the main tectonic features of the region including the continental shelf margins, Gakkel Ridge, Lomonosov Ridge, and Chukchi Borderland[28]. The ICESat gravity field reveals new tectonic details north of 81.5°N including (i) a possible extinct spreading centre in the Makarov Basin around 170-180°E 81-83°N and (ii) the extension of the Marvin Spur centered at the location 158°E 82-85°N (*D. McAdoo*, personal communication).

A region bounded by the coordinates: longitude 150°E to 220°E, latitude 75°N to 81°N, which is common to both gravity maps, was selected for further statistical analysis. This region encompasses parts of the Canada Basin, Chukchi Borderland, Mendeleev Ridge, Makarov Basin and the Siberian continental shelf[5] and is illustrated as a white box in Figure 6.3. The ERS and ICESat estimates of the gravity field within the white box are highly correlated, with a correlation coefficient of 0.87.

[28] Refer to Figure 1.7 for the location of the major bathymetric features of the Arctic Ocean.

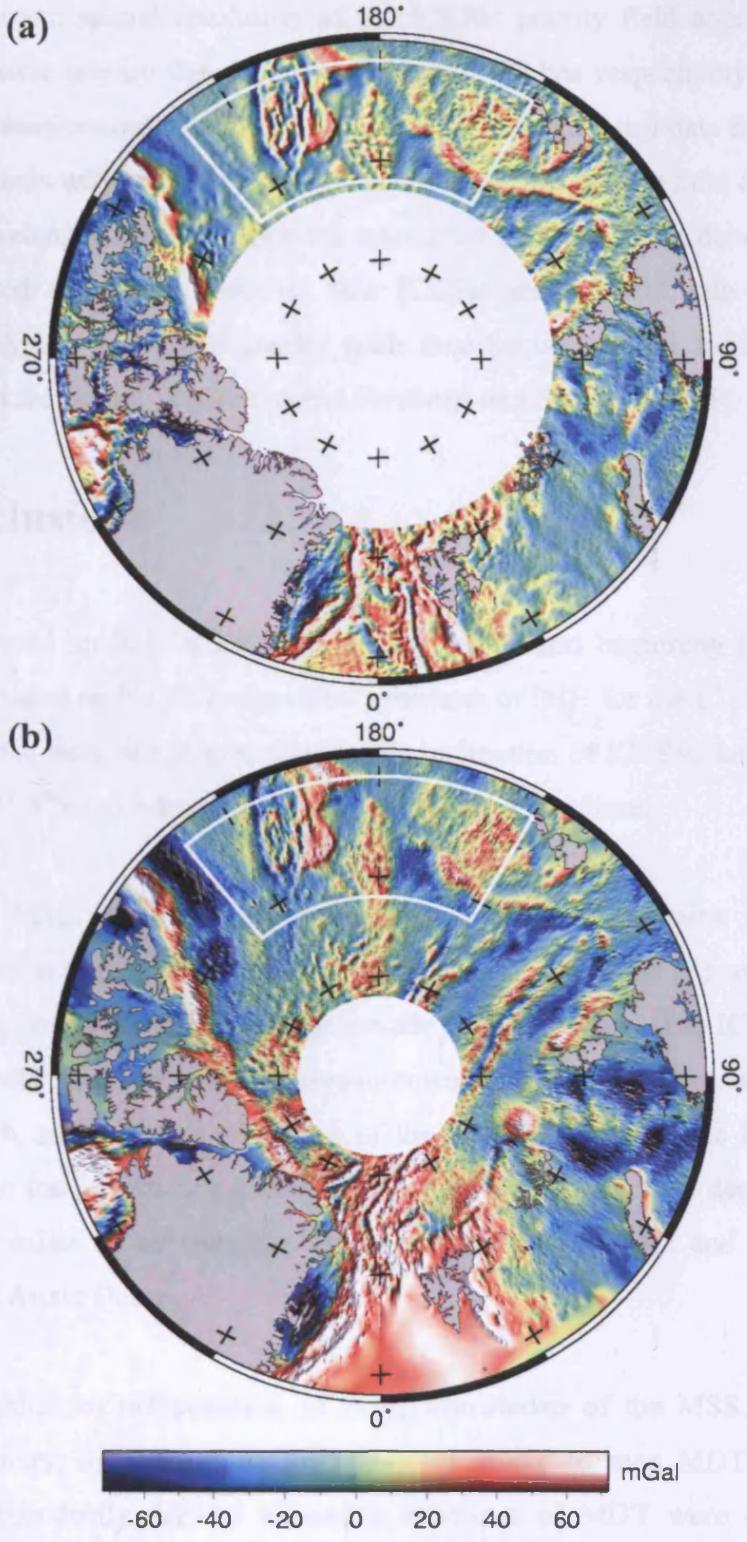

Figure 6.3 Gravity field of the Arctic Ocean. Gravity field estimates were derived from (a) ERS-1 radar altimetry and shown for an area between 74°N and 81.5°N [*Laxon and McAdoo*, 1998] and (b) ICESat laser altimetry between 74°N and 86°N. The solid white box is described in the text. Data for this figure was provided courtesy of *D. McAdoo*.

The accuracy and spatial resolution of the ICESat gravity field approaches that of ERS-1 altimetric gravity data at ~4 mGal and ~45 km respectively (*D. McAdoo*, personal communication). Inclusion of further ICESat altimetry data from other laser operation periods will likely improve the accuracy of the gravity field data, especially at longer wavelengths, and enhance the resolution of the tectonic details of the high Arctic revealed thus far. Moreover new ICESat gravity field data should further enhance the ArcGP geoid and gravity grids (see Section 4.2.1.1 for further details) particularly in the eastern Arctic Ocean [*Forsberg and Skourup*, 2005].

6.4 Conclusions

We have derived an ICESat MSS for a two-year period beginning February 2003. This MSS is based on the UCL algorithm estimates of SSH for the L1, L2a, L2b, L3a, and L3b ICESat laser campaigns. Due to the inclination of ICESat, knowledge of the MSS above 81.5°N has been extended to 86°N for the first time.

The ICESat MSS is preliminary in nature since (i) it contains surface height information from five laser campaigns (~ 5 months of data) and (ii) some of the data used have not yet been corrected for systematic pointing errors. The ICESat MSS will therefore benefit from further SSH measurements from the ICESat laser campaigns following L3b, and future reprocessing of the available data by the ICESat science team. Despite the preliminary nature of the ICESat MSS we have demonstrated that the potential exists to use satellite laser altimetry for geodetic and oceanographic studies of the Arctic Ocean.

We have highlighted the potential of using knowledge of the MSS, derived from satellite altimetry, in conjunction with a geoid model to map MDT in the Arctic Ocean. Independently derived altimetric estimates of MDT were correlated and showed good spatial agreement over long wavelengths. Comparisons with the OCCAM model prediction of MDT indicated that remaining differences between observational and model data may be due to (i) a lack of bathymetric detail in the numerical model and (ii) remaining small-scale errors in the marine geoid.

ICESat SSH data were used to estimate gravity field anomalies in the Arctic Ocean covering the region 74°N to 86°N. The ICESat gravity map depicts the major features of the Arctic Ocean bathymetry including the Lomonosov and Gakkel Ridges and the Canada, Makarov and Eurasian Basins. Although the ICESat gravity field is noisier than the equivalent ERS-1 data, and long wavelength errors exists, there is good agreement between the ERS-1 and ICESat gravity estimates at shorter wavelengths. Indeed in a region spanning parts of the Canada Basin, the Chukchi Borderland, the Makarov Basin and the Siberian continental shelf, gravity anomalies from the two satellite datasets are highly correlated. We may therefore have confidence in the ICESat gravity field of the high Arctic above 81.5°N. New details of the tectonic fabric of the high Arctic have been revealed for the first time, including a possible extinct spreading centre in the Makarov Basin (*D. McAdoo*, personal communication). The amplitude and spatial resolution of the ICESat gravity field should be improved via inclusion of additional data from other ICESat laser campaigns. The information contained in the ICESat gravity field could contribute to the enhancement of the Arctic Gravity Project (ArcGP) gravity grids in the future.

7 Cryospheric Applications of ICESat Altimetry in the Arctic Ocean

7.1 Introduction

Following the discussion of exploitation of sea surface height (SSH) measurements for oceanographic and geodetic applications in Chapter 6, we now investigate the application of SSH data for cryospheric studies.

We illustrate the potential of using time-varying sea surface height measurements in conjunction with altimetric elevation measurements over sea ice to estimate snow freeboard. We evaluate the use of the UCL algorithm SSH estimates as compared to ENVISAT SSH estimates for deriving snow freeboard from ICESat. We provide snow freeboard maps for two autumn campaigns and a spring laser campaign. This analysis enables us to compare the algorithms and to carry out a qualitative investigation of the seasonal variability in sea ice freeboard. Next we compare snow freeboard estimates from ICESat laser altimetry with contemporaneous ice freeboard estimates from ENVISAT radar altimetry. Finally we explore the feasibility of combining satellite laser and radar altimetric measurements of sea ice freeboard to measure the depth of snow loading on sea ice. The ENVISAT sea ice freeboard and sea surface height data presented in this chapter are preliminary and was provided by A. L. Ridout of CPOM.

7.2 Arctic Snow Freeboard from ICESat

Derivation of sea ice freeboard using satellite altimetry is viable if estimates of both sea ice and sea surface topography are known (Eqn. 2.8). Radar altimetric estimates of sea ice freeboard (h_f) characterise the portion of sea ice above the water surface, while laser altimetric freeboard measurements define the snow freeboard (h_{sf}), or the height of the air/snow interface of a sea ice floe above the water surface (i.e. comprising both the sea ice freeboard and any overlying snow). We refer the reader to Section 1.5.4 and Figure 1.20 for further discussion.

7.2.1 Laser Altimetric and Radar Altimetric SSH Measurements for the Derivation of Snow Freeboard

On of the key results presented in Chapter 5 revealed that ENVISAT SSH estimates were more self-consistent than the contemporaneous ICESat SSH estimates, suggesting that the ENVISAT SSH retrievals were more accurate than the ICESat measurements (see Section 5.3). We therefore explore the use of ENVISAT SSH estimates in conjunction with ICESat surface elevation measurements to derive snow freeboard (Eqn. 7.2).

Analysis presented in Chapter 5 also suggested that, in terms of SSH retrievals derived from ICESat data, the UCL algorithm performed better than the GSFC algorithm during the autumn campaigns, and that the algorithms perform similarly during the spring campaigns (Sections 5.4.3 and 5.5). We therefore use ICESat SSH estimates, derived using the UCL algorithm, in conjunction with ICESat surface elevation measurements, to derive "ICESat only" snow freeboards (Eqn. 7.1). We compare these snow freeboard estimates to equivalent measurements derived using the ICESat/ENVISAT combination described above.

Following Eqn. 2.8 we use ICESat surface elevation measurements over the Arctic Ocean in conjunction with along-track SSH measurements estimated using (i) the UCL algorithm and (ii) ENVISAT radar altimetry data, to derive two different estimates of snow freeboard, h_{sf}:

$$h_{sf\_UCL} = h_{alt} - h_{ssh\_LA\_UCL} \tag{7.1}$$

$$h_{sf\_RA} = h_{alt} - h_{ssh\_RA} \tag{7.2}$$

where, h_{alt} is the ICESat surface elevation measurement, $h_{ssh\_LA\_UCL}$ is the sea surface height estimate derived using the UCL algorithm (see Chapter 4 for a detailed description of the algorithm), and h_{ssh_RA} is the sea surface height derived from ENVISAT radar altimetry data.

As part of the dual-satellite crossover analysis presented in Chapter 5 we identified periods when crossover height differences between ENVISAT SSH estimates and contemporaneous ICESat UCL algorithm SSH estimates were small (i.e. between ± 3 cm). These time periods are outlined in Table 7.1. Since the SSH estimates during these time periods are consistent we can use the ENVISAT SSH measurements in place of the equivalent ICESat SSH measurements to calculate snow freeboard. A small bias, derived from the dual-satellite crossover height differences (see Figures 5.9 to 5.11, third panel), was applied to ICESat surface elevation measurements so as to align the data accurately to the ENVISAT SSH data.

Following Eqn. 7.1 we first calculated h_{sf_UCL} using the ICESat surface elevation measurements and the UCL SSH estimates for ice-covered ocean regions between 65°N and 86°N. We then replaced the UCL algorithm SSH estimates with contemporaneous ENVISAT SSH estimates and re-calculated snow freeboard, h_{sf_RA}, using Eqn. 7.2. The freeboard estimates were interpolated onto a grid with a 4° by 1°, longitude by latitude spacing.

The results are shown in Figures 7.1 to 7.6. In each figure there are five panels: (a) snow freeboard estimates averaged over observation period I, (b) snow freeboard estimates pertaining to observation period II, (c) the distribution of freeboard heights for period I, (d) the distribution of freeboard heights for period II and (e) a scatter plot of freeboard estimates for observation period II versus period I [29]. The number of points in each scatter plot as well as the correlation coefficient (R^2) for a linear relationship of the form $y = ax + b$ are also shown in each scatter plot. Since the observation periods in this analysis are short, there are less data points available for analysis and hence more empty (grey) grid cells in the freeboard maps.

As with the analysis carried out in Section 5.5, a comparison of snow freeboard estimates from observation period I with those from period II should give some indication of the consistency of the results. We expect a strong relationship, and hence a high correlation, between the snow freeboard results from the first

[29] Only data in the latitudinal band 78°N to 81.5°N were included in the histogram and scattergram analysis as this represented the band where a similar number and distribution of grid-cells were available for both observation period I and II.

observation period with those from the second observation period. Fluctuations in snow accumulation, and growth of new sea ice, between the two observation periods are likely. However, since we compute the correlation coefficients for the h_{sf_UCL} and h_{sf_RA} estimates over the same observation periods, we account for such fluctuations since they would have equal effects on the correlation coefficients of both datasets.

Laser Campaign	Observation Period	
	I	II
L1	21 Feb - 01 Mar 2003 *-2.0*	02 Mar - 07 Mar 2003 *0.5*
L2A	04 Oct - 18 Oct 2003 *1.3*	25 Oct - 11 Nov 2003 *0.3*
L3A	09 Oct - 15 Oct 2004 *0.5*	21 Oct - 26 Oct 2004 *1.7*

Table 7.1 Dates of the observation periods during three ICESat laser campaigns when ENVISAT and ICESat SSH estimates are consistent. Values given in italics are the biases (cm) applied to the ICESat surface elevation measurements to align the data to the contemporaneous ENVISAT SSH estimates.

The results presented in Figures 7.1 to 7.6 illustrate the effect of the SSH measurement on freeboard retrieval and the possible errors introduced if inaccurate sea surface topography is used. The snow freeboard estimates based on the ENVISAT SSH measurements have higher correlation coefficients than those based on the ICESat UCL algorithm SSH measurements for all three laser operations periods. The correlation coefficients for snow freeboards derived using ENVISAT SSH estimates are 0.21, 0.68, and 0.77 respectively for the L1, L2a, and L3a laser campaigns. The snow freeboards derived using ICESat SSH estimates have R^2 values of 0.16, 0.53, and 0.33 respectively for the L1, L2a, and L3a laser campaigns. Furthermore there is less scatter in the scatter plots based on the ENVISAT SSH estimates. These results indicate that the use of the ICESat SSH estimates to generate Arctic snow freeboard maps is problematic and any inaccuracies in the sea surface topography will manifest themselves as anomalous freeboard estimates. We suggest therefore that ICESat elevation measurements used in conjunction with contemporaneous ENVISAT SSH estimates represents a useful method for obtaining self-consistent snow freeboard estimates from ICESat. Furthermore this procedure is only applicable when (i) biases between the radar and laser altimetric elevations are small or (ii) biases are well-known and consequently accounted for sufficiently.

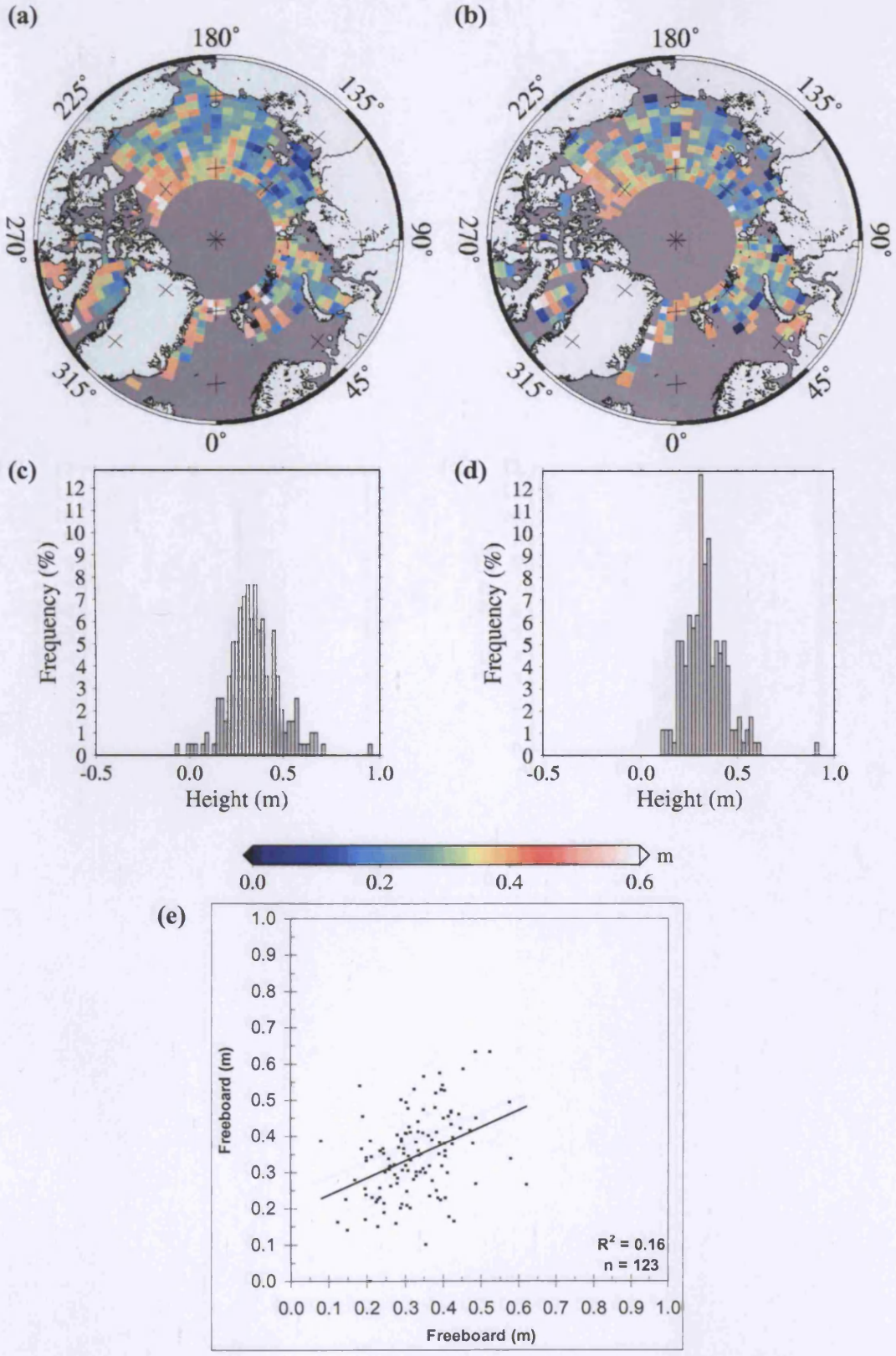

Figure 7.1 Arctic snow freeboard, h_{sf_UCL}, during spring 2003 derived from ICESat elevations measured with respect to UCL algorithm SSH measurements. Snow freeboard for (a) observation period I and (b) observation period II. Distribution of snow freeboard between 78°N and 81.5°N for (c) period I and (d) period II. (e) Scatter plot of snow freeboard between 78°N and 81.5°N for period II (*x-axis*) versus period I (*y-axis*). See Table 7.1 for the dates of each observation period.

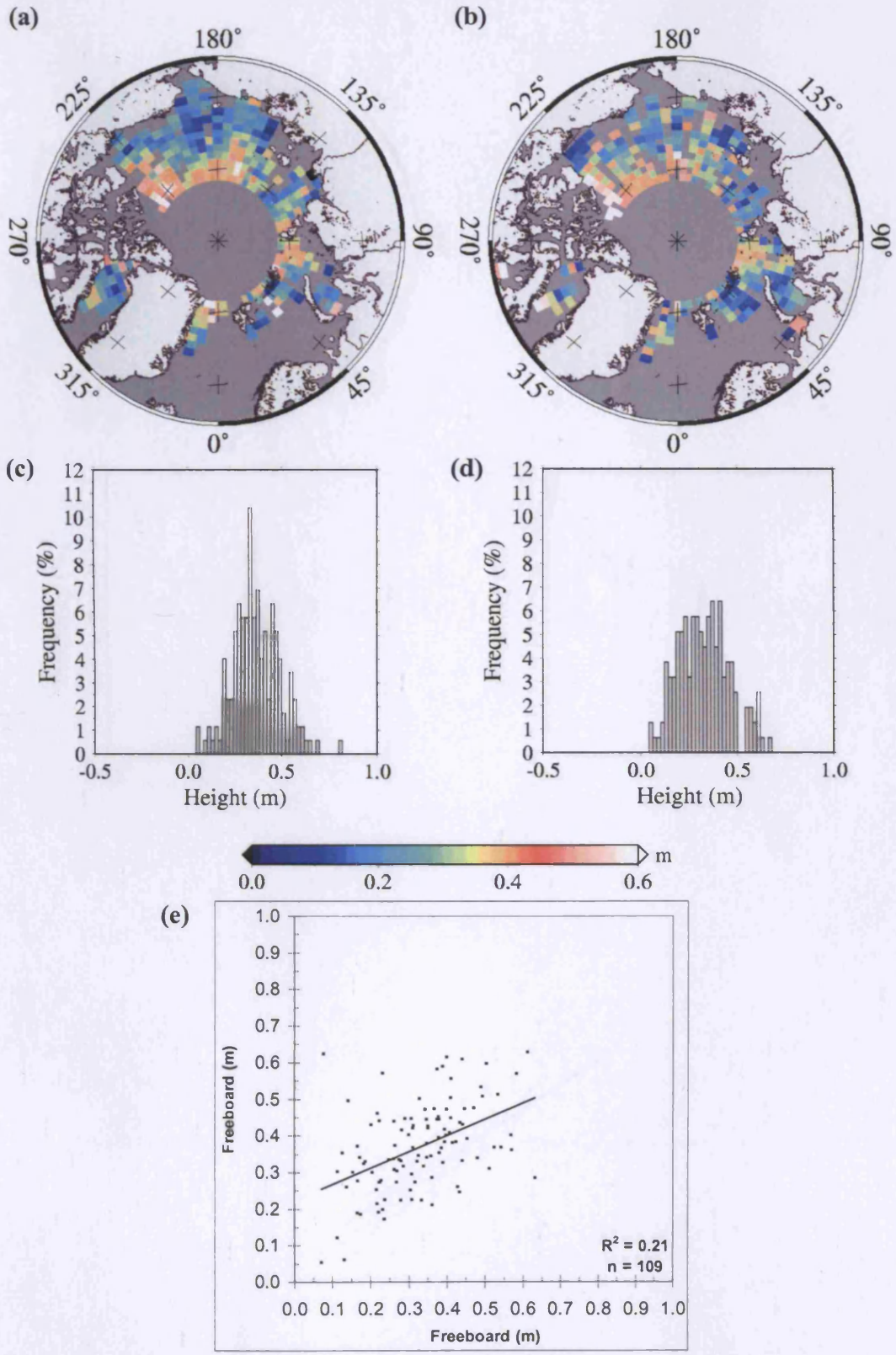

Figure 7.2 Arctic snow freeboard, h_{sf_RA}, during spring 2003 derived from ICESat elevations measured with respect to ENVISAT SSH measurements. Labelling as for Figure 7.1.

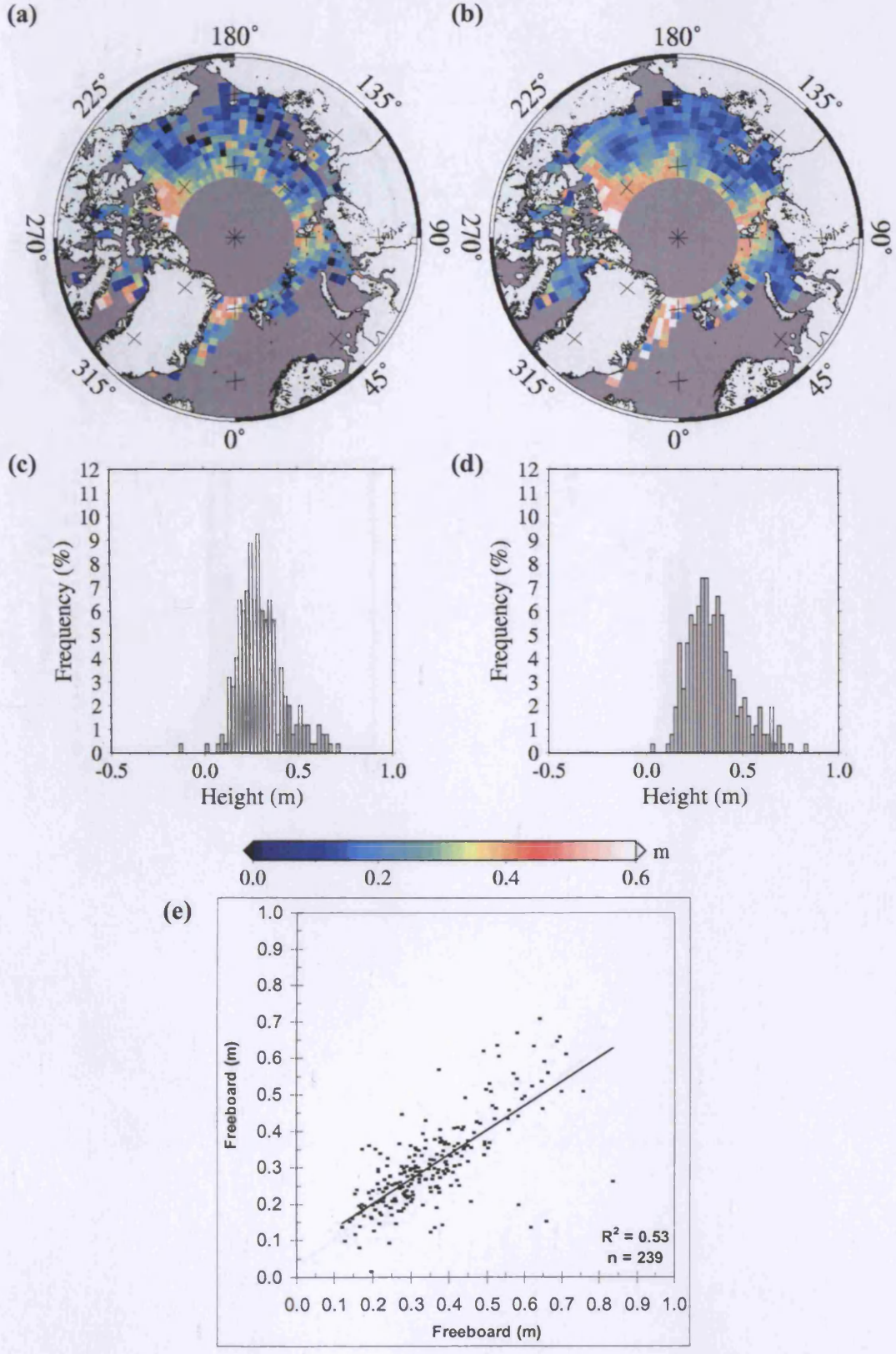

Figure 7.3 Arctic snow freeboard, h_{sf_UCL}, during autumn 2003 derived from ICESat elevations measured with respect to UCL algorithm SSH measurements. Labelling as for Figure 7.1.

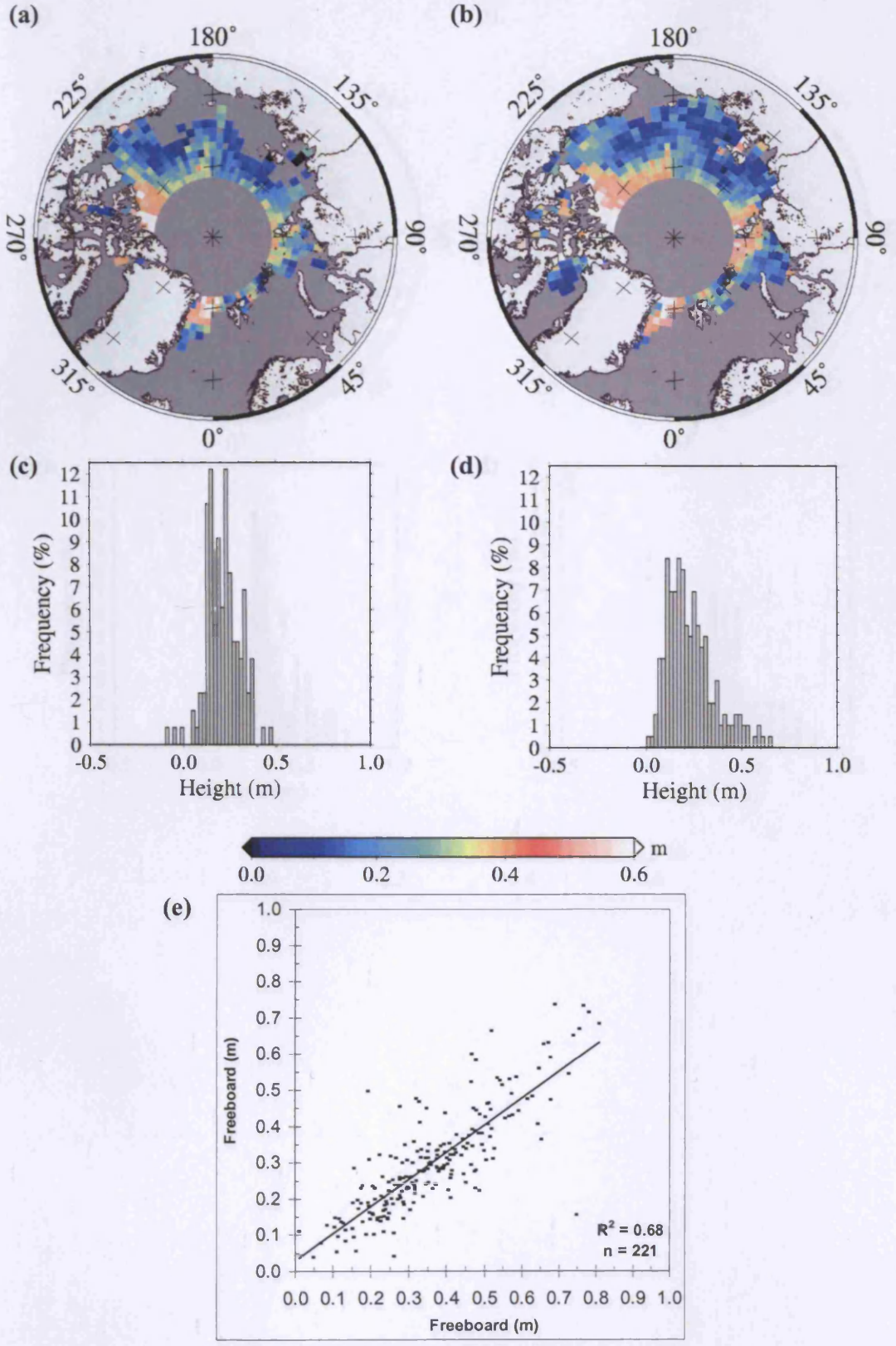

Figure 7.4 Arctic snow freeboard, h_{sf_RA}, during autumn 2003 derived from ICESat elevations measured with respect to ENVISAT SSH measurements. Labelling as for Figure 7.1.

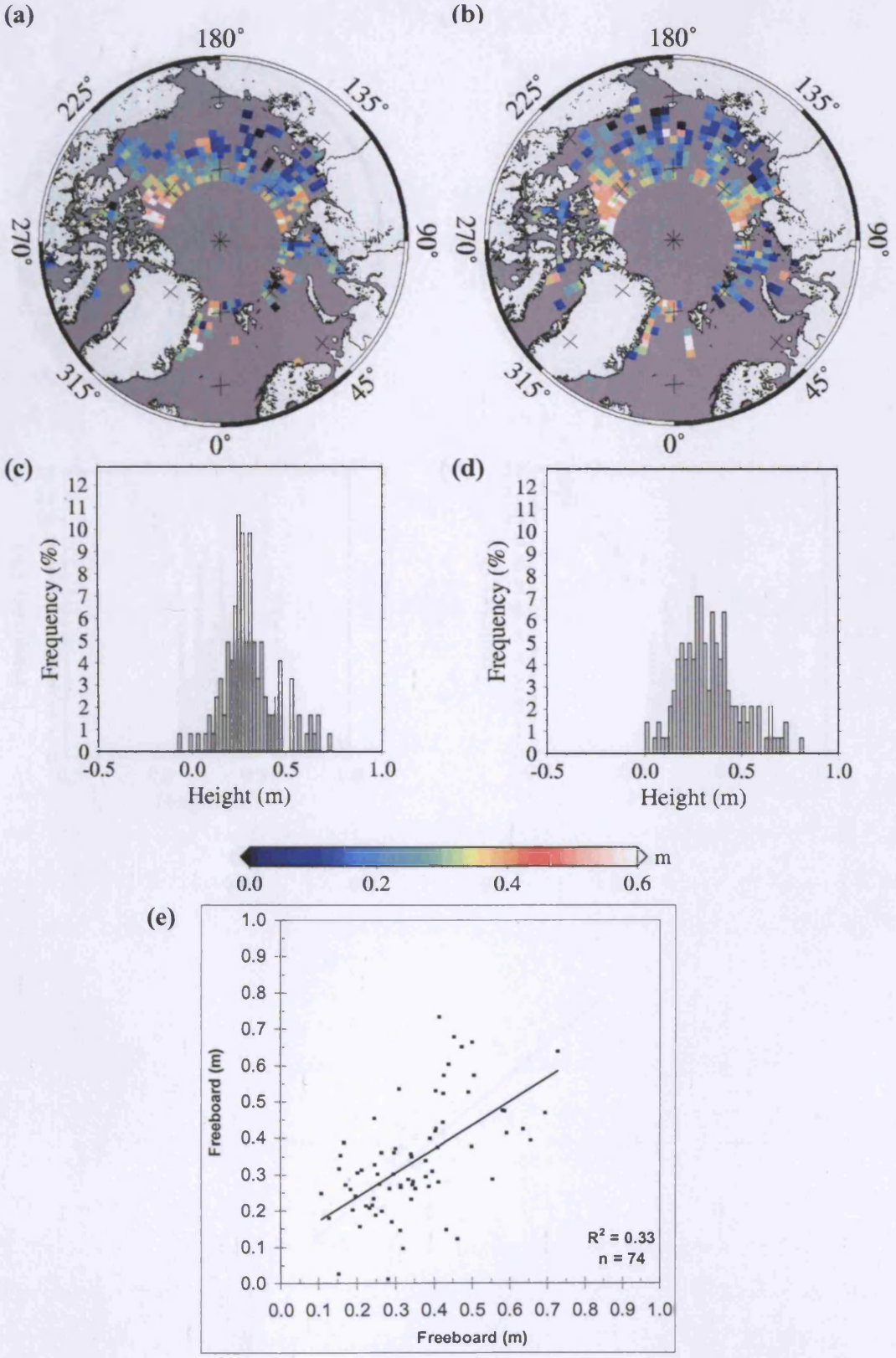

Figure 7.5 Arctic snow freeboard, h_{sf_UCL}, during autumn 2004 derived from ICESat elevations measured with respect to UCL algorithm SSH measurements. Labelling as for Figure 7.1.

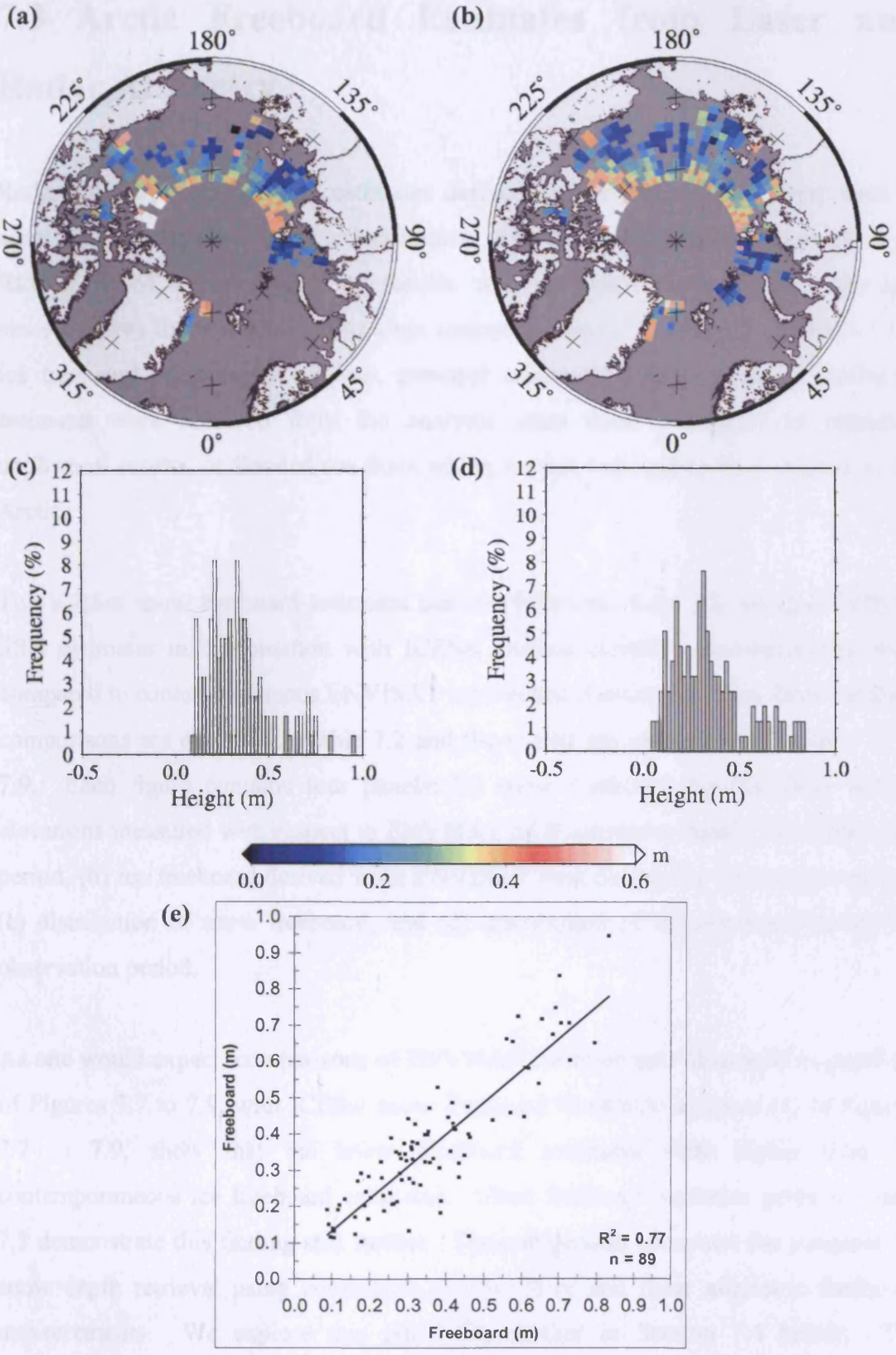

Figure 7.6 Arctic snow freeboard, h_{sf_RA}, during autumn 2004 derived from ICESat elevations measured with respect to ENVISAT SSH measurements. Labelling as for Figure 7.1.

7.3 Arctic Freeboard Estimates from Laser and Radar Altimetry

Radar altimetric ice freeboard estimates derived from ENVISAT data were used to assess the ICESat snow freeboard estimates. The data were provided courtesy of A. Ridout, CPOM, and are preliminary results. A 12 cm bias has been applied to the data since this was the bias required to align contemporaneous ENVISAT and ERS-2 sea ice freeboard estimates (*A. Ridout*, personal communication). Negative freeboard estimates were removed from the analysis since these are likely to represent unphysical results, or flooded sea floes which are not believed to be prevalent in the Arctic.

The ICESat snow freeboard estimates derived following Eqn. 7.2, using ENVISAT SSH estimates in combination with ICESat surface elevation measurements, were compared to contemporaneous ENVISAT ice freeboard estimates. The dates for these comparisons are outlined in Table 7.2 and the results are presented in Figures 7.7 to 7.9. Each figure contains four panels: (a) snow freeboard derived from ICESat elevations measured with respect to ENVISAT SSH estimates during the observation period, (b) ice freeboard derived from ENVISAT data during the observation period, (c) distribution of snow freeboard, and (d) distribution of ice freeboard during the observation period.

As one would expect, comparisons of ENVISAT ice freeboard illustrated in panel (b) of Figures 7.7 to 7.9, with ICESat snow freeboard illustrated in panel (a) of Figures 7.7 to 7.9, show that the snow freeboard estimates were higher than the contemporaneous ice freeboard estimates. Mean freeboard statistics given in Table 7.3 demonstrate this finding still further. The comparison illustrates the potential for snow depth retrieval using coincident satellite laser and radar altimetric freeboard measurements. We explore this possibility further in Section 7.4 below. The delineation between multi-year and first-year sea ice was clearer in the satellite laser altimetric freeboard estimates than in the radar altimetric estimates.

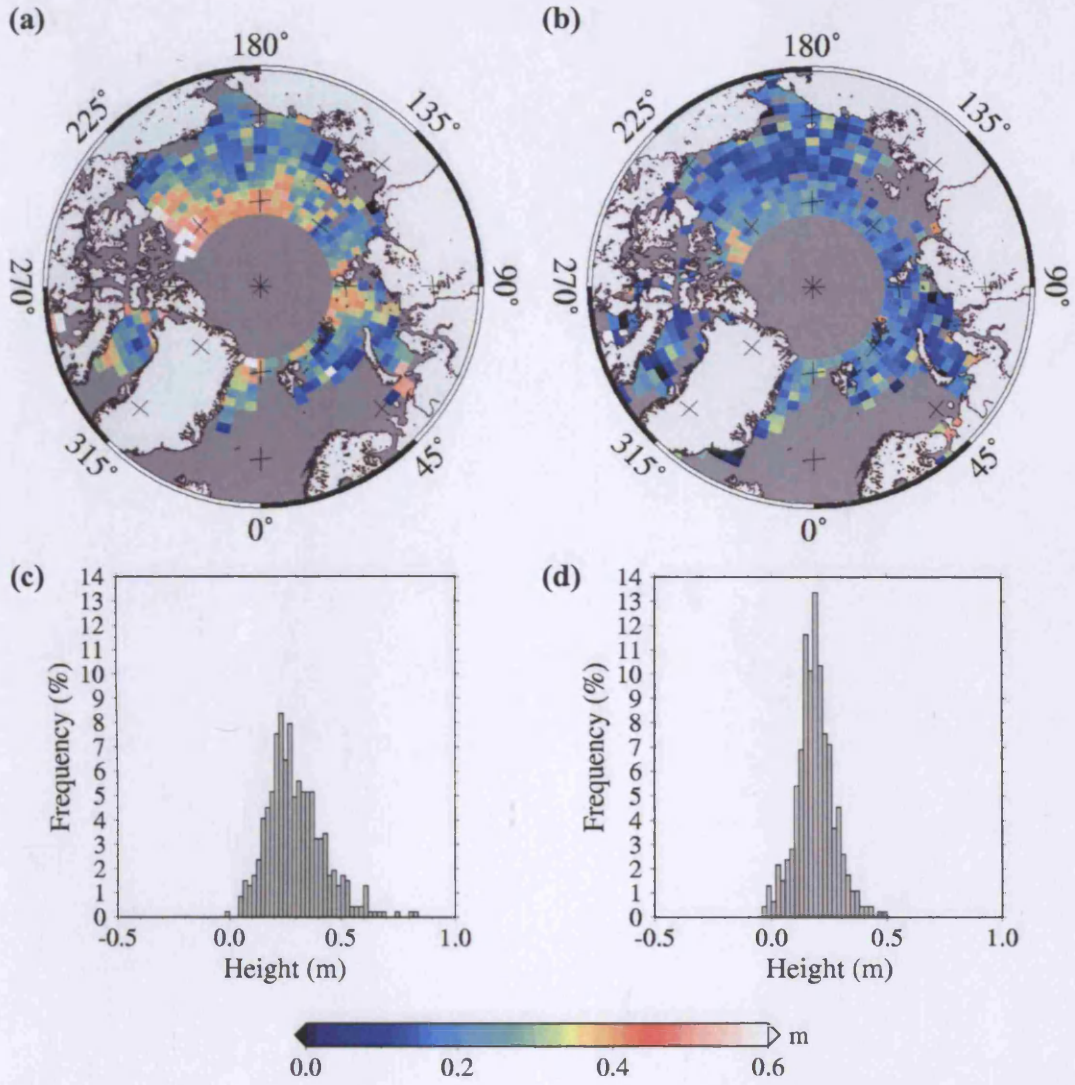

Figure 7.7 Comparison of satellite laser and radar altimetric estimates of Arctic sea ice freeboard during spring 2003. (a) Snow freeboard derived from ICESat elevations measured with respect to ENVISAT RA-2 SSH measurements during the observation period. (b) Ice freeboard derived from ENVISAT RA-2 data during the observation period. (c) Distribution of snow freeboard and (d) ice freeboard during the observation period. Data for Figures 7.7 (b) and (d) were provided courtesy of *A. Ridout*; these data are preliminary. See Table 7.2 for the dates of the observation period.

Laser Campaign	Observation Period
L1	21 Feb - 07 Mar 2003
L2A	04 Oct - 18 Oct and 25 Oct - 11 Nov 2003
L3A	09 Oct - 15 Oct and 21 Oct - 26 Oct 2004

Table 7.2 Dates for comparison of ICESat snow freeboards with ENVISAT ice freeboards.

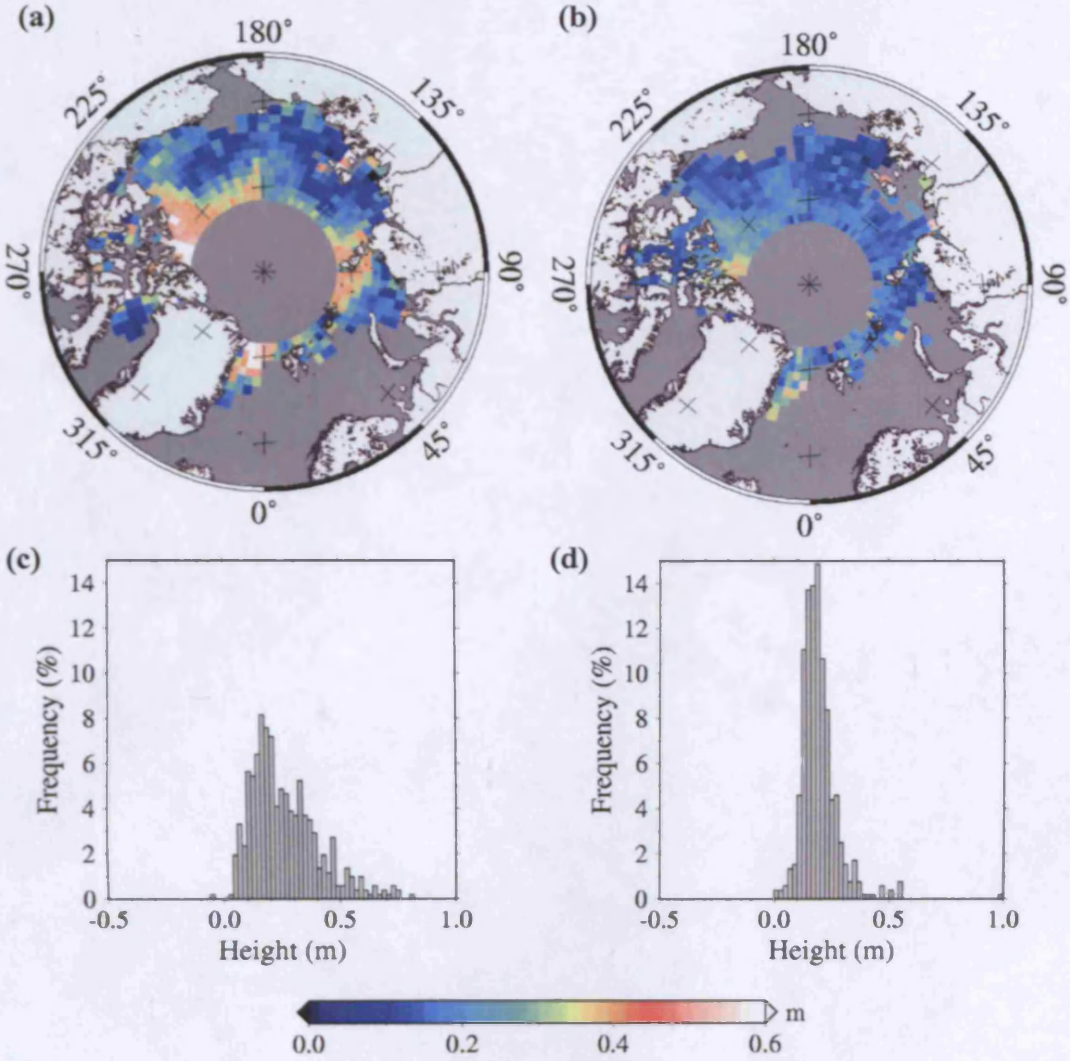

Figure 7.8 Comparison of satellite laser and radar altimetric estimates of Arctic sea ice freeboard during autumn 2003. Labelling as for Figure 7.7. Data for Figures 7.8 (b) and (d) were provided courtesy of *A. Ridout*; these data are preliminary. See Table 7.2 for dates of the observation period.

Laser Campaign	Mean h_{sf_RA}	Mean h_f
L1	0.30	0.17
L2A	0.26	0.15
L3A	0.28	0.14

Table 7.3 Comparison of mean snow freeboard derived from satellite laser altimetry with mean ice freeboard derived from satellite radar altimetry for the three observation periods outlined in Table 7.2.

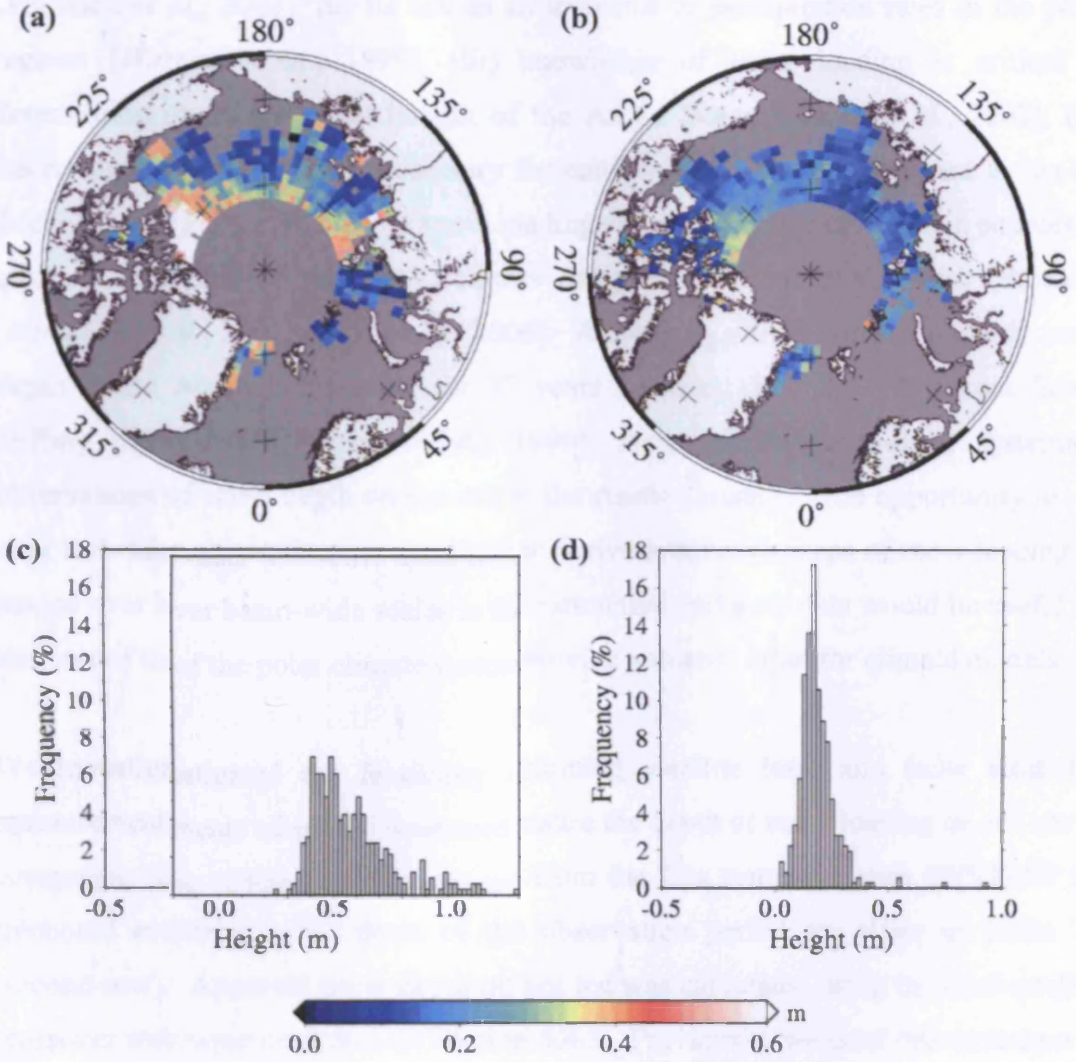

Figure 7.9 Comparison of satellite laser and radar altimetric estimates of Arctic sea ice freeboard during autumn 2004. Labelling as for Figure 7.7. Data for Figures 7.9 (b) and (d) were provided courtesy of *A. Ridout*; these data are preliminary. See Table 7.2 for dates of the observation period.

7.4 Snow Loading on Sea Ice

Since the laser pulse reflected from a sea ice floe is treated as a reflection from the air/snow interface and a radar return pulse is assumed to be a reflection from the snow/ice interface it is theoretically possible to deduce snow loading on sea ice from simultaneous measurements of sea ice freeboard from satellite laser and radar altimetry. Snow loading is an important parameter in cryospheric studies for various reasons including (i) its influence on sea ice growth during the winter growing season

[*Perovich et al.*, 2003], (ii) its use as an indicator of precipitation rates in the polar regions [*Warren et al.*, 1999], (iii) knowledge of snow loading is critical in determining the overall heat budget of the Arctic Ocean [*Sturm et al.*, 2002], (iv) knowledge of snow depth is necessary for conversion of sea ice freeboard to sea ice thickness (see Eqn. 1.2), and (v) snow loading on sea ice is one of the main sources of error in estimates of sea ice thickness using satellite radar and laser altimetry [*Wingham et al.*, 2001; *Kwok et al.*, 2006]. Although a climatology of monthly snow depth in the Arctic is available for 37 years between 1954 and 1991 from Soviet drifting buoy data [*Warren et al.*, 1999], there are no up-to-date, systematic observations of snow depth on sea ice in the Arctic Ocean[30]. The opportunity to use laser and radar altimetric measurements to derive systematic maps of snow loading on sea ice over basin-wide scales is therefore attractive and such data would be useful for analysis of the polar climate system and provide valuable input for climate models.

We investigated the feasibility of combining satellite laser and radar altimetric measurements of sea ice freeboard to measure the depth of snow loading on sea ice by comparing ICESat snow freeboard data from the L2a campaign with ENVISAT ice freeboard estimates. The dates of the observation period are given in Table 7.2 (second row). Apparent snow depth on sea ice was calculated using the dual-satellite crossover technique described in Section 5.4.3. Previously, we used this technique to calculate differences between satellite laser and radar estimates of SSH. At locations where the ICESat and ENVISAT ground tracks cross, two independent measurements of sea ice freeboard are available. We calculated the crossover height differences as the ICESat snow freeboard minus the ENVISAT ice freeboard and the results are presented in Figure 7.10 (a). A small percentage of negative snow depth estimates were removed from the analysis since they represent unphysical results. The monthly snow depth climatology provided in *Warren et al.* [1999] was used to calculate average snow depth for the months of October and November and this is presented in Figure 7.10 (b) for comparison with the satellite altimetric estimates.

[30] Satellite passive microwave retrievals of snow depth on sea ice from the AMSR-E sensor are only available for regions of first-year sea ice and multi-year ice with an SSM/I concentration of $\leq 20\%$ [*Cavalieri and Comiso*, 2000].

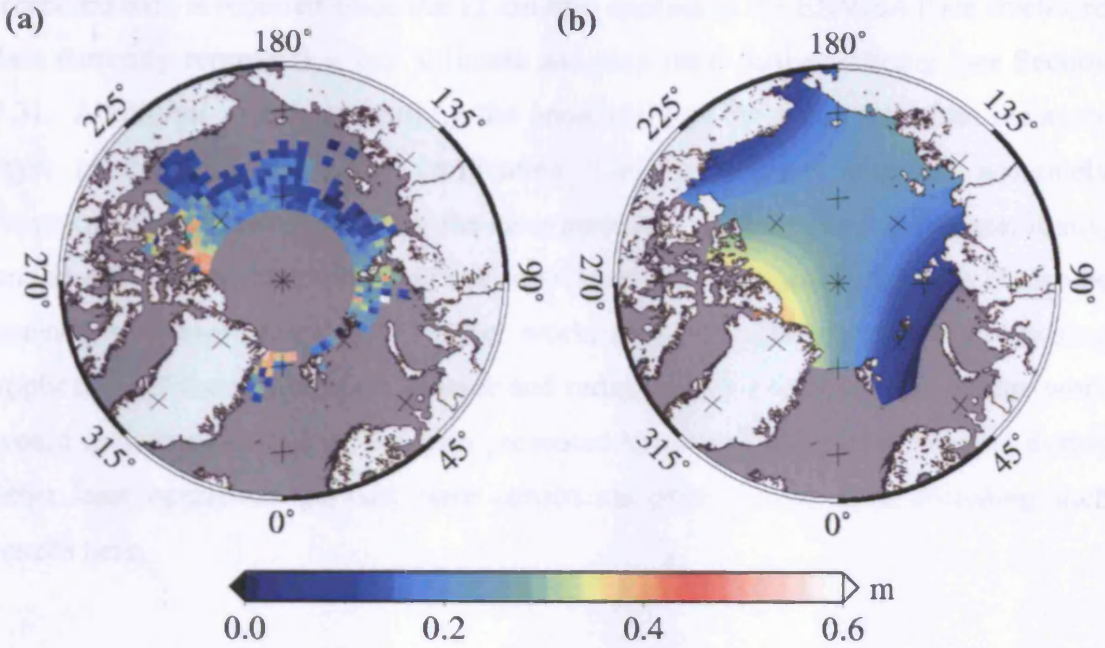

Figure 7.10 Arctic snow loading on sea ice during autumn 2003. (a) Apparent snow depth derived from ICESat snow freeboard estimates differenced with ENVISAT ice freeboard estimates. (b) Snow depth climatology averaged for October and November [*Warren et al.*, 1999].

There is some agreement between the regional distribution of snow depth derived from the altimetric freeboard estimates and that of the climatology. The altimetric estimates of snow depth are higher close to the Queen Elizabeth Islands and in the Fram Strait than in other regions of the Arctic Ocean. This spatial pattern agrees with the climatology. Furthermore, the mean freeboard difference, as derived from the altimetric data, is 20 cm during the observation period and this compares well to the average snow depth during the Oct – Nov period which is 21 cm, based on the climatology [*Warren et al.*, 1999]. There are however some notable differences between the magnitude of the altimetric snow depth estimates and the climatology (e.g. north of New Siberian Islands and near Severnaya Zemlya). We note also that the snow depth climatology may not accurately represent actual snow loading on sea ice during the autumn 2003 period which we analyse here.

The method we describe for determining snow depth on sea ice is dependent on accurate estimates of both snow and ice freeboard. There remain uncertainties in both the satellite laser and radar altimetric retrievals of sea ice freeboard and inaccuracies in either of the freeboard estimates will give rise to anomalous estimates of snow depth. Further investigation into the biases involved in the radar altimetry sea ice

freeboard data is required since the 12 cm bias applied to the ENVISAT ice freeboard data currently represents a best estimate and may need further refining (see Section 7.3). Additional research regarding the penetration of the radar pulse into the snow layer is also required, as is verification that the air/snow interface accurately represents the reflecting layer that the laser pulse encounters. The dependence, if any, on the effect of the temperature of the snow layer on pulse penetration should also be considered. Nevertheless, with further work, this technique represents an exciting application of the combination of laser and radar altimetry over sea ice. Future work would include repeating the analysis presented here for ICESat data gathered during other laser operations periods; time constraints prevented us from including such results here.

7.5 Conclusions

We have highlighted the potential of satellite laser altimetry data from ICESat for the retrieval of snow freeboard in the Arctic Ocean. The use of ENVISAT SSH estimates in place of ICESat SSH estimates for the retrieval of more accurate snow freeboards was described. We have compared the snow freeboard estimates we derived from ICESat altimetry with cotemporaneous estimates of sea ice freeboard from ENVISAT. We have also explored the feasibility of combining satellite laser and radar altimetric retrievals of freeboard to deduce snow loading on sea ice.

We found that ICESat elevation measurements used in conjunction with contemporaneous ENVISAT SSH estimates resulted in freeboard comparisons which had the strongest correlations. Of the methods considered, this method represented the ideal procedure for obtaining the most consistent snow freeboard estimates from ICESat data. We also demonstrated that the use of the ICESat SSH estimates to generate Arctic snow freeboard maps was problematic and any inaccuracies in the sea surface topography manifest themselves as anomalous freeboard estimates.

Comparison of ICESat snow freeboard estimates with contemporaneous ENVISAT ice freeboard estimates illustrated that, as expected, the snow freeboard estimates were higher than the equivalent ice freeboard estimates. This result illustrates the

potential for snow depth retrieval using coincident satellite laser and radar altimetric freeboard measurements.

The determination of snow depth on Arctic sea ice using satellite laser and radar altimetry data is dependent on accurate estimates of both snow and ice freeboard. Although the spatial distribution of snow depth derived from the altimetric freeboard estimates showed some agreement with the monthly climatology, the magnitude of snow loading on sea ice differed to that predicted by the climatology in some regions. Further investigation of (i) the biases associated with each of the freeboard estimates and (ii) the penetration of the laser and radar pulses into the snow are required. Nevertheless, with additional research, this technique represents an exciting application of the combination of laser and radar altimetry over sea ice for the retrieval of a parameter of significant climatological interest.

8 Conclusions

8.1 Introduction

In the final chapter we summarise the achievements of the work presented in this thesis. We reiterate the primary aims of this work and we assess how these objectives have been achieved. We present a summary of the key findings and the contribution these results make to advance the knowledge of the climate-related processes of the Arctic Ocean. Finally we conclude with some recommendations for future work in the field of satellite altimetry over sea ice.

8.2 Assessment of Achievements

8.2.1 Primary Aims

We outlined the main aims of the work presented in this thesis at the end of Chapter 3. We now recap on these objectives investigating the extent to which they have been achieved.

- To understand further the origins of ICESat laser pulse returns from sea ice covered regions to enable identification of returns from leads and thin ice within the ice pack.

While it is possible to distinguish returns that originate over leads in radar altimetric data due to the distinct, specular shape of the echo, identifying returns from open water or leads in laser altimetric data is more complex since laser returns from both smooth water surfaces and smooth snow/ice surfaces have similar, specular shapes. For a reflection from a lead, we assume that in clear, calm conditions, the shape of the GLAS received pulse is near-specular in shape and highly correlated with the shape of the transmitted pulse. We derived a number of parameters associated with the shape of the transmitted and received laser pulses including pulse full-width half-maximum and skewness. We also calculated the cross-correlation between the transmitted and

received pulses. Furthermore we investigated the relationship between ICESat elevations and surface reflectivity and we computed the along-track, standard deviation of elevation. Based on comparisons with satellite imagery, we derived thresholds associated with these parameters that could be used to discriminate laser returns from open water and leads.

- To assess existing methods for determination of sea surface height in the presence of sea ice over the Arctic Ocean.

We have described an existing method, referred to here as the "GSFC algorithm", for estimating sea surface height (SSH) in the ice-covered Arctic Ocean. This method is based on work carried out by *Zwally et al.* [2003]. We assessed the SSH estimates derived using the GSFC algorithm in terms of comparisons with (i) two newly-developed algorithms designed to discriminate echoes reflected from leads and open water and (ii) SSH estimated derived from contemporaneous ENVISAT radar altimetry. We also assessed the accuracy of the GSFC algorithm lead detections using coincident satellite imagery.

- To improve current techniques through the development of a new algorithmic-based method for sea surface height estimation over Arctic sea ice.

We have developed two new algorithms for the retrieval of SSH in the Arctic Ocean. The "UCL algorithm" is designed to distinguish laser returns from leads and open water and calculate SSH estimates based on the elevations associated with these echoes. The "large lead algorithm" is designed to identify leads greater than ~ 5 km wide. This algorithm was used to obtain a baseline reference set of SSH measurements, against which the SSH estimates of the GSFC and UCL algorithms could be assessed. The UCL and large lead algorithms are valid for ice-covered ocean across basin-wide scales, for both the autumn and spring seasons.

- To investigate the ability of algorithmic-based methods to identify openings within the ice pack (e.g. leads) using spatially and temporally coincident satellite imagery from MODIS and AATSR.

We compared laser pulse returns identified by the GSFC and UCL algorithms as reflections from the sea surface with two coincident satellite images which contained good examples of individual sea ice floes and leads. We analysed a 250-m resolution MODIS image acquired in March 2003 and a 1-km AATSR image acquired in March 2005. However, at a resolution of 170-m, the ICESat footprint is smaller than the resolution of the satellite imagery and it is therefore possible that leads detected by the GSFC and UCL algorithms were not visible to the human eye. We found that each algorithm had advantages and limitations associated with discriminating leads. The GSFC algorithm identified more leads than the UCL algorithm, thus providing more data points for the calculation of local SSH. The GSFC algorithm was however associated with more false alarms than the UCL algorithm, so that SSH estimates derived using the GSFC algorithm may be contaminated with elevations from sea ice floes.

- To map sea surface height in the Arctic Ocean for the time periods associated with ICESat operations.

We generated monthly average SSH estimates for five ICESat laser operations periods and we compared the results derived from the UCL, GSFC, and large lead algorithms. We also derived an ICESat mean sea surface (MSS) based on data from five ICESat laser campaigns gathered over a two-year period between February 2003 and March 2005. The ICESat MSS extends knowledge of the MSS above 81.5°N, to 86°N, for the first time.

- To compare sea surface height measurements derived from ICESat data with coincident measurements from ENVISAT RA-2 data.

We have provided the first maps of comparisons between ICESat and ENVISAT estimates of the sea surface topography in the Earth's ice-covered polar regions. We presented our comparison of SSH estimates in terms of SLA differences, where SLA were calculated with respect to the long term MSS and extended to 81.5°N. We presented comparisons of ICESat SLA with contemporaneous ENVISAT SLA over monthly and 3-day time scales. Comparisons of spatially and temporally coincident data, through crossover analysis, minimised differences due to varied sampling (as a

result of different satellite orbit patterns) of the natural variability of the sea surface topography (i.e. the time-variant component of dynamic ocean topography).

- To use knowledge of the sea surface in conjunction with an accurate geoid model to map dynamic ocean topography.

We highlighted the potential of using knowledge of the MSS, derived from satellite altimetry, in conjunction with a geoid model to map mean dynamic topography (MDT). We used the ICESat MSS in combination with the hybrid geoid to derive apparent MDT in the Arctic Ocean. We compared our results to MDT estimates calculated using the ArcGICE MSS derived from ERS-2 radar altimetry, as well as to the OCCAM numerical model of MDT.

- To investigate the potential for using sea surface height measurements collected throughout various ICESat laser campaigns to map gravity anomalies in the Arctic Ocean up to the limit of coverage at 86°N.

In collaboration with Dr. D. McAdoo, we estimated gravity field anomalies in the Arctic Ocean covering a region between 74°N and 86°N using ICESat SSH data. The ICESat gravity map depicted the major features of Arctic Ocean bathymetry including the Lomonosov and Gakkel Ridges and the Canada, Makarov and Eurasian Basins.

- To examine the use of ICESat data in conjunction with sea level estimates derived from satellite altimetry data to measure snow ice freeboard, from which sea ice thickness can be deduced, and to compare these measurements with contemporaneous radar altimetric estimates of ice freeboard.

We demonstrated the potential of satellite laser altimetry data from ICESat for the retrieval of snow freeboard in the Arctic Ocean. We compared retrievals based on ICESat SSH estimates derived using the UCL algorithm with those derived using the GSFC algorithm. We also verified that ENVISAT SSH estimates can be used in place of ICESat SSH estimates for the retrieval of snow freeboards. We compared laser altimetric snow freeboard estimates with coincident radar altimetric estimates of sea ice freeboard from ENVISAT.

- To investigate the feasibility of combining satellite laser and radar altimetric measurements of sea ice freeboard to measure snow loading on sea ice.

We explored the possibility of combining satellite laser and radar altimetric retrievals of freeboard to deduce snow loading on sea ice by comparing ICESat snow freeboard data gathered during autumn 2003 with coincident ENVISAT ice freeboard estimates. Although the spatial distribution of snow depth derived from the altimetric freeboard estimates showed some agreement with the climatology, the magnitude of snow loading on sea ice differed to that predicted by the climatology in some regions.

8.2.2 Summary of Key Findings

Through achieving the primary objectives set out above we obtained a number of key results. We summarise these findings here.

- **Sea surface topography of the Arctic Ocean**

Analysis of the variability of sea surface topography of the Arctic Ocean comprised a major portion of the results presented in this thesis. Outlined below are the main findings associated with this research.

During the autumn ICESat laser campaigns the UCL algorithm produced SSH estimates that compared better to contemporaneous ENVISAT SSH estimates than the GSFC algorithm. During the spring campaigns the two algorithms produce SSH estimates of similar accuracy.

The ICESat L2a and L3a campaigns provided data which compared best to coincident ENVISAT data with differences of ≤ 2 cm for monthly averaged SLA estimates. The L1 SSH data also compared well to the ENVISAT SSH measurements and the difference in monthly averaged SLA estimates was ≤ 5 cm. Estimates of 3-day mean SLA derived from all four methods (ENVISAT RA-2 algorithm, ICESat UCL algorithm, ICESat GSFC algorithm, and ICESat large lead algorithm) were consistent in the cases of the best available ICESat data (i.e. the L2a and L3a datasets).

The ENVISAT SSH estimates were more self-consistent over 3-day periods than the ICESat SSH estimates. This suggests that the ENVISAT SSH retrievals are more accurate than contemporaneous ICESat measurements.

There remain systematic biases in the ICESat laser elevation data. Biases of up to ±10 cm with respect to coincident ENVISAT data were recorded. These biases may be attributable to remaining systematic pointing errors in the ICESat data.

We revealed that there is a large variability in the SLA signal, as derived from satellite altimetry, over short timescales. This signal can be up to ±10 cm. We believe that there may be errors associated with this signal possibly as a result of problems in the corrections applied to the altimetry data. This finding therefore requires further investigation.

Large dual-satellite crossover differences exist in both the radar and laser altimetric datasets, where one or both of the SSH estimates are incorrect. These differences could be due in part to errors in the SSH retrieval process (i.e. poor performance of one or both of the algorithms) and a time-dependent error in the retrieval process remains a possibility. Crossover differences may also be due to geophysical effects, for example due to (i) the application of inconsistent ocean tide corrections between the two satellite datasets, or (ii) remaining errors in the inverse barometer correction. Further investigation is required to explore these possibilities.

We identified five periods in the datasets when dual-satellite crossover height differences were small (i.e. $\leq \pm 3$ cm). During these time periods, the SSH estimates are consistent between ICESat and ENVISAT. Comparisons of geophysical data such as sea ice freeboard should therefore be possible during these time periods.

- **Arctic sea ice freeboard**

ICESat ranges to the air/snow interface of a sea ice floe and thus the laser altimetric freeboard measurement comprises both the sea ice freeboard and any overlying snow, a quantity we refer to as the "snow freeboard". We used ICESat surface elevation measurements gathered over the Arctic Ocean in conjunction with along-track SSH

measurements estimated derived from (i) the UCL algorithm, (ii) the GSFC algorithm, and (iii) ENVISAT radar altimetry data, to calculate three different estimates of Arctic snow freeboard. To investigate the internal consistency of each snow freeboard dataset we compared snow freeboard estimates from two distinct observation periods during each laser campaign. We expect a strong relationship between the snow freeboard results from the first half of a given laser campaign with those from the second half of the campaign.

During the autumn laser campaigns the snow freeboard retrievals based on the UCL algorithm SSH estimates had higher correlation coefficients than those based on the GSFC algorithm SSH estimates. This result was consistent with a key finding relating to the SSH analysis, where the dual-satellite crossover height differences between the SSH estimates from ENVISAT and the UCL algorithm were smaller than those between the SSH estimates from ENVISAT and the GSFC algorithm, during the autumn campaigns. The correlation coefficients associated with the spring-time snow freeboards using the two alternative ICESat SSH estimates were similar. The correlations were also stronger during the spring periods than during the autumn periods.

We found that ICESat elevation measurements used in conjunction with contemporaneous ENVISAT SSH estimates resulted in freeboard comparisons which had the strongest correlations. This method represented the ideal procedure for obtaining snow freeboards which were the most consistent, from ICESat. We also demonstrated any inaccuracies in the sea surface topography manifest themselves as anomalous freeboard estimates using our methodology.

Comparison of ICESat snow freeboard estimates with contemporaneous ENVISAT ice freeboard estimates illustrated that, as expected, the snow freeboard estimates were higher than the equivalent ice freeboard estimates. This result illustrates the potential for snow depth retrieval using coincident satellite laser and radar altimetric freeboard measurements.

- **Snow depth on Arctic sea ice**

The determination of snow depth on Arctic sea ice using satellite laser and radar altimetry data is dependent on accurate estimates of both snow and ice freeboard. There remain uncertainties in both the satellite laser and radar altimetric retrievals of sea ice freeboard and inaccuracies in either freeboard estimate will give rise to inaccurate snow depths. Although the spatial distribution of snow depth derived from the altimetric freeboard estimates showed some agreement with the climatology, the magnitude of snow loading on sea ice differed to that predicted by the climatology in some regions. Further investigation of (i) the biases associated with each of the freeboard estimates and (ii) the penetration of the laser and radar pulses into the snow is required. Nevertheless, with additional research, this technique represents an exciting application of the combination of laser and radar altimetry over sea ice for the retrieval of a parameter of significant climatological interest.

- **Mean dynamic topography in the Arctic Ocean**

Estimates of MDT derived from two independent altimetric MSS datasets (the ICESat MSS and the ArcGICE MSS) were correlated and showed good spatial agreement over long wavelengths. Comparisons with the OCCAM model prediction of MDT indicated that remaining differences between observational and model data may be due to (i) a lack of bathymetric detail in the numerical model and (ii) remaining small-scale errors in the marine geoid.

- **Marine gravity field of the Arctic Ocean**

Although the gravity field of the Arctic Ocean is not directly related to the climatic processes of the Arctic region, it is of interest in terms of global geodesy and marine geophysics. The ICESat gravity map covers the region 74°N to 86°N and depicts the major features of Arctic Ocean bathymetry including the Lomonosov and Gakkel Ridges and the Canada, Makarov and Eurasian Basins. Long wavelength errors exist in the ICESat gravity field but there is good agreement between the ERS-1 and ICESat gravity estimates at shorter wavelengths. New details of the tectonic fabric of the high Arctic (i.e. above 81.5°N) were revealed for the first time, including a possible extinct spreading centre in the Makarov Basin (*D. McAdoo*, personal

communication). The information contained in the ICESat gravity field could contribute to the enhancement of the Arctic Gravity Project (ArcGP) gravity grids in the future.

8.3 Directions for Future Work

8.3.1 Inclusion of supplementary ICESat data

The ICESat data presented in this thesis represents data gathered during five laser campaigns over a two-year period beginning March 2003. The data can be updated in the future by including results from the L3d and L3e laser campaigns as well as those from forthcoming campaigns. Furthermore ground-segment reprocessing of each laser campaign is on-going. Data processed under high releases should improve the overall accuracy of the ICESat data and correct for remaining sources of error such as the effects of systematic pointing biases. The accuracy and spatial resolution of both the ICESat MSS and the ICESat gravity field should be improved via inclusion of additional data from other ICESat laser campaigns and higher data releases.

8.3.2 Development of an optimised algorithm for sea surface height retrieval

Each of the algorithms described in Chapter 4 for the retrieval of SSH measurements from ICESat data had advantages and limitations. For each algorithm there was a compromise between unambiguous identification of surface returns from leads versus the inclusion of more data points with possible contamination from elevations associated with sea ice floes. We suggest that the development of an optimised algorithm comprising aspects of all three methods for detecting SSH in the Arctic Ocean would be a reasonable next step. Further work should include determination of the optimal combination of parameters associated with the standard deviation of elevation, reflectivity, and pulse shape, to provide the highest number of surface returns from leads and open-ocean whilst avoiding contamination by sea ice in the measurements. Furthermore an adaptive algorithm which could take into account the seasonal and regional distribution of the leads in the ice pack would be an advantage.

8.3.3 Investigation of the sea level anomaly signal

We revealed that there was a large variability in the sea level anomaly (SLA) signal over short timescales, which could be up to ±10 cm. Further investigation is required to ascertain whether some of the variability may be due to problems in the corrections applied to the altimetry data. For example, additional research is needed to test whether the inverse barometer correction is fully compensating for atmospheric pressure loading and wind effects over the Arctic Ocean.

8.3.4 Investigation of the differences between radar and laser altimetric estimates of SSH

We demonstrated that large dual-satellite crossover differences exist between the satellite laser and radar estimates of Arctic Ocean SSH. The differences exist where one or both of the SSH estimates are incorrect. These differences could be due in part to (i) errors in the SSH retrieval process or (ii) the fact that the tidal corrections applied to the radar and laser datasets were based on alternative tide models. In addition, further investigation of geophysical effects, such as the application of inconsistent ocean tide corrections between the two satellite datasets, or possible remaining errors in the inverse barometer correction, is required.

8.3.5 Snow depth retrieval

We presented an application of the combination of laser and radar altimetry over sea ice for the retrieval of snow depth. The technique requires accurate estimates of both snow and ice freeboard derived from laser and radar altimetry. There remain uncertainties in both the satellite laser and radar altimetric retrievals of sea ice freeboard which can result in anomalous estimates of snow depth. Further investigation of (i) the biases associated with each of the freeboard estimates and (ii) the penetration of the laser and radar pulses into the snow is required. Nevertheless, early snow depth results derived from comparisons of coincident laser and radar altimetry showed some agreement with the existing snow depth climatology. We conducted our analysis for data gathered during the ICESat L2A campaign. Future

work could include repeating the analysis for ICESat data gathered during other laser operations periods.

8.3.6 Extending the analysis to Antarctic sea ice

The work presented in this thesis focused on applications of ICESat data over the Arctic Ocean. The analysis can however be extended to the Antarctic region for the study of sea ice in the Southern Ocean. The sea ice regime in the marginal seas surrounding Antarctica is different to that of the Arctic Ocean. There is a higher percentage of first year sea ice and little of the sea ice formed during the winter survives the summer melt season. Precipitation in the region is also higher than in the Arctic, so that snow loading on sea ice is more significant. This can give rise to flooded sea ice floes, where the snow/ice interface is below the water surface. The algorithms described in this thesis for the retrieval of SSH, and snow freeboard, from ICESat data may need to be amended to take account of the different ice regime in the Antarctic region. Further work could also include combining sea surface height derived from ENVISAT radar altimetry with ICESat elevation measurements to retrieve estimates of Antarctic sea ice freeboard.

Finally, the development of an updated MSS in the Southern Ocean offshore Antarctica would be useful to improve the existing marine geoid models of the region. Such a MSS could potentially combine time-averaged laser and radar altimetric estimates of SSH, providing any biases between the satellite estimates were accounted for. An accurate geoid model could be useful for future studies of ocean circulation in the Southern Ocean.

Appendix A: List of Acronyms

ACIA: Arctic Climate Impact Assessment
AOGCM: Atmosphere-Ocean Global Climate Model
ArcGP: Arctic Gravity Project
CPOM: Centre for Polar Observation and Modelling
CRS: Collimated Reference Source
DOT: Dynamic Ocean Topography
GLAS: Geoscience Laser Altimeter System
GPS: Global Positioning System
GRACE: Gravity Recovery and Climate Experiment
GSAS: GLAS Science Algorithm Software
GSFC: Goddard Space Flight Centre
ICESat: Ice, Cloud and land Elevation Satellite
IPCC: Intergovernmental Panel on Climate Change
ISIPS: ICESat-Science Investigator-led Processing System.
IST: Instrument Star Tracker
ITRF: IERS Terrestrial Reference Frame
LASER: Light Amplification by Stimulated Emission of Radiation
LiDAR: Light distance and ranging
LRA: Laser Retroreflector Array
LRS: Laser Reference Sensor
MOLA: Mars Orbiting Laser Altimeter
MDT: Mean dynamic topography
MSS: Mean Sea Surface
OCCAM: Ocean Circulation and Climate Advanced Modelling
PAD: Precision Attitude Determination
POD: Precision Orbit Determination
RADAR: Radio Detection and Ranging
RGPS: RADARSAT Geophysical Processor System
SHA: Surface Height Anomalies
SLA: Sea Level Anomalies
SMC: Scan Manoeuvre Calibrations
SSH: Sea Surface Height
SSM/I: Special Sensor Microwave/Imager
SRES: Special Report on Emissions Scenarios
SRS: Stellar Reference System

Appendix B: Deriving Thresholds for the Discrimination of Leads from ICESat data

To identify GLAS echoes that originate over flat-water surfaces such as leads, we derived a set of criteria based on the characteristics of the received (Rx) pulse. Analysis of a set of five ICESat profiles of elevation, reflectivity, and the parameters describing pulse shape, in combination with near-coincident MODIS (250 m resolution) and AATSR (1 km resolution) imagery, allowed us to derive parameter thresholds that indicate laser returns from flat, water surfaces. The dates of the ICESat overpasses and the near-coincident imagery are presented in Table B.1. Using the imagery we identified the location of leads in the along-track profiles of the relevant ICESat parameters. Based on these profiles we were able to derive parameter thresholds which were associated with leads within the ice pack. These results are presented in Table B.2.

Track #	Image Type	ICESat Track	Satellite Image	Time Difference (hours)
1	MODIS	13 March 2003 05:05	13 March 2003 00:05	5
2	AATSR	13 March 2003 08:14	12 March 2003 22:01	10
3	MODIS	09 March 2003 10:50	09 March 2003 21:55	11
4	AATSR	07 March 2005 04:36	07 March 2005 08:14	3.6
5	RADARSAT	01 March 2004 14:10	03 March 2004 12:58	47

Table B.1 Dates and times of ICESat overpasses presented in Figures B.1 to B.5 and the near-coincident satellite imagery.

The analysis of satellite images and along-track ICESat profiles is presented in Figures B.1 to B.5. Leads are identified with yellow numbers in the imagery, and blue markings and numbers in the ICESat profiles. The derived parameter thresholds are indicated with green lines. Note that the ICESat elevations presented here are calculated with respect to the hybrid geoid (see Section 4.2.1.2).

Track #	Elevation (m) (*elev*)	Xcorrel_max (*Xcorrel_max*)	Reflectivity (*i_reflctUncorr*)	Received pulse FWHM (*Rx_fwhm*)	FWHM deviation (*Rx_fwhm - Tx_fwhm*)	Skewness deviation (*Rx_skew - Tx_skew*)
1	-0.4 - -0.1	0.975 - 0.992	0.25 - 0.45	6.5 - 8.0	0.30 - 2.00	-0.30 - 0.30
2	-0.1 - 0.1	0.975 - 0.990	0.13 - 0.48	6.8 - 8.0	0.75 - 1.70	-0.25 - 0.25
3	-0.1 - 0.1	0.975 - 0.990	0.25 - 0.50	6.5 - 8.3	0.00 - 2.00	-0.60 - 0.20
4	-0.2 - 0.0	0.975 - 1.000	0.15 - 0.48	5.3 - 6.0	-0 40 - 0.50	-0.30 - 0.30
5	-0.3 - 0.1	0.976 - 1.000	0.16 - 0.47	6.0 - 7.0	-0.40 - 0.50	-0.30 - 0.45

Table B.2 ICESat parameter thresholds associated with leads in the near-coincident satellite imagery.

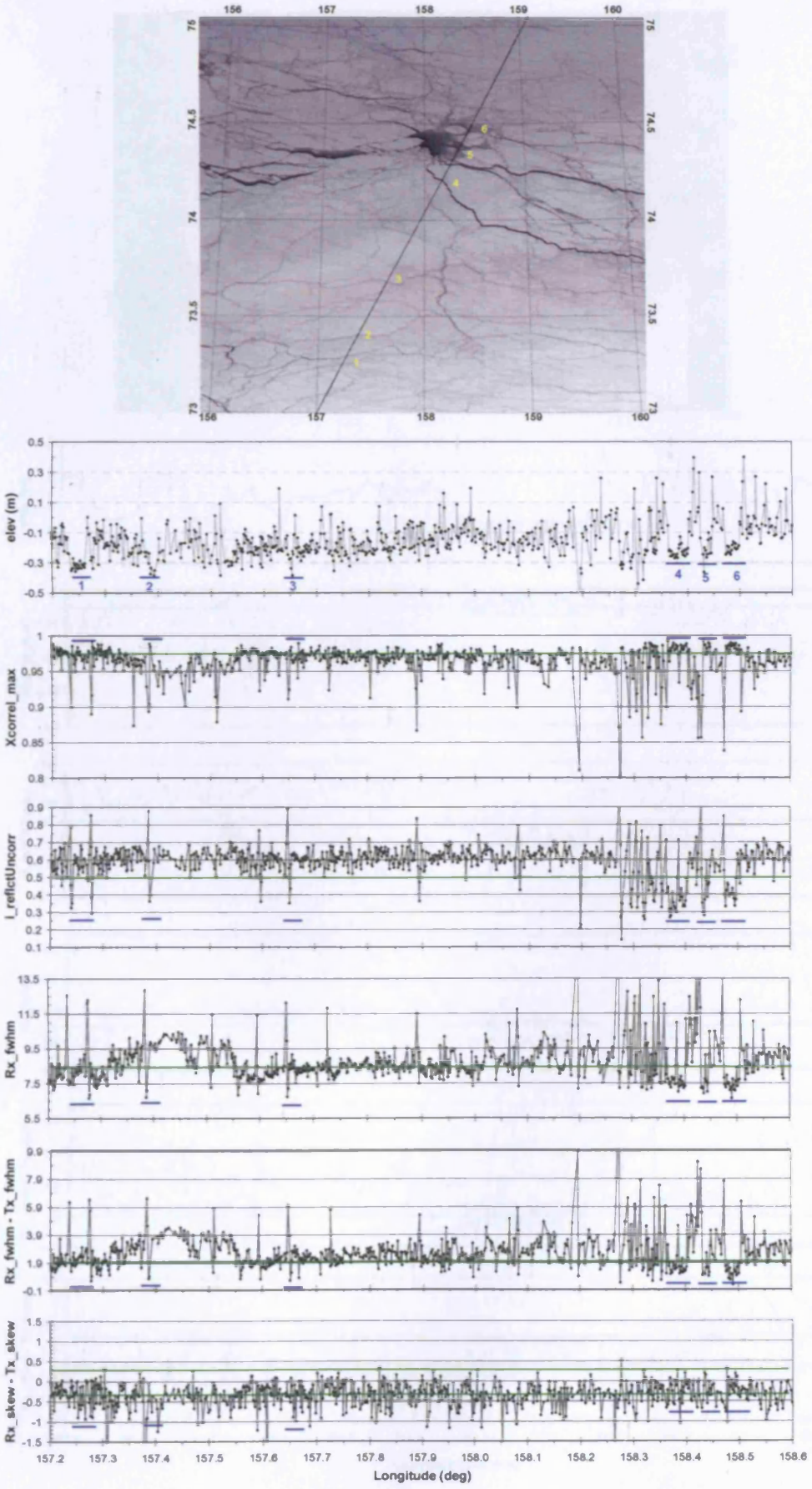

Figure B.1. Near-coincident MODIS and ICESat data acquired on 13th March 2003 (*Track 1*).

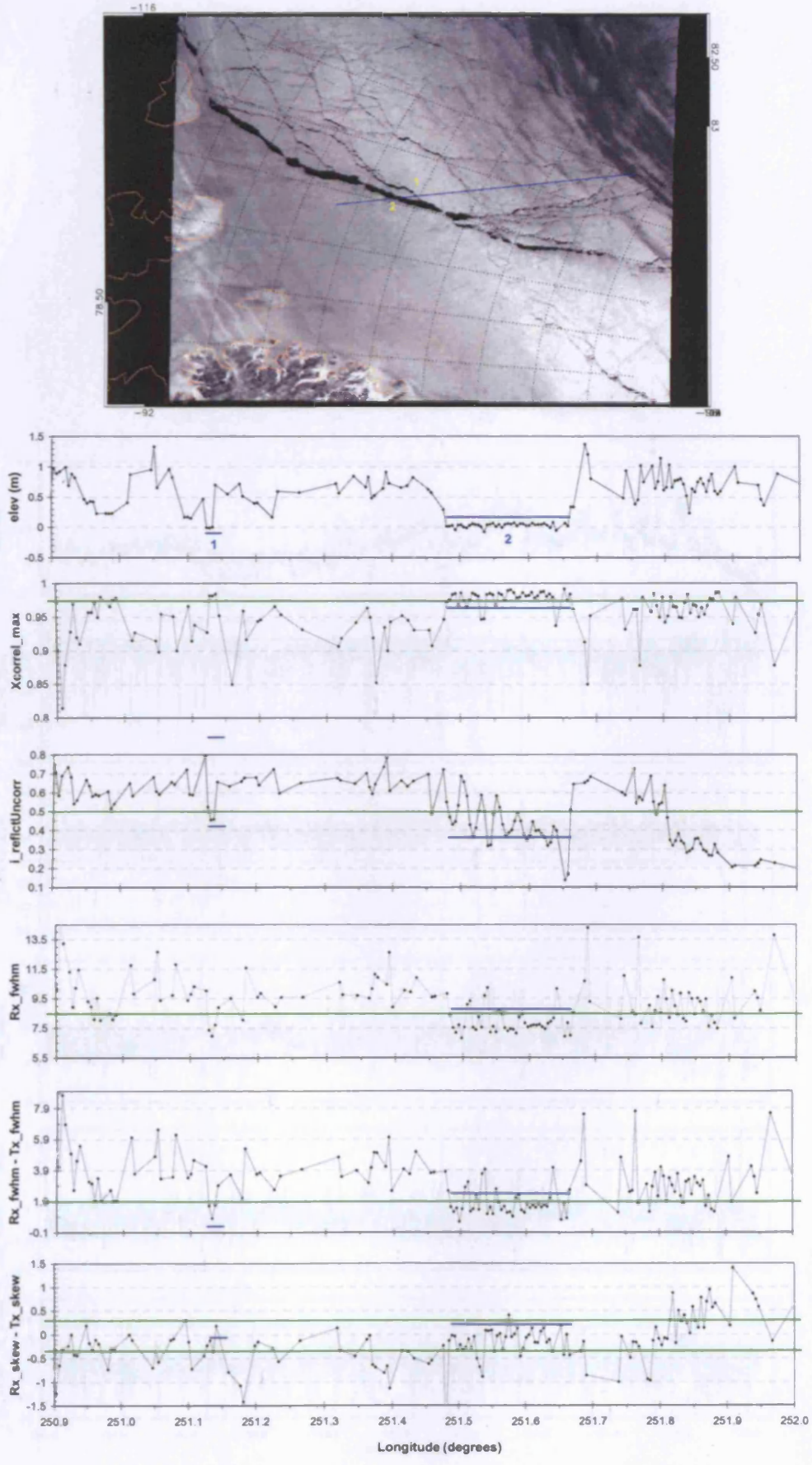

Figure B.2. Near-coincident AATSR and ICESat data acquired on 13th March 2003 (*Track 2*).

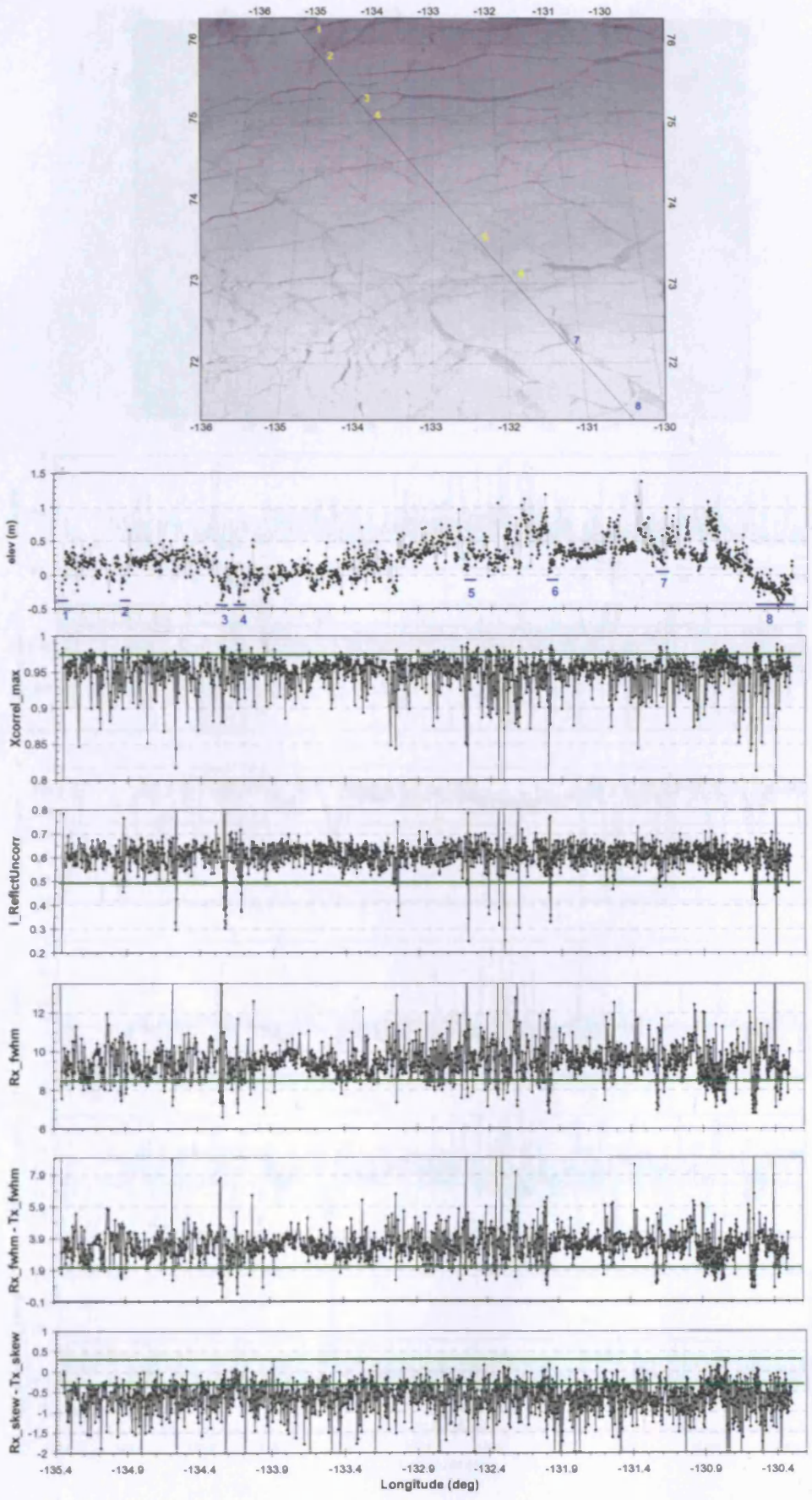

Figure B.3. Near-coincident MODIS and ICESat data acquired on 9th March 2003 (*Track 3*).

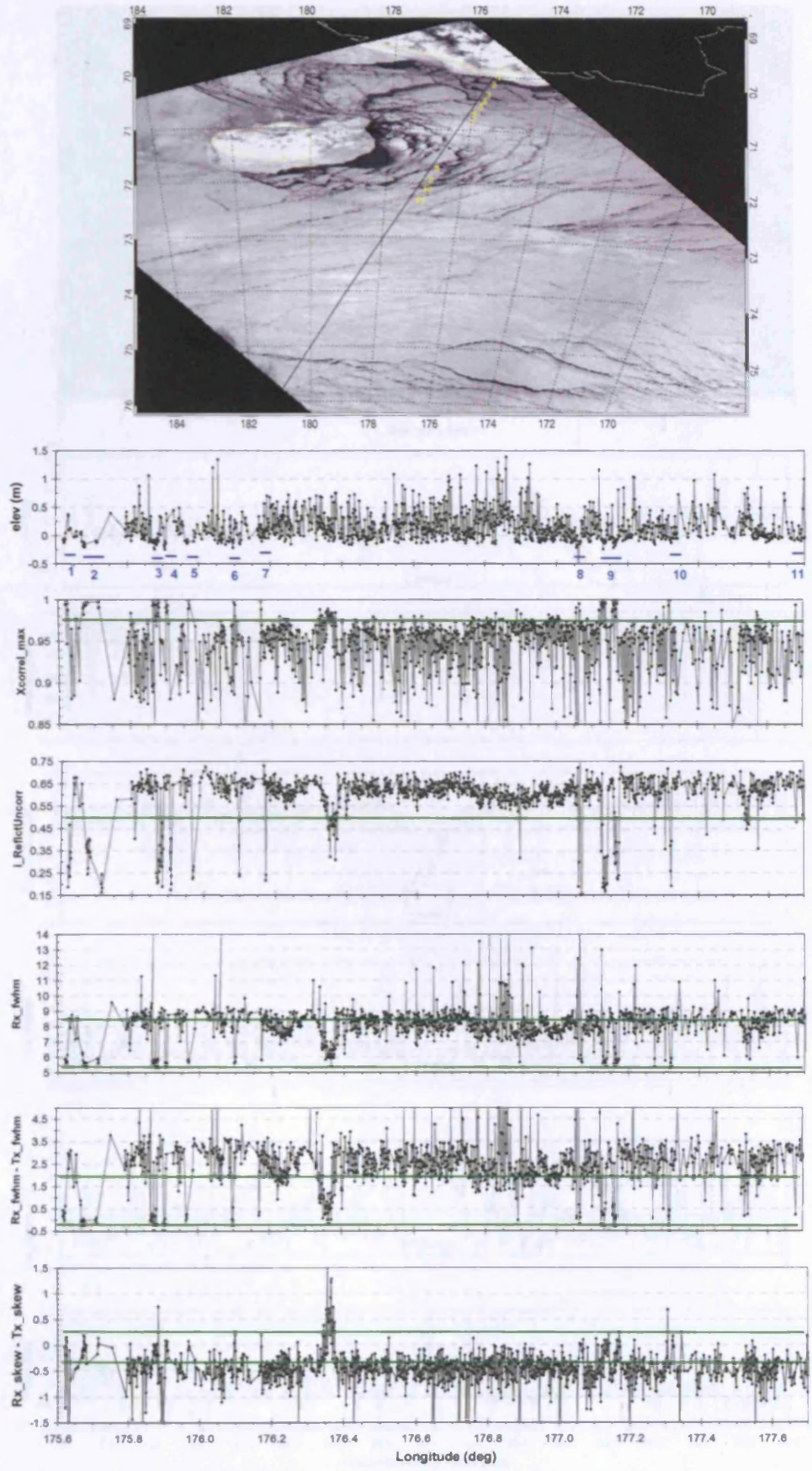

Figure B.4. Near-coincident AATSR and ICESat data acquired on 7th March 2004 (*Track 4*).

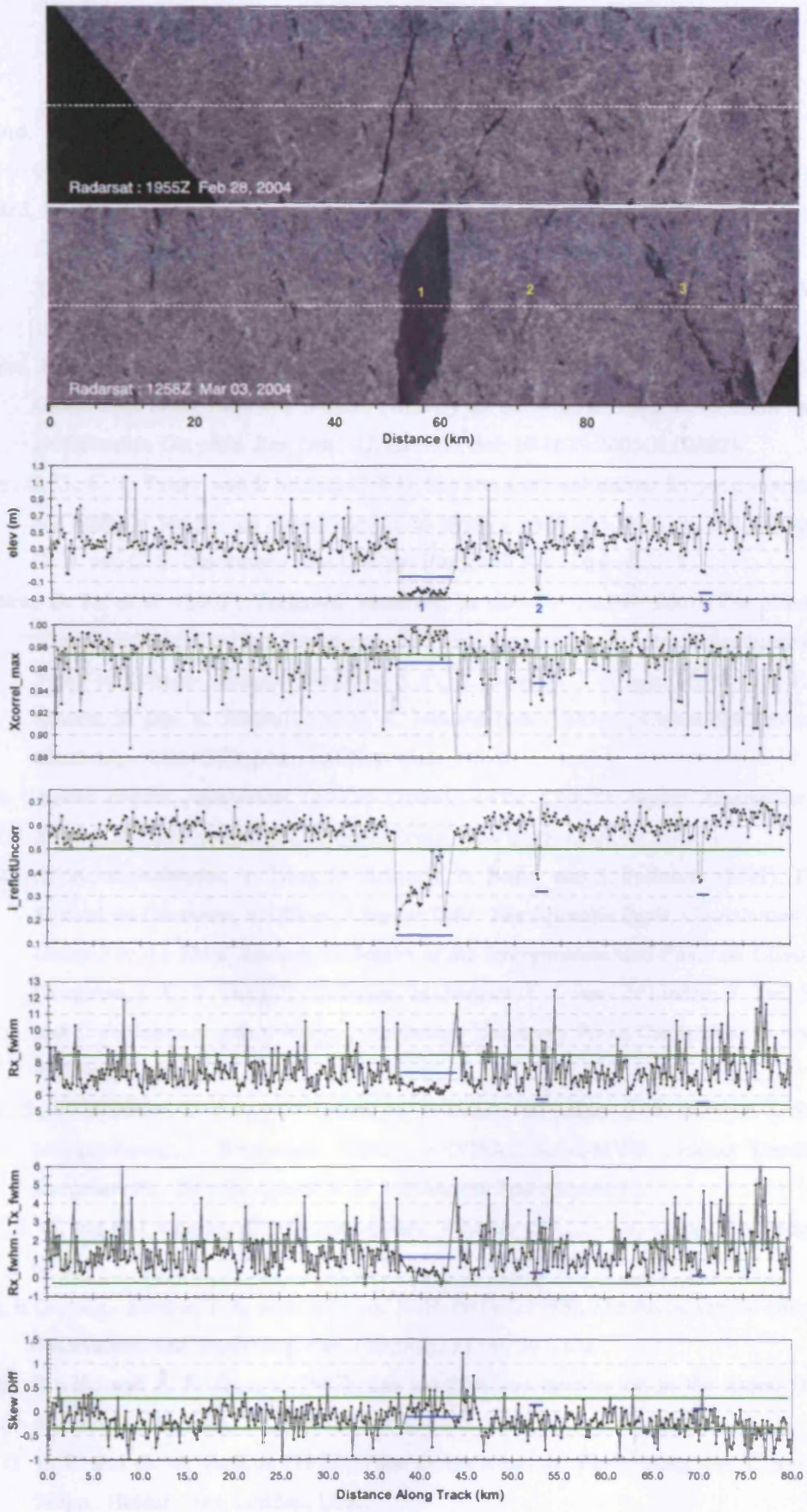

Figure B.5. Near-coincident RADARSAT and ICESat data acquired on 1st March 2005 (*Track 5*). The satellite imagery is re-produced from Figure 12 in *Kwok et al.* [2006].

Bibliography

Aagaard, K. and E. C. Carmack (1989), The role of sea ice and other fresh water in the Arctic circulation, *J. Geophys. Res.*, *94*, 14485-14498.

Aagaard, K. and E. C. Carmack (1994), The Arctic Ocean and climate: a perspective, in *The Polar Oceans and Their Role in Shaping the Global Environment*, Johannessen, O. M., R. D. Muench and J. E. Overland (eds.), Geophysical Monograph, 85, 525pp., AGU, Washington DC, USA, 1994.

Abshire, J. B., X. Sun, H. Riris, J. M. Sirota, J. F. McGarry, S. Palm, D. Yi, and P. Liiva (2005), Geoscience Laser Altimeter System (GLAS) on the ICESat Mission: On-orbit measurement performance, *Geophys. Res. Lett.*, *32*, L21S02, doi: 10.1029/2005GL024028.

Ainley, D. G., C. T. Tynan, and I. Stirling (2003), Sea ice: a critical habitat for polar marine mammals and birds, in *Sea Ice: an introduction to its physics, chemistry, biology, and geology*, Thomas, D. N. and G. S. Dieckmann (eds.),402pp, Blackwell Sci., Oxford, U. K.

Albritton, D. L., et al. (2001), Technical Summary, in *Climate Change 2001: The Scientific Basis, Contribution of Working Group I to the Third Assessment Report of the Intergovernmental Panel on Climate Change*, Houghton, J. T., Y. Ding, D. J. Griggs, M. Noguer, P. J. van der Linden, X. Dai, K. Maskell, and C. A. Johnson (eds.), 881pp., Cambridge University Press, Cambridge, United Kingdom and New York, USA.

Arctic Climate Impact Assessment (ACIA) (2004), *Arctic Climate Impact Assessment: Scientific Report*, 200pp., Cambridge University Press, New York, USA.

Baede, A.P.M., E. Ahlonsou, Y. Ding, D. Schimel, B. Bolin, and S. Pollonais (2001), The Climate System: an Overview, in *Climate Change 2001: The Scientific Basis, Contribution of Working Group I to the Third Assessment Report of the Intergovernmental Panel on Climate Change*, Houghton, J. T., Y. Ding, D. J. Griggs, M. Noguer, P. J. van der Linden, X. Dai, K. Maskell, and C. A. Johnson (eds.), 881pp., Cambridge University Press, Cambridge, United Kingdom and New York, USA.

Baker, S., O. Bombaci, C. Zeli, P. Venditti, O. Z. Zanife, B. Soussi, J. P. Dumont, J. Stum, M. P. Milagro-Perez, J. Benveniste (2002), ENVISAT RA-2/MWR Product Handbook, *ESA Document PO-TN-ESR-RA-0050, v1.2*, European Space Agency.

Barry, R. G. and R. J. Chorley (2003), *Atmosphere, Weather and Climate*, 421pp., Routledge, London, U. K.

Barry, R G., M. C. Serreze, J. A. Maslanik, and R. H. Preller (1993), The Arctic sea ice-climate system: observations and modelling, *Rev. Geophys.*, *31* (4), 397-422.

Bourke, R. H., and R. P. Garrett (1987), Sea ice thickness distribution in the Arctic Ocean, *Cold Regions Sci. Technol.*, *13*, 259-280.

Box, G. E. P. and G. M. Jenkins (1976), *Time Series Analysis: Forecasting and Control*, rev. ed., 545pp., Holden-Day, London, U. K.

Brenner, A. C., R. A. Bindschadler, R. H. Thomas, H. J. Zwally (1983), Slope-induced errors in radar altimetry over continental ice sheets, *J. Geophys. Res.*, *88* (C3): 1617-1623.

Brenner, A., J. Zwally, C. Bentley, B. Csatho, D. Harding, M. Hofton, B. Minster, L. Roberts, J. Saba, R. Thomas, D. Yi (2003), Derivation of range and range distributions from laser pulse waveform analysis for surface elevations, roughness, slope and vegetation heights, *GLAS ATBD, v. 4.1*, NASA Goddard Space Flight Centre, Greenbelt, MD, U.S.A.

Bufton, J. L. (1989), Laser altimetry measurements from aircraft and spacecraft, *Proc. of IEEE*, 77(3), 463–477.

Carrere, L., and F. Lyard (2003), Modeling the barotropic response of the global ocean to atmospheric wind and pressure forcing - comparisons with observations, *Geophys. Res. Lett.*, *30*(6), 1275, doi:10.1029/2002GL016473.

Cavalieri, D. J. and J. C. Comiso (2000), Algorithm theoretical basis document (ATBD) for the AMSR-E sea ice algorithm, *AMSR-E ATBD*, NASA Goddard Space Flight Centre, Greenbelt, MD, U.S.A.

Cavalieri, D. J., C. L. Parkinson, and K. Y. Vinnikov (2003), 30-Year satellite record reveals contrasting Arctic and Antarctic decadal sea ice variability, *Geophys. Res. Lett.*, *30*(18), 1970, doi:10.1029/2003GL018031.

Chelton, D. B., J. C. Ries, B. J. Haines, L. L. Fu and P. S. Callahan (2001), Satellite Altimetry, in *Satellite Altimetry and Earth Sciences: a handbook of techniques and applications*, *International geophysics series*, *v. 69*, Lee-Leung Fu and Anny Cazenave (eds.), 463pp., Academic Press, London, U. K.

Church, J. A., et al. (2001), Changes in Sea Level, in *Climate Change 2001: The Scientific Basis, Contribution of Working Group I to the Third Assessment Report of the Intergovernmental Panel on Climate Change*, Houghton, J. T., Y. Ding, D. J. Griggs, M. Noguer, P. J. van der Linden, X. Dai, K. Maskell, and C. A. Johnson (eds.), 881pp., Cambridge University Press, Cambridge, United Kingdom and New York, USA.

Coachman, L. K. and K. Aagaard (1988), Transports through Bering Strait: Annual and interannual variability, *J. Geophys. Res.*, *93*, 15535-15539.

Cochran, J. R., M. H. Edwards, B. J. Coakley (2006), Morphology and structure of the Lomonosov Ridge, Arctic Ocean, *Geochem. Geophys. Geosyst.*, *7*, Q05019, doi:10.1029/2005GC001114.

Comiso, J. C. (2002), A rapidly declining perennial sea ice cover in the Arctic, *Geophys. Res. Lett.*, *29*(20), 1956, doi:10.1029/2002GL015650.

Comiso, J. C. (2003), Large-scale characteristics and variability of global sea ice cover, in *Sea Ice: an introduction to its physics, chemistry, biology, and geology*, Thomas, D. N. and G. S. Dieckmann (eds.), 402pp., Blackwell Science, Oxford, U. K.

Comiso and Parkinson (2004), Satellite-observed changes in the Arctic, *Phys. Today*, *57*(8), 38–44.

Cubasch, U., et al. (2001), Projections of Future Climate Change, in *Climate Change 2001: The Scientific Basis, Contribution of Working Group I to the Third Assessment Report of the Intergovernmental Panel on Climate Change*, Houghton, J. T., Y. Ding, D. J. Griggs, M.

Noguer, P. J. van der Linden, X. Dai, K. Maskell, and C. A. Johnson (eds.), 881pp., Cambridge University Press, Cambridge, United Kingdom and New York, USA.

Curry, J. A., J. L. Schramm and E. E. Ebert (1995), Sea ice-albedo climate feedback mechanism, *J. of Climate*, *8*(2), 240-247.

Dickson, R. R., E. M. Gmitrowicz and A. J. Watson (1990), Deep-water renewal in the northern North Atlantic, *Nature*, *344*, 848-850.

Diekmann G. S. and H. H. Hellmer (2003), The importance of sea ice: an overview, in *Sea Ice: an introduction to its physics, chemistry, biology, and geology*, Thomas, D. N. and G. S. Dieckmann (eds.), 402pp., Blackwell Science, Oxford, U. K.

Divine, D. V., and C. Dick (2006), Historical variability of sea ice edge position in the Nordic Seas, *J. Geophys. Res.*, *111*, C01001, doi:10.1029/2004JC002851.

Duda, D. P., J. D. Spinhirne and E. W. Eloranta (2001), Atmospheric multiple scattering effects on GLAS altimetry - Part I: Calculations of single pulse bias, *IEEE Trans. Geosci. Rem. Sens.*, *39*, 92-101.

Eicken H. (2003), From the microscopic, to the macroscopic, to the regional scale: growth, microstructure and properties of sea ice, in *Sea Ice: an introduction to its physics, chemistry, biology, and geology*, Thomas, D. N. and G. S. Dieckmann (eds.), 402pp., Blackwell Science, Oxford, U. K.

Ekholm, S., J. L. Bamber, W. B. Krabill (2002), The use of airborne laser data to calibrate satellite radar altimetry data over ice sheets, *J. Geodyn.*, *34*, 377-390.

Farrell, S. L., S. W. Laxon, H. J. Zwally, A. C. Brenner and D. Yi (2003), Sea ice elevation from ICESat/GLAS laser altimetry, *Eos Trans. AGU*, *84*(46), Fall Meet. Suppl., Abstract C31A-07.

Folland, C.K., et al. (2001), Observed Climate Variability and Change, in *Climate Change 2001: The Scientific Basis, Contribution of Working Group I to the Third Assessment Report of the Intergovernmental Panel on Climate Change*, Houghton, J. T., Y. Ding, D. J. Griggs, M. Noguer, P. J. van der Linden, X. Dai, K. Maskell, and C. A. Johnson (eds.), 881pp., Cambridge University Press, Cambridge, United Kingdom and New York, USA.

Forsberg, R., and H. Skourup (2005), Arctic Ocean gravity, geoid and sea-ice freeboard heights from ICESat and GRACE, *Geophys. Res. Lett.*, *32*, L21502, doi:10.1029/2005GL023711.

Fricker, H. A., A. Borsa, B. Minster, C. Carabajal, K. Quinn, and B. Bills (2005), Assessment of ICESat performance at the salar de Uyuni, Bolivia, *Geophys. Res. Lett.*, *32*, L21S06, doi:10.1029/2005GL023423.

Giles, K. A. (2006), Combined airborne laser and radar altimeter measurements over sea ice, *in preparation*.

Gill, A. E. (1982), Atmosphere-Ocean Dynamics, *International geophysics series*, v.*30*, 662 pp., Academic Press, London, U. K.

Giorgi, F., et al. (2001), Regional Climate Information – Evaluation and Projections, in *Climate Change 2001: The Scientific Basis, Contribution of Working Group I to the Third Assessment Report of the Intergovernmental Panel on Climate Change*, Houghton, J. T., Y. Ding, D. J.

Griggs, M. Noguer, P. J. van der Linden, X. Dai, K. Maskell, and C. A. Johnson (eds.), 881pp., Cambridge University Press, Cambridge, United Kingdom and New York, USA.

GSAS v4.0 Release Notes (2004), GSAS Team, NASA Goddard Flight Centre, Greenbelt, MD, U.S.A., available at: http://nsidc.org/data/icesat/gsas_v4.0_release.pdf

GSAS v4.1 Release Notes (2004), GSAS Team, NASA Goddard Flight Centre, Greenbelt, MD, U.S.A., available at: http://nsidc.org/data/icesat/gsas_v4.1_release.pdf

GSAS v4.3 Release Notes (2005), GSAS Team, NASA Goddard Flight Centre, Greenbelt, MD, U.S.A., available at: http://nsidc.org/data/icesat/isips_release.html

Haas, C. (2003), Dynamics versus thermodynamics: the sea ice thickness distribution, in *Sea Ice: an introduction to its physics, chemistry, biology, and geology*, Thomas, D. N. and G. S. Dieckmann (eds.), 402pp., Blackwell Science, Oxford, U. K.

Harding, D.J., Bufton, J. L., Frawley, J. J. (1994), Satellite laser altimetry of terrestrial topography – vertical accuracy as a function of surface slope, roughness, and cloud cover, *IEEE Trans. Geosci. Rem. Sens.*, *32*(2), 329-339.

Herring, T and K. Quinn (2001), Atmospheric Delay Correction to GLAS Laser Altimeter Ranges, *GLAS ATBD, v. 2.1*, NASA Goddard Space Flight Centre, Greenbelt, MD, U.S.A.

Holland, M. M., and C. M. Bitz (2003), Polar amplification of climate change in coupled models, *Clim. Dyn.*, *21*, 221-232.

Holloway, G. and T. Sou (2002), Has Arctic sea ice rapidly thinned? *J. Clim.*, *15*, 1691-1701.

Hu, Z.-Z., S. I. Kuzmina, L. Bengtsson, and D. M. Holland (2004), Sea-ice change and its connection with climate change in the Arctic in CMIP2 simulations, *J. Geophys. Res.*, *109*, D10106, doi:10.1029/2003JD004454.

Hvidegaard, S. M., and R. Forsberg (2002), Sea-ice thickness from airborne laser altimetry over the Arctic Ocean north of Greenland, *Geophys. Res. Lett.*, *29*(20), 1952, doi:10.1029/2001GL014474.

Intergovernmental Panel on Climate Change (IPCC) (1994), *Climate Change 1994: Radiative Forcing of Climate Change and an Evaluation of the IPCC IS92 Emission Scenarios*, Houghton, J. T., L. G. Meira Filho, J. Bruce, Hoesung Lee, B. A. Callander, E. Haites, N. Harris and K. Maskell (eds.), 339pp., Cambridge University Press, Cambridge, U. K.

Johannessen, O. M., L. Bengtsson, M. W. Miles, S. I. Kuzmina, V A. Semenov, G. V. Alekseev, A. P. Nagurnyi, V. F. Zakharov, L. P. Bobylev, L. H. Pettersson, K. Hasselmann and H. P. Cattle (2004), Arctic climate change: observed and modelled temperature and sea-ice variability, *Tellus*, *56A*, 328-341, doi:10.1111/j.1600-0870.2004.00060.x

Johannessen, O.M., E. V. Shalina and M. W. Miles (1999), Satellite evidence for an Arctic sea ice cover in transformation, *Science*, *286*, 1937-1939.

Kenyon, S., and R. Forsberg (2001), Arctic Gravity Project: A status, in *Gravity, Geoid and Geodynamics 2000*, M. G. Sideris (ed), *Int. Assoc. Geod. Symp.*, *v. 123*, 391– 395, Springer, New York, U.S.A.

Kowalik, Z. and A. Yu. Proshutinsky (1994), The Arctic Ocean tides, in *The Polar Oceans and their Role in Shaping the Global Environment*, O. M. Johannessen, R. D. Muench, and J. E. Overland (eds.), *Geophysical Monograph*, *85*, 137-158, AGU, USA.

Krabill, W., E. Frederick, S. Manizade, C. Martin, J. Sonntag, R. Swift, R. Thomas, W. Wright, J. Yungel (1999), Rapid thinning of parts of the Southern Greenland ice sheet, *Science*, *283*, 1522-1524.

Kwok, R. (2002), Sea ice concentration estimates from satellite passive microwave radiometry and openings from SAR ice motion, *Geophys. Res. Lett.*, *29*(9), 1311,doi:10.1029/2002GL014787.

Kwok, R. and G. F. Cunningham (2002), Seasonal ice area and volume production of the Arctic Ocean: November 1996 through April 1997, *J. Geophys. Res.*, *107*(C10), 8083, doi:10.1029/2000JC000469.

Kwok, R., G. F. Cunningham, H. J. Zwally, and D. Yi (2006), ICESat over Arctic sea ice: Interpretation of altimetric and reflectivity profiles, *J. Geophys. Res.*, *111*, C06006, doi:10.1029/2005JC003175.

Kwok, R., H. J. Zwally and D. Yi (2004), ICESat Observations of Arctic Sea Ice: A First Look, *Geophys. Res. Lett.*, *31*, L16401, doi:10.1029/2004GL020309.

Laxon, S and D. McAdoo (1994), Arctic Ocean gravity field derived from ERS-1 satellite altimetry, *Science*, *265* (5172), 621- 624.

Laxon, S and D. McAdoo (1998), Satellites provide new insights into polar geophysics, *EOS*, *79* (6), 69, 72-73.

Laxon, S. W., N. Peacock and D. Smith (2003), High interannual variability of sea ice thickness in the Arctic region, *Nature*, *425*, 947-949.

Le Provost, C. (2001), Ocean Tides, in *Satellite Altimetry and Earth Sciences: a handbook of techniques and applications*, *International geophysics series*, *v.69*, Lee-Leung Fu and Anny Cazenave (eds), 463pp., Academic Press, London, U.K.

Lemoine F. G., Kenyon S. C., Factor J. K., Trimmer R. G., Pavlis N. K., Chinn D. S., Cox C. M., Klosko S. M., Luthcke S. B., Torrence M. H., Wang, Y. M., Williamson R. G., Pavlis E. C., Rapp R. H., Olson T. R. (1998), The development of the joint NASA GSFC and the National Imagery and Mapping Agency (NIMA) geopotential model EGM96, *NASA Technical Paper NASA/TP-1998-206861*, Goddard Space Flight Centre, Greenbelt, MD, U.S.A.

Lindsay, R.W. and D. A. Rothrock (1995), Arctic sea ice leads from advanced very high resolution radiometer images. *J. Geophys. Res.*, *100*, 4533–4544.

Lindsay, R. W. and J. Zhang (2005), The thinning of Arctic sea ice, 1988-2003: Have we passed a tipping point? *J. Climate*, *18*, 4879-4894.

Lisano, M. E., Schutz, B.E. (2001), Arcsecond-level pointing calibration for ICESat laser altimetry of ice sheets, *Journal of Geodesy*, *75* (2-3), 99-108.

Luthcke, S. B., D. D. Rowlands, T. A. Williams, and M. Sirota (2005), Reduction of ICESat systematic geolocation errors and the impact on ice sheet elevation change detection, *Geophys. Res. Lett.*, *32*, L21S05, doi:10.1029/2005GL023689.

Mahesh, A., J. D. Spinhirne, D. P. Duda and E. W. Eloranta (2002), Atmospheric multiple scattering effects on GLAS altimetry - Part II: Analysis of expected errors in Antarctic altitude measurements, *IEEE Trans. Geo. Rem. Sens.*, *40*, 2353 – 2362.

Mann, M. E., R. S. Bradley and M. K. Hughes (1999), Northern Hemisphere temperatures during the past millennium: inferences, uncertainties, and limitations, *Geophys. Res. Lett.*, *26*(6), 759-762.

McAdoo, D., S. Farrell, S. Laxon, C. Wagner and V Childers (2006), A new GRACE-based Arctic Ocean geoid for oceanographic and sea ice altimetric investigations, *in preparation*.

McAdoo, D. C., and K. M. Marks (1992), Gravity fields of the southern ocean from Geosat data, *J. Geophys. Res.*, *97*, 3247-3260.

McAdoo, D. C., K. M. Marks, S. Laxon, A. L. Ridout and S. L. Farrell (2004), Inter-comparison of Altimetric, Surface and GRACE gravity over the Arctic Ocean (poster), *CDROM Proceedings of IAG Symposium*, Gravity, Geoid and Space Missions – GGSM2004, Porto, Portugal, September 2004.

McAdoo, D., C. Wagner and S. W. Laxon (2005), Improvements in Arctic gravity and geoid from CHAMP and GRACE: An evaluation, in *Earth Observation with CHAMP: Results from Three Years in Orbit*, C. Reigber, H. Luhr, P. Schwintzer, J. Wickert (eds.), 37-46, Springer Verlag, Berlin.

Meier, W., J. Stroeve, F. Fetterer, K. Knowles (2005), Reductions in Arctic sea ice cover no longer limited to summer, *EOS Trans. AGU*, *86*(36), 326-326.

Mitchell, J.F.B., et al. (2001), Detection of Climate Change and Attribution of Causes, in *Climate Change 2001: The Scientific Basis, Contribution of Working Group I to the Third Assessment Report of the Intergovernmental Panel on Climate Change*, Houghton, J. T., Y. Ding, D. J. Griggs, M. Noguer, P. J. van der Linden, X. Dai, K. Maskell, and C. A. Johnson (eds.), 881pp., Cambridge University Press, Cambridge, United Kingdom and New York, USA.

Moore III, B., W.L. Gates, L.J. Mata, A. Underdal, R.J. Stouffer, B. Bolin, A. Ramirez Rojas (2001), Advancing Our Understanding, in *Climate Change 2001: The Scientific Basis, Contribution of Working Group I to the Third Assessment Report of the Intergovernmental Panel on Climate Change*, Houghton, J. T., Y. Ding, D. J. Griggs, M. Noguer, P. J. van der Linden, X. Dai, K. Maskell, and C. A. Johnson (eds.), 881pp., Cambridge University Press, Cambridge, United Kingdom and New York, USA.

NSIDC 2006, *ICESat/GLAS Data Releases*, ICESat documentation available at: http://nsidc.org/data/icesat/data.html

Osterkamp, T. E. and V. E. Romanovsky (1999), Evidence for warming and thawing of discontinuous permafrost in Alaska, *Permafrost Periglacial Proc.*, *10*, 17-37.

Overpeck, J. T., M. Sturm, J. A. Francis, D. K. Perovich, M. C. Serreze, R. Benner, E. C. Carmack, S. Chapin III, S. C. Gerlach, L. C. Hamilton, L. D. Hinzman, M. Holland, H. P. Huntington, J. R. Key, A. H. Lloyd, G. M. MacDonald, J. McFadden, D. Noone, T. D. Prowse, P. Schlosser, and C. Vörösmarty (2005), Arctic system on trajectory to new, seasonally ice-free state, *EOS Trans. AGU*, *86*(34), 10.1029/2005EO340001.

Padman, L., and H. A. Fricker (2005), Tides on the Ross Ice Shelf observed with ICESat, *Geophys. Res. Lett.*, *32*, L14503, doi:10.1029/2005GL023214.

Padman, L., M. King, D. Goring, H. Corr, and R. Coleman (2003), Ice shelf elevation changes due to atmospheric pressure variations, *J. Glaciol.*, *49* (167), 521-526.

Parkinson, C. L. and D. J. Cavalieri (2002), A 21 year record of Arctic sea ice extents and their regional, seasonal and monthly variability and trends, *Ann. Glaciol.*, *34*, 441-446.

Parkinson, C. L., D. J. Cavalieri, P. Gloersen, H. J. Zwally and J. C. Comiso (1999), Arctic sea ice extents, areas and trends, 1978-1996, *J. Geophys. Res.*, *104*, 20837-20856.

Peacock, N. R., and S. W. Laxon (2004), Sea surface height determination in the Arctic Ocean from ERS altimetry, *J. Geophys. Res.*, *109*, C07001, doi:10.1029/2001JC001026.

Peacock, N. R., S. W. Laxon, W. Maslowski, D. P. Winebrenner and R. J. Arthern (1998), Geophysical signatures from precise altimetric height measurements in the Arctic Ocean, *Proc. of Intl. Geosci. Rem. Sens. Symp.*, 1964-1966, IGARSS 98, Seattle, U.S.A.

Peixoto, J. P. and A. H. Oort (1992), *Physics of Climate*, 520 pp., American Institute of Physics, New York, U.S.A.

Perovich, D. K. (1996), The optical properties of sea ice, *CRREL Monograph*, *96-1*, 24pp., U.S. Army Corps of Engineers, CRREL, Hanover, New Hampshire, U.S.A.

Perovich, D. K., T. C. Grenfell, J. A. Richter-Menge, B. Light, W. B. Tucker III, and H. Eicken (2003), Thin and thinner: Sea ice mass balance measurements during SHEBA, *J. Geophys. Res.*, *108*(C3), 8050, doi:10.1029/2001JC001079.

Phillips, H. A., J. R. Ridgway, J. B. Minster, D. Yi, C. Bentley (1999), Tidal Corrections, *GLAS ATBD, v. 2.0*, NASA Goddard Space Flight Centre, Greenbelt, MD, U.S.A.

Ray, R. (1999), A Global ocean tide model from T/P altimetry: GOT99.2, *NASA Tech. Mem.*, *209478*, NASA Goddard Space Flight Centre, Greenbelt, MD, USA.

Robinson, I. S. (2004), *Measuring the Oceans from Space: The principles and methods of satellite oceanography*, Praxis Publishing Ltd., Chichester, UK.

Rothrock, D. A., R. Kwok, and D. Groves (2000), Satellite views of the Arctic Ocean freshwater balance, in *The Freshwater Budget of the Arctic Ocean*, Lewis, E., P. Jones, P. Lemke, T. Prowse, P. Wadhams(eds.), p.409-451, Kluwer Ac. Pub., The Netherlands.

Rothrock, D. A., Y. Yu and G. A. Maykut (1999), Thinning of the Arctic sea ice cover, *Geophys. Res. Lett.*, *26*(23), 3469-3472.

Rothrock, D. A., J. Zhang and Y. Yu (2003), The Arctic ice thickness anomaly of the 1990s: A consistent view from observations and models, *J. Geophys. Res.*, *108* (C3), 3083, doi: 10.1029/2001JC001208.

Rudels, B. (1995), The thermohaline circulation of the Arctic Ocean and the Greenland Sea, in *The Arctic and Environmental Change*, Wadhams, P., J. A. Dowdeswell, A. N. Schofield (eds)., 193pp., Gordon and Breach Science Publishers, The Netherlands.

Schulson, E. M. (2004), Compressive shear faults within arctic sea ice: Fracture on scales large and small, *J. Geophys. Res., 109*, C07016, doi:10.1029/2003JC002108.

Schutz, B. E. (2002), Laser footprint location (geolocation) and surface profiles, *GLAS ATBD, v. 3.0*, NASA Goddard Space Flight Centre, Greenbelt, MD, U.S.A.

Schutz, B. E., H. J. Zwally, C. A. Shuman, D. Hancock, and J. P. DiMarzio (2005), Overview of the ICESat mission, *Geophys. Res. Lett.*, *32*, L21S01, doi:10.1029/2005GL024009.

Semiletov, I. P., N. I. Savelieva, G. E. Weller, I. I. Pipko, S. P. Pugach, A. Yu. Gukov, and L. N. Vasilevskaya (2000), The dispersion of Siberian river flows into coastal waters: meteorological, hydrological and hydrochemical aspects, in *The Freshwater Budget of the Arctic Ocean*, Lewis, E. L., P. Jones, P. Lemke, T. D. Prowse, P. Wadhams (eds.), p. 323–366, Kluwer Academic Pub., The Netherlands.

Serreze, M. C., J. A. Maslanik, T. A. Scambos, F. Fettere, J. Stroeve, K. Knowles, C. Fowler, S. Drobot, R. G. Barry and T. M. Haran (2003), A record minimum arctic sea ice extent and area in 2002, *Geophys. Res. Lett.*, *30*(3), 1110, doi: 10.1029/2002GL016406.

Sirota, J. M., S. Bae, P. Millar, D. Mostofi, C. Webb, B. Schutz, and S. Luthcke (2005), The transmitter pointing determination in the Geoscience Laser Altimeter System, *Geophys. Res. Lett.*, *32*, L22S11, doi:10.1029/2005GL024005.

Smith, D. M. (1998), Recent increase in the length of the melt season of perennial Arctic sea ice, *Geophys. Res. Lett.*, *25*, 655–658.

Stocker, T. F., et al. (2001), Physical Climate Processes and Feedbacks, in *Climate Change 2001: The Scientific Basis, Contribution of Working Group I to the Third Assessment Report of the Intergovernmental Panel on Climate Change*, Houghton, J. T., Y. Ding, D. J. Griggs, M. Noguer, P. J. van der Linden, X. Dai, K. Maskell, and C. A. Johnson (eds.), 881pp., Cambridge University Press, Cambridge, UK, and New York, USA.

Stroeve, J. C., M. C. Serreze, F. Fetterer, T. Arbetter, W. Meier, J. Maslanik, and K. Knowles (2005), Tracking the Arctic's shrinking ice cover: Another extreme September minimum in 2004, *Geophys. Res. Lett.*, *32*, L04501, doi: 10.1029/2004GL021810.

Sturm, M., J. Holmgren, and D. K. Perovich (2002), Winter snow cover on the sea ice of the Arctic Ocean at the Surface Heat Budget of the Arctic Ocean (SHEBA): Temporal evolution and spatial variability, *J. Geophys. Res.*, *107*(C10), 8047, doi:10.1029/2000JC000400.

Tapley, B. D., S. Bettadpur, M. Watkins and C. Reigber (2004), The gravity recovery and climate experiment: Mission overview, *Geophys. Res. Lett.*, *31*, L09607, doi:10.1029/2004GL019920.

Thomas, R., C. Davis, E. Frederick, S. Manizade, J. Sonntag, W. Krabill, and J. McConneh (1999), Greenland ice sheet elevation change since 1978 from radar and laser altimetry, *Polar Geography*, *23*(3), 169-184.

Tin, T. and M. O. Jeffries (2001), Sea-ice thickness and roughness in the Ross Sea, Antarctica, *Ann. Glaciol.*, *33*, 187-193.

Urban, T. J., and B. E. Schutz (2005), ICESat sea level comparisons, *Geophys. Res. Lett.*, *32*, L23S10, doi:10.1029/2005GL024306.

Vinje, T. (2001), Anomalies and trends of sea ice extent and atmospheric circulation in the Nordic Seas during the period 1864–1998, *J. Clim.*, 14, 255–267.

Wadhams, P. (1995), Arctic sea ice thickness and extent, in *The Arctic and Environmental Change*, Wadhams, P., J. A. Dowdeswell, A. N. Schofield (eds)., 193pp., Gordon and Breach Science Publishers, The Netherlands.

Wadhams, P. (2000), *Ice in the ocean*, 351pp., Gordon and Breach Science Pub., Australia.

Wadhams, P. and N. R. Davis (2000), Further evidence of the ice thinning in the Arctic Ocean, *Geophys. Res. Lett.*, *27*(24), 3973-3975.

Wadhams, P. and R. J. Horne (1980), An analysis of ice profiles obtained by submarine sonar in the Beaufort Sea, *J. Glaciol.*, *25*, 401-424.

Warren, S.G., I.G. Rigor, N. Untersteiner, V.F. Radionov, N.N. Bryazgin, Y.I. Aleksandrov, and R. Colony (1999), Snow depth on Arctic sea ice, *J. Clim.*, *12*(6), 1814– 1829.

Webb, D. J., B. A. de Cuevas and A. C. Coward (1998), The first main run of the OCCAM global ocean model, internal report of James Rennel Div., Southampton Oceanog. Cent., 50pp., Southampton, England, U.K

Wensnahan, M., and D. A. Rothrock (2005), Sea-ice draft from submarine-based sonar: Establishing a consistent record from analog and digitally recorded data, *Geophys. Res. Lett.*, *32*, L11502, doi:10.1029/2005GL022507.

Wingham, D. J. (1995), A method for determining the average height of a large topographic ice-sheet from observations of the echo received by a satellite altimeter, *J. Glaciol.*, *41*, 137, 125-141.

Wingham, D. J. and the CryoSat Science Advisory Group (2001), CryoSat calibration and validation concept, *ESA Document CS-PL-UCL-SY-0004*, 91pp., London, U.K (available at: http://cryosat.esa-ao.org/description/data/CVC.pdf)

Woodgate, R. A., K. Aagaard, R. D. Muench, J. Gunn, G. Björk, B. Rudels, A. T. Roach and U. Schauer (2001), The Arctic Ocean Boundary Current along the Eurasian slope and the adjacent Lomonosov Ridge: Water mass properties, transports and transformations from moored instruments, *Deep Sea Research - Part I: Oceanographic Research Papers*, *48*(8), 1757-1792.

Yi, D., C.R. Bentley and M.D. Stenoien (1997), Seasonal variation in the apparent height of the East Antarctic ice sheet, *Ann. Glaciol.*, *24*, 191-198.

Zwally, H. J. (1989), Growth of the Greenland ice sheet: interpretation, *Science*, *246*, 1589-1591.

Zwally, H. J., W. Abdalati, T. Herring, K. Larson, J. Saba, and K. Stefan (2002), Surface melt-induced acceleration of Greenland ice-sheet flow, *Science*, *297*, 218-222.

Zwally, H. J., A. C. Brenner, S. L. Farrell, S. W. Laxon and D. Yi (2003), Deriving sea ice freeboard height distributions and estimates of ice thickness from ICESat/GLAS laser altimetry, *Eos Trans. AGU*, *84*(46), Fall Meet. Suppl., Abstract C32A-0442.

Zwally, H. J., B. Schutz, W. Abdalati, J. Abshire, C. Bentley, A. Brenner, J. Bufton, J. Dezio, D. Hancock, D. Harding, T. Herring, B. Minster, K. Quinn, S. Palm, J. Spinhirne, R. Thomas (2002), ICESat's laser measurements of polar ice, atmosphere, ocean and land, *J. Geodynamics*, *34*, 405-445.

Zwally, H. J., R. H. Thomas and R. A. Bindschadler (1981), Ice-sheet dynamics by satellite laser altimetry, *NASA Technical Memorandum*, *82128*, NASA GSFC, Greenbelt, MD, U.S.A.